

# PROBING EXCITATION SPECTRA OF ULTRACOLD 2D AND 3D FERMIONIC SUPERFLUIDS

Dissertation  
zur Erlangung des Doktorgrades  
an der Fakultät für Mathematik, Informatik und Naturwissenschaften  
Fachbereich Physik  
der Universität Hamburg

vorgelegt von  
Hauke Biss

Hamburg, im August  
2023

Gutachter der Dissertation	Prof. Dr. Henning Moritz Prof. Dr. Ludwig Mathey
Zusammensetzung der Prüfungskommission	Prof. Dr. Henning Moritz Prof. Dr. Ludwig Mathey Prof. Dr. Michael Potthoff Prof. Dr. Roman Schnabel Jun.-Prof. Dr. Ralf Riedinger
Vorsitzender der Prüfungskommission	Prof. Dr. Michael Potthoff
Datum der Disputation	27.09.2023
Vorsitzender des Fach-Promotionsausschusses Physik	Prof. Dr. Günter H. W. Sigl
Leiter des Fachbereichs Physik	Prof. Dr. Wolfgang J. Parak
Dekan der Fakultät MIN	Prof. Dr.-Ing. Norbert Ritter

## ABSTRACT

This thesis focuses on experimental studies of strongly correlated fermionic superfluids in the crossover from a Bose-Einstein condensate (BEC) of molecules to a Bardeen-Cooper-Schrieffer (BCS) superfluid of weakly bound Cooper pairs. In the first part of the thesis we prepare homogeneous 3D ultracold Fermi gases and probe the full momentum-resolved low-energy excitation spectrum with Bragg spectroscopy. This allows us to directly observe the smooth crossover from a bosonic to a fermionic superfluid that takes place in the BEC-BCS crossover. Furthermore, we use the excitation spectra to extract key quantities of the many-body system, the speed of sound and the pairing gap, which provide quantitative benchmarks for theoretical predictions. In subsequent experiments, we study Fermi gases with a strong vertical confinement to probe the excitation spectrum of 2D Fermi gases, allowing us to compare the stability of 2D and 3D fermionic superfluids.

In the second part of the thesis we present the creation of spin-imbalanced ultracold Fermi gases in box potentials. They are close to the 2D regime ( $k_B T \ll \hbar\omega_z, \mu \approx \hbar\omega_z$ ) and we achieve temperatures about a factor of 2 lower than in previous works for 2D harmonically trapped gases for spin-imbalances smaller than  $P = 0.2$ . We experimentally observe that the gases are locally imbalanced with a nearly constant imbalance over the entire cloud. We do not observe any experimental indication of phase separation predicted by most theoretical works, which expect a first-order phase transition at very low temperatures resulting in formation of balanced domains and domains hosting the majority excess.



## ZUSAMMENFASSUNG

Diese Arbeit konzentriert sich auf experimentelle Studien von stark korrelierten fermionischen Suprafluiden im Übergang von einem Bose-Einstein-Kondensat (BEC) von Molekülen zu einem Bardeen-Cooper-Schrieffer (BCS) Suprafluid von schwach gebundenen Cooper-Paaren. Im ersten Teil der Arbeit präparieren wir homogene 3D ultrakalte Fermigase und untersuchen das vollständig impuls aufgelöste niederenergetische Anregungsspektrum mit Bragg-Spektroskopie. Dies ermöglicht es uns, den graduellen Übergang von einem bosonischen zu einem fermionischen Suprafluid, der im BEC-BCS-Übergang stattfindet, direkt zu beobachten. Darüber hinaus verwenden wir die Anregungsspektren, um wichtige Größen des Vielteilchensystems, die Schallgeschwindigkeit und die Energielücke, zu extrahieren und diese mit theoretischen Vorhersagen quantitativ zu vergleichen. In anschließenden Experimenten untersuchen wir Fermigase mit einer starken vertikalen Einschließung, um das Anregungsspektrum von 2D Fermigasen zu untersuchen. Dies ermöglicht es uns, die Stabilität von 2D und 3D fermionischen Suprafluiden zu vergleichen.

Im zweiten Teil der Arbeit präsentieren wir die Erzeugung von spin-unausgeglichene ultrakalten Fermigasen in Boxpotentialen. Sie befinden sich nahe dem 2D-Regime ( $k_B T \ll \hbar \omega_z$ ,  $\mu \approx \hbar \omega_z$ ), und wir erreichen Temperaturen, die um den Faktor 2 niedriger sind als in früheren Arbeiten mit 2D harmonisch eingeschlossenen Gasen für Spin-Ungleichgewichte kleiner als  $P = 0.2$ . Wir beobachten experimentell, dass die Gase lokal unausgeglichene sind und das Spin-Ungleichgewicht über die gesamte Wolke nahezu konstant bleibt. Wir beobachten keine experimentellen Hinweise auf eine Phasentrennung, die von den meisten theoretischen Arbeiten vorhergesagt wird. Diese erwarten einen Phasenübergang erster Ordnung bei sehr niedrigen Temperaturen, der zur Bildung von ausgeglichenen Domänen und Domänen, die den Überschuss beherbergen, führt.



## PUBLICATIONS

The following research articles have been published in the course of this thesis:

- *Propagation and Quantum-Limited Damping in a Two-Dimensional Fermi Gas*  
M. Bohlen, L. Sobirey, N. Luick, H. Biss, T. Enss, T. Lompe, and H. Moritz,  
*Physical Review Letters*, 124(24), 240403 (2020).
- *Superfluidity in a Strongly Correlated Two-Dimensional Fermi Gas*  
L. Sobirey, N. Luick, M. Bohlen, H. Biss, H. Moritz, and T. Lompe,  
*Science*, 372(6544), 844–846 (2021).
- *Excitation Spectrum and Superfluid Gap of an Ultracold Fermi Gas*  
H. Biss, L. Sobirey, N. Luick, M. Bohlen, J. J. Kinnunen, G. Bruun, T. Lompe, and H. Moritz,  
*Physical Review Letters*, 128(10), 100401 (2022)
- *Influence of Reduced Dimensionality on Fermionic Superfluids*  
L. Sobirey, H. Biss, N. Luick, M. Bohlen, H. Moritz, and T. Lompe,  
*Physical Review Letters*, 129(8), 083601 (2022).



# CONTENTS

1	Introduction .....	9
<b>I</b>	<b>Balanced Fermi gases</b> .....	<b>11</b>
2	Theory of the BEC-BCS crossover .....	13
2.1	Tuning interactions .....	13
2.2	Many-body ground state .....	15
2.3	Excitations at the mean-field level .....	19
2.4	Probing methods .....	24
2.5	Dynamic structure factor of a BEC .....	30
2.6	Dynamic structure factor of a Fermi gas .....	31
3	Excitation spectrum of ultracold 3D Fermi gases .....	37
3.1	Preparing homogeneous 3D Fermi gases .....	37
3.2	Implementation of Bragg spectroscopy .....	39
3.3	Measuring the excitation spectrum .....	43
3.4	The collective mode .....	45
3.5	The pair-breaking continuum and the pairing gap .....	46
4	Two-dimensional Fermi gases .....	51
4.1	The BKT phase transition .....	51
4.2	Scattering in two dimensions .....	52
4.3	The 2D BEC-BCS crossover .....	56
5	Spectroscopy in 2D Fermi gases .....	59
5.1	Sound propagation in a 2D Fermi gas .....	59
5.2	Critical velocity of a 2D Fermi gas .....	61
6	Comparing 2D and 3D superfluids .....	67
6.1	Dynamic structure factor in 2D Fermi gases .....	67
6.2	The pairing gap in 2D Fermi gases .....	68
6.3	Comparing pairing gaps in 2D and 3D Fermi gases .....	70
<b>II</b>	<b>Imbalanced Fermi gases</b> .....	<b>73</b>
7	Spin-imbalanced superfluids in two dimensions .....	75
7.1	Superfluidity with spin-imbalance .....	75
7.2	Studies of 3D spin-imbalanced Fermi gases .....	76
7.3	Studies of 2D spin-imbalanced Fermi gases .....	77
8	Preparing a spin-imbalanced 2D Fermi gas .....	81
8.1	Overview of the preparation .....	81
8.2	Detailed discussion of the preparation .....	82

9	Study of spin-imbalanced 2D Fermi gases .....	93
9.1	Density profiles and momentum distribution .....	93
9.2	Excitation spectrum .....	95
10	Classification of the observed imbalanced phase .....	97
10.1	Mean-field phases .....	98
10.2	Beyond mean-field in the BEC regime .....	105
10.3	Exotic phases .....	108
10.4	Finite temperature phases .....	109
	<b>CONCLUSION</b> .....	113
A	Calibration of auxiliary imaging system .....	117
B	Density calibration .....	119
C	Speed of sound from QMC calculations .....	121
D	Systematic uncertainties on the pairing gap .....	123
E	Magnetic field dependence of the ground state .....	125
F	The accordion lattice .....	127
	<b>BIBLIOGRAPHY</b> .....	129
	<b>ACKNOWLEDGEMENTS</b> .....	144

When studying systems of many quantum particles, it is intriguing that adding more particles can lead to emergent phases with spontaneously broken symmetries which simplify the description of many-body systems [1]. Prominent examples are ferromagnetism or superfluidity: In ferromagnets the ground state spontaneously breaks the rotational spin symmetry and the new order parameter emerging is the macroscopic magnetization. In fermionic superfluids the fermions form a macroscopic wavefunction  $\psi$ , serving as the new order parameter. The fixed phase  $\phi$  of the order parameter  $\psi \propto \Delta e^{-i\phi}$  breaks the  $U(1)$  symmetry.

Spontaneous symmetry breaking can show striking experimental consequences such as a macroscopic magnetic moment or an abruptly vanishing viscosity. We would also like to understand why this happens. For that microscopic theories are needed. Bardeen, Cooper, and Schrieffer (BCS) put forward a microscopic mechanism explaining superfluidity: a weak attractive interaction leads to correlations between fermions with opposite momentum and spin, resulting in the formation of so-called Cooper pairs [2]. These Cooper pairs, in turn, form a new macroscopic quantum state which is protected by a pairing gap.

The power of this microscopic theory is that it quantitatively predicts the emergent property of the broken symmetry phase, the value of the pairing gap, which turns out to be the amplitude of the order parameter,  $\Delta$ . The gap protects the system against Cooper pair breaking and from external perturbations and thus allows for dissipationless flow of the fluid around an impurity moving slower than a critical velocity [3].

However, for strongly correlated many-body systems, solving the microscopic theory exactly becomes excessively hard and often impossible because of the large Hilbert space. In some cases, this can make it extremely challenging to even find the qualitative nature of the ground state (e.g. high-temperature superconductors), and in other cases it only leads to quantitative errors with respect to approximate theories.

For  $s$ -wave superfluids in the strongly correlated regime, several open questions remain, which we will address in this thesis. One concerns the size of the pairing gap for strongly correlated superfluids, where advanced theories are available, but further experimental input is needed. Another open question raised by the field of high-temperature superconductors is the effect of enhanced quantum fluctuations on the pairing gap in two-dimensional (2D) systems. Furthermore, the introduction of spin-imbalance in 2D Fermi gases gives rise to numerous qualitative questions regarding the phase diagram. These concern the stability of predicted phases, the order of phase

transitions between them, and the potential existence of exotic phases with spatially varying order parameters.

In recent years, a new approach used to address such questions is the concept of quantum simulations [4]. These try to solve complex problems in physics using well-controlled quantum systems and ideally should provide qualitative and quantitative answers to the raised questions.

In this thesis, we perform quantum simulations using ultracold Fermi gases [5–7]. These gases consist of neutral fermionic atoms that interact via contact interactions, which can be controlled using Feshbach resonances [8]. This allows us to realize superfluids in the BEC-BCS crossover [9–11]. The crossover is characterized by a transition from the bosonic limit, where fermions form weakly interacting bosonic pairs, to the fermionic limit, where they form Cooper pairs. Within the crossover region, the fermions create a strongly correlated many-body system.

In the first part of this thesis, we prepare homogeneous 3D Fermi gases in the BEC-BCS crossover and measure their excitation spectrum. For that, we probe the systems with a two-photon process called Bragg spectroscopy. We observe both collective and single-particle excitations, showing how the superfluid is protected by a pairing gap and how a collective mode emerges. When the interaction strength is changed, the excitation spectrum reveals very clearly how a repulsive Bose gas transforms into an attractive Fermi gas. Furthermore, we extract quantitative values for the speed of sound and the pairing gap in the strongly interacting regime, allowing for a benchmark to theories.

In a next step, we study the effect of reduced dimensionality by preparing homogeneous 2D Fermi gases in the BEC-BCS crossover and probe their excitation spectrum. This allows us to extract the critical velocity, the speed of sound, and the superfluid gap. We compare the pairing gap of the 2D Fermi gases to the 3D counterpart and observe very comparable values of the gap for similar interactions, suggesting that the impact of the interaction strength is more significant than the influence of dimensionality.

In the second part of this thesis, we study spin-imbalanced 2D Fermi gases. If a spin-imbalance is introduced, the underlying pairing mechanism in BCS theory, Cooper pairing, is challenged, which can trigger a phase transition into the normal phase or more exotic phases. We prepare spin-imbalanced Fermi gases close to the 2D regime in a box potential at significantly lower temperatures than previously achieved. Interestingly, we do not see a phase separation, indicating that no first-order transition is present at the achieved temperatures and spin imbalances. These experiments are accompanied by an in-depth discussion of the theoretical phase diagram for 2D spin-imbalanced Fermi gases.

Part I

BALANCED FERMI GASES



# 2

## THEORY OF THE BEC-BCS CROSSOVER

After the discovery of superconductivity in 1911 [12], explaining the phenomenon by finding a microscopic theory proved to be very difficult. One reason were that electrons are fermions, which do not allow for condensation into a single-particle state, thereby excluding simple Bose-Einstein condensation. In 1957, however, Bardeen, Cooper, and Schrieffer (BCS) [2] formulated a theory which was ground-breaking for explaining superconductivity in various materials. They showed that pairing in momentum space of electrons with opposite momentum into so-called Cooper pairs is the central mechanism to form a macroscopically occupied quantum state. This state is protected in energy, allowing for a dissipationless flow of electrons. In the limit of weak attractive interactions between the fermions, the corresponding size of the Cooper pairs is much larger than the interparticle spacing.

However, if the attractive interaction becomes stronger, these pairs transform into tightly bound dimers that can form a Bose-Einstein condensate (BEC) (Fig. 2.1). Fascinatingly, the crossover from BCS to BEC is already included in the BCS theory [13, 14].

In this thesis, we study a phenomenon closely related to superconductivity, superfluidity, where the dissipationless flow of neutral atoms instead of electrons can occur, and we examine the BEC-BCS crossover. For that we use fermionic lithium atoms, tune their attractive interaction using a Feshbach resonance, and probe the excitation spectrum.

In this chapter, we first discuss how two-body interactions can be tuned using a Feshbach resonance. Then, we progress to the many-body problem and review the mean-field BEC-BCS theory with a particular emphasis on the excitation spectrum. In a next step, we discuss possible methods for probing the system and extracting the excitation spectrum. Lastly, we review previous measurements of the excitation spectrum for both BECs and Fermi gases.

### 2.1 Tuning interactions

For ultracold Fermi gases, pairwise interactions between atoms reduce to contact interactions in the s-wave channel. The reason for this is that the spatial extent of the interatomic van der Waals interaction potential becomes much smaller than the de-Broglie wavelength  $\lambda_{dB}$  and the interparticle distance which follows the inverse Fermi wavevector  $k_F^{-1}$ . For Fermi gases s-wave scattering between particles in the same spin state is excluded because the relative pair wavefunction must be antisymmetric. Thus, interactions are only possible between different spin states.

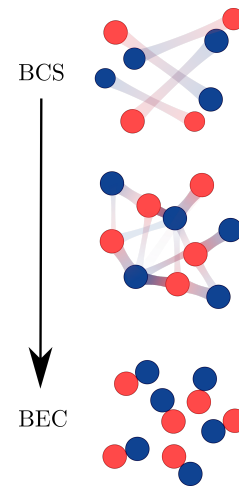
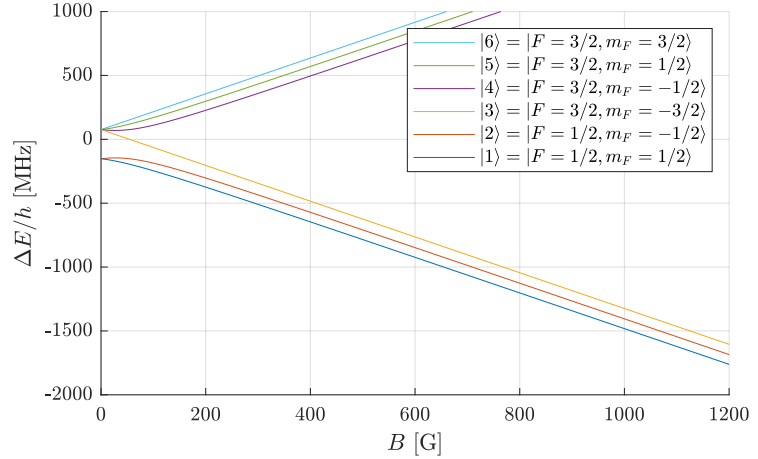


**Figure 2.1:** Visualization of the crossover from a BCS gas of large Cooper pairs (top) to a BEC of tightly bound dimers (bottom).

**Figure 2.2:** The ground state  $^2S_{1/2}$  of  $^6\text{Li}$  splits into six hyperfine states. They are labeled in ascending energy from  $|1\rangle$  to  $|6\rangle$ . For large fields, the coupling to the electron spin  $m_j = \pm 1/2$  dominates, resulting in two triplets of high- and low-field seeking states.



The interaction strength can be parameterized by a single parameter, the scattering length  $a$  [5]. Its sign is positive (negative) for a repulsive (attractive) interaction.

Experimentally, the scattering length of a spin mixture can be changed using a Feshbach resonance [8]. It is based on the mechanism that two atoms collide in an entrance channel at an energy that becomes resonant with a molecular bound state in a closed channel. By applying an external magnetic field, the energy of these two channels can be tuned with respect to each other. If the energy of the closed channel is above the entrance channel, the fermions interact attractively. If both channels become resonant, the scattering length diverges to  $a \rightarrow -\infty$ , marking the unitary point. Below the unitary point a two-body bound state enters the system such that bosonic dimers form. These dimers, in turn, interact repulsively with  $a > 0$ .

In this way, the Feshbach resonance smoothly tunes the inverse scattering length  $\eta = (k_F a)^{-1}$  from  $\eta \gg 0$  (weakly repulsive) to  $\eta \ll 0$  (weakly attractive), allowing the crossover from a BEC of molecules to a fermionic BCS state. To first approximation, the resonance of the scattering length follows the expression [8]

$$a = a_{\text{bg}} \left( 1 - \frac{\Delta_B}{B - B_0} \right), \quad (2.1)$$

where  $a_{\text{bg}}$  is the background scattering length,  $\Delta_B$  the width of the resonance and  $B_0$  the resonance position.

In our experiment, we use the broad Feshbach resonance of  $^6\text{Li}$  between the lowest two hyperfine states (see Fig. 2.2). For the experiments in the first part of this thesis, we prepare 50 % of the atoms in the lowest hyperfine state  $|1\rangle$  and 50 % of the atoms in state  $|2\rangle$ . The scattering lengths between the lowest three hyperfine states were precisely measured in Ref. [15] (Fig. 2.3) and resulted in  $a_{\text{bg}} = 1582(1)a_0$ ,  $B_0 = 832.18(8)$  G and  $\Delta_B = 262.3(3)$  G for the interaction between  $|1\rangle$  and  $|2\rangle$ .

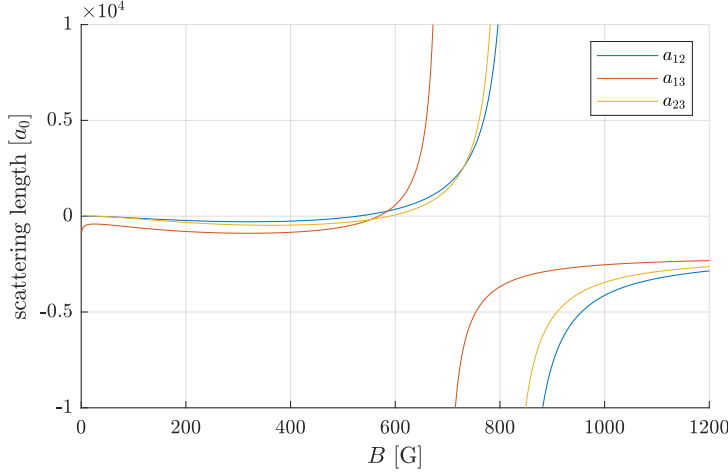


**Figure 2.3:** The scattering length  $a$  quantifies the interaction strength between the lowest three hyperfine state. The sign determines if the interaction is repulsive (positive) or attractive (negative). In this thesis, we will use mixtures of hyperfine states  $|1\rangle$  and  $|2\rangle$  which has a broad resonance at  $B = 832$  G. A more narrow pole at  $B = 543$  G is not visible in the data. The scattering lengths are taken from [15].

## 2.2 Many-body ground state

After discussing two-body interactions, we address the many-body problem, where  $N$  fermions are equally distributed into two hyperfine states denoted in the following with spin up ( $\uparrow$ ) and spin down ( $\downarrow$ ). For that we review the wavefunction of the many-body system in the mean-field BEC-BCS crossover at  $T = 0$ .

If both spin states do not interact, we can obtain the ground state by minimizing the total kinetic energy. The many-body wavefunction  $\Psi = \Psi(\mathbf{r}_1, \dots, \mathbf{r}_N)$  is then created using second quantization by populating the vacuum  $|0\rangle$  with fermions of both spin states up to the Fermi wavevector  $k_F$ ,

$$|\Psi_F\rangle = \prod_{|\mathbf{k}| < k_F, |\mathbf{k}'| < k_F} c_{\mathbf{k},\uparrow}^\dagger c_{\mathbf{k}',\downarrow}^\dagger |0\rangle, \quad (2.2)$$

where  $c_{\mathbf{k},\uparrow}^\dagger$  and  $c_{\mathbf{k},\downarrow}^\dagger$  are the creation operators of fermions with momentum  $\mathbf{k}$  and spin up and spin down, respectively. If we introduce an interaction between both spin states, this wavefunction does not coincide with the ground-state wavefunction anymore. If we assume a contact interaction and thus a momentum independent interaction, the Hamiltonian is

$$\hat{H} = \sum_{\mathbf{k}, \sigma \in \{\uparrow, \downarrow\}} \epsilon_{\mathbf{k}} c_{\mathbf{k},\sigma}^\dagger c_{\mathbf{k},\sigma} + V \sum_{\mathbf{k}, \mathbf{k}', \mathbf{q}} c_{\mathbf{k}+\mathbf{q},\uparrow}^\dagger c_{-\mathbf{k},\downarrow}^\dagger c_{\mathbf{k}'+\mathbf{q},\downarrow} c_{-\mathbf{k}',\uparrow}, \quad (2.3)$$

where the first term contains the kinetic energy  $\epsilon_{\mathbf{k}} = \frac{\hbar^2 \mathbf{k}^2}{2m}$ , and the second term the contact interaction<sup>1</sup> parameterized by its strength  $V < 0$ . Reading the interaction term from right to left, a spin-up fermion with momentum  $-\mathbf{k}'$  and a spin-down fermion with momentum  $\mathbf{k}' + \mathbf{q}$  scatter into a spin-up fermion with momentum  $\mathbf{k} + \mathbf{q}$  and spin-down fermion with momentum  $-\mathbf{k}$ .

In order to find the BCS ground state, we will now perform a drastic simplification: We only take scattering events with center-of-mass momentum  $\mathbf{q} = 0$  into account<sup>2</sup>. This approximation retains the most

<sup>1</sup> We use here the definition where  $V$  has units of energy. There is also a definition used, for example, in Ref. [6] where the interaction strength scales with the volume of the system  $\Omega$ , then the factor  $V$  is replaced by  $V/\Omega$ .

<sup>2</sup> Although this is not obvious, this approximation turns out to be a mean-field approximation, setting fluctuations in the Cooper pair number and pairing gap to zero.

relevant scattering processes, i.e. all the scattering processes that occur between particles on the Fermi surface. These processes have by far the highest phase space since even when including interactions most states inside (outside) the Fermi surface are occupied (empty). This so-called reduced Hamiltonian is given by

$$\hat{H} = \sum_{\mathbf{k}, \sigma=\{\uparrow, \downarrow\}} \epsilon_{\mathbf{k}} c_{\mathbf{k}, \sigma}^{\dagger} c_{\mathbf{k}, \sigma} + V \sum_{\mathbf{k}, \mathbf{k}'} c_{\mathbf{k}, \uparrow}^{\dagger} c_{-\mathbf{k}, \downarrow}^{\dagger} c_{\mathbf{k}', \downarrow} c_{-\mathbf{k}', \uparrow}. \quad (2.4)$$

As it turns out, the exact ground state of this simplified Hamiltonian can be found by starting with the BCS ansatz

$$|\Psi_{\text{BCS}}\rangle = \prod_{\mathbf{k}} (u_{\mathbf{k}} + v_{\mathbf{k}} c_{\mathbf{k}, \uparrow}^{\dagger} c_{-\mathbf{k}, \downarrow}^{\dagger}) |0\rangle. \quad (2.5)$$

It contains for each momentum  $\mathbf{k}$  a superposition of creating two particles of opposite spin and opposite momentum ( $\mathbf{k}\uparrow$  and  $-\mathbf{k}\downarrow$ ) or not creating such a ( $\mathbf{k}\uparrow, -\mathbf{k}\downarrow$ ) pair at all. Both scenarios are weighted by the variational parameters  $v_{\mathbf{k}}$  and  $u_{\mathbf{k}}$ , respectively. The solution for these parameters describing the ground state can be found in the grand canonical ensemble, where the chemical potential  $\mu$  is fixed, by minimizing the free energy  $H - \mu N$  of the system. One obtains [2]

$$u_{\mathbf{k}} = \sqrt{\frac{1}{2} \left( 1 + \frac{\xi_{\mathbf{k}}}{E_{\mathbf{k}}} \right)}, \quad (2.6)$$

$$v_{\mathbf{k}} = \sqrt{\frac{1}{2} \left( 1 - \frac{\xi_{\mathbf{k}}}{E_{\mathbf{k}}} \right)}, \quad (2.7)$$

where we introduce the equations  $\xi_{\mathbf{k}} = \epsilon_{\mathbf{k}} - \mu$  and

$$E_{\mathbf{k}} = \sqrt{\xi_{\mathbf{k}}^2 + \Delta^2}, \quad (2.8)$$

$$\Delta = -V \sum_{\mathbf{k}} u_{\mathbf{k}} v_{\mathbf{k}}, \quad (2.9)$$

with the chemical potential  $\mu$  and the parameter  $\Delta$ . Later, we will see that the quantity  $E_{\mathbf{k}}$  we just introduced corresponds to the energy to create a single particle excitation (e.g. pair breaking). The minimum of  $E_{\mathbf{k}}$ , the parameter  $\Delta$ , is therefore the excitation gap<sup>3</sup>.

Fascinatingly, the solutions given for  $u_{\mathbf{k}}$  and  $v_{\mathbf{k}}$  (Eq. 2.6 and Eq. 2.7) are valid throughout the BEC-BCS crossover. Only two parameters, the gap  $\Delta$  and the chemical potential  $\mu$ , change with the strength of the interaction  $V$ , which in turn can be parameterized by the inverse s-wave scattering length<sup>4</sup>  $1/(k_{\text{F}}a)$ . For a given interaction strength, solutions for  $\Delta$  and  $\mu$  can be found by solving a set of two equations, the number and the gap equation, in a self-consistent way [16] which can be done numerically using elliptic integrals [17].

The solutions for the gap and the chemical potential are plotted in Fig. 2.4. In the BCS limit, the chemical potential approaches the chemical potential of a non-interacting Fermi gas  $\mu = E_{\text{F}}$  and the gap  $\Delta$  the limiting value  $\Delta_{\text{BCS}} = 8 \exp(-\pi 2/(k_{\text{F}}|a|))$ . The gap here corresponds to the minimal energy required to break a Cooper pair (see Sect. 2.3.1).

<sup>3</sup> Which is also called *pairing gap* or *superfluid gap*.

<sup>4</sup> For that Eq. 94 in [6] must be used.

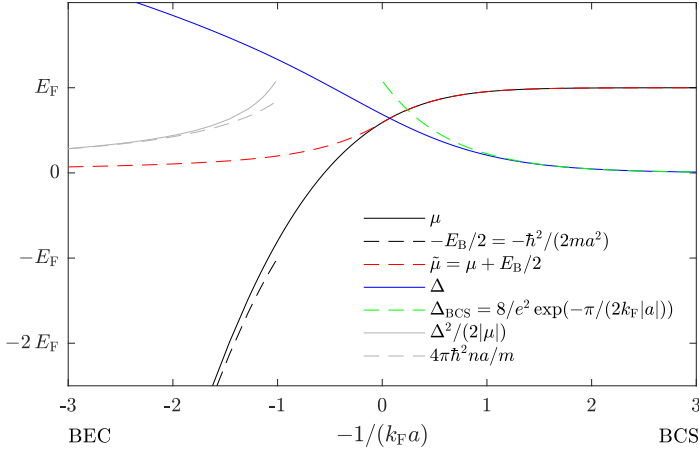


**Figure 2.4:** Behavior of the chemical potential  $\mu$  (black solid line) and the gap  $\Delta$  (blue solid line) in the mean-field description of the BEC-BCS crossover. The chemical potential smoothly connects the two-body binding energy  $-E_B/2$  (black dashed line) in the BEC limit to the Fermi energy  $E_F$  in the BCS limit. We can remove the binding energy to obtain a reduced chemical potential  $\tilde{\mu}$  (red dashed) that corresponds to the energy needed to add a paired fermion. The gap approaches the limit  $\Delta_{\text{BCS}}$  (green dashed line) in the BCS regime. In the BEC limit the quantity  $\Delta^2/(2|\mu|)$  (gray solid line) converges to the mean-field shift of a fermion interacting with the bath of dimers (gray dashed line).

In the BEC limit, repulsively interacting dimers with two-body binding energy<sup>5</sup>  $E_B = \hbar^2/(ma^2) = 2E_F/(k_F a)^2$  form. The chemical potential approaches<sup>6</sup>  $\mu = -E_B/2 + gn/2$  where  $g$  characterizes the bosonic interaction strength. The energy scale given by the gap  $\Delta$  has no physical meaning in the BEC limit, but rather the combination  $\Delta^2/(2|\mu|)$  which is the energy required to add an *unpaired* fermion to the system of dimers [6]. The energy required to add a *paired* fermion<sup>7</sup> is given by the reduced chemical potential

$$\tilde{\mu} = \mu + E_B/2,$$

where we remove the binding energy such that only the contribution from interactions between the dimers remain (red line in Fig. 2.4). The reduced chemical potential smoothly connects the BEC limit with weak repulsive interactions between dimers ( $\tilde{\mu} \approx gn/2$ ) to the BCS limit with weak attractive interactions between fermions ( $\tilde{\mu} \approx E_F$ ).

Equipped with solutions for the gap and the chemical potential throughout the crossover, we now look at the BCS wavefunction in more detail (Fig. 2.5). We plot the quantity  $v_k^2$  which corresponds to the probability of having a  $(\mathbf{k}\uparrow, -\mathbf{k}\downarrow)$  pair and the quantity  $u_k^2$  which is the probability of not having such a pair. Hence, the number of pairs is  $N = \sum_{\mathbf{k}} v_k^2$ . In addition, the fermionic momentum distribution of both spin states follows  $n_{\mathbf{k}} = v_k^2$ .

In the BCS limit (Fig. 2.5 d), the momentum distribution  $n_{\mathbf{k}}$  resembles a Fermi-Dirac distribution broadened by  $\delta k \sim \Delta/E_F \cdot k_F$  at the Fermi surface. We will show now that this broadening is essential to achieve condensation, a macroscopic occupation of a single-particle state. This is required to have off-diagonal long-range order and thus superfluidity [18].

The broadening of the momentum distribution is caused by the superposition of the absence and the occurrence of  $(\mathbf{k}\uparrow, -\mathbf{k}\downarrow)$  pairs around the Fermi surface. This superposition can be quantified by the correlation function  $\psi_{\mathbf{k}} = u_{\mathbf{k}}v_{\mathbf{k}}$  (red curve in Fig. 2.5 d). The available phase space due to this superposition allows a  $(\mathbf{k}\uparrow, -\mathbf{k}\downarrow)$

<sup>5</sup> Throughout this thesis we define two-body binding energies to be positive.

<sup>6</sup> Each dimer contains two fermions resulting in factors  $1/2$ .

<sup>7</sup> To do that we have to add a second fermion paired to the first fermion at the same time. Therefore, it is also useful to consider the bosonic chemical potential which gives the energy required to add a whole dimer. It is twice the reduced chemical potential,  $\mu_d = 2\tilde{\mu}$ .

**Figure 2.5:** Behavior of the particle occupation  $n_{\mathbf{k}} = v_{\mathbf{k}}^2$  and hole occupation  $u_{\mathbf{k}}^2$  in the BEC-BCS crossover (a-d). In the BEC limit (a), the particle occupation number becomes very small signaling the formation of deeply bound molecules. Here, the correlation wavefunction  $\psi_{\mathbf{k}}$  responsible for Cooper pair formation (red) and the fermionic pair wavefunction  $\varphi_{\mathbf{k}}$  of bound dimers (blue) collapse. Towards the BCS limit (d) Pauli blocking becomes important and the occupation number below  $k_{\text{F}}$  approaches unity. Around  $k_{\text{F}}$  both holes and particles are part of the ground state in a momentum range  $\delta k \sim \Delta/E_{\text{F}} \cdot k_{\text{F}}$ . Here, pairs can scatter and form Cooper pairs marked by the peak of the correlation wavefunction  $\psi_{\mathbf{k}}$ .

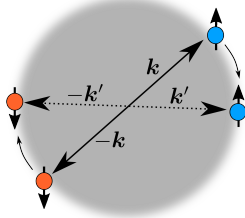
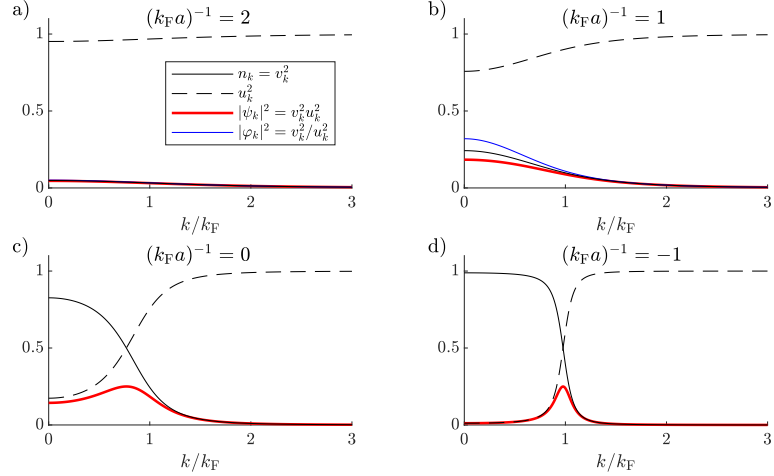


**Figure 2.6:** At the Fermi surface, a  $(\mathbf{k} \uparrow, -\mathbf{k} \downarrow)$  pair can scatter into a  $(\mathbf{k}' \uparrow, -\mathbf{k}' \downarrow)$  pair.

<sup>8</sup> This single-particle wavefunction is the complex order parameter [19] and related to the excitation gap by  $\Delta = -V \cdot \psi(\mathbf{r} = 0)$  (cf. Eq. 2.9.)



pair to interact by scattering into a  $(\mathbf{k}' \uparrow, -\mathbf{k}' \downarrow)$  pair (Fig. 2.6). These  $(\mathbf{k} \uparrow, -\mathbf{k} \downarrow)$  pairs, which can scatter at the Fermi surface, are Cooper pairs. However, the  $(\mathbf{k} \uparrow, -\mathbf{k} \downarrow)$  pairs deep within the Fermi sea cannot scatter because all states are fully occupied such that they do not contribute to Cooper pairing.

The Cooper pairs are described by a macroscopically occupied single-particle state. This state is given by the two-particle correlation we obtain when summing over all correlations in momentum space<sup>8</sup> [19, 20],

$$\begin{aligned} \psi(\mathbf{r} \equiv \mathbf{r}_1 - \mathbf{r}_2) &= \langle \Psi_{\text{BCS}} | \Psi_{\uparrow}^{\dagger}(\mathbf{r}_1) \Psi_{\downarrow}(\mathbf{r}_2) | \Psi_{\text{BCS}} \rangle \\ &= \sum_{\mathbf{k}} \langle \Psi_{\text{BCS}} | c_{\mathbf{k},\uparrow} c_{-\mathbf{k},\downarrow} | \Psi_{\text{BCS}} \rangle e^{i\mathbf{k} \cdot \mathbf{r}} = \sum_{\mathbf{k}} \psi_{\mathbf{k}} e^{i\mathbf{k} \cdot \mathbf{r}}. \end{aligned} \quad (2.10)$$

The number of Cooper pairs is given by  $N_0 = \sum_{\mathbf{k}} \psi_{\mathbf{k}}^2$  [21] which corresponds to the area under the red curve in Fig. 2.5 d.

Towards the BEC regime, the extent of the correlation function in the momentum space becomes broader and this total area increases (Fig. 2.5 c-a). Therefore, the number of Cooper pairs increases which we can quantify by normalizing it with the total number of  $(\mathbf{k} \uparrow, -\mathbf{k} \downarrow)$  pairs to obtain the condensate fraction [5, 22, 23],

$$\lambda = \frac{N_0}{N} = \frac{1}{N} \sum_{\mathbf{k}} |\psi_{\mathbf{k}}|^2 = \frac{1}{N} \sum_{\mathbf{k}} u_{\mathbf{k}}^2 v_{\mathbf{k}}^2.$$

The condensate fraction is  $\lambda \sim \Delta/E_{\text{F}}$  in the BCS regime and increases to 1 in the BEC regime (Fig. 2.7).

An complementary explanation why the condensate fraction approaches 1 in the BEC regime is that the system crosses over to a bosonic condensate where all fermions form dimers. To form local pairs, the fermions paired in real space have to occupy a large region in momentum space. Thus, the occupation number  $v_{\mathbf{k}}^2$  is much smaller than 1 and is distributed over a wide momentum range (see Fig. 2.5 a).

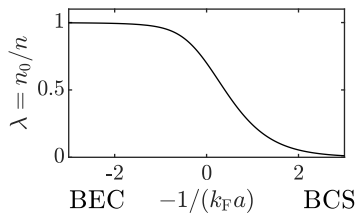


**Figure 2.7:** The condensate fraction in the BEC-BCS crossover approaches  $\lambda = 1$  in the BEC limit and  $\lambda = 3\pi e^{-2} \Delta/E_{\text{F}}$  in the BCS limit [22].

The condensed dimers can be described with a bosonic creation operator

$$b_0^\dagger = \sum_{\mathbf{k}} \varphi_{\mathbf{k}} c_{\mathbf{k},\uparrow}^\dagger c_{-\mathbf{k},\downarrow}^\dagger, \quad (2.11)$$

where the fermionic creation operators are weighted by the Fourier transform  $\varphi_{\mathbf{k}}$  of the fermionic pair wavefunction<sup>9</sup> [13], which differs from the correlation function  $\psi_{\mathbf{k}}$ . We see in Fig. 2.5 a that  $\psi_{\mathbf{k}}$  and  $\varphi_{\mathbf{k}}$  collapse, which shows that the correlations that create Cooper pairs evolve into the momentum distribution of fermions bound within dimers.

With that, we now have a good understanding of how the ground state crosses from a BCS state to a BEC of dimers. However, the truly interesting region lies in between, where the system cannot be clearly regarded as a fermionic or bosonic system: In this crossover regime, the mean-field theory presented here neglects strong many-body correlations between pairs of fermions [10] such that it yields quantitatively incorrect results, as we will see for the pairing gap  $\Delta$  in Chap. 3. The so-called unitary point<sup>10</sup> located at  $1/(k_F a) = 0$  falls into this regime and we would like to briefly discuss it.

At this point the two-body binding energy of the dimers becomes zero and the positive *s*-wave scattering length diverges. Therefore, the scattering length disappears from the many-body problem, and only the interparticle distance sets the relevant length scale. By expressing everything in Fermi units, e.g. Fermi energy or Fermi wavevector, the properties of the many-body system become universal and apply also to other unitary limited systems, e.g. dilute neutron matter which has a scattering length which is about 10 times larger than the interparticle distance, such that  $1/k_F a = 0.04$  [25].

The name *unitarity* or *unitary limit* comes from the fact that, in general, the scattering matrix (S matrix) must be unitary to conserve probability during a scattering event. The unitarity of the S matrix results in an upper limit of the *s*-wave scattering cross section of  $\sigma = \lambda_{dB}^2/\pi$ , which is reached in the unitary limit [26]. Its strong interactions combined with its universality make the unitary Fermi gas an interesting system to study [27–34]. The first studies concentrated on universal thermodynamic quantities [27, 28], which revealed a sudden change in the specific heat at the transition temperature from the normal to superfluid phase, analogous to the lambda peak observed in <sup>4</sup>He. In later studies, the density-density response [29], contact parameter [31], collective modes [32–34], and the highly spin-imbalanced case [30] were investigated.

### 2.3 Excitations at the mean-field level

After this brief discussion of the ground state, we will now address possible many-body excitations of the BCS state. There are two kinds of excitations: Excitations of single atoms and collective excitations in which multiple atoms are involved.

<sup>9</sup> Expressed in the variational parameters we used above, one obtains  $\varphi_{\mathbf{k}} = v_{\mathbf{k}}/u_{\mathbf{k}}$  [6].

<sup>10</sup> For detailed reviews please refer to [24] and Chap. 5 in [9].

### 2.3.1 Single-particle excitations

In a non-interacting Fermi gas single-particle excitations are given by hole excitations  $c_{\mathbf{k},\{\downarrow,\uparrow\}}$  for momenta  $\mathbf{k} < k_F$  where a fermion inside the Fermi sea is removed from the system and particle excitations  $c_{\mathbf{k},\{\downarrow,\uparrow\}}^\dagger$  for momenta  $\mathbf{k} > k_F$  where a fermion is added to the system. When inspecting the BCS ground state (Eq.2.5), we notice that these hole and particle excitations are already partly present at all momenta weighted by  $u_{\mathbf{k}}$  and  $v_{\mathbf{k}}$ . Therefore, the BCS ground state is not the vacuum state with respect to these excitations, i.e.  $c_{\mathbf{k},\{\downarrow,\uparrow\}} |\Psi_{\text{BCS}}\rangle \neq 0 \forall \mathbf{k}$  and  $c_{\mathbf{k},\{\downarrow,\uparrow\}}^\dagger |\Psi_{\text{BCS}}\rangle \neq 0 \forall \mathbf{k}$ .

Instead, we will derive new single-particle excitations  $\gamma$  as linear combinations of  $c$  and  $c^\dagger$  which are orthogonal to the BCS ground state. To do that, we transform the Hamiltonian in Eq. 2.4 such that it only contains diagonal terms  $\gamma^\dagger \gamma$ . If this is the case, the excitation number is conserved over time, i.e. the excitations are long-lived. However, this transformation is not possible because the interaction term contains four single-particle operators of the form  $c^\dagger c^\dagger c c$ .

Here, a mean-field approximation comes to our rescue: We have seen above that the BCS ground state consists of pairs of states  $(\mathbf{k} \uparrow, -\mathbf{k} \downarrow)$  that are occupied or unoccupied such that there is a finite expectation value  $\psi_{\mathbf{k}} = \langle c_{\mathbf{k},\uparrow} c_{-\mathbf{k},\downarrow} \rangle$  [6]. We now perform the mean-field approximation by taking four operators and replacing two of them with these expectation values. This results in the mean-field Hamiltonian

$$\hat{H}_{\text{MF}} = \sum_{\mathbf{k},\sigma=\{\uparrow,\downarrow\}} \xi_{\mathbf{k}} c_{\mathbf{k},\sigma}^\dagger c_{\mathbf{k},\sigma} + V \sum_{\mathbf{k},\mathbf{k}'} c_{\mathbf{k},\uparrow}^\dagger c_{-\mathbf{k},\downarrow}^\dagger \psi_{\mathbf{k}'} + \psi_{\mathbf{k}'} c_{\mathbf{k}',\downarrow} c_{-\mathbf{k}',\uparrow} - \psi_{\mathbf{k}'} \psi_{\mathbf{k}},$$

which only contains terms with two single-particle operators.

Now we can diagonalize the Hamiltonian into

$$\hat{H}_{\text{MF}} = \sum_{\mathbf{k}} E_{\mathbf{k}} (\gamma_{\mathbf{k},\uparrow}^\dagger \gamma_{\mathbf{k},\uparrow} + \gamma_{\mathbf{k},\downarrow}^\dagger \gamma_{\mathbf{k},\downarrow}) + \text{const.}$$

by using the Bogoliubov transformation [35, 36]

$$\gamma_{\mathbf{k},\uparrow}^\dagger = u_{\mathbf{k}} c_{\mathbf{k},\uparrow}^\dagger - v_{\mathbf{k}} c_{-\mathbf{k},\downarrow}, \quad (2.12)$$

$$\gamma_{-\mathbf{k},\downarrow} = v_{\mathbf{k}} c_{\mathbf{k},\uparrow}^\dagger + u_{\mathbf{k}} c_{-\mathbf{k},\downarrow}, \quad (2.13)$$

and the excitation energy

$$E_{\mathbf{k}} = \sqrt{\xi_{\mathbf{k}}^2 + \Delta^2}. \quad (2.14)$$

Similarly to the ground state, which is created by a superposition of fermionic excitations, these excitations are also superpositions of fermionic excitations weighted by the same parameters  $u_{\mathbf{k}}$  and  $v_{\mathbf{k}}$  that are also found in the definition of the ground state in Eq. 2.5.<sup>11</sup> We can recover the bare fermionic hole and particle excitation if we take the non-interacting limit by setting  $u_{\mathbf{k}} = 0, v_{\mathbf{k}} = 1$  for  $\mathbf{k} < k_F$  and  $u_{\mathbf{k}} = 1, v_{\mathbf{k}} = 0$  for  $\mathbf{k} > k_F$ . As the BCS ground state does not contain excitations, we obtain

$$\gamma_{\mathbf{k},\uparrow} |\Psi_{\text{BCS}}\rangle = \gamma_{-\mathbf{k},\downarrow} |\Psi_{\text{BCS}}\rangle = 0.$$

<sup>11</sup>The creation operators of these excitations are superpositions of fermionic creation and annihilation operators. Such an excitation that does not conserve the number of fermions is allowed because we are in the grand canonical ensemble and can remove or add fermions from a reservoir.

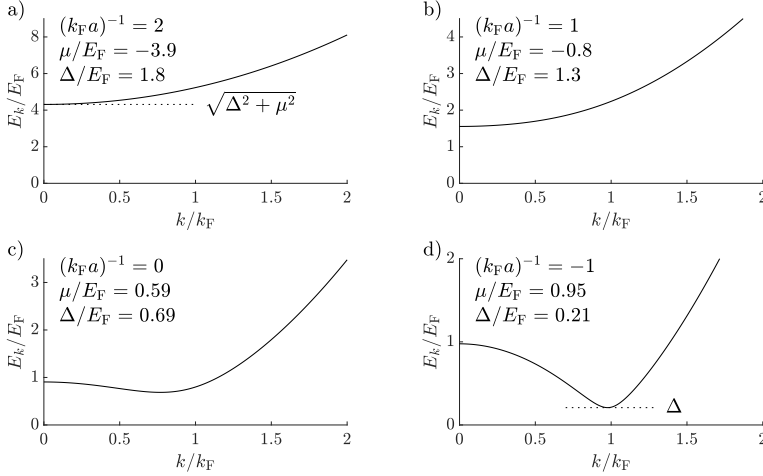


**Figure 2.8:** Single-particle excitation energy  $E_k$  in the BEC-BCS crossover. (a-b) In the BEC limit the gap in the excitation energy is located at  $k = 0$  and given by  $\sqrt{\mu^2 + \Delta^2}$ . (c-d) Between  $(k_F a)^{-1} = 1$  and  $(k_F a)^{-1}$  the chemical becomes positive. From here on, the minimum is  $\Delta$  and located at finite momentum  $k_\mu = \sqrt{2m\mu/\hbar^2}$  which approaches  $k_F$  in the BCS limit.

Thus, the BCS ground state forms the vacuum state for these excitations. In addition, the operators  $\gamma_{k,\uparrow}^\dagger$  and  $\gamma_{-k,\downarrow}^\dagger$  obey the fermionic commutator relations. Because of that, these single-particle excitations are also called quasiparticles.

Both spin-up and spin-down quasiparticles have a spin-independent eigenenergy given by  $E(k)$  (Eq. 2.14) which we already used above in the definition of the parameters  $u_k$  and  $v_k$ . As shown in Fig.2.8, the minimal excitation energy for single-particle excitation is  $\Delta$  in the BCS limit. These excitations are located at  $k = k_F$ . Towards the BEC limit, the minimal energy increases as the gap  $\Delta$  increases and the location of the corresponding excitation moves to a smaller momentum. When  $\mu$  becomes smaller than zero at  $1/(k_F a) = 0.55$ , the minimum in the excitation energy is located at  $k = 0$  and has the value  $\sqrt{\mu^2 + \Delta^2}$ . In this regime, the excitations correspond to the removal of one fermion from an interacting molecule.

The single-particle excitations derived so far were very successful in the 1950s in describing various quantities and observations in superconductors [37]. But one problem remained: For the description of the Meissner effect observed in superconductors the derivation turned out to be not gauge-invariant [37, 38]. This problem was solved by Anderson [39] by also considering collective modes in the system, which correspond to density oscillations.

In a superconductor, the collective excitations are pushed to large energies due to the Coulomb repulsion between the electrons. This is the reason why just considering single-particle excitation is still sufficient for the derivation of observables in a BCS superconductor because the single-particle excitations are the lowest-lying excitations of the system. However, in a neutral superfluid Coulomb repulsion is missing, and collective excitations already appear at low energy, which make them relevant for our system such that we will discuss them now.

## 2.3.2 Collective excitations

Up to this point, we neglected in the interaction term any scattering events with nonzero center-of-mass momentum  $q$  (see Eq.2.3 and Eq.2.4). Therefore, we did not encounter any collective excitations because they arise due to interactions between fermionic pairs with nonzero center-of-mass momentum.

If we relax this restriction by also including fermionic pairs with nonzero momentum, solving the resulting equations becomes more difficult but it can be done using either a dynamic BCS model [40] or, equivalently, a random phase approximation (RPA) [39, 41, 42]. The result of these calculations is, at low momentum, a gapless excitation throughout the crossover, whose energy scales linearly with momentum, a sound wave. We show the slope of this excitation, the speed of sound, in the BEC-BCS crossover in Fig. 2.9. We will now look at the general mechanism resulting in a Bogoliubov-Anderson phonon in a superfluid [39] and discuss the Bogoliubov mode in the BEC limit [43].

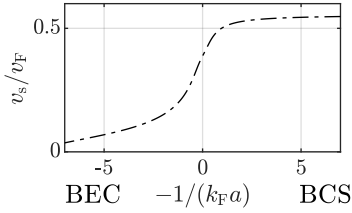


**Figure 2.9:** The speed of sound increases over the BEC-BCS crossover as the gas becomes more fermionic. In the BCS regime, it approaches the weakly interacting limit  $v_F/\sqrt{3}$ . Taken from QMC calculations [44].

In the BEC-BCS crossover, the gapless Nambu-Goldstone mode is not a pure phase fluctuation but a superposition of a fluctuation in the phase and amplitude of the order parameter. Furthermore, for positive  $\mu$ , an additional collective mode, the amplitude mode exists with a minimal energy of  $2\Delta$ . In this mode the amplitude of the order parameter oscillates. This mode is expected to reside within the single-particle continuum [46] and is not visible in our measurements, probably because of strong damping into single-particle excitations. Therefore, we do not discuss the amplitude mode in this thesis and refer to the excellent review by Pekker and Varma [47] instead.

In a superfluid, the Bogoliubov-Anderson phonon arises because the superfluid order parameter  $\psi \propto \Delta e^{-i\phi}$  spontaneously breaks the  $U(1)$  symmetry of the underlying Hamiltonian, resulting in a Nambu-Goldstone mode [45]. The Hamiltonian is symmetric with respect to the phase of the order parameter, and the energy of the ground state is independent of the phase. Below the critical temperature, the rise of an order parameter with a specific phase spontaneously breaks this symmetry, leading to a gapless Nambu-Goldstone mode corresponding to phase fluctuations of the order parameter. The Nambu-Goldstone mode forms the phononic excitation in the BCS regime. It persists when one crosses over into a BEC, which also has a nonzero order parameter. However, its slope, which corresponds to the speed of sound, decreases when the gas becomes less fermionic and therefore less stiff (see Fig. 2.9).

In the BEC limit, the sound excitation corresponds to the Bogoliubov mode of a weakly-interacting Bose gas [43]. It arises because the dimers with mass  $m_d = 2m$  and chemical potential  $\mu_d$  have a repulsive dimer-dimer contact interaction with the s-wave scattering length  $a_d = 0.6a_{12}$  [48]. Due to the repulsive interaction, collective excitations emerge at low momentum, which are superpositions of the pair creation and annihilation operators,  $b^\dagger$  and  $b$  introduced in Eq. 2.11. These superpositions are again given by a Bogoliubov transformation

$$\alpha_k = u_{k,B} b_k + v_{k,B} b_k^\dagger \quad (2.15)$$

$$\alpha_k^\dagger = u_{k,B} b_k^\dagger + v_{k,B} b_k \quad (2.16)$$

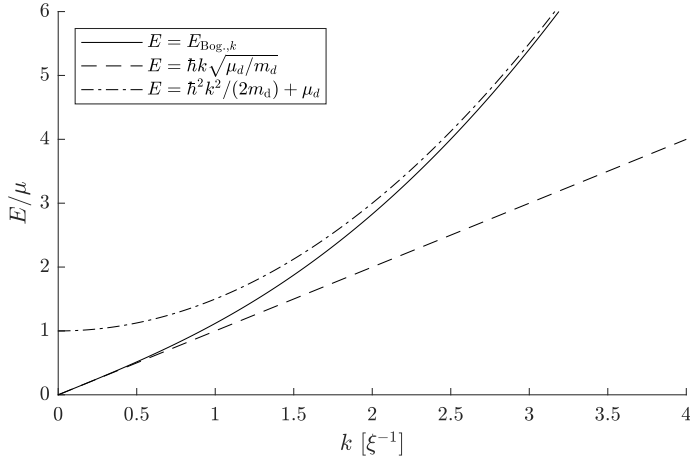


**Figure 2.10:** The excitations of a repulsive Bose gas follow the Bogoliubov dispersion (solid line, Eq. 2.17). At the inverse healing length  $\xi^{-1}$ , it transforms from a linear dispersion (dashed line) into a free particle dispersion shifted by the chemical potential (dashed dotted line)

with the variational parameters

$$u_{k,B} = \frac{1 + \zeta_k^{-1/2}}{2\zeta_k^{-1/4}},$$

$$v_{k,B} = \frac{1 - \zeta_k^{-1/2}}{2\zeta_k^{-1/4}}$$

and definitions

$$\zeta_k = 1 + 2\mu_d/\epsilon_{k,d},$$

$$\epsilon_{k,d} = \frac{\hbar^2 k^2}{2m_d}.$$

The eigenenergies of these excitations are given by the Bogoliubov dispersion

$$E_{\text{Bog.},k} = \sqrt{\epsilon_{k,d}(\epsilon_{k,d} + 2\mu_d)}, \quad (2.17)$$

shown in Fig. 2.10. For momenta below the inverse healing length,  $k \ll \xi^{-1} = \sqrt{m_d \mu_d}/\hbar$ , the dispersion relation becomes linear,  $E_{\text{Bog.},k} \rightarrow \hbar k \sqrt{\mu_d/m_d}$ . This linear part of the dispersion relation is a sound mode with a speed of sound  $v_s = \sqrt{\mu_d/m_d}$ . For wavelengths  $k \gg \xi^{-1}$ , the dispersion approaches a quadratic free-particle dispersion of free molecules shifted by the chemical potential,  $E_{\text{Bog.},k} \rightarrow \epsilon_{k,d} + \mu_d$ .

In summary, we expect collective excitations throughout the BEC-BCS crossover, from which we can extract the speed of sound. In addition, we expect single-particle excitations, which also contain valuable information about the system, for instance, the pairing gap  $\Delta$ . Therefore, it would be intriguing to measure the energy of these excitations by perturbing the system, which we discuss next.

## 2.4 Probing methods

<sup>12</sup> For a detailed review of spectroscopic measurements in ultracold gases we refer the reader to the excellent review by C. Vale and M. Zwierlein [49].

The two measurement techniques relevant for us are radio frequency (RF) spectroscopy and Bragg spectroscopy<sup>12</sup>. The main difference between both is that RF spectroscopy perturbs the system by coupling fermions in one hyperfine state to a third hyperfine state while Bragg spectroscopy conserves the hyperfine state. In the following, we give a summary of RF spectroscopy. Then, we discuss the technique used in this thesis, Bragg spectroscopy.

### 2.4.1 RF spectroscopy

The basic idea of RF spectroscopy is to measure the energy needed to transfer an atom from one hyperfine states to a third hyperfine state using a radio frequency field. In the following, we will summarize how RF spectroscopy is suited to measure the excitation spectrum of the many-body system. For that, we briefly repeat the derivation of the RF spectrum presented in Sec. 4.7.2 in [6] and summarize the most relevant measurements.

We start with a balanced two-spin mixture with particles in two hyperfine states  $|1\rangle$  and  $|2\rangle$  from which some particles shall be excited into a third state  $|3\rangle$ . Assuming that the third state does not interact with the other two hyperfine states and using the fact that RF photons carry a negligible momentum<sup>13</sup> the RF coupling from one hyperfine state (we choose  $|2\rangle$ ) to a third state  $|3\rangle$  with a Rabi frequency  $\omega_R$  is described by the operator

<sup>13</sup> For a typical RF frequency  $\nu = 100\text{MHz}$  the wavevector is  $k = 0.3 \times 10^{-6} \mu\text{m} \approx 1 \times 10^{-7} k_F$ .

$$\hat{V} = \frac{\hbar\omega_R}{2} \sum_{\mathbf{k}} c_{\mathbf{k},3}^\dagger c_{\mathbf{k},2} + c_{\mathbf{k},2}^\dagger c_{\mathbf{k},3}.$$

Without interactions the energy required for these excitations is given by the bare hyperfine splitting  $\Delta E = \hbar\omega_{23}$  between states  $|2\rangle$  and  $|3\rangle$ . In a many-body system, interactions can shift the resonance frequency of the RF photon. In particular, if we take the BCS ground state derived in Sec. 2.2, the resonant RF energy to excite a fermion in  $|2\rangle$  with momentum  $\mathbf{k}$  into state  $|3\rangle$  is shifted. The reason is that the energy cost to remove a fermion in  $|2\rangle$  is given by<sup>14</sup>  $E_{\mathbf{k}} - \mu$  while the energy cost<sup>15</sup> to add a fermion in state  $|3\rangle$  is given by the kinetic energy  $\epsilon_{\mathbf{k}}$ . The resonant energy is, therefore, given by

<sup>14</sup> The chemical potential must be subtracted because the spin state of the fermion is changed.

<sup>15</sup> We neglect shifts due to interactions of state 3 with state 2 and 1.

$$\hbar\Omega_{\mathbf{k}} = \hbar\omega_{23} + (E_{\mathbf{k}} - \mu) + \epsilon_{\mathbf{k}}. \quad (2.18)$$

Inserting the expression for  $E_{\mathbf{k}}$  from Eq. 2.8 the energy to excite a particle with respect to the bare transition has a minimum at  $\mathbf{k} = 0$ . We obtain a threshold energy of [6]

$$\hbar\omega_{\text{th}} - \hbar\omega_{23} = \sqrt{\mu^2 + \Delta^2} - \mu = \begin{cases} \frac{\Delta^2}{2E_F} & \text{in the BCS limit,} \\ 0.31E_F & \text{at the unitary point,} \\ E_B = \frac{\hbar^2}{ma^2} & \text{in the BEC limit.} \end{cases} \quad (2.19)$$

We see here that the threshold energy scales with the binding energy in the BEC limit and with  $\Delta^2/E_F$  in the BCS limit. Thus, RF spectroscopy allows for a precise measurement of the binding energy by measuring the shift of the bare transition due to interactions. This was used to determine the exact location of the broad Feshbach resonance in lithium-6 using a low-density system [15].

However, for larger densities, final-state interactions of atoms in  $|3\rangle$  with atoms in state  $|1\rangle$  or  $|2\rangle$  must be considered. In the first RF measurements it was assumed that these effects are just mean-field shifts which should cancel out in the crossover [50–52]. As it turned out, this is not the case for a mixture of 1-2 in the crossover regime because the final interaction strengths between 2-3 and 1-3 are very large, which allows the transition of a bound molecule to another bound molecule instead of dissociation into free particles [53].

This can be mitigated by using a 1-3 mixture instead to create a unitary Fermi gas. Here, the scattering lengths with the third state  $|2\rangle$  ( $a_{23}$  and  $a_{12}$ ) are so weak that no final bound state competes with the dissociation into free particles. By measuring the dissociation spectrum of a 1-3 mixture the fermionic pair size could be extracted, which shows a smooth crossover over the crossover [53]. However, the onset of these measurements does not reveal the pairing gap  $\Delta$  directly, but measures the dissociation threshold in Eq. 2.19.

To measure the pairing gap directly, a different method called quasiparticle spectroscopy can be used [54]. Here, not a balanced but a slightly spin-imbalanced system is probed, where more spin-up than spin-down atoms are present. The state of such an imbalanced system is given by the balanced BCS state plus excess fermions. These excess fermions correspond to quasiparticle excitations  $\gamma_{\uparrow,k}^\dagger$  around the minimum of the BCS dispersion  $E_k$  (Eq. 2.8) gapped with respect to the paired particles by  $\Delta$  (Fig. 2.11 a).

When spin-up atoms are transferred from this spin-imbalanced gas to a third state, the dissociation spectrum of the paired atoms and a second quasiparticle peak from the excess fermions is detected (Fig. 2.11 b). With respect to the bare transition  $\omega_{\uparrow 3}$  the dissociation spectrum starts at  $\sqrt{\mu^2 + \Delta^2} - \mu$  (Eq. 2.19) while the quasiparticle peak is located at  $-\Delta$ . Therefore, the pairing gap can be extracted from both features if the chemical potential is obtained from a different measurement or calculation<sup>16</sup>. Using that, a pairing gap  $\Delta$  was extracted for four different interaction strengths in the BEC-BCS crossover ( $(k_F a)^{-1} = 0.99 - (-0.25)$ ) [54]. In particular, at unitarity, a large pairing gap of  $\Delta = 0.44 E_F$  was measured.

In the spectra discussed so far the excitation energy was not measured in a momentum resolved way. To achieve that, we recall that a particle ejected from the many-body system is projected to a free-particle state with unchanged momentum because the momentum added by the RF photon is negligible. The momentum distribution of the atoms transferred to the third state can be obtained by a time of flight (ToF) measurement. This technique is called angle-resolved

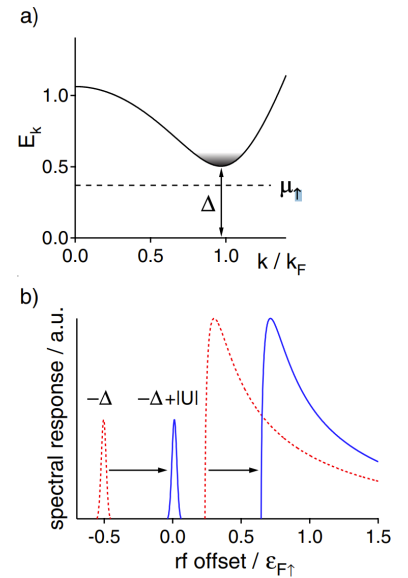


**Figure 2.11:** Quasiparticle spectroscopy for measuring the pairing gap. (a) A slight spin-imbalance adds excitations at the minimum of the BCS dispersion (gray shaded area) that are gapped by  $\Delta$  from the paired condensate. (b) The RF spectrum (red dotted) shows a quasiparticle peak at negative frequencies and a broad dissociation spectrum at positive frequencies. A Hartree mean-field shift  $U$  moves both features towards higher frequencies (solid blue line). Adapted from [54].

<sup>16</sup> In addition, both peaks are shifted with respect to the bare transition by a Hartree mean-field shift, but this cancels out.

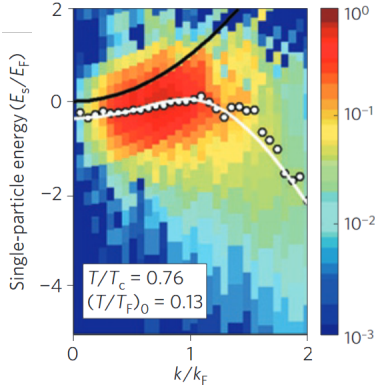


**Figure 2.12:** ARPES measurement of a Fermi gas at  $1/(k_{\text{Fa}}) \approx 0.15$  below the critical temperature. The color scale indicates the fraction of atoms coupled to the third state. The spectrum differs from the quadratic free particle dispersion (black line). The white dots indicate the centers of a Gaussian fit to each trace, the white line a fit with a BCS dispersion. Adapted from [57].

photoemission spectroscopy (ARPES) and is a well-established probing technique for solid state systems [55, 56].

When the free-particle dispersion of the third state and the chemical potential of the many-body system are taken into account, it can measure a part of the single-particle spectral function. In the BEC-BCS mean-field theory, the full single-particle spectral function is given by

$$A(\mathbf{k}, \omega) = v_{\mathbf{k}}^2 \delta(\omega + E_{\mathbf{k}}) + u_{\mathbf{k}}^2 \delta(\omega - E_{\mathbf{k}}).$$

The first branch describes the ejection of particles from and the second term injection into the many-body system. The weighting with  $v_{\mathbf{k}}^2$  and  $u_{\mathbf{k}}^2$  ensures occupation or vacancy, respectively. We see here that a measurement of  $A(\mathbf{k}, \omega)$  gives us direct access to the single-particle excitation spectrum  $E_{\mathbf{k}}$ . Compared to the parabolic excitation spectrum of a noninteracting Fermi gas, the excitation spectrum  $E_{\mathbf{k}}$  is gapped and shows a characteristic backbending for  $k \gtrsim k_{\text{F}}$ . In fact, measurements of the occupied part of the single-particle spectral function in a unitary Fermi gas showed backbending for large momenta [57, 58] (Fig. 2.12). Interestingly, these experiments also observed backbending above  $T_c$  which could be associated with a pseudogap. However, this interpretation should be treated with caution. It could also be caused by the universal  $1/k^4$  tail [59] in the momentum distribution due to contact interaction [60]. Therefore, this backbending is not direct evidence of a gapped excitation spectrum.

We see that ARPES can give many insights into the excitation spectrum, but there are some difficulties. One challenge of ARPES is that the momentum resolution can be limited by interactions of the third state with the remaining system during the time of flight. The second challenge comes from the fact that only the occupied part of the excitation spectrum is probed. However, for low temperatures and small excitation gaps, the occupation of states where the single-particle excitation energy shows backbending becomes small. For example, for an interaction energy  $1/(k_{\text{Fa}}) = -1$ , in the region where the excitation energy  $E(\mathbf{k})$  shows backbending (see Fig. 2.8) the occupation number  $v_{\mathbf{k}}^2$  decreases rapidly (see Fig. 2.5). The technique we want to discuss next, optical Bragg spectroscopy, circumvents these two disadvantages by not using a third spin state at all and allowing for occupation of higher momentum states.

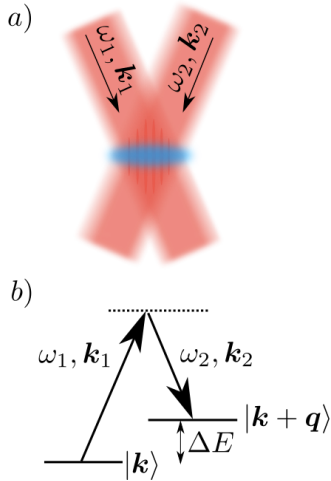


**Figure 2.13:** (a) Bragg spectroscopy uses two light fields with energy  $\hbar\omega_1$  and  $\hbar\omega_2$  and momenta  $\hbar\mathbf{k}_1$  and  $\hbar\mathbf{k}_2$ . (b) These beams can stimulate a two-photon process in which the energy difference  $\Delta E = \hbar(\omega_1 - \omega_2)$  and the momentum difference  $\hbar\mathbf{q} = \hbar(\mathbf{k}_1 - \mathbf{k}_2)$  are absorbed, exciting the atom from the state  $|\mathbf{k}\rangle$  into the state  $|\mathbf{k} + \mathbf{q}\rangle$ .

#### 2.4.2 Bragg spectroscopy

The basic principle of Bragg spectroscopy is to perturb the many-body system with a moving periodic potential, which can be created by two crossed laser beams (Fig. 2.13 a). The perturbation can be understood as a two-photon transition. First, a photon from the first light field with energy  $\hbar\omega_1$  and momentum  $\hbar\mathbf{k}_1$  is absorbed, transferring one atom to a virtual state. Then, the second light field with frequency  $\omega_2$  and wavevector  $\mathbf{k}_2$  induces a stimulated emission of a photon with energy  $\hbar\omega_2$  and momentum  $\hbar\mathbf{k}_2$ , transferring the atom to an excited

state. Thus, the total energy and momentum of the excited state are

$$\Delta E = \hbar(\omega_1 - \omega_2) \equiv \hbar\omega, \quad (2.20)$$

$$\hbar\mathbf{q} = \hbar(\mathbf{k}_1 - \mathbf{k}_2). \quad (2.21)$$

Bragg spectroscopy allows us to probe the inelastic scattering rate of a many-body system. As we will derive below, it gives access to the dynamic structure factor  $S(\mathbf{q}, \omega)$ , which is the Fourier transform of the density-density correlation function [61],

$$S(\mathbf{q}, \omega) = \frac{1}{2\pi} \int dt e^{i\omega t} \int d\mathbf{r} \int d\mathbf{r}' \frac{1}{N} \langle \rho(\mathbf{r}, 0) \rho(\mathbf{r}', t) \rangle.$$

By expressing the density operator  $\rho(\mathbf{r}, t)$  in the basis of excited states  $|n\rangle$  with eigenenergies  $E_n$  we obtain<sup>17</sup> [61]

$$S(\mathbf{q}, \omega) = \sum_n |\langle n | \delta\hat{\rho}^\dagger(\mathbf{q}) | 0 \rangle|^2 \delta(\omega - (E_n - E_0)/\hbar) \quad (2.22)$$

with the Fourier transform of the density fluctuation operator

$$\delta\hat{\rho}^\dagger(\mathbf{q}) = \sum_{\mathbf{k}, \sigma} c_{\mathbf{k}+\mathbf{q}, \sigma}^\dagger c_{\mathbf{k}, \sigma} \quad (2.23)$$

This operator contains the two-photon process of Bragg spectroscopy: Annihilation of a fermion at momentum  $\mathbf{k}$  ( $c_{\mathbf{k}, \sigma}$ ) and creation fermion at momentum  $\mathbf{k} + \mathbf{q}$  ( $c_{\mathbf{k}+\mathbf{q}, \sigma}^\dagger$ ). This process is only allowed if it has an overlap with an excitation of the system and it can thus give insights in both single-particle and collective excitations. In the following, we start historically by addressing the elastic Bragg scattering of X-rays. Then we discuss inelastic Bragg scattering used in this thesis.

## ELASTIC SCATTERING

In 1912, both Nobel Prize winners, William Lawrence Bragg, and his father, William Henry Bragg, studied the reflection of X-rays from crystalline lattices [62]. They discovered that reflection occurs only at specific angles of the incident beam. This happens because of constructive interference of light waves scattered from parallel lattice planes. The incoming wavevector  $\mathbf{k}_i$  and the reflected wavevector  $\mathbf{k}_r$  have to satisfy the Laue equations  $\Delta\mathbf{k} = \mathbf{k}_r - \mathbf{k}_i = \mathbf{G}$  where  $\Delta\mathbf{k}$  is the momentum transferred by the crystal and must match a reciprocal lattice vector<sup>18</sup>  $\mathbf{G}$ . In addition to momentum conservation, we can consider the scattering process to be elastic because the crystal is not moving. Therefore, the energy and thus the wavelength of the light is conserved, yielding a second equation,  $|\mathbf{k}_r| = |\mathbf{k}_i|$ . Combining both, we can derive Bragg's law

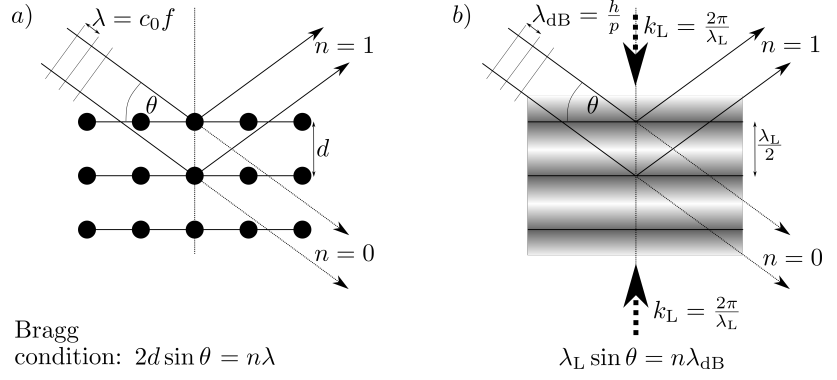
$$2d \sin \theta = n\lambda. \quad (2.24)$$

Under angles  $\theta$  that satisfy this condition, light scattered from the crystal planes interferes constructively. This gives rise to well-defined diffraction orders, which are used, for instance, in crystallography to determine the crystal structure using X-ray diffraction. Interestingly,

<sup>17</sup> We show the  $T = 0$  result and denote the ground state as  $|0\rangle$ .

<sup>18</sup> A reciprocal lattice vector has the length  $|\mathbf{G}| = \frac{2\pi}{d}n$  where  $d$  is the distance between two adjacent crystal lattice planes and  $n$  an integer.

**Figure 2.14:** (a) Sketch of Bragg scattering of an electromagnetic wave by a crystalline structure (b) and Bragg scattering of a matter wave by a standing-wave potential created with two counter-propagating laser beams.



Bragg scattering in a solid can also be understood in a particle picture: the incoming photon is scattered by a crystal phonon with momentum  $\hbar\mathbf{G}$ .

Following this perspective, in 1933, Kapitza and Dirac proposed an experiment in which electrons and photons change their role [63]. Instead of light waves being scattered by a periodic electron distribution in a crystal, they had the idea that matter waves, more specifically electrons, could also be reflected by a periodic light field. This periodic light field is created by two counter-propagating light fields with wavevector  $k_L = 2\pi/\lambda_L$ .

To derive Bragg's law for this new situation one can describe the incoming particle as a matter wave. Its wavelength is the de Broglie wavelength  $\lambda_{dB} = h/p$  where  $p$  is the momentum of the particle.<sup>19</sup> Instead of being scattered by a phonon with momentum  $\hbar\mathbf{G}$ , the momentum of the incoming particle changes due to the scattering of two photons<sup>20</sup> with total momentum  $2\hbar k_L$  or multiples thereof. Therefore, the Laue condition becomes

$$\Delta\mathbf{k} = \mathbf{k}_r - \mathbf{k}_i = 2n\mathbf{k}_L \quad (2.25)$$

yielding the Bragg condition<sup>21</sup>

$$\lambda_L \sin \theta = n\lambda_{dB}. \quad (2.26)$$

Both cases, scattering of a light wave from a crystal and scattering of a matter wave from a standing-wave potential, are compared in Fig. 2.14.

To create a detectable scattering probability for the Kapitza-Dirac experiment high light intensities are required, which made the experiment unfeasible at the time of its proposal. Only more than 50 years later, the invention of the laser made it possible to observe the Kapitza-Dirac process by scattering sodium atoms [64] or electrons [65] in a standing wave laser field.

#### INELASTIC SCATTERING

For cold atoms, Bragg scattering was first performed in a Bose condensate in 1999 [66, 67]. In this experiment, in contrast to the previous discussion, the atoms do not move but are stationary. Instead, the

<sup>19</sup> Here, we approximate the particle with a plane wave. A real particle corresponds to a moving wave packet of finite extent. Still, its Fourier transform will peak at the wavevector  $2\pi/\lambda_{dB}$ .

<sup>20</sup> For electrons, the absorption of one photon is not allowed, but stimulated Compton scattering involving two-photons is.

<sup>21</sup> This result is obtained by replacing  $|\mathbf{G}| = \frac{2\pi}{d}n \rightarrow 2n\frac{2\pi}{\lambda_L}$  in Eq. 2.24.

scattering potential is moving through the cloud of atoms, providing a specific energy to the system. This makes the process inelastic. Only if an excitation at the energy and momentum provided by the lattice is available, so if Eq. 2.20 and Eq. 2.21 are fulfilled, scattering can occur. These two equations take over the role the Bragg condition had in the elastic scattering process.

The moving lattice potential<sup>22</sup> is created by detuning the frequency of both laser beams with respect to each other resulting in a velocity  $v = \Delta\nu\lambda_L/2$ , where  $\Delta\nu = \omega/2\pi$  is the relative detuning. The momentum gain can be detected by measuring the density distribution after ToF. An example using a  $^{87}\text{Rb}$  condensate, is shown in Fig. 2.15. The density distribution shows two clouds, an unscattered and scattered condensate. Revisiting the connection to x-ray scattering, the left (black) denser condensate corresponds to the transmitted ray, whereas the right (gray) less dense condensate is the reflected beam.

We will now calculate the scattering rate of this inelastic process and its connection to the dynamic structure factor  $S(\mathbf{q}, \omega)$ . We assume that both laser beams are far-detuned such that the coupling to both spin states is the same. In addition, they have a small frequency detuning  $\omega$  with respect to each other and a wavevector difference  $\mathbf{q}$ . The perturbation caused by both beams can then be expressed by the Hamiltonian [69]

$$\hat{H}_B(\mathbf{q}, \omega) = \frac{\hbar\Omega_B}{2} \sum_{\mathbf{k}, \sigma} [c_{\mathbf{k}+\mathbf{q}, \sigma}^\dagger c_{\mathbf{k}, \sigma} e^{-i\omega t} + c_{\mathbf{k}+\mathbf{q}, \sigma} c_{\mathbf{k}, \sigma}^\dagger e^{i\omega t}] \quad (2.27)$$

$$= \frac{\hbar\Omega_B}{2} (\delta\hat{\rho}^\dagger(\mathbf{q})e^{-i\omega t} + \delta\hat{\rho}(\mathbf{q})e^{i\omega t}) \quad (2.28)$$

with the two-photon Rabi frequency<sup>23</sup>  $\Omega_B$ , the fermionic creation and annihilation operators  $c_{\mathbf{k}, \sigma}^\dagger$  and  $c_{\mathbf{k}, \sigma}$ , and the Fourier transform of the density fluctuation operator  $\delta\hat{\rho}^\dagger(\mathbf{q})$  (Eq. 2.23). The probability per particle to excite the many-body system from its ground state  $|0\rangle$  to an excited state  $|n\rangle$  due to this perturbation depends on the matrix element

$$\langle n | \hat{H}_B(\mathbf{q}, \omega) | 0 \rangle = \frac{\hbar\Omega_B}{2} \langle n | \delta\hat{\rho}^\dagger(\mathbf{q})e^{-i\omega t} + \delta\hat{\rho}(\mathbf{q})e^{i\omega t} | 0 \rangle.$$

With Fermi's golden rule we obtain the scattering rate

$$\Gamma_{|0\rangle \rightarrow |n\rangle} = \frac{2\pi}{\hbar} (\hbar\Omega_B)^2 |\langle n | \delta\hat{\rho}^\dagger(\mathbf{q}) | 0 \rangle|^2 \delta(\hbar\omega - (E_n - E_0)) \quad (2.29)$$

with the eigenenergies  $E_0$  and  $E_n$ .

To calculate the transition rate<sup>24</sup> for an excitation of the many-body system from its ground state  $|0\rangle$  to any excited state by transferring the momentum  $\hbar\mathbf{q}$  and energy  $\hbar\omega$  we sum over all possible excited states  $n$  and obtain<sup>25</sup>

$$\Gamma(\mathbf{q}, \omega) = 2\pi\Omega_B^2 \sum_n |\langle n | \delta\hat{\rho}^\dagger(\mathbf{q}) | 0 \rangle|^2 \delta(\omega - (E_n - E_0)/\hbar). \quad (2.30)$$

Here we note that the properties of both laser beams are contained in the Rabi rate. The excitation spectrum, however, is contained in the

<sup>22</sup> This experiment can be mapped to the experiment envisioned by Kapitza and Dirac by going into a frame of reference moving with the running lattice potential. Here, the lattice potential is stationary. Atoms enter the periodic potential when the light field is switched on, moving with velocity  $-v$ , are scattered and gain momentum, and leave the periodic potential when the light field is switched off.

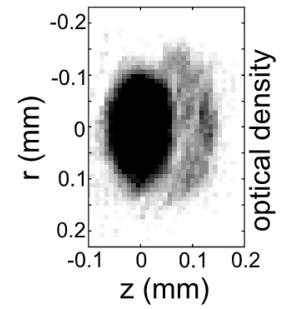


**Figure 2.15:** Absorption image of a  $^{87}\text{Rb}$  BEC after applying a resonant Bragg pulse and time of flight of 38 ms. The condensate is split into two: Most atoms are not scattered (black region), while the scattered atoms moved towards the right (grey region). Adapted from [68].

<sup>23</sup> The two-photon Rabi frequency is given by [70]  $\Omega_B = \hbar \frac{\Gamma^2}{4\Delta} \frac{\sqrt{I_1 I_2}}{I_{\text{sat}}}$  with the linewidth of the atomic transition  $\Gamma$ , the common detuning  $\Delta$ , and the intensities of both laser beams  $I_1$  and  $I_2$  normalized by the saturation intensity  $I_{\text{sat}}$ .

<sup>24</sup> The transition rate is the probability per unit time and particle that the transition happens.

<sup>25</sup> Starting from Eq. 2.29 we add the sum over all excited states  $|n\rangle$  and use the scaling property of the Dirac delta function  $\delta(\alpha x) = \delta(x)/\alpha$ . We can check the physical dimension of the scattering rate. The scattering rate has the unit  $1/\text{s}$  as it is given as the product of the square of the Rabi rate ( $\text{Hz}^2$ ), the matrix element (1) and the Dirac Delta function ( $1/\text{Hz}$ ). Thus, the dynamic structure factor defined in Eq. 2.22 has dimensions of time.

sum, which we identify with the dynamic structure factor in Eq. 2.22 to obtain the simple relation

$$\Gamma(\mathbf{q}, \omega) = 2\pi\Omega_B^2 S(\mathbf{q}, \omega). \quad (2.31)$$

Thus, the momentum and energy dependency of the scattering rate are solely given by the dynamic structure factor  $S(\mathbf{q}, \omega)$ .

In this treatment, we have assumed that the system is in the ground state and no excitations are present. This is not true at finite temperature, where thermal excitations are present in the unperturbed system. As described in detail in [71], this effect can be accounted for by detailed balancing. The temperature dependence of the density-density response one measures with the Bragg beam is then given by

$$\chi''(\mathbf{q}, \omega) \propto \left(1 - e^{-\frac{\hbar\omega}{k_B T}}\right) S(\mathbf{q}, \omega).$$

However, these effects are small in systems where the temperatures are  $T \approx 0.1T_F$  and the excitation gap  $\Delta$  is of the order  $E_F$ . Therefore, we will use the approximation  $\chi''(\mathbf{q}, \omega) \approx S(\mathbf{q}, \omega)$  throughout this thesis. As discussed in more detail in [16], finite temperatures could have an effect on  $S(\mathbf{q}, \omega)$  itself, for instance, the value of the excitation gap  $\Delta$ , the speed of sound, or the broadening of the collective mode. However, for systems close to  $T = 0$ , these quantities are expected to have a weak temperature dependence.

## 2.5 Dynamic structure factor of a BEC

In the following, we start the discussion of measured dynamic structure factors by considering repulsively interacting bosons forming a BEC.

As discussed in detail in [67], the dynamic structure factor of a BEC is

$$S(\mathbf{q}, \omega) = N_0(u_{\mathbf{q},B} - v_{\mathbf{q},B})^2 \delta(\omega - E_{\text{Bog},\mathbf{q}}/\hbar), \quad (2.32)$$

with the Bogoliubov dispersion  $E_{\text{Bog},\mathbf{q}}$  (Eq. 2.17) and the factors  $u_{\mathbf{q},B}$  and  $v_{\mathbf{q},B}$  from the Bogoliubov transformation (Eq. 2.15 and Eq. 2.16). We notice that the dynamic structure factor is only nonzero if  $\hbar\omega = E_{\text{Bog},\mathbf{q}}$ . The reason is that only transitions from the macroscopically occupied ground state to an excited state are allowed while higher momentum states in the ground state, which will be present due to quantum depletion and temperature, are neglected. Furthermore, there is a suppression at small momenta due to the coherence factor  $(u_{\mathbf{q},B} - v_{\mathbf{q},B})$ .

The momentum-dependent dynamic structure factor was measured by Steinhauer et al. by repeating the measurement shown in Fig. 2.15 for different values of  $\mathbf{q}$  and  $\omega$  [68]. For these measurements, a change in frequency detuning is easy to achieve experimentally using RF electronics. However, a variation of the wave vector difference  $\mathbf{q} = \mathbf{k}_2 - \mathbf{k}_1$  is technically more difficult. This is achieved by adjusting the angle between both beams, which can be challenging, as access through the vacuum chamber is required for a range of angles.

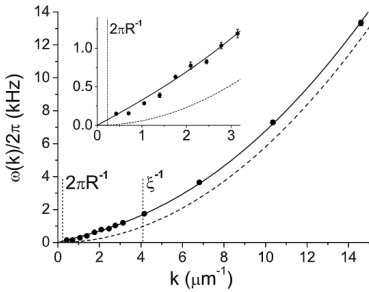


**Figure 2.16:** Dispersion relation of a BEC measured using Bragg spectroscopy. The points are fitted maxima of the dynamic structure factor. They agree perfectly with the expected Bogoliubov dispersion (black line) while disagreeing with the free particle dispersion (dashed line). Adapted from [68].

In the experiment, they observed for each momentum slice a narrow peak at a specific frequency. By extracting the maximum response they obtain the dispersion relation shown in Fig. 2.16. The dispersion relation is linear up to the characteristic momentum given by the inverse healing length  $\xi^{-1}$  as the gas can be excited collectively, and transforms into a free particle excitation at large momentum. Thus, it matches perfectly the Bogoliubov dispersion of a repulsive Bose gas.

## 2.6 Dynamic structure factor of a Fermi gas

After briefly covering Bragg spectroscopy of an interacting Bose gas, we now continue with interacting Fermi gases. Also here, collective excitations contribute to the dynamic structure factor. In addition, single-particle excitations derived in Sect. 2.3.1 have to be considered. Therefore, we first discuss the contribution of single-particle excitations before reviewing the experimental results.

### 2.6.1 Contribution of single-particle excitations

We start our discussion with the dynamic structure factor of a non-interacting Fermi gas. Then we will derive the dynamic structure factor of the BCS state.

The ground state<sup>26</sup>  $|\Psi_F\rangle$  of a non-interacting Fermi gas has two kinds of single-particle excitations:

1. For  $k < k_F$ , a fermion can be removed from the Fermi gas to create a hole excitation  $|h_{\mathbf{k}}\rangle = c_{\mathbf{k}}|\Psi_F\rangle$ . The excitation energy is given by the kinetic energy to lift a particle to the Fermi surface,  $E_h(\mathbf{k}) = E_F - \epsilon_{\mathbf{k}}$  with  $\epsilon_{\mathbf{k}} = \hbar^2 k^2 / (2m)$ , visualized in Fig. 2.17.
2. For  $k > k_F$ , a fermion can be added to the Fermi gas to create a particle excitation  $|p_{\mathbf{k}}\rangle = c_{\mathbf{k}}^\dagger |\Psi_F\rangle$  with an excitation energy  $E_p(\mathbf{k}) = \epsilon_{\mathbf{k}} - E_F$ .

We summarize the energies of both excitations to  $E(\mathbf{k}) = |\epsilon_{\mathbf{k}} - E_F|$ .

In order to calculate the dynamic structure factor, we consider first which kinds of excitations are created by the density fluctuation operator

$$\delta\hat{\rho}^\dagger(\mathbf{q}) = \sum_{\mathbf{k},\sigma} c_{\mathbf{k}+\mathbf{q},\sigma}^\dagger c_{\mathbf{k},\sigma}.$$

Apparently, it can create two excitations: A hole excitation is created if the state at  $\mathbf{k}$  is occupied and a particle excitation is created if the state  $\mathbf{k} + \mathbf{q}$  is not occupied. We denote this excited state by  $|n\rangle = |p_{\mathbf{k}+\mathbf{q},\sigma} h_{\mathbf{k},\sigma}\rangle$ . The density fluctuation operator applied to the ground state of the non-interacting Fermi gas is thus

$$\begin{aligned} \delta\hat{\rho}^\dagger(\mathbf{q})|\Psi_F\rangle &= \sum_{\mathbf{k},\sigma} c_{\mathbf{k}+\mathbf{q},\sigma}^\dagger c_{\mathbf{k},\sigma} |\Psi_F\rangle \\ &= \sum_{\mathbf{k},\sigma} \sqrt{n_F(\mathbf{k}) \cdot (1 - n_F(\mathbf{k} + \mathbf{q}))} |p_{\mathbf{k}+\mathbf{q},\sigma} h_{\mathbf{k},\sigma}\rangle, \end{aligned} \quad (2.33)$$

<sup>26</sup> We set the energy of the ground state to  $E_0 = 0$ .

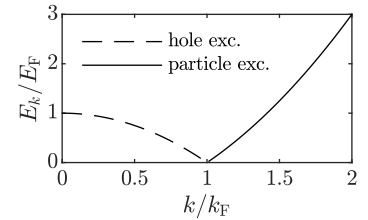
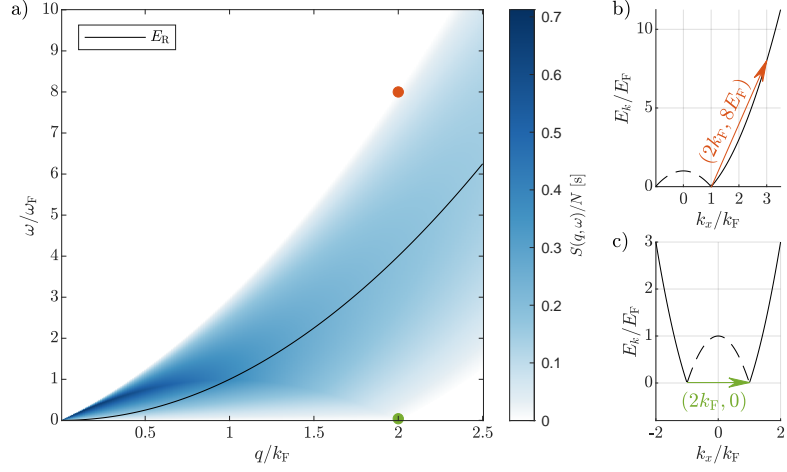


**Figure 2.17:** Energy of particle and hole excitations in a non-interacting Fermi gas.

**Figure 2.18:** (a) Dynamical structure factor  $S(\mathbf{q}, \omega)$  of a 3D non-interacting Fermi gas for excitations with momentum  $\hbar\mathbf{q} = \hbar\mathbf{q} \cdot \mathbf{e}_x$  and energy  $E = \hbar\omega$ . The structure factor is centered around the recoil energy  $E_r = \hbar^2 q^2 / (2m)$  but is broadened due to the extent of the Fermi sea, as we illustrate for the red and green points. (b) For a momentum transfer of  $q = 2k_F$ , the largest energy transfer (red arrow) can occur if a fermion is moved from the Fermi surface at  $k_x = k_F$  to  $k_x = 3k_F$ . This corresponds to a hole excitation (dashed line) at  $k_x = k_F$  and particle excitation at  $k_x = 3k_F$ . (c) No energy transfer is required, if the momentum of a fermion at the Fermi surface is flipped from  $k_x = -k_F$  to  $k_x = k_F$ .



where the square root ensures occupation at  $\mathbf{k}$  and vacancy at  $\mathbf{k} + \mathbf{q}$ .

Both excitations together preserve the number of particles because a fermion is removed at momentum  $\mathbf{k}$  and placed at a new momentum  $\mathbf{k} + \mathbf{q}$ . The summed energy of one hole and one particle excitation is  $E_n = E(\mathbf{k}) + E(\mathbf{k} + \mathbf{q}) = \epsilon_{\mathbf{k}+\mathbf{q}} - \epsilon_{\mathbf{k}}$  which is just the kinetic energy required to increase the momentum of a fermion by  $\hbar\mathbf{q}$ .

Inserting Eq. 2.33 into the dynamic structure factor (Eq. 2.22),

$$S(\mathbf{q}, \omega) = \sum_n |\langle n | \delta\hat{\rho}^\dagger(\mathbf{q}) | \Psi_F \rangle|^2 \delta(\omega - (E_n - E_0)/\hbar)$$

we notice that the sum over the excited states  $\langle n |$  is only nonzero for excited states  $\langle n | = \langle p_{\mathbf{k}+\mathbf{q},\sigma} h_{\mathbf{k},\sigma} |$  such that we obtain

$$S(\mathbf{q}, \omega) = \sum_{\mathbf{k}, \sigma} n_F(\mathbf{k}) \cdot (1 - n_F(\mathbf{k} + \mathbf{q})) \delta(\omega - (\epsilon_{\mathbf{k}+\mathbf{q}} - \epsilon_{\mathbf{k}})/\hbar). \quad (2.34)$$

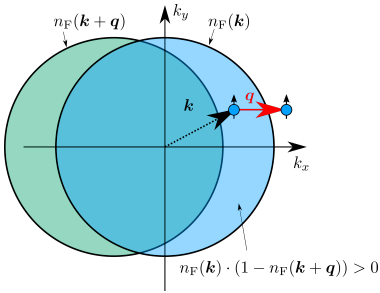


**Figure 2.19:** The factor in Eq. 2.34 ensures that a fermion within the Fermi sea (blue) is moved outside the Fermi sea. For given momentum  $\hbar\mathbf{q}$ , the contributing momentum space is a crescent-shaped area which fulfills  $n_F(\mathbf{k})(1 - n_F(\mathbf{k} + \mathbf{q})) > 0$ .

Only terms where the factor in the front of the Dirac delta function is nonzero contribute to the dynamic structure factor. For a  $T = 0$  Fermi gas, this can be visualized graphically by a crescent-shaped area resulting from two shifted Fermi surfaces (Fig. 2.19). By restricting the  $\mathbf{k}$ -space to values allowed by the overlap of both Fermi surfaces and the Dirac delta function, we can calculate the dynamic structure factor (Fig. 2.18).

The extent of the Fermi distribution in momentum-space results in a spread-out region of allowed excitation energies for a specific momentum. The processes behind the minimum and maximum excitation energy are illustrated as an example for a momentum transfer of  $q = 2k_F$  (Fig. 2.18 b-c). For a given momentum  $\mathbf{q}$  the dynamic structure factor achieves its maximum value when the number of possible excitations is the largest. This maximum is located at the recoil energy  $E_R(\mathbf{q}) = \hbar^2 q^2 / (2m)$  for momenta  $q > k_F$ .

As a next step, we will take interactions into account by repeating the evaluation using the single-particle excitations of the BCS ground state  $|\Psi_{\text{BCS}}\rangle$ . The single-particle excitations given by  $\gamma_{\mathbf{k},\uparrow}^\dagger$  and  $\gamma_{-\mathbf{k},\downarrow}$  (Eq. 2.12 and Eq. 2.13) with excitation energies  $E_{\mathbf{k}}$  (Eq. 2.14) constitute

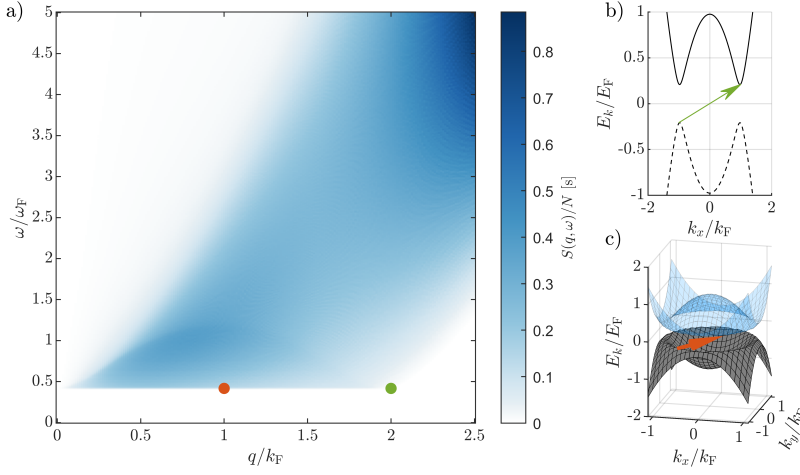


**Figure 2.20:** (a) Dynamic structure factor of a 3D Fermi gas at  $(k_F a)^{-1} = -1$  ( $\mu = 0.95 E_F$ ,  $\Delta = 0.21 E_F$ ) for excitations with momentum  $\hbar \mathbf{q} = \hbar q \cdot \mathbf{e}_x$  and energy  $E = \hbar \omega$ . The dynamic structure factor has an excitation gap of  $2\Delta$ . The region of possible excitations has a similar shape in the  $q, \omega$ -plane as the non-interacting Fermi gas (Fig. 2.18) but is blurred along the edge at low momentum. (b) For the green point in (a), we illustrate both underlying excitations by plotting  $-E_{\mathbf{k}}$  for the hole excitation (dashed line) and  $E_{\mathbf{k}}$  for the particle excitation (solid line). The total momentum and energy required for both excitations is illustrated by the green arrow. First, a hole excitation at  $k_x = -k_F$  at cost  $\Delta$ , then a particle excitation at  $k_x = k_F$  at cost  $\Delta$  is created, breaking in total two Cooper pairs. (c) At smaller momentum transfer, e.g.  $q = k_F$  (red dot in a), pair-breaking excitations at  $2\Delta$  can occur for fermions with an initial momentum along one other spatial directions (e.g.  $y$ -axis). The red arrow indicates how two excitations with a total momentum of  $q = k_F$  and energy of  $E = 2\Delta$  can be realized. Hole excitations are visualized by  $-E_{\mathbf{k}}(k_x, k_y, k_z = 0)$  (gray mesh) and particle excitations by  $E_{\mathbf{k}}(k_x, k_y, k_z = 0)$  (blue mesh).

the well-defined single-particle excitations of the BCS state. They are the analogues to the particle and hole excitations in the non-interacting Fermi gas. We express the fermionic operators in  $\delta \hat{\rho}^\dagger(\mathbf{q})$  in terms of these operators<sup>27</sup>,

$$\begin{aligned} c_{\mathbf{k}+\mathbf{q},\uparrow}^\dagger c_{\mathbf{k},\uparrow} |\Psi_{\text{BCS}}\rangle &= (u_{\mathbf{k}+\mathbf{q}} \gamma_{\mathbf{k}+\mathbf{q},\uparrow}^\dagger + v_{\mathbf{k}+\mathbf{q}} \gamma_{-\mathbf{k}-\mathbf{q},\downarrow}) (u_{\mathbf{k}} \gamma_{\mathbf{k},\uparrow} + v_{\mathbf{k}} \gamma_{-\mathbf{k},\downarrow}^\dagger) |\Psi_{\text{BCS}}\rangle \\ &= u_{\mathbf{k}+\mathbf{q}} v_{\mathbf{k}} \gamma_{\mathbf{k}+\mathbf{q},\uparrow}^\dagger \gamma_{-\mathbf{k},\downarrow}^\dagger |\Psi_{\text{BCS}}\rangle \end{aligned}$$

where we used the fact that the BCS ground state does not contain any single-particle excitations at  $T = 0$ , e.g.  $\gamma_{\mathbf{k},\uparrow} |\Psi_{\text{BCS}}\rangle = 0$ . The excited state  $|e\rangle = \gamma_{\mathbf{k}+\mathbf{q},\uparrow}^\dagger \gamma_{-\mathbf{k},\downarrow}^\dagger |\Psi_{\text{BCS}}\rangle$  contains two single-particle excitations with a total energy of  $E = E_{\mathbf{k}+\mathbf{q}} + E_{\mathbf{k}}$ . Similarly to the noninteracting case, the sum over excited states  $\langle n|$  in the dynamic structure factor is only nonzero if  $\langle n| = \langle e| = \langle \Psi_{\text{BCS}} | \gamma_{-\mathbf{k},\downarrow} \gamma_{\mathbf{k}+\mathbf{q},\uparrow}^\dagger$ . This removes again the sum over  $n$  such that we obtain the dynamic structure factor

$$\begin{aligned} S(\mathbf{q}, \omega) &= \sum_{\mathbf{k}} u_{\mathbf{k}+\mathbf{q}}^2 v_{\mathbf{k}}^2 \delta(\omega - (E_{\mathbf{k}} + E_{\mathbf{k}+\mathbf{q}})/\hbar) \\ &= \sum_{\mathbf{k}} (1 - n_{\mathbf{k}+\mathbf{q}}) n_{\mathbf{k}} \delta(\omega - (E_{\mathbf{k}} + E_{\mathbf{k}+\mathbf{q}})/\hbar), \end{aligned}$$

with the fermionic occupation number

$$n_{\mathbf{k}} = v_{\mathbf{k}}^2 = \frac{1}{2} \left( 1 - \frac{\xi_{\mathbf{k}}}{E_{\mathbf{k}}} \right).$$

We see similar to the non-interacting Fermi gas that a fermion can be promoted to a larger momentum only if its initial state at momentum  $\mathbf{k}$  is occupied and the final state at momentum  $\mathbf{k} + \mathbf{q}$  is vacant.

The new insight is that the energy  $E_{\mathbf{k}} + E_{\mathbf{k}+\mathbf{q}}$  of the excited state is the sum of two single-particle excitations. Each of these single-particle excitations requires a minimal energy of  $\Delta$  because we break Cooper pairs: When removing a spin-up particle at momentum  $\mathbf{k}$  we break a Cooper pair because an unpaired spin-down particle at momentum  $-\mathbf{k}$  is left over. Similarly, by adding it back to the system, we create an

<sup>27</sup> We assume  $q \neq 0$  here. The  $q = 0$  case results in so-called excited-pair excitations  $\gamma_{\mathbf{k},\uparrow}^\dagger \gamma_{-\mathbf{k},\downarrow}^\dagger |\Psi_{\text{BCS}}\rangle$ , which are located at the same energy as two single-particle excitations ( $2E_{\mathbf{k}}$ ) but contain similar to the ground state a coherent superposition  $\propto (v_{\mathbf{k}} - u_{\mathbf{k}} c_{\mathbf{k},\uparrow}^\dagger c_{-\mathbf{k},\downarrow}^\dagger)$  of the absence and the occurrence of a  $(\mathbf{k}\uparrow, -\mathbf{k}\downarrow)$  pair [6].

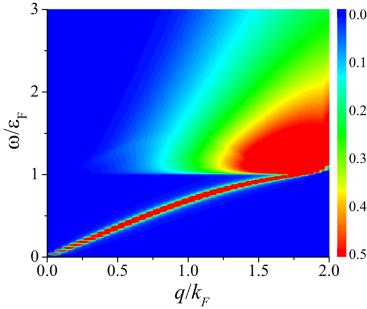


**Figure 2.21:** Calculation of the dynamic structure factor of a unitary Fermi gas using the random phase approximation. Similar to the previous calculations, a continuum of single-particle excitations exists which is gapped by  $2\Delta \approx \epsilon_F$ . In addition, a collective sound mode exists in at low energy. When it approaches the continuum of excitations, it is pushed down before merging with the continuum. Adapted from [72].

At high momentum, also the spin-spin dynamic structure factor was studied [77]. For these measurements, Bragg beams that have a coupling of opposite sign to both spin states are used. This makes these studies technically very challenging, because spontaneous emission must be minimized. Therefore, short pulses must be used, which result in a large uncertainty of  $\omega$  due to Fourier broadening, so a delicate balance must be found.

unpaired spin-up particle at momentum  $\mathbf{k} + \mathbf{q}$  that breaks a second Cooper pair [6].

If we want to evaluate the dynamic structure factor, we encounter two challenges compared to the non-interacting case. One reason is that solving the energy condition imposed by the Dirac delta function is more complicated; another reason is that the fermionic occupation number is smeared out at the Fermi surface. Therefore, the region in  $k$ -space constructed graphically for the non-interacting case is not sharp anymore. Due to these complications, we evaluate the sum over  $k$  for a set of  $(\mathbf{q}, \omega)$ -pairs numerically (Fig. 2.20).

Compared to the non-interacting case, the area of a nonzero dynamic structure factor does not have a sharp edge at low momentum but is smeared out. This is the result of the blurred occupation number. In addition, the minimal energy required to create a two-particle excitation is now lifted from 0 to  $2\Delta$  because this is the minimal energy to create two pair-breaking excitations.

### 2.6.2 Contribution from collective excitations

To include collective excitations in the dynamic structure factor, a random phase approximation (RPA) technique can be used which has been done in [72] using a density functional. The resulting dynamic structure factor at unitarity is shown in Fig. 2.21. These calculations also show a continuum of single-particle excitations gapped by  $2\Delta$ . In addition, they capture the collective mode at low energy. If the energy of the collective mode is well below the single-particle gap, it remains linear. However, for larger energies, it is pushed down before merging with the continuum [40].

### 2.6.3 Bragg spectroscopy of Fermi gases

Experiments using Bragg spectroscopy were first proposed for Fermi gases in [73] and performed in the Vale group [74]. Similar to the experiments with bosons, the dynamic structure factor was measured by determining the amount of scattered atoms after ToF. In the early experiments, the focus was on Bragg spectroscopy at large momentum. The dynamic structure factor at high momentum contains valuable information on the properties of the short-range interaction potential, allowing studies of Tan's contact [59] over the BEC-BCS crossover [75, 76]. In following experiments, the Vale group investigated the low-momentum excitation spectrum in the BEC-BCS crossover [78] by using a crossing angle of both laser beams which is smaller compared to their previous experiments. The measured spectra for a fixed momentum  $q \approx k_F/2$  are shown in Fig. 2.22.

They observe both modes predicted by theory (Fig. 2.21). In the BEC regime, a well-defined collective mode is present which persists well into the crossover regime. In the crossover regime, in addition, a

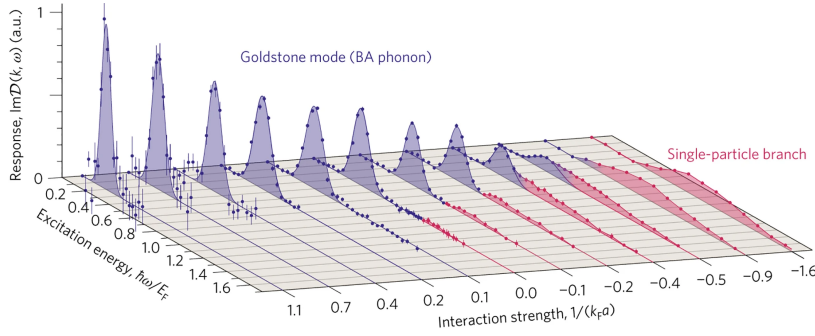


**Figure 2.22:** Dynamic structure factor  $S(q \approx k_F/2, \omega)$  over the BEC-BCS crossover (left to right). The red and blue points are experimental data. Two distinct kinds of excitations, a collective mode (blue Gaussian fit) and continuum of pair breaking excitations (red fit) are observed. Adapted from [78].

gapped continuum of pair-breaking excitations appears and becomes more pronounced on the BCS side of the crossover.

Both contain valuable information about the many-body system: The collective mode tells us how fast density waves propagate and dissipate in the system. Its peak position was used to extract the speed of sound over the crossover<sup>28</sup>. The pair-breaking continuum, on the other hand, contains information about how well pairs are protected. The fact that the onset of the pair-breaking continuum is at  $2\Delta$  allowed them to extract the pairing gap  $\Delta$  at unitarity and slightly into the BCS regime ( $(k_F a)^{-1} = 0$  to  $(k_F a)^{-1} = -0.2$ ). The challenge for these measurements was that the coupling to the broad pair-breaking continuum is not as strong as the coupling to the collective mode (see Fig. 2.22) which they overcame by increasing the intensity of both Bragg beams.

In the next chapter, we will extend these results by performing Bragg spectroscopy over a large momentum range of  $q = 0.2k_F - 2k_F$  for homogeneous Fermi gases in the BEC-BCS crossover.

<sup>28</sup> Here, the fact that the collective mode was taken at finite momentum and not in the  $q \rightarrow 0$  limit was considered and a correction based on theoretical input was applied.



In this chapter I present the excitation spectra of ultracold homogeneous 3D Fermi gases measured with momentum-resolved Bragg spectroscopy. These measurements uncover the evolution of single-particle and collective excitations in the BEC-BCS crossover. Furthermore, we can extract the speed of sound from the collective mode, while the shifting onset of the single-particle pair-breaking continuum reveals the evolution of the superfluid gap throughout the BEC-BCS crossover. Finally, we compare current state-of-the-art theories with our measurement of the gap. These results are published in [79]

H. Biss, L. Sobirey, N. Luick, M. Bohlen, J. J. Kinnunen, G. Bruun, T. Lompe, and H. Moritz,  
Physical Review Letters, 128(10), 100401 (2022)

Parts of this chapter are reproduced from this publication with modifications. Together with the creation of imbalanced Fermi gases presented in part II these results constitute the main result of this thesis.

In this chapter, we prepare a homogeneous 3D Fermi gas in a box potential (Sect. 3.1) and implement Bragg spectroscopy (Sect. 3.2). Then we perform measurements of the excitation spectrum (Sect. 3.3), analyze the behavior of the collective mode (Sect. 3.4) and extract the superfluid gap from the pair-breaking continuum (Sect. 3.5).

### 3.1 Preparing homogeneous 3D Fermi gases

For our measurement, we prepare an ultracold Fermi gas with a homogeneous density distribution such that all many-body parameters, e.g. chemical potential, are constant throughout the trapped gas. Therefore, elaborated reconstructions of local parameters, such as an inverse Abel transformation, are not required. Furthermore, measurements of dynamics that depend on density and extend spatially, e.g. sound propagation, benefit greatly from the fact that the density is constant. In recent years, these advantages have led to an increased use of homogeneous bosonic and fermionic gases [80].

In the experiment, we prepare an ultracold Fermi gas using a well-established cooling scheme<sup>29</sup>. In short, lithium-6 atoms are laser cooled and trapped with a combination of a Zeeman slower and a magneto-optical trap. Then, the atoms are transferred into a resonator-enhanced dipole trap for evaporate cooling before they are moved with a transport dipole trap into a flat glass cell which allows close access with microscope objectives. Here, a further transfer into an oblate red-detuned dipole trap occurs.

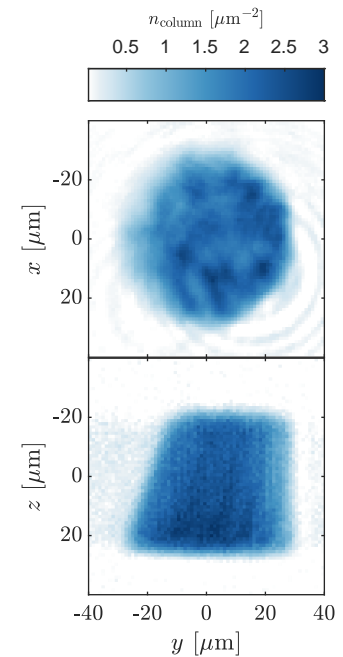


**Figure 3.1:** Three-dimensional homogeneous Fermi gas trapped in a box potential. The upper panel depicts the column density  $n(x, y) = \int n(x, y, z) dz$  retrieved from absorption imaging through the microscope objective along  $z$ . The circular interference pattern on the lower right is probably caused by a dust grain in the optical path and does not correspond to a density fluctuation. The lower panel shows the density  $n(y, z) = \int n(x, y, z) dx$  from one side (in arbitrary units).

<sup>29</sup> The preparation scheme up to the box trap is the same as described in [81].

Then, as a final step, we transfer the gas into a box potential resulting in a homogeneous gas (Fig. 3.1). We use a combination of repulsive optical potentials, where we follow a similar approach to Refs. [82, 83]. For vertical confinement, we use two endcaps, which are formed by two blue-detuned elliptical beams (for the optical setup see Fig. 3.2).

We confine the gas along the two remaining directions with a blue-detuned ring potential, which is projected onto the atoms using a high-resolution microscope<sup>30</sup>. As the diameter of the ring potential changes slightly over the vertical extent of the box, the density distribution of the gas deviates from a perfect cylinder and has the form of a truncated cone (see Fig. 3.1). Its diameter increases from the bottom to the top by 15 % and is on average  $d = 50 \mu\text{m}$ .

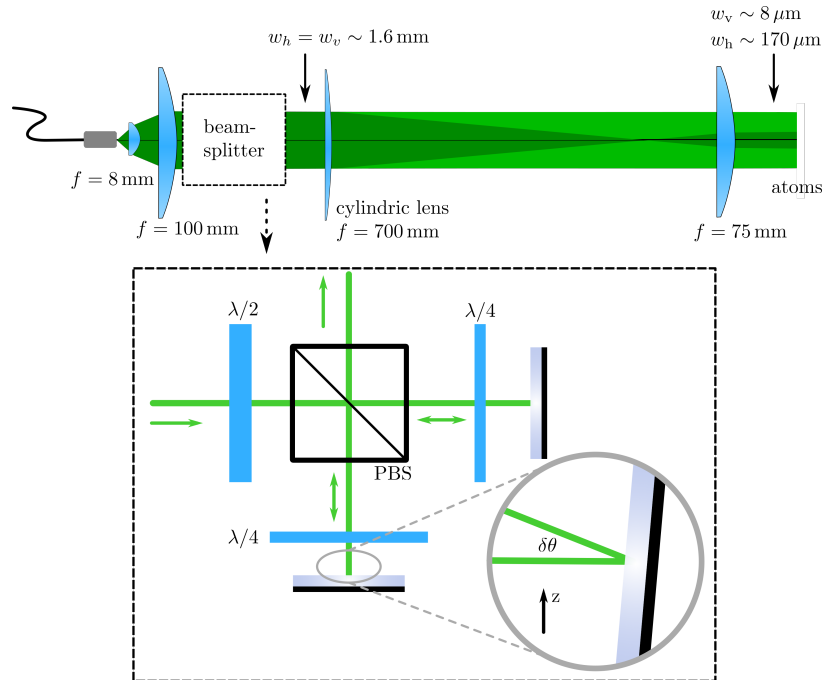
<sup>30</sup>The optical setup to create this ring potential uses a combination of three axicons described in detail in [85].

#### DENSITY CALIBRATION

To measure the 3D density we first determine the 2D column density  $n_{2D}$  with high intensity absorption imaging along the  $z$ -direction calibrated as described in [86]. In the next step, we average over the central region where the vertical distribution is not cut off by the truncated cone and divide it by the box height  $b$  to obtain the three-dimensional density  $\tilde{n}_{3D} = n_{2D}/b$ . We obtain the box height  $b = 43 \mu\text{m}$  by imaging the gas from the side and taking the full width at half maximum of its vertical extent. The calibration of the auxiliary imaging system used for this purpose is explained in detail in Appendix A.

However, it turns out, despite careful calibration, that the reconstructed 3D density is systematically too low. We attribute this to tech-

**Figure 3.2:** Optical setup to create two elliptical beams with a small vertical waist (dark green) and large horizontal waist (bright green) used as upper and lower endcaps for the box potential. Both endcap beams are created using a polarizing beam splitter (PBS) and a  $\lambda/4$ -waveplates, which allows individual vertical displacement using a small angular displacements  $\Delta\theta$ . The drawing is adapted from [84].



nical errors such as imperfect polarization and off-resonant light in the imaging beam, as well as systematic effects such as multiple scattering of photons in the optically dense sample. Therefore, we calibrate the density using a system with a known equation of state (EOS), a unitary Fermi gas, which is described in Appendix B.

The calibration yields a constant density per spin state of  $n_{3D} \approx 0.4/\mu\text{m}^3$ , which corresponds to a Fermi energy of  $E_F \approx h \times 7 \text{ kHz}$ , and a total atom number per spin state of  $N = n_{3D} \cdot V = n_{3D} \cdot \pi d^2/4 \cdot b = 3.4 \times 10^4$ . The curvature of the magnetic offset field leads to a small inhomogeneity of the box potential, which is of the order of  $100 \text{ Hz} \approx 0.02 E_F$ .

#### TEMPERATURE OF THE GAS

The temperature of homogeneous Fermi gases in the BEC-BCS crossover is challenging to measure when homogeneity and strong interactions are combined, since the density of state of a gas with low  $T/T_F$  and strong interactions is a priori not known. One way to mitigate this is to create a low-density region where  $T/T_F$  is large and the density of state can be approximated by a Boltzmann distribution. Another approach is to measure the momentum distribution with time of flight. However, strong interactions result in a large scattering rate during the flight time, which hinders free expansion.

We measure the absolute entropy and temperature of the homogeneous gas at unitarity using a technique based on measuring the total energy developed in Ref. [30]. It is based on performing an isoenergetic expansion of the homogeneous gas into a harmonic trap and using the equation of state to determine the total energy  $E$  from the density distribution of the expanded system. We obtain a value of  $E/E_0 = 0.43 \pm 0.02$  with the total energy of a non-interacting Fermi gas  $E_0 = 3/5 N E_F$ . This energy corresponds according to the equation of state measured in Ref. [28] to an entropy per particle of  $S/Nk_B = 0.29 \pm 0.09$  and a temperature of  $T = 0.128(8) T_F$ . Thus, our gas is below the critical temperature  $T_c = 0.17 T_F$  of a unitary Fermi gas [28].

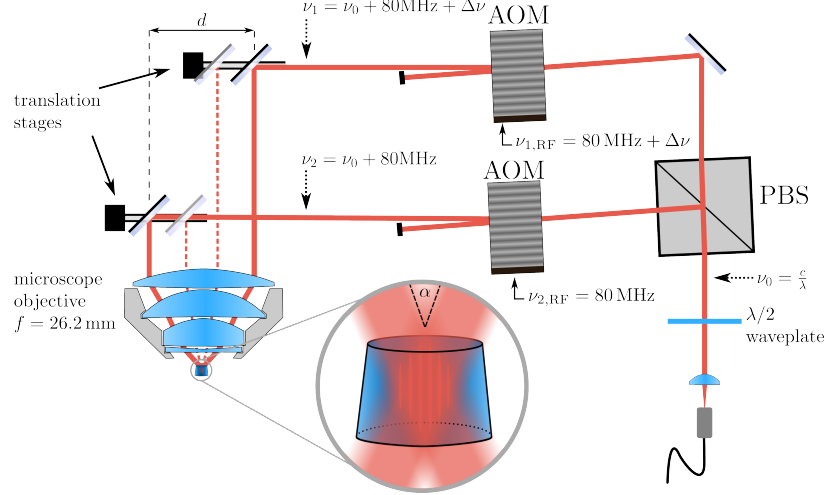
After determining the temperature at unitarity, we ramp the magnetic field slowly to tune the interaction strength. While this changes the temperature of the gas, in a homogeneous system, the entropy per particle  $S/N$  remains constant if the change is adiabatic<sup>31</sup>.

<sup>31</sup> We will show that the ramps are adiabatic at the end of the next section (Fig. 3.6).

### 3.2 Implementation of Bragg spectroscopy

To measure the excitation spectrum we employ Bragg spectroscopy, which uses a moving lattice to perturb the system. We create the optical lattice by projecting two intersecting laser beams with a high-resolution microscope objective onto the atoms (Fig. 3.3). We use red-detuned light at a wavelength  $\lambda = 780 \text{ nm}$  in order to suppress single-photon scattering. However, a stimulated scattering process can occur

**Figure 3.3:** Sketch of the Bragg setup. First, a collimated 780 nm laser beam (solid red line) is split up using a polarizing beam splitter (PBS) into two beams which are passed individually through acousto-optic modulators (AOM). The first refracted orders, shifted in frequency by  $\nu_{1,\text{RF}}$  and  $\nu_{2,\text{RF}}$ , respectively, are then reflected from mirrors mounted on translation stages. This allows for the tuning of the distance  $d$  between both beams (compare solid and dashed yellow line). In the last step, both beams pass a microscope objective that crosses them at an angle  $\alpha = d/f$ , where  $f$  denotes the effective focal length of the microscope objective, and focuses them down to a waist of  $\sim 20 \mu\text{m}$ . This results in a periodic interference pattern at the atom position (see also Fig. 3.4).



where a photon is absorbed from one beam and remitted into the other beam.

To define the energy transferred  $\Delta E = \hbar\omega$  two acousto-optic modulators are used to set a small frequency difference  $\omega = 2\pi \times \Delta\nu$  between both beams. The transferred momentum is changed by adjusting the angle between both beams. In detail, we use two motorized translation stages to set the distance  $d$  between both beams in front of the microscope objective. This, in turn, determines the crossing angle of the beams  $\alpha = d/f$  at the atom position. During the two-photon process first a photon with momentum  $\hbar\mathbf{k}_1$  is absorbed and then a photon with momentum  $\hbar\mathbf{k}_2$  is emitted, where  $\mathbf{k}_1$  and  $\mathbf{k}_2$  are the wavevectors of both intersecting beams. Therefore, the total momentum transfer is  $\hbar\mathbf{q} = \hbar(\mathbf{k}_1 - \mathbf{k}_2)$ . Since the system is isotropic, we can restrict our discussion to the absolute value of the wavevector difference  $q = |\mathbf{q}|$ . It is given by

$$q \equiv |\mathbf{q}| = |\mathbf{k}_1 - \mathbf{k}_2| = 2k_1 \sin(\alpha/2) = 2k_1 \sin\left(\frac{d}{2f}\right),$$

where we introduced the wave vector of the incident light  $k_1 = 2\pi/\lambda$ . For the case  $\alpha = \pi$  we recover the well-known case of two counter-propagating beams which results in a lattice with twice the periodicity of both incident beams,  $q = 2k_1$ .

In our setup, only small crossing angles are realized. Therefore we can use a small-angle approximation and obtain the simple relation

$$q = k_1 \alpha = k_1 \frac{d}{f}. \quad (3.1)$$

We extract the magnitude of the wave vector  $q$  directly from images of the interference pattern at the atom position. The achievable values are shown in Fig. 3.4.

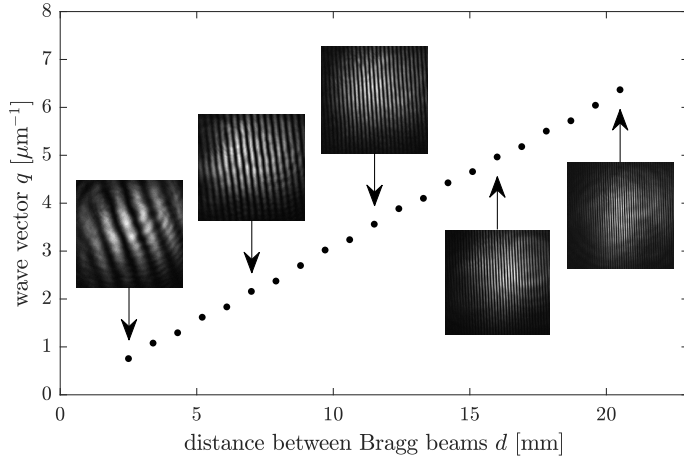


**Figure 3.4:** By varying the distance between both Bragg beams before entering the microscope objective in the range of  $d = 2.5$  mm to  $20.5$  mm wavevectors  $q$  in the range of  $q = 0.8 \mu\text{m}^{-1}$  to  $6.3 \mu\text{m}^{-1}$  can be accessed. The insets show the imaged interference pattern covering a region of  $46 \times 46 \mu\text{m}^2$  used to determine the wave vector  $q$ . The small rotation of the interference pattern when changing the distance does not influence the measurements as the probed systems are isotropic.

We now use the Bragg lattice at a given energy  $\hbar\omega$  and momentum  $\hbar q$  to perturb the gas. The probability per unit time and particle to excite the many-body system from its ground state  $|0\rangle$  by transferring the momentum  $\hbar q$  and energy  $\hbar\omega$  is given by Fermi's golden rule (Eq. 2.31)

$$\Gamma(\mathbf{q}, \omega) = 2\pi\Omega_R^2 S(\mathbf{q}, \omega),$$

where  $S(\mathbf{q}, \omega)$  denotes the dynamic structure factor. As each excitation adds an energy  $\Delta E = \hbar\omega$  to the system, the perturbation leads to a heating rate  $dE/dt$  which is directly related to the dynamic structure factor  $S(\mathbf{q}, \omega)$  by [87]

$$\frac{dE}{dt} = \hbar\omega\Gamma(\mathbf{q}, \omega) = 2\pi\hbar\omega\Omega_R^2 S(\mathbf{q}, \omega). \quad (3.2)$$

In our experiment, we use two different methods to measure the amount of energy that was deposited by the Bragg lattice. On unitarity, we can follow the procedure described above where we release the gas into a harmonic potential and use the known equation of state to calculate the total energy from the resulting density distribution. The results for Bragg pulses of different lengths are shown in Fig. 3.5. We observe that the energy increases linearly with the length of the Bragg pulse, which is in excellent agreement with the prediction from linear response theory.

However, this method has a rather low signal-to-noise ratio and is quite sensitive to offsets in the density measurements. Therefore, we instead use the change of the condensate fraction in the BEC regime to determine the effect of the Bragg lattice on the system.

To do this, we measure the height of the condensate peak  $A(\mathbf{q}, \omega)$  using matter wave imaging [81] and define the response

$$r(\mathbf{q}, \omega) = \frac{A_0}{A(\mathbf{q}, \omega)} - 1, \quad (3.3)$$

where  $A_0$  is the height of the condensate peak when no energy is deposited by the lattice ( $\omega = 0$ ). Similarly to the measurements of the

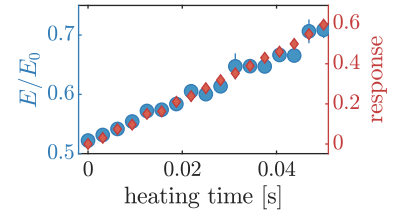


**Figure 3.5:** Energy measurement of a unitary Fermi gas in a box potential. The total energy, normalized by the energy of a non-interacting Fermi gas  $E_0$  (blue dots), increases linearly with the heating time. Here, the gas is transferred into a hybrid trap to determine the total energy from in situ images using the known equation of state. The response (red diamonds) utilizing the condensate peak in the BEC regime as a thermometer shows a similar linear behavior and can be used as an alternative to measure the heating rate.

total energy on unitarity, the response scales linearly with the length of the Bragg pulse  $\Delta t$  (Fig. 3.6). This means that  $r$  is proportional to the total energy  $\Delta E$  deposited by the Bragg pulse, which gives us access to the heating rate,

$$\frac{dE}{dt} \approx \frac{\Delta E}{\Delta t} \propto \frac{r}{\Delta t}. \quad (3.4)$$

We insert this relation into the left-hand side of Eq. 3.2 and solve for  $S(q, \omega)$  to obtain the final relation to calculate the dynamic structure factor from our measurements,

$$S(q, \omega) \propto \frac{r(q, \omega)}{\omega \Delta t}. \quad (3.5)$$

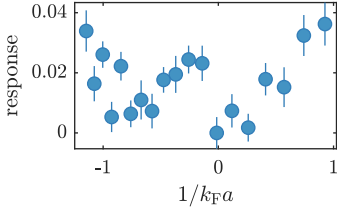


**Figure 3.6:** Response of the gas after ramping to different interaction strengths in the BEC-BCS crossover. It varies by less than 4%. Using the relationship found in Fig. 3.6, this suggests a variation of the entropy per particle  $S/N$  by about  $0.07 k_B$ .

One notable difference of our experiments compared to the majority of other Bragg spectroscopy experiments in ultracold gases is that we use a much weaker probe ( $V = h \cdot (300 - 600) \text{ Hz} = 0.04 - 0.09 E_F$ ) for much longer times ( $\Delta t = 15 - 400 \text{ ms}$ ). Consequently, the Fourier width of the Bragg pulse does not affect the frequency resolution of our measurements.

With the response established as a good proxy for measuring the added temperature, we verify that our interaction ramps do not cause large amounts of technical heating, so we can change the interaction strength  $1/(k_F a)$  adiabatically. We prepare our system at the unitary point and ramp to different interaction strengths, where we hold the system, and finally ramp to the BEC regime to measure the response. We find a variation of less than 4% (Fig. 3.6). As the peak height scales with the entropy per particle this measurement allows us to estimate the variation in  $S/N$  of less than  $0.07 k_B$  for our measurements<sup>32</sup>.

<sup>32</sup> We use the relation between the peak height and  $E/E_0$  from Fig. 3.5 and  $S/N = 0.29$

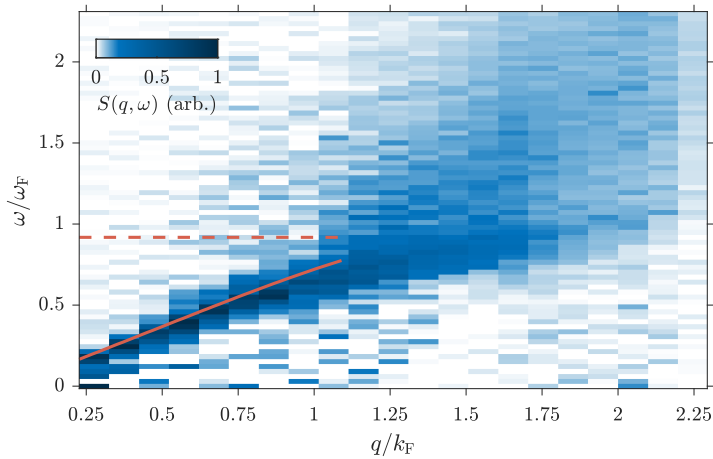


**Figure 3.7:** Measurement of the dynamic structure factor  $S(q, \omega)$  of a unitary Fermi gas. At low energy and momentum transfer, the Goldstone mode of the superfluid manifests itself as a linear phononic mode with a slope that corresponds to the speed of sound  $v_s$ . For larger energy and momentum transfers, pair-breaking excitations occur as a broad continuum, with a clear onset at an energy corresponding to twice the pairing gap  $\Delta$  of the system. For comparison, the expected value of  $2\Delta$  on unitarity [88] is shown as a red dashed line, a numerical QRPA calculation of the center of the Goldstone mode is shown as a red solid line.

### 3.3 Measuring the excitation spectrum

We now proceed to measure the excitation spectrum of our system using Bragg spectroscopy. For our first measurement, we prepare a gas at the unitary point where the scattering length diverges and  $1/(k_F a) = 0$ . At this point, the only relevant length scale in the system is the inverse Fermi momentum  $1/k_F$  and the system becomes scale-invariant [9, 89]. The gas is also very strongly interacting, with a collision rate that is comparable to the inverse Fermi time  $E_F/\hbar$  of the system.

Our measurement of the dynamic structure factor of the unitary Fermi gas is shown in Fig. 3.7. Two distinct types of excitations are immediately visible. First, there is a narrow, well-defined mode whose energy is approximately proportional to its momentum, which we identify as the sound mode of the Fermi gas. For very low energies, where collisions have time to restore local thermal equilibrium, it can be understood in terms of hydrodynamics [90] whereas for higher frequencies or weaker coupling strengths it is a Goldstone mode [32, 78] that is driven by phase fluctuations of the superfluid order parameter.

The second type of excitations are single-particle excitations in which a single fermion receives the total momentum and energy of the excitation. These excitations appear as a broad continuum in our spectra, as a fermion inside the Fermi sea can be excited to a continuum of unoccupied states at a larger energies. However, as the fermions are paired, this requires an energy of at least twice the pairing gap  $\Delta$ , resulting in a well-defined onset of the so-called pair-breaking continuum. The overall behavior of our measured dynamic structure factors is in excellent agreement with theoretical expectations<sup>33</sup> [40].

While in the limits of small or large momentum transfer, the response of the system can be clearly identified as either a collective or single-particle excitation, there is a range of intermediate momenta where this is not as straightforward. In particular, as the collective

<sup>33</sup> See also the RPA calculations in Fig. 2.21 on p. 34 and Fig. 3.13 on p. 50.

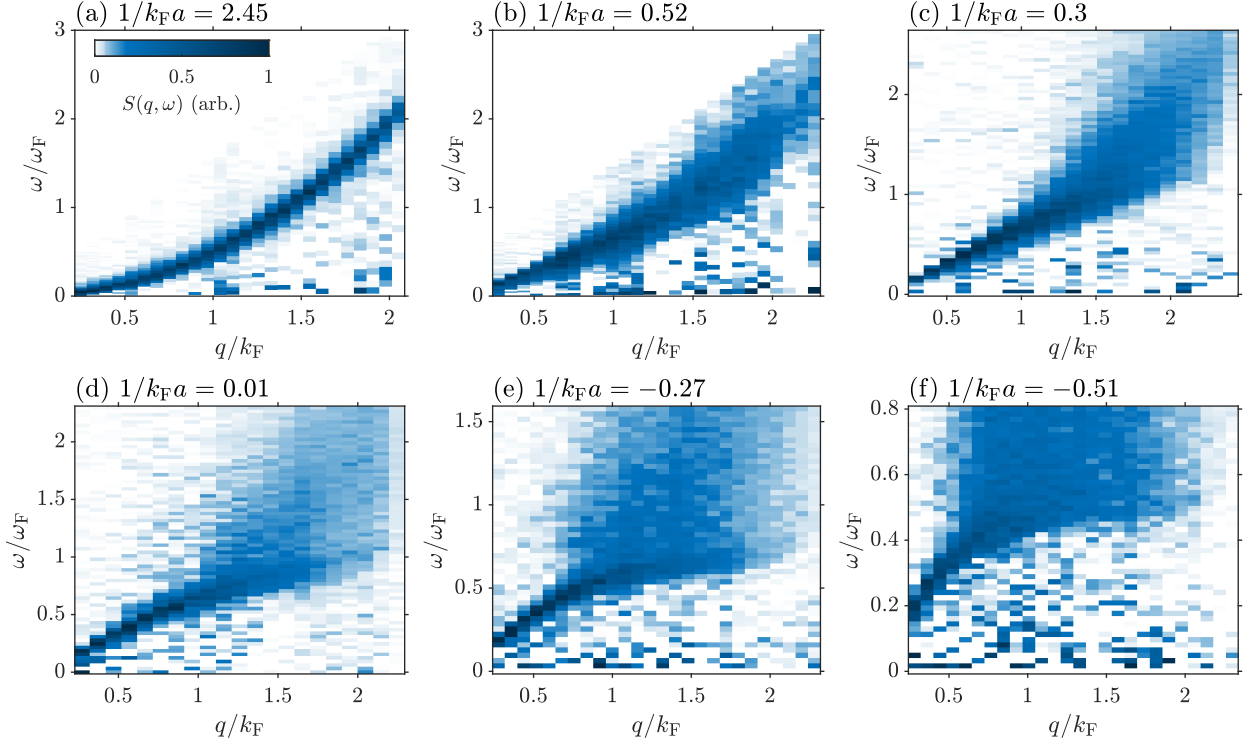


**Figure 3.8:** Evolution of the excitation spectrum in the BEC-BCS crossover. Note that the y-axes are scaled differently. (a) In the deep BEC regime, the excitation spectrum follows the Bogoliubov dispersion of an interacting Bose gas, with a linear sound mode at low momenta and a quadratic dispersion of single-molecule excitations at high momenta. (b,c) When moving into the crossover regime, the compressibility of the system decreases, and consequently the linear branch has a steeper slope and persists to higher momenta. At the same time, the high-momentum part of the dispersion shows a strongly reduced curvature and starts to broaden, which indicates the transition to pair-breaking excitations. (d) At the unitary point, there is already a strong pair-breaking continuum, which becomes even more pronounced when going further into the BCS regime (e,f). Note that the increased noise at small energy transfers in the spectra is an artifact of dividing a very small heating rate  $dE/dt$  by a small frequency  $\omega$  to obtain the dynamic structure factor  $S(q, \omega) \propto \omega^{-1} dE/dt$  (see Eq. 3.5).

mode approaches the pair-breaking continuum, it no longer follows the linear slope given by the speed of sound and instead starts to bend down. This behavior is reminiscent of an avoided crossing with the onset of the pair-breaking continuum, and indicates the existence of a coupling between the Goldstone mode and the excitation of single particles from the superfluid via pair breaking. Such a coupling has been predicted by theory [40, 72, 78, 91], but had not been observed yet in experiments.

After examining the general structure of the excitation spectrum, we now proceed to measure the dynamic structure factor at interaction strengths ranging from the deep BEC to the BCS regime. The results are presented in Fig. 3.8 and clearly show the evolution of the superfluid throughout the BEC-BCS crossover.

Our first observation is that the collective mode is present throughout the entire BEC-BCS crossover. This is a direct consequence of the fact that the presence of a well-defined Goldstone mode is a fundamental feature of any neutral superfluid [32, 39, 78].

In contrast, the nature of the single-particle excitations changes completely in the crossover. On the BCS side of the resonance (Fig. 3.8 e,f), the pairs are large and weakly bound and we observe a broad continuum of pair-breaking excitations. This continuum becomes less pronounced as the pairs become more tightly bound in the crossover regime and completely disappears from our spectra in the BEC regime (Fig. 3.8 a,b). This is caused by the pairs turning into deeply bound molecules, which are only broken at very high energy and momentum transfers. Consequently, when going towards the

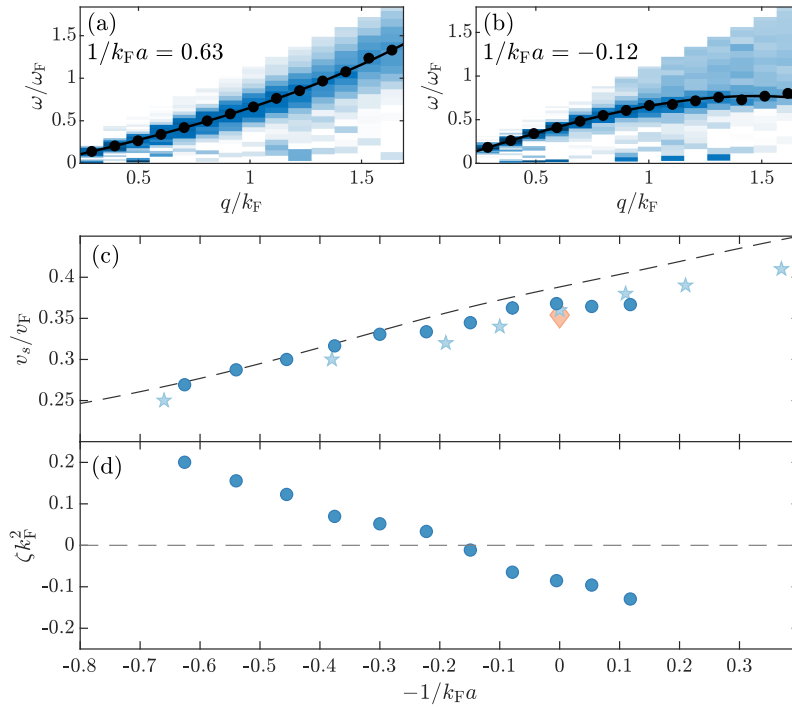


**Figure 3.9:** Measurements of the collective mode on the BEC (a) and BCS (b) side of the resonance. The black dots show the fitted center of the collective mode for each momentum slice, the black line is a fit according to the equation  $\omega = v_s q(1 + \zeta q^2)$ . (c) Speed of sound  $v_s$  across the BEC-BCS crossover (blue dots) extracted from the fit to the collective mode. We find good agreement with a previous measurement of the speed of sound performed via fixed-momentum Bragg spectroscopy [78] (light blue stars), a measurement of the Bertsch parameter at unitarity [28] (orange diamond) and a quantum Monte Carlo calculation of the equation of state [44] (dashed line). (d) Prefactor  $\zeta$  of the  $q^3$  correction to the collective mode. In the BEC regime, the dispersion bends upwards and  $\zeta > 0$ . When moving towards the crossover regime, the value of  $\zeta$  decreases until it changes sign at an interaction strength of  $1/k_F a \approx 0.2$ . For interaction parameters  $1/k_F a \lesssim 0.2$ , the collective mode bends down and  $\zeta < 0$ . The statistical uncertainties of the data points shown in (c) and (d) are smaller than the marker size.

BEC regime, pair breaking is gradually replaced by a different single-particle excitation where a single unbroken molecule is ejected from the condensate.

Our measurements directly show the evolution from a BCS superfluid of weakly bound Cooper pairs to a BEC of deeply bound molecules. Furthermore, the measured spectra agree well with the dynamic structure factor calculated by our collaborators J. Kinnunen and G. Bruun using a quasiparticle random-phase approximation<sup>34</sup> (QRPA) shown in Fig. 3.13 on p. 50.

In the following, we discuss the properties of the collective mode and the pair-breaking continuum in more detail and extract the speed of sound and the pairing gap over the crossover.

### 3.4 The collective mode

First, we consider the behavior of the collective mode. We extract its dispersion relation from Bragg measurements at low momentum by determining for each momentum  $\hbar q$  the frequency with the maximum response and fitting these maxima with the expression  $\omega(q) = v_s q(1 + \zeta q^2)$  following [92–94] (Fig. 3.9 a,b).

The first dominant contribution in the dispersion relation is linear in  $q$ . It is a collective density oscillation, namely, a sound wave. For larger momenta, the next-to-leading contribution is a  $q^3$ -dependency which has important consequences for the damping processes allowed in the system and has been the subject of theoretical discussion [95, 96].

<sup>34</sup> This method is in detail described in the supplementary materials of Ref. [78]

We note that if all quantities are expressed in Fermi units, a factor  $\frac{v_F k_F}{\omega_F} = 2$  must be considered when converting the slope of the collective mode to the speed of sound expressed in  $v_F$  because

$$\frac{\omega}{\omega_F} = v_s \frac{q}{\omega_F} = \frac{v_F k_F}{\omega_F} \frac{v_s}{v_F} \frac{q}{k_F} = 2 \frac{v_s}{v_F} \frac{q}{k_F}.$$

The fitted parameters show an increase of the speed of sound (Fig. 3.9 c) towards the BCS regime. This is expected because towards the BCS regime, the Fermi pressure becomes more relevant and makes the gas stiffer and the gas therefore less compressible. The extracted speed of sound agrees with previous results using fixed-momentum Bragg spectroscopy [78] and the speed of sound at unitarity from the Bertsch parameter,  $c_s = \sqrt{\xi/3} v_F$ . Furthermore, the results agree with the prediction of quantum Monte Carlo (QMC) calculations<sup>35</sup>.

<sup>35</sup> The extraction of the speed of sound from QMC calculations is explained in detail in Appendix C.

For the second extracted quantity, the curvature  $\zeta$  of the dispersion, we find that the dispersion is convex ( $\zeta > 0$ ) in the BEC regime, but when going towards the resonance  $\zeta$  smoothly decreases until it changes sign at an interaction strength of  $1/k_{Fa} \approx 0.2$  and the dispersion becomes concave ( $\zeta < 0$ ). At unitarity, we obtain a value of  $\zeta = -0.085(8)/k_F^2$ , which is in very good agreement with [92, 94].

### 3.5 The pair-breaking continuum and the pairing gap

In this section, we will first discuss the properties of the pair-breaking continuum and then extract the size of the pairing gap in the BEC-BCS crossover.

The measured continuum shows a clear dependence on both the energy and momentum transfer (see e.g. Fig. 3.8 e). On the energy axis, there is a sharp threshold of the continuum at a well defined energy, whereas the momentum axis shows a more gradual onset of pair-breaking excitations. Both of these observations are directly related to important properties of the pairs.

The suppression of excitations at low momentum and resulting existence of an onset on the momentum axis can be understood by comparing the wavelength of the excitation to the size of the pairs [97, 98]. If the size of the pairs is large compared to the wavelength of the excitation, a single particle can be excited and the pair can be broken. However, if the pair is smaller than the wavelength of the Bragg lattice, the excitation exerts almost no differential force on the atoms and they are preferentially excited as an unbroken pair. Therefore, as the size of the pairs changes in the BEC-BCS crossover, the onset of the continuum changes with the interaction strength. In the BCS regime, the pairs are large and we observe a broad pair-breaking continuum (Fig. 3.8 f). Going through the crossover, the pairs become more tightly bound and the onset of the continuum correspondingly moves to higher momenta, until we reach the deep BEC regime of tightly bound molecules, where pair-breaking excitations are strongly suppressed and no continuum is visible<sup>36</sup> (Fig. 3.8 a). In this regime, the gas has essentially become a strongly interacting Bose gas and pair-breaking excitations only occur at very high momenta and energies.

<sup>36</sup> This behaviour can be utilized to extract the pair size from the inverse of the momentum onset [16].

The threshold on the energy axis is caused by the existence of the pairing gap  $\Delta$ , which describes the energy cost associated with breaking a Cooper pair. The systems we consider in the following have a positive chemical potential. Therefore, we expect that the onset

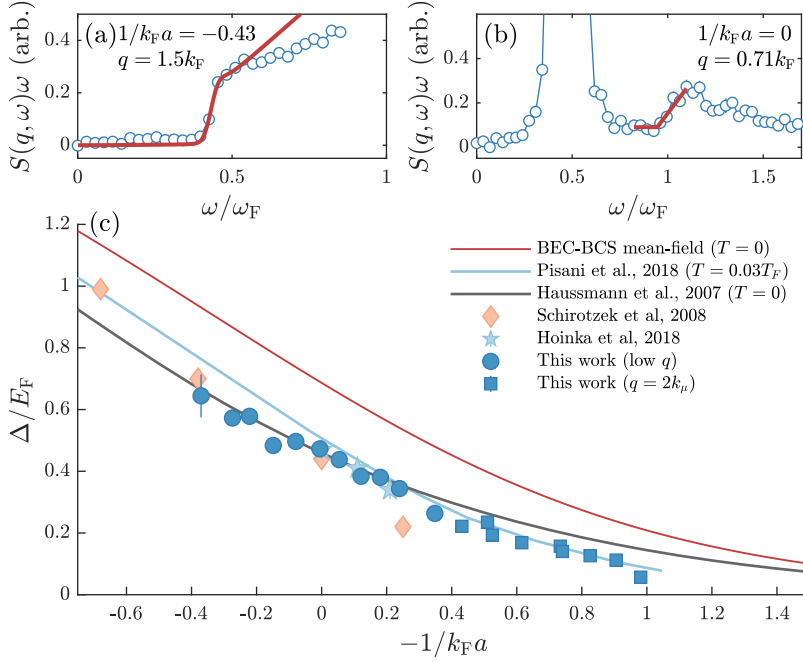


**Figure 3.10:** (a) Heating rate  $S(q, \omega)\omega$  on the BCS side of the resonance ( $1/k_F a = -0.44$ ) measured at a fixed momentum transfer of  $\hbar q = 1.5\hbar k_F$ . The onset of the pair-breaking continuum is clearly visible; the red line shows a fit of a lineshape from QRPA calculations used to extract the value of the pairing gap  $\Delta$  (blue squares in panel (c)). (b) Close to resonance, we perform measurements at low momentum to separate the onset of the pair-breaking continuum from the collective mode. The resulting onset determined from a bilinear fit (red) is shown in panel (c) as blue dots. (c) Pairing gap  $\Delta$  across the BEC-BCS crossover. The error bars denote the  $1\sigma$  confidence interval of the fit and are (mostly) smaller than the symbol size. Our data is in good agreement with previous measurements (orange diamonds [54], blue stars [78]). When comparing to theory, we find excellent agreement with self-consistent T-matrix calculations [88] close to resonance and in the BEC regime (black solid line), but towards the BCS regime calculations including Gor'kov-Melik-Barkhudarov corrections [99] (light blue line) are closer to our data.

of the pair-breaking continuum is at a momentum-independent<sup>37</sup> energy transfer of  $\omega = 2\Delta$  for momenta  $q < 2k_\mu = 2\sqrt{2m\mu/\hbar^2}$  [40].

This allows us to extract the pairing gap  $\Delta$  in the crossover, which we will do in the following. The challenge is to effectively separate the onset of the pair-breaking continuum from the collective mode.

In the BCS regime, we perform Bragg spectroscopy at fixed momentum transfers of  $q = 1.5 - 1.7 k_F$  where the collective mode merged already into the continuum and fit<sup>38</sup> the response  $r(\omega)$  with a lineshape from QRPA calculations convoluted with a Gaussian kernel of width  $\sigma_{\omega\omega_F} = 0.02$  (Fig. 3.10a.). The fitted gap is obtained by scaling the value of the gap used as input for the QRPA calculation with the optimal rescaling of the detuning axis from the fit.

This method works well in the BCS regime, but in the crossover the onset of the continuum is masked by the Goldstone mode because it does not merge into the continuum at low momenta (see Fig. 3.8 c,d). In this regime, we therefore employ the method developed in Ref. [78] and separate the pair-breaking excitations from the Goldstone mode by strong driving at low momentum transfer (Fig. 3.10 b). As this strongly saturates the Goldstone mode, these spectra are not well described by the QRPA calculation which assumes the system to be in the linear response regime. For these data points we therefore determine the onset of the pair-breaking mode from the transition point of a phenomenological bilinear fit (Fig. 3.10 b).

The gaps determined by our fits to the excitation spectra are shown in Fig. 3.10 c. We find excellent agreement with previous experiments performed in the BEC and crossover regimes [54, 78]. Next, we compare our data to T-matrix calculations that self-consistently include strong-pairing correlations (black line in Fig. 3.10 c [88]). Taking the

<sup>37</sup> This expectation is supported by the QRPA calculations (see Fig. 3.13 f,h) and is in excellent agreement with our measurements in the BCS regime.

<sup>38</sup> For the fit the detuning  $\omega/\omega_F$  and response  $r$  of the line-shape is rescaled such that the lowest least square deviation to the data is reached.

We estimate that the systematic uncertainty for the pairing gap arising from the different fit functions used for the two methods is  $0.03 E_F$  (Appendix D).

The systematic uncertainties on the extracted pairing gaps are discussed in Appendix D.

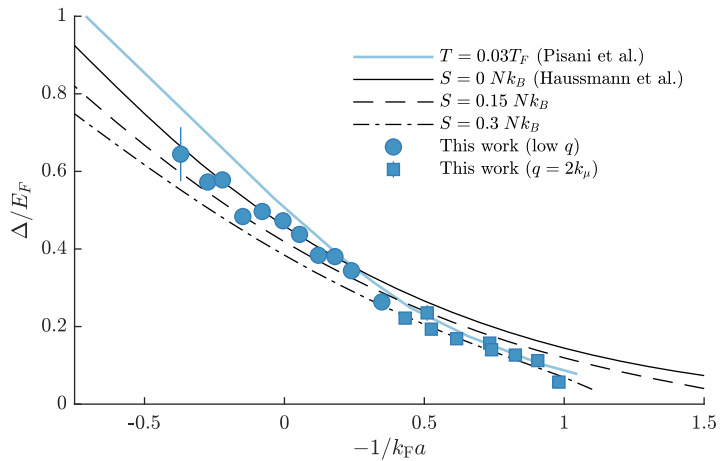
zero-temperature result, this theory is in excellent agreement with our data in the BEC and crossover regimes, but lies significantly above our measurements in the BCS regime.

When comparing our data to finite-entropy T-matrix calculations (Fig. 3.11), we find that our data is compatible with an entropy per particle of  $S/N \approx 0.1 k_B$  in the crossover and BEC regimes. However, in the BCS regime an entropy per particle on the order of  $0.3 k_B$  is required for data and theory to match. This difference is significantly larger than the variation of  $S/N$  of about  $0.07 k_B$  we estimate for our experiments. Thus, while the reduction of the gap could in principle be explained by finite-temperature effects, the results of the T-matrix calculation are inconsistent with our experimental observation that the system remains at almost constant entropy while ramping through the BEC-BCS crossover.

Another possible explanation could be that the size of the gap is influenced by particle-hole fluctuations. These fluctuations are not expected to be important at unitarity, but lead to the famous Gor'kov-Melik-Barkhudarov (GMB) correction [100, 101] in the BCS limit. This effect is taken into account in a recent strong coupling calculation [99], which is in good agreement with our data in the BCS regime, but lies significantly above our measurements on the BEC side of the resonance (blue line in Fig. 3.10). Interestingly, the smaller pairing gap in the BCS regime is also predicted by zero-temperature quantum Monte Carlo (QMC) calculations (Fig. 3.12).

We can conclude that neither the T-matrix calculations [88] nor the approach that takes into account particle hole fluctuations [99] are fully consistent with our data throughout the crossover. The explanation for this could lie on both the theoretical and experimental sides of the problem, and further work will be needed in both areas to resolve this question.

**Figure 3.11:** Measurement of the pairing gap in the BEC-BCS crossover in comparison to finite temperature T-matrix calculations (dashed and dashed-dotted black lines). While the measured gap and zero-temperature theory are in excellent agreement in the crossover and BEC regimes, in the BCS regime calculations for a finite entropy per particle of  $S/N = 0.3 k_B$  are much closer the data. This is inconsistent with our observations suggesting a nearly constant entropy of the gas throughout the BEC-BCS crossover.



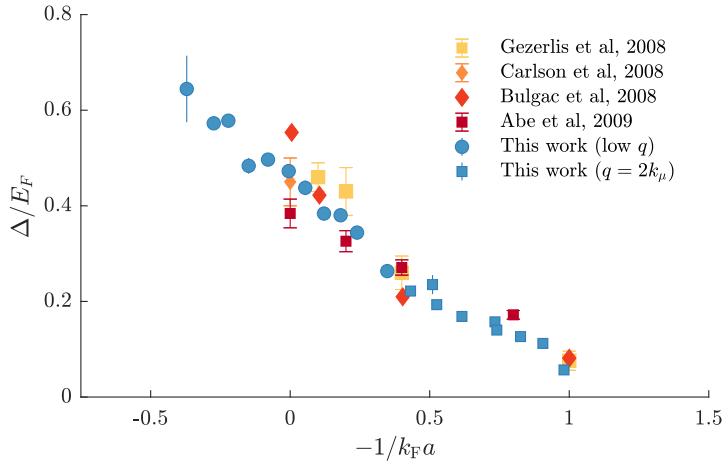


**Figure 3.12:** Measurement of the pairing gap in the BEC-BCS crossover in comparison to various zero-temperature QMC results [102–105].

## CONCLUSION

We have presented momentum and energy-resolved measurements of the excitation spectrum of a homogeneous ultracold Fermi gas. These measurements directly reveal the transformation from tightly bound molecules to weakly bound Cooper pairs that takes place in the BEC-BCS crossover. Moreover, this realization of a quantum simulator of a strongly correlated system allows us to determine essential parameters of the many-body system. The evolution of the collective mode allows extraction of the speed of sound and the onset of the pair breaking continuum the extraction of the pairing gap in the BEC-BCS crossover. The values found can be used to benchmark our theoretical understanding and calculations.

This setup is also ideally suited to study Fermi gases, where on top of the interaction strength other parameters are altered, for instance the dimensionality or the spin-balance. Both scenarios we will discuss in the following chapters.

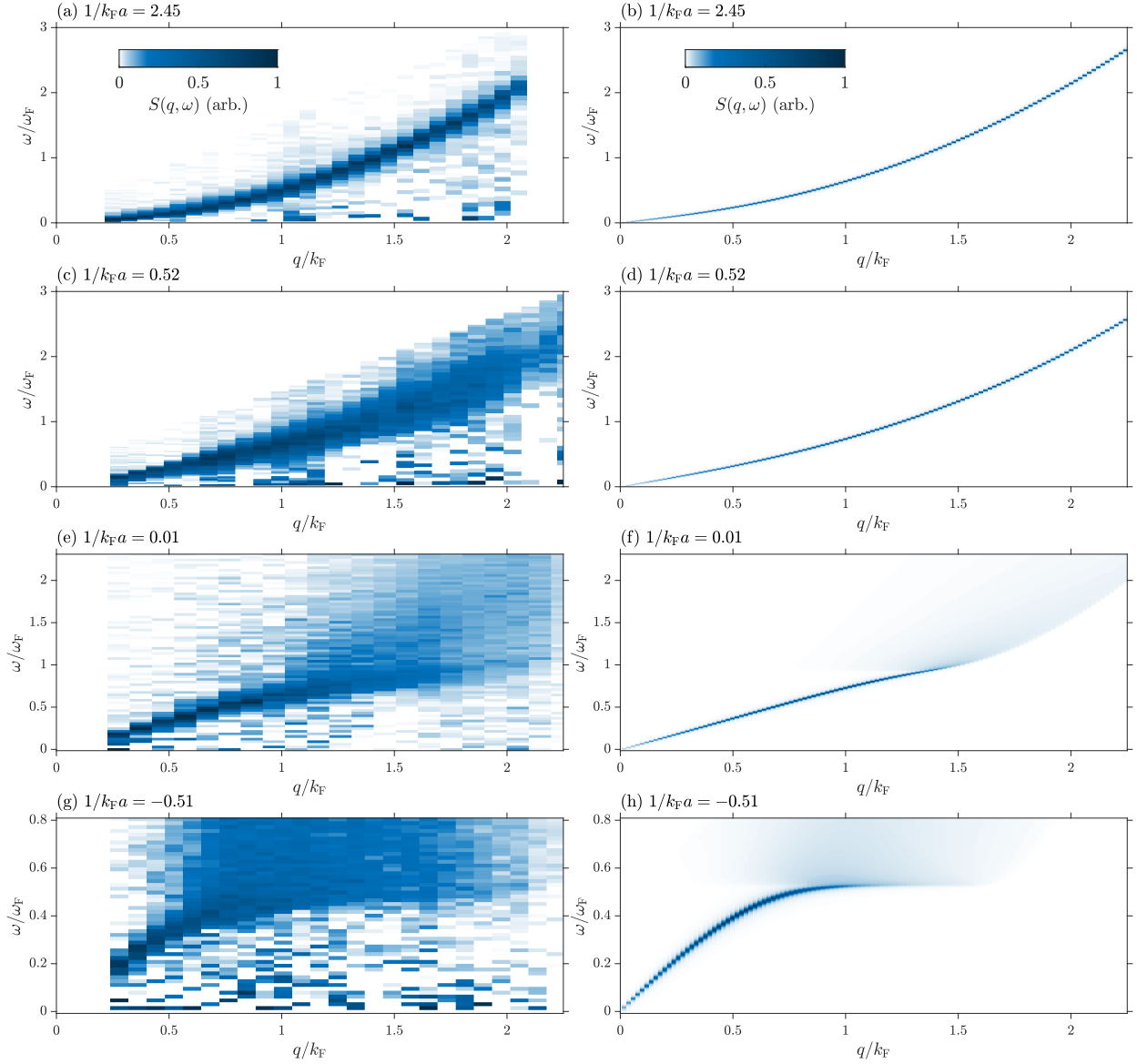


**Figure 3.13:** Comparison of the measured excitation spectra (left column) with spectra calculated using the quasiparticle random-phase approximation (right column). While the qualitative evolution of both the pair-breaking continuum and the collective mode agrees, there are some notable differences. On the BEC side, the collective mode is much narrower in the theoretical spectra. This can be a result of both finite temperature and instrumental broadening of the measurements, which could for example be caused by residual inhomogeneities of the gas. As the spectra are normalized, the sharper collective mode in the theoretical spectra makes the continuum appear weaker, which is particularly notable for the unitary system. However, despite this effect and the broadening present in the experimental data, important qualitative features such as the downbending of the collective mode and the overall shape of the continuum are still clearly visible in both the theoretical and experimental spectrum. In the BCS regime, there is excellent agreement between the experimental result and QRPA theory, with the only significant difference being the slightly different onset of the pair-breaking continuum. This, however, is expected as the theoretical pairing gaps from self-consistent T-matrix theory [88] which were used as inputs for the QRPA calculation are higher than our measurements in the BCS regime (see Fig. 3.10).

# 4

## TWO-DIMENSIONAL FERMI GASES

In the following chapters, we study 2D Fermi gases. Their lack of true long-range order due to the larger influence of fluctuation [106] establishes two dimensions as the marginal number of dimensions for the existence of superfluidity [107]. In this chapter, we discuss how a quasi-long-range order is restored through the BKT mechanism [107, 108]. Then, we explore scattering physics in quasi-2D systems and apply it to the BEC-BCS crossover allowing us to study 2D strongly interacting fermionic superfluids in the next chapters.

### 4.1 The BKT phase transition

In three dimensions, most phase transitions arise when a new long-range order occurs. In particular, the emergence of long-range phase coherence gives rise to the superfluid phase. For that we have to consider the first-order correlation function [109]

$$g_1(\mathbf{r}) = \langle \psi^\dagger(\mathbf{r})\psi(0) \rangle$$

where  $\psi(\mathbf{r})$  is a bosonic creation operator<sup>39</sup>. If long-range phase coherence exists,  $g_1(\mathbf{r})$  acquires a finite value for  $r \rightarrow \infty$ . In this case, the phase of the order parameter remains correlated throughout the whole system. This gives rise to superfluidity: If the phase is perturbed at one point in the fluid, the phase difference with respect to any other position in the fluid is well defined and a superfluid flow will emerge trying to cancel the phase difference.

However, for 1D and 2D systems with short-range interaction the Mermin-Wagner theorem tells us that for the physically relevant case of finite temperatures no true long-range order is supported because the first-order correlation function always tends to zero for  $r \rightarrow \infty$  [106, 110]. The reason is that, for lower dimensions, phase fluctuations are favored, since more phase space is available for thermal excitations at low energy.

There are two kinds of excitation to consider, phonons and free vortices. While low-energy phonons manifest themselves in long-wavelength phase fluctuations, the effect of free vortices is detrimental: Around an isolated single vortex, the phase winds by  $2\pi$ . This has a global effect and results in an exponential decay of the first-order correlation, which destroys any long-range phase coherence.

In 2D, there is a mechanism to keep vortices from perturbing the phase found by Berenzinskii [108] and Kousterlitz and Thouless [107], the BKT transition. If the temperature is lowered below a critical temperature  $T_{\text{BKT}}$  vortices start to pair into vortex-antivortex pairs. These perturb the phase only locally because the superposition of the

<sup>39</sup>For a fermionic BCS superfluid, the operator  $\psi(\mathbf{r})$  is the two-point pair correlation function defined in Eq. 2.10 [19].

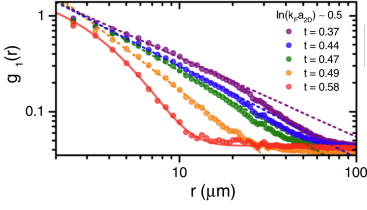


**Figure 4.1:** Change of the first-order correlation for a 2D Fermi gas with interaction strength  $\ln(k_F a_{2D}) \sim 0.5$  from an algebraic to an exponential decay for increasing temperatures given in  $t = T/T_{\text{BEC}}^0$  where  $T_{\text{BEC}}^0$  is the condensation temperature of an ideal 2D Bose gas. Adapted from [111].

<sup>40</sup> The reason is that the superfluid density jumps from  $n_s = 0$  to  $n_s = 4/\lambda^2$  when  $T_{\text{BKT}}$  is crossed from above.

phase windings  $-2\pi$  and  $2\pi$  neutralizes the effect of each individual vortex at larger distances.

Thus, for  $T < T_{\text{BKT}}$  only the long-range phase fluctuations of thermally excited phonons remain. They just create an algebraic decay of the phase coherence [109]

$$g_1(r) \propto \left(\frac{1}{r}\right)^\eta$$

where the exponent is given by the superfluid density  $n_s$  and the de-Broglie wavelength  $\lambda$  via  $\eta = \frac{1}{n_s \lambda^2}$ . The change from exponential to algebraic decay has been observed experimentally in 2D Fermi gases (Fig. 4.1).

For  $T < T_{\text{BKT}}$  the superfluid density is always<sup>40</sup>  $n_s \geq 4/\lambda^2$ . Therefore, the exponent of the algebraic decay  $\eta < 1/4$ , which results in a slow decay of the first-order correlation function. Still,  $g_1$  approaches zero for large distances, which is in agreement with the Mermin-Wagner theorem. However, the slow decay allows for quasi-condensation in finite-size systems. In these systems, there is a maximum distance  $r = L$  that two particles can be apart, and the first-order correlation  $\sim g_1(L)$  remains finite throughout the entire system.

## 4.2 Scattering in two dimensions

For a detailed review of scattering in 2D and the 2D BEC-BCS crossover, please see Refs. [112, 113].

In this section, we discuss the scattering problem in pure 2D systems, where a third dimension is absent, and in quasi-2D systems, where the gas is tightly confined along the third dimension. The objective is to establish a relationship between the scattering processes in these systems which allows us to compare experimental results from quasi-2D systems to theoretical predictions of pure 2D systems.

### PURE 2D SCATTERING

First, we consider a pure 2D system and two atoms (in different hyperfine states) with an attractive contact interaction. The two-body scattering amplitude is given by [113]

$$f(k, E_B) = \frac{4\pi}{\ln(-E_{B,2D}/E(k))}, \quad (4.1)$$

where  $E(k) = \hbar^2 k^2 / (2m_r)$  is the energy of the scattering particles with reduced mass  $m_r = m/2$  and  $E_{B,2D}$  the binding energy<sup>41</sup> of the bound state between both atoms. In 2D, this bound state exists for any arbitrarily weak attractive interaction between two fermions [114]. Its binding energy can be expressed in terms of a two-dimensional scattering length  $a_{2D}$ ,

$$E_{B,2D} = \frac{\hbar^2}{m a_{2D}^2}. \quad (4.2)$$

This allows us to rewrite the scattering amplitude to

$$f(k, a_{2D}) = \frac{4\pi}{-2 \ln(ka_{2D}) + i\pi}, \quad (4.3)$$

<sup>41</sup> We define the binding energy to be positive.

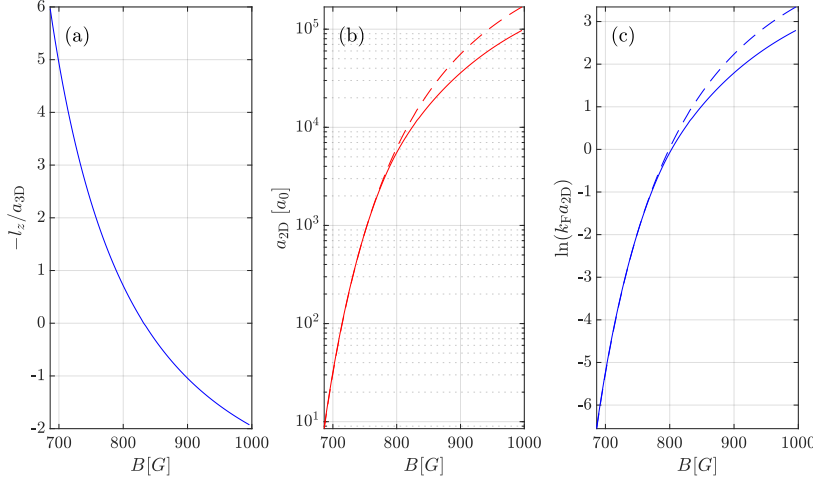


**Figure 4.2:** (a) Inverse 3D scattering length  $l_z/a_{3D}$  for a vertical trapping frequency of  $\omega_z = 2\pi \times 10$  kHz from the BEC regime (low magnetic field) to the BCS regime (high magnetic field) (b) Quasi-2D scattering length in the low-momentum approximation  $kl_z \ll 1$  (dashed, Eq. 4.6). If scattering at momenta comparable to  $l_z^{-1}$  occurs, the scattering length becomes density dependent (Eq. 4.7). The solid line shows the scattering length for a density of  $n_{2D} = 0.7 \mu\text{m}^{-2}$ , which corresponds to  $E_F/\hbar\omega_z = 0.74$ . (c) Resulting 2D interaction parameters using  $k_F = 3.0 \mu\text{m}^{-1}$  corresponding to  $n_{2D} = 0.7 \mu\text{m}^{-2}$ .

where an analytical continuation of the logarithm was used in order to deal with its negative argument. For a fermionic gas, scattering events can only occur close to the Fermi surface where  $k = k_F$ , thus  $\ln(k_F a_{2D})$  is commonly used to parametrize the interaction in 2D. Alternatively, the binding energy normalized by the Fermi energy,  $E_B/E_F$ , can be used as a parametrization for the interaction strength. As we will see in the following, this equivalence between both parametrizations does not exist in quasi-2D.

#### QUASI-2D SCATTERING

In our 3D world, we cannot create a pure 2D system as the third dimension cannot be removed. However, we can add a strong confinement along one spatial direction to freeze out the movement which results in a quasi-2D system.

For a non-interacting Fermi gas, we obtain a quasi-2D system when the separation of the ground state to any excited state along the confining direction is so large that all fermions occupy only the ground state and their degrees of freedom are distributed along the other two spatial dimensions. For a harmonic confinement with trapping frequency  $\omega_z$ , this happens when the Fermi energy is  $E_F < \hbar\omega_z$ . At finite temperature and with interactions, we in addition take care to keep the thermodynamic energy scales<sup>42</sup>, the chemical potential  $\mu$  and the temperature  $k_B T$ , below  $\hbar\omega_z$ .

The s-wave scattering process we want to consider is inherently three-dimensional, so the question arises of how the 3D scattering length can be related to the 2D scattering length (Eq. 4.3). This question was addressed by Petrov and Shlyapnikov [117] who derived the quasi-2D scattering amplitude

$$f_{\text{quasi,2D}}(k, a_{3D}, l_z) = \frac{4\pi}{\sqrt{2\pi}l_z/a_{3D} + w(k^2 l_z^2/2)}, \quad (4.4)$$

where the harmonic oscillator length  $l_z = \sqrt{\hbar/(m\omega_z)}$  and the complex function  $w(x)$  were defined. The function  $w(x)$  contains

<sup>42</sup> It is a topic of debate if the criterion  $\mu < \hbar\omega_z$  is sufficient in the strongly interacting regime to remain in the 2D regime, see discussion in Chap. 9 in Ref. [113] and the summary on p. 33 in Ref. [115] regarding the experiments performed in Ref. [116].

the momentum-dependent contributions to the scattering amplitude given by

$$w(x) = \lim_{N \rightarrow \infty} \left( 2\sqrt{\frac{N}{\pi}} \log\left(\frac{N}{e^2}\right) - \sum_{j=0}^N \frac{(2j-1)!!}{(2j)!!} \log(j-x-i0) \right).$$

This function simplifies in the low momentum limit  $kl_z \rightarrow 0$  to

$$w_0 \equiv \lim_{kl_z \rightarrow 0} w(k^2 l_z^2 / 2) = -\ln\left(\frac{2\pi}{A} \frac{k^2 l_z^2}{2}\right) + i\pi$$

with  $A \approx 0.915$  which results in

$$f_{\text{quasi,2D},0}(k, a_{3D}, l_z) = \frac{4\pi}{\sqrt{2\pi} l_z / a_{3D} - \ln\left(\frac{2\pi}{A} \frac{k^2 l_z^2}{2}\right) + i\pi} \quad (4.5)$$

By equating the pure 2D scattering amplitude (Eq. 4.3) with this simplified quasi-2D scattering amplitude (Eq. 4.5) we obtain a relation between the 2D scattering length and the 3D scattering length,

$$a_{2D,0} = l_z \sqrt{\frac{\pi}{A}} e^{-\sqrt{\frac{\pi}{2}} l_z / a_{3D}}. \quad (4.6)$$

The inverse 3D scattering length, the 2D scattering length, and the resulting 2D interaction parameter are computed for a vertical trapping frequency of  $\omega_z = 2\pi \times 10$  kHz and density of  $n_{2D} = 0.7 \mu\text{m}^{-2}$  in Fig. 4.2. While the interaction parameter  $1/(k_F a_{3D})$  depends on the scattering length and the density, the resulting interaction parameter  $\ln(k_F a_{2D,0})$  also depends on the strength of the vertical confinement.

The low-momentum limit that we used to simplify  $w(x)$  is applicable if two particles with relative momentum  $k \ll l_z^{-1}$  would scatter. However, this limit is difficult to reach experimentally, as the momenta  $k \sim k_F \propto \sqrt{n_{2D}}$  are close to the achievable  $l_z^{-1} \propto \omega_z$ . Therefore, we follow the approach in Ref. [118] and consider as the characteristic energy of two scattering particles the chemical potential<sup>43</sup>. This results in a characteristic wavelength of  $k = k_\mu = \sqrt{\mu/(2m)}$  yielding  $x = k^2 l_z^2 / 2 = \frac{\mu}{\hbar\omega_z}$ . By equating the pure 2D scattering amplitude (Eq. 4.3) with the quasi-2D scattering amplitude (Eq. 4.4) we obtain the scattering length

$$a_{2D} = a_{2D,0} e^{-\frac{1}{2} \Delta w\left(\frac{\mu}{\hbar\omega_z}\right)}, \quad (4.7)$$

where  $\Delta w(x) = w(x) - w_0(x)$  is the difference of the  $w$ -function with respect to its  $kl_z \rightarrow 0$  limit used to derive  $a_{2D,0}$  (Eq. 4.6). As we see in Fig. 4.2, considering the term  $-\frac{1}{2} \Delta w(x)$  in Eq. 4.7 reduces the interaction parameter  $\ln(k_F a_{2D})$  by up to  $\sim 0.5$  in the BCS regime.

Similar to a pure 2D system, a bound state exists for arbitrarily weak attractive interactions in a quasi-2D system. These bound pairs exist throughout the 3D Feshbach resonance and interact repulsively, which explains the positive scattering length in Eq. 4.7 for both positive and negative  $a_{3D}$ . In the BCS regime, the binding energy of these confinement induced pairs follows Eq. 4.2 with  $a_{2D}$  from Eq. 4.6. In the regime, where pairs can exist also in 3D ( $a_{3D} > 0$ ,  $E_{B,3D} = \frac{\hbar^2}{2ma_{3D}^2}$ ) and

<sup>43</sup> In the BEC-BCS crossover, we use the reduced chemical potential  $\tilde{\mu} = \mu - E_B/2$  from the QMC calculations in Ref. [119], which smoothly connects the BEC limit ( $\tilde{\mu} \sim gn$ ) and the BCS limit ( $\tilde{\mu} \sim E_F$ ).

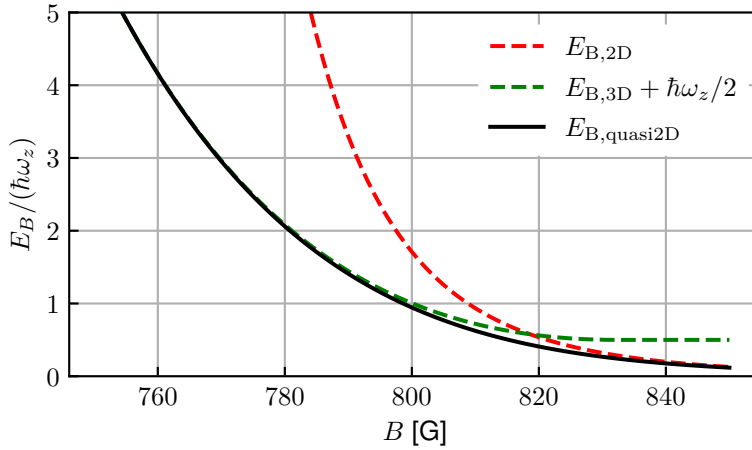


**Figure 4.3:** Confinement induced binding energy  $E_{B,\text{quasi-2D}}$  in a vertical confinement of  $\omega_z = 2\pi \times 10$  kHz throughout the BEC-BCS crossover (black solid, Eq. 4.8). In the BCS limit, it agrees with  $E_{B,2D}$  (red dashed, Eq. 4.2) as the pairs are purely 2D. As the pairs become smaller, the third dimension becomes important and the binding energy crosses over into the 3D binding energy shifted by  $\hbar\omega_z/2$  (green dashed).

the pair size  $\sim a_{3D}$  becomes comparable to  $l_z$ , the pairs do not notice the 2D confinement and the confinement-induced bound state crosses over into a 3D bound state with a binding energy of  $E_{B,3D} + \hbar\omega_z/2$ , where the last term is a shift in energy due to the 2D confinement. The binding energy covering both limits and the crossover regime can be obtained by numerically solving the integral equation [5]

$$\frac{l_z}{a_{3D}} = F\left(\frac{E_{B,\text{quasi-2D}}}{\hbar\omega_z}\right) \quad (4.8)$$

for  $E_{B,\text{quasi-2D}}$  where the function on the right side is defined by

$$F(x) = \int_0^\infty \frac{du}{\sqrt{4\pi}u^3} \left(1 - \frac{e^{-xu}}{\sqrt{[1 - e^{-2u}]/(2x)}}\right).$$

The resulting binding energy is shown in Fig. 4.3.

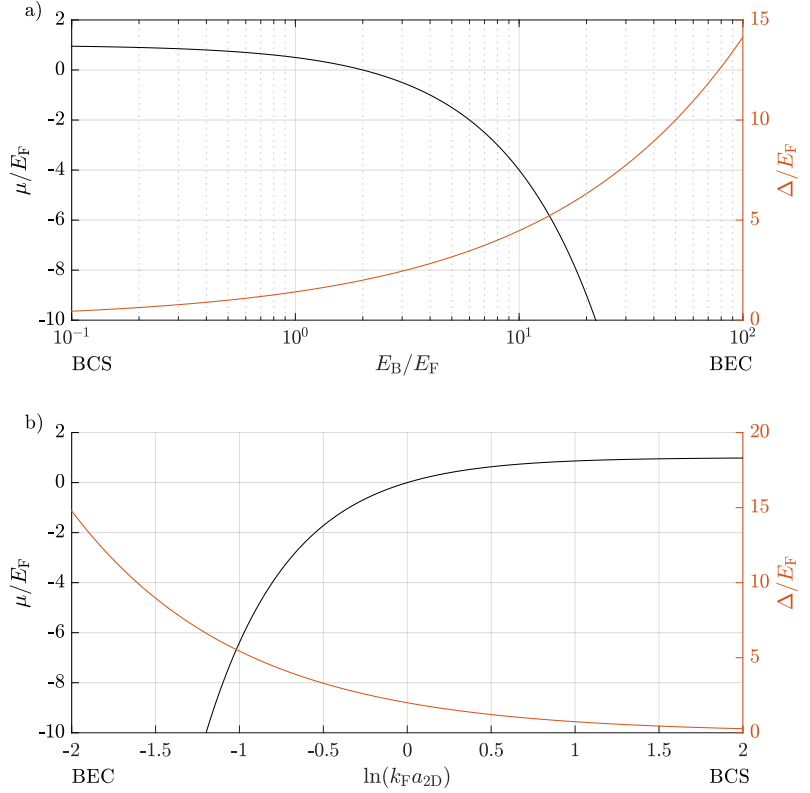
We see here that the universal relation<sup>44</sup> between the binding energy and scattering amplitude does not exist in a quasi-2D system because the binding energy is subject to a 2D to 3D crossover when approaching the BEC regime.

This gives rise to the question which quantity should be used to parametrize the interaction strength. If the scattering physics in a quasi-2D system shall be connected with the scattering physics in a pure 2D system, the scattering length in Eq. 4.7 is the correct choice because its derivation involved the comparison of both scattering amplitudes. The other possible choice, taking the confinement induced binding energy from Eq. 4.8 and assuming that it represents the binding energy in a pure 2D system, so setting  $E_B = E_{B,\text{quasi-2D}}$  and solving for  $a_{2D}$  on the LHS does not work, as was also shown in [120].

Thus, if we want to compare experimental results from a quasi-2D system with theoretical calculations for a pure 2D system we have to use the definition of the scattering length in Eq. 4.7. After creating a connection to the pure 2D system, we could use as an alternative representation of the interaction strength the binding energy in the pure 2D system by inserting  $a_{2D}$  (Eq. 4.7) into  $E_{B,2D}$  (Eq. 4.2). This

<sup>44</sup> See Eq. 4.2 and Eq. 4.3 in the pure 2D system.

**Figure 4.4:** Mean-field chemical potential (black) and gap (red) in the 2D BEC-BCS crossover as a function of the binding energy  $E_B/E_F$  (a) or 2D interaction parameter  $\ln(k_F a_{2D})$  (b). In the BCS limit  $\mu \sim E_F$  the gap decreases exponentially. In the BEC limit, the chemical potential approaches  $\mu \sim -E_B/2$ .



binding energy, however, is not the binding energy in the quasi-2D system ( $E_{B,\text{quasi-2D}}$ ), it merely is the binding energy of a pure 2D system with the same scattering amplitude.

### 4.3 The 2D BEC-BCS crossover

After covering two-body interactions in 2D, we will now turn our attention to the many-body problem and discuss very shortly the 2D BEC-BCS crossover on a mean-field level, which was first considered by Mohit Randeria et al. in 1989 [121, 122].

In 2D, the gap and number equation in the mean-field BEC-BCS theory are much simpler than in 3D, where integrals to be evaluated numerically remained. Solving the gap and number equations self-consistently, two simple analytical results are obtained for the gap and the chemical potential,

$$\mu = E_F - \frac{E_{B,2D}}{2}, \quad (4.9)$$

$$\Delta = \sqrt{2E_{B,2D}E_F}, \quad (4.10)$$

where we use the binding energy  $E_{B,2D}$  to parametrize the crossover in a pure 2D system. Both are plotted in Fig. 4.4.

The BCS limit is reached for  $E_B \ll E_F$  where the chemical potential  $\mu = E_F$  and the gap<sup>45</sup>

<sup>45</sup> We insert Eq. 4.2 in Eq. 4.10

$$\Delta = E_F \frac{2}{k_F a_{2D}} = 2E_F e^{-\eta}$$

approaches zero as  $a_{2D} \rightarrow \infty$  or  $\eta = \ln(k_F a_{2D}) \rightarrow \infty$ . At  $E_B/E_F = 2$  and  $\ln(k_F a_{2D}) = 0$  the fermionic chemical potential  $\mu$  becomes negative and the system becomes more bosonic. The BEC limit is reached for  $E_B \gg E_F$  or  $\ln(k_F a_{2D}) \rightarrow -\infty$ . Here, the chemical potential approaches<sup>46</sup>  $\mu \sim -E_B/2$ .

In the next chapter, we will investigate the excitation spectrum of 2D Fermi gases modeling the 2D BEC-BCS crossover we introduced here.

<sup>46</sup> On the mean-field level in 2D, the BEC-BCS theory does not contain any dimer-dimer interactions and the reduced chemical potential  $\tilde{\mu} = \mu + E_B/2$  stays at  $E_F$  instead of decreasing to  $\tilde{\mu} \sim gn/2$  as in 3D. We discuss this question and the limitations of the 2D mean-field BEC-BCS crossover in more detail in Sect. 10.2.



# 5

## SPECTROSCOPY IN 2D FERMI GASES

In this chapter, I summarize two studies on the excitation spectrum showing sound propagation and superfluidity in the 2D BEC-BCS crossover. For that, I give a summary of the measurement of the speed of sound published in [123]

M. Bohlen, L. Sobirey, N. Luick, H. Biss, T. Enss, T. Lompe, and H. Moritz,  
*Physical Review Letters*, 124(24), 240403 (2020).

and the critical velocity published in [124]

L. Sobirey, N. Luick, M. Bohlen, H. Biss, H. Moritz, and T. Lompe,  
*Science*, 372(6544), 844–846 (2021).

Parts of this chapter are reproduced from these publications with some modifications. For a detailed discussion of these results, I would like to refer to the respective PhD theses of the lead authors Markus Bohlen [125] and Lennart Sobirey [16]. I contributed to the development of the experimental Bragg setup, the execution of the experiments, and the interpretation of our results.

### 5.1 Sound propagation in a 2D Fermi gas

As we discussed in Chap. 2 a superfluid features long-lived collective excitations which manifest in sound waves. The goal of the first experiment is to excite these long-wavelength excitations by creating a propagating sound wave. For that, the 2D Fermi gas is loaded into a repulsive box potential which has a rectangular form of dimensions  $l_x \times l_y = 30 \times 40 \mu\text{m}$  (Fig. 5.1).

To excite a sound wave in the box, we imprint a relative phase between the lower and upper halves of the system by illuminating one half with a spatially homogeneous optical potential for a short duration which is smaller than the respective Fermi time,  $\tau < \hbar/E_F$ .

We then observe the change in density by imaging the density distribution after different hold times using in situ absorption imaging (Fig. 5.2). This reveals that a sound wave travels back and forth between two sides of the box. Apparently, the phase imprinting creates a superposition of phononic excitations that form a wave package, which is reflected by the repulsive box potential.

In order to measure the speed of sound, we use the circumstance that the sound wave is moving back and forth with a periodicity given by the time it takes for the sound wave to cover twice the length of the box. Thus, we expect an oscillation frequency of  $f = c/(2l_x)$  where  $c$  is the speed of sound. We take the relative particle imbalance defined as  $\Delta n/n = 2(n_t - n_b)/(n_t + n_b)$  with densities  $n_t$  and  $n_b$  in the top and bottom halves of the box to extract this oscillation frequency. This quantity is then fitted with a damped sinusoidal of the form

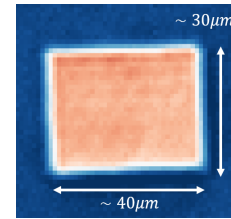


**Figure 5.1:** Averaged density distribution of the Fermi gas trapped in a box potential used to study sound propagation.

**Figure 5.2:** The upper panel shows the propagation of a sound wave in a box potential. Here, the density profiles are averaged along the  $y$  axis that is perpendicular to the propagation direction ( $x$  axis) and normalized to the average density within the box. The quantity shown is  $n(x, t)/n(t) = \sum_y n(x, y, t) / \sum_{x,y} n(x, y, t)$ . We see a density wave propagating through the box and being reflected at the upper and lower box boundaries. The lower panel shows the relative density imbalance between the upper and lower sides of the box for the same data set and a damped sinusoidal fit (solid line) to the data.

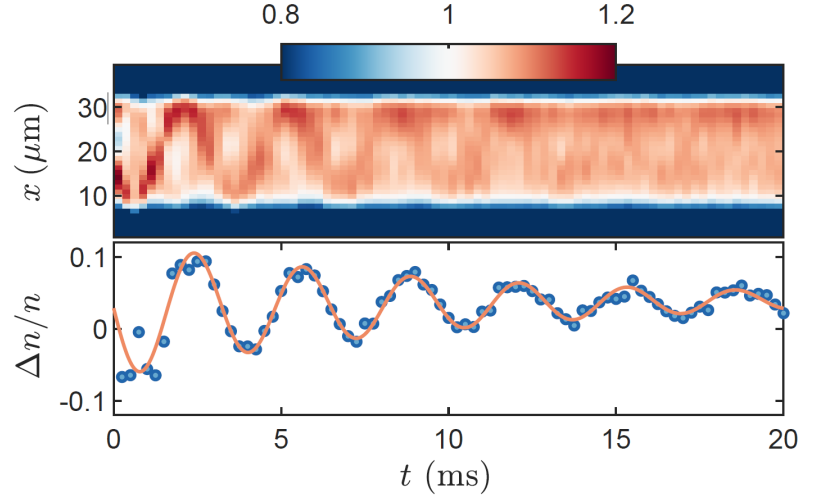
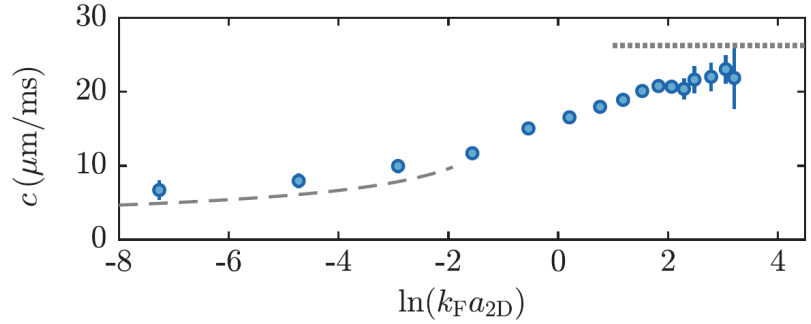


**Figure 5.3:** The speed of sound across the BEC-BCS crossover increases as the gas becomes stiffer due to a higher Fermi pressure. It approaches its theoretical limits in the BEC (grey dashed) and BCS (grey dotted) regimes, respectively. In the BEC regime, it is given by  $c_B = \sqrt{\mu/m_d} = \sqrt{gn/(2m)}$  arising from a repulsive interaction strength  $g$  between dimers of mass  $m_d = 2m$ . On the BCS side, the speed of sound approaches the universal value of  $c = v_F/\sqrt{d}$  of a weakly-attractive Fermi gas with the number of spatial dimensions  $d = 2$  and Fermi velocity  $v_F = \hbar k_F/m$ .



$A(t) = A_0 \cos(2\pi f t + \phi) \exp(-\Gamma t/2) + b$  to extract the frequency  $f$  and the damping  $\Gamma$  (Fig. 5.2). The sound speed can then be easily obtained<sup>47</sup> as  $c = 2l_x f$ .

As a next step, we probe the speed of sound as a function of the 2D interaction strength by performing the same measurements at different magnetic fields. We plot the speed of sound extracted from the oscillation frequencies as a function of the 2D interaction parameter in Fig. 5.3. First, we observe that in both the BEC and BCS regime the theoretical limits are approached. The second observation is that the speed of sound increases from the BEC regime to the BCS regime, which is expected since the compressibility of a Fermi gas is much lower than that of a weakly repulsive Bose gas. In the BCS regime, the gas is thus stiffer with respect to density fluctuations, and sound waves propagate faster than in the BEC regime<sup>48</sup>.

The second quantity that we extract from the oscillation is the damping of the sound wave. Damping is caused by collisions of particles with the medium of other particles. In the strongly correlated system we study, the mean free path of particles is much smaller than the oscillation wavelength. Therefore, we are in the so-called hydrodynamic regime. Here, diffusive currents of the longitudinal momentum, the transverse momentum<sup>49</sup> cause a dampening of the sound wave. The damping can be expressed in a scale-invariant sound

<sup>47</sup> We ensured that the extracted speed of sound is independent of the box size  $l_x$ . Therefore, edge effects are negligible.

<sup>48</sup> This fact can be used to extract the compressibility  $\partial n/\partial \mu$  of the system through the BEC-BCS crossover and compare it to independent measurement of the equation of state  $\mu(n)$  and theoretical predictions, where we would like to refer the reader to the original publication and Markus Bohlen's thesis [123, 125].

<sup>49</sup> These diffusive currents result from a finite bulk viscosity, shear viscosity, and heat conductivity.

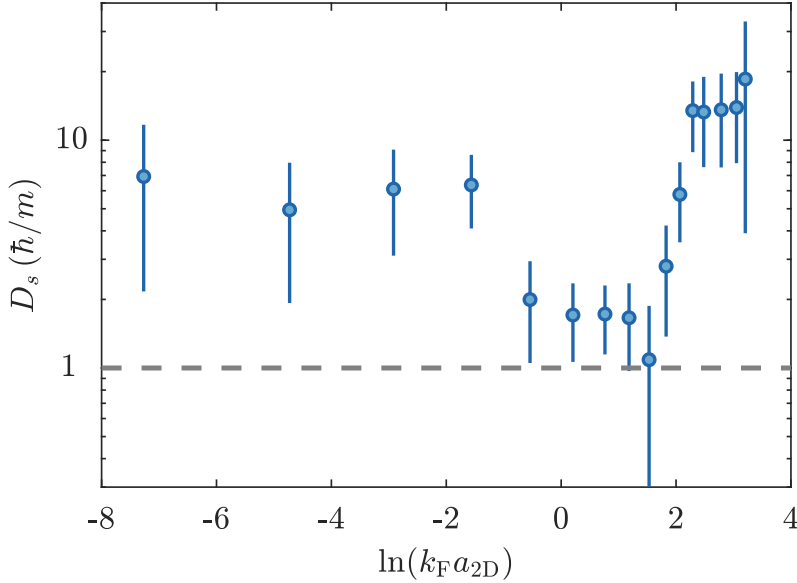


**Figure 5.4:** Sound diffusion coefficient in the BEC-BCS crossover. In the strongly correlated regime, the diffusion coefficient reaches a minimum which agrees well with the universal quantum bound for diffusion at  $\hbar/m$  (dashed line).

diffusion  $D_s = \Gamma/k_0^2$  where  $k_0$  is the strongest wave component in the propagating wave package given by  $k_0 = 2\pi/(2l_x) = \pi/l_x$ .

We see in Fig. 5.4 that the sound diffusion coefficient reaches a minimum in the strongly correlated regime around  $\ln(k_F a) = 0$ . The value corresponds to the so-called quantum limit  $D_s \sim \hbar/m$  that we can obtain by a simple scaling argument using the kinetic theory of gases: Here, the diffusivity is given by the mean free path  $l_{\text{mfp}}$  and the velocity  $v$  through the relation  $D_s \sim v l_{\text{mfp}}$ . In the strongly interacting regime, the mean free path  $l_{\text{mfp}}$  is on the order of the interparticle distance  $n^{-1/2}$  while the velocity is on the order of the Fermi velocity  $v \sim v_f \sim \hbar n^{1/2}/m$ . Thus, these measurements show that quantum-limited transport occurs in the strongly correlated regime of the 2D BEC-BCS crossover.

## 5.2 Critical velocity of a 2D Fermi gas

In the following experiment, we show that low-temperature 2D Fermi gases are superfluid in the BEC-BCS crossover. According to the two-fluid model, superfluids have a superfluid fraction that has zero viscosity and can flow along a surface without experiencing any friction. One manifestation is that when a superfluid contained in a ring potential is set into rotation, it can flow forever without being damped by friction [126]. This is analogous to an electric current in a superconducting ring which persists indefinitely. These metastable currents have been observed in neutral superfluids of bosons [127–129] and, very recently, fermions [130, 131]. The metastable flow does not experience any drag as long as its velocity with respect to the container wall is less than a critical velocity<sup>50</sup>.

This critical velocity is given by the Landau criterion  $v_c = \min_p \epsilon(p)/p$  where  $\epsilon(p)$  is the dispersion relation of the gas [3]. Below this critical

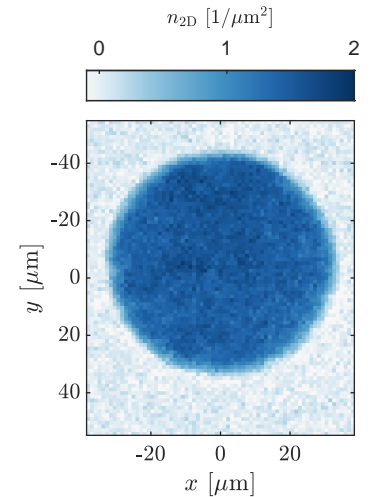
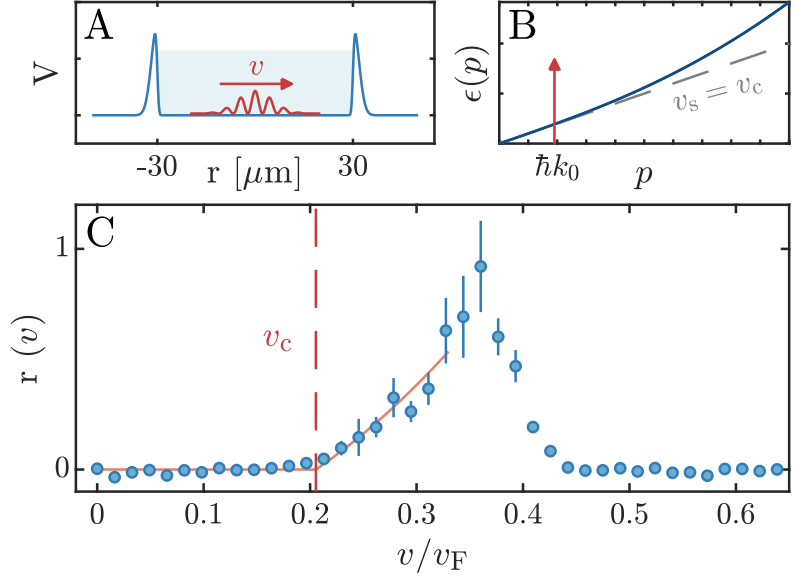


**Figure 5.5:** Density distribution of the 2D Fermi gas used to study the critical velocity.

<sup>50</sup> To be more detailed, in the two-fluid model, only the superfluid fraction does not experience any drag below a critical velocity. However, the normal component does experience drag at any velocity. But if the system is rotated, the flow of the normal component will quickly decay, leaving only the superfluid fraction to persist.

**Figure 5.6:** (A) The periodic Bragg potential (red) is moved through the gas at variable velocities  $v$  trapped in repulsive optical ring potential (blue). (B) This sketch of the excitation spectrum in the BEC regime shows that we probe the excitation spectrum at one specific momentum  $p_0 = \hbar k_0$  (red vertical line) whereas in Landau's gedankenexperiment a stirrer moving with velocity  $v$  probes the excitation spectrum at all momenta  $p$  and corresponding energies  $\epsilon(p) = vp$ . (C) The response  $r(v)$  of a 2D Fermi gas at an interaction strength of  $\ln(k_{\text{Fa}2\text{D}}) = -0.8$  to the Bragg lattice with wavevector  $k_0 \approx 0.15 k_{\text{F}}$ . We observe that no dissipation occurs at low lattice velocities, but there is a sharp increase in the response above a critical velocity  $v_c$ . The fact that Bragg lattice probes the system at a constant wavevector results in a decrease of the response at high lattice velocities. The critical velocity is extracted by a fit (red solid line) to the expression  $r(v) = A \cdot \max(0, v^2 - v_c^2)$  [137].



<sup>51</sup> The normal fraction of the superfluid could give rise to a background of excitations at velocities  $v < v_c$ . We do not observe such a background.

velocity, any perturbations within the fluid or from the container wall cannot create excitations in the superfluid. This holds if we change the frame of reference: A stationary superfluid cannot be excited by an impurity moving through it with a velocity  $v < v_c$ . Instead, the superfluid flows around the impurity without friction<sup>51</sup>. This phenomenon can be used to measure the critical velocity in BECs and Fermi gases with a moving optical stirrer [132–136].

However, a measurement of the critical velocity and the evidence of superfluidity of a 2D Fermi gas in the BEC-BCS crossover are still missing. To address this, we create an impurity using our Bragg lattice setup, as described in Sect. 3.2. The frequency detuning  $\Delta\omega$  between the two laser beams causes the optical lattice to move at a constant speed  $v = \Delta\omega/k_0$ , where  $k_0 = 2\pi/L$  with the spacing  $L$  between two maxima of the periodic potential.

To measure the critical velocity in our system, we move the optical lattice through the gas at different velocities and observe the response of the system by ramping it to the BEC side. As in the 3D measurements, we measure the energy deposited by the potential using the relative reduction in the condensate peak height. A typical measurement of the response (Eq. 3.3) of the system as a function of the lattice velocity is shown in Fig 5.6 C. We observe that the gas remains unaffected until a critical velocity is reached, at which point a sharp onset of dissipation occurs.

Unlike previous experiments [132–135], we observe that the response decreases again at higher velocities. This is caused by the fact that the optical lattice is not a point-like stirrer, but probes the system at a specific momentum  $\hbar k_0$ , whereas the impurity in Landau's gedankenexperiment can excite the system at all momenta. Therefore, a moving optical lattice with varying velocity probes the dispersion re-

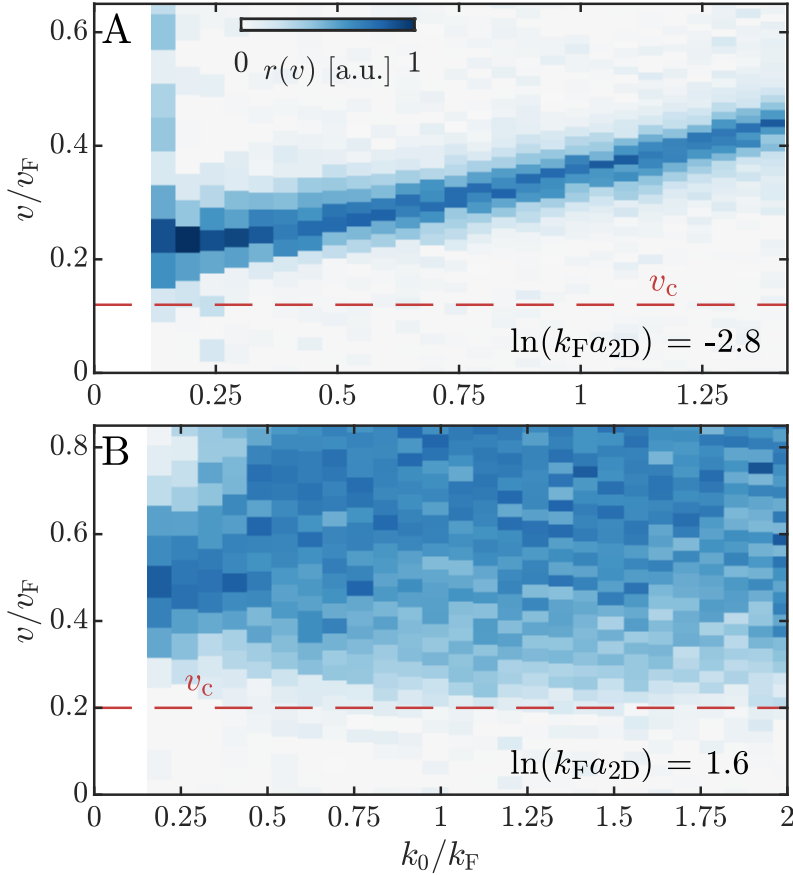


**Figure 5.7:** (A) In the BEC regime, the response  $r(v)$  of a gas to excitations with varying lattice wavevector  $k_0$  and velocity  $v$  shows a well-defined mode. For small wavevectors, phonons are excited peaked around a constant velocity which corresponds to the sound velocity  $v_s$ . This corresponds to the linear part of the Bogoliubov dispersion. For larger wavevectors, the peak in the response moves to linearly higher velocities because we enter the quadratic part of the Bogoliubov excitation spectrum where single-particle excitations are created. (B) In the BCS regime, we observe a continuum of excitations with a minimum of the onset velocity at  $k_0 = 2 k_F$ . Here, pair-breaking excitations gapped in frequency by  $2\Delta/\hbar$  are created resulting in a critical velocity  $v_c = \frac{2\Delta/\hbar}{2k_F}$ . In both regimes, the heating rate is negligible for excitations that move slower than the critical velocity (red dashed lines, taken from Fig. 5.8C). To enhance the visibility of weaker excitations, each column in both panels has been linearly rescaled to range from 0 to 1.

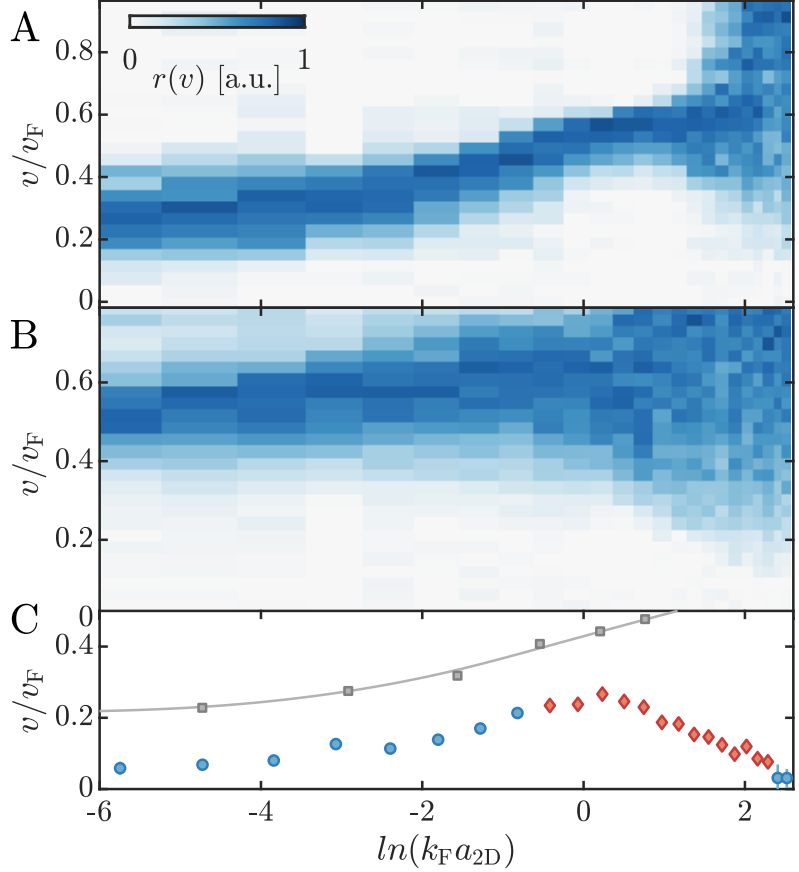
lation of the gas on a vertical line of constant momentum  $p = \hbar k_0$  as visualized in Fig. 5.6 B.

Our Bragg setup, however, allows us to change the momentum  $\hbar k_0$  in a large range. We use it to measure the response  $r(v, k_0)$  of the system as a function of the lattice velocity  $v$  and the lattice wavevector  $k_0$ . Our measurements in the BEC and BCS regime are depicted in Fig. 5.7. Compared to the measurements of the dynamic structure factor in Chap. 3 and in Chap. 6, we chose to plot here the response  $r(v, k_0)$  instead of the dynamic structure factor because we are interested in the lowest possible velocity below which no excitations are present. Both are related by  $r(v, k_0) = \omega S(k_0, \omega)|_{\omega=k_0 v}$ .

The resulting responses in the BEC and BCS regime show the difference in the excitation spectra of bosonic and fermionic superfluids. In bosonic superfluids, the lowest velocity at which excitations can be created is at small wavevectors. Here, the obstacle moving close to the speed of sound creates phononic excitations. In BCS superfluids, phononic excitations at low  $k_0$  can still be created, but the lowest onset velocity is found at  $k_0 \approx 2 k_F$  because here pair-breaking excitations gapped in frequency by  $\omega = 2\Delta/\hbar$  can be excited at corresponding lower velocity  $v_c = \frac{2\Delta/\hbar}{2k_F}$ . In both regimes, we clearly observe a critical velocity below which no excitations are created, which gives evidence of superfluidity.

All measurements presented here probe superfluids at the lowest possible temperatures we can reach. If we heat up the system it is expected that the critical temperature becomes zero as the temperature approaches the critical temperature. This allows for the measurement of the critical entropy over the 2D BEC-BCS crossover which is discussed in [16, 138].

**Figure 5.8:** (A,B) Measurement of the response of a 2D Fermi gas by a moving lattice with wavevectors  $k_0 \approx 0.3 k_F$  (A) and  $k_0 \approx 2 k_F$  (B) at different interaction strengths. In the BEC regime ( $\ln(k_F a_{2D}) < -1$ ), we observe a well defined excitation that corresponds to a sound mode for  $k_0 \approx 0.3 k_F$  and single particle excitations for  $k_0 \approx 2 k_F$ . When going to the BCS side of the crossover, the peak broadens into a continuum of pair breaking excitations. To enhance the visibility of weaker excitations, each column has been linearly rescaled to range from 0 to 1. (C) We determine the critical velocity as a function of interaction strength as the lower of the two onset velocities obtained from the data shown in (A,B). In the BEC regime, the critical velocity is limited by excitations at small wavevectors (blue dots), whereas in the crossover the lowest onset velocities occur at  $2 k_F$  (red diamonds). We find that the 2D Fermi gas is superfluid throughout the 2D BEC-BCS crossover with the highest critical velocities found in the crossover regime at  $\ln(k_F a_{2D}) \approx 0$ . For comparison, we show the speed of sound  $v_s$  (grey squares) discussed in the previous chapter, the grey line is a guide to the eye. The error bars denote the  $1\sigma$  confidence intervals of the fit and are smaller than the symbol size for most data points.



After establishing that our system is superfluid in the BEC and BCS limits, we study the evolution of the critical velocity in the crossover between these regimes. To take into account both the phononic and pair-breaking excitations shown in Fig. 5.7 A and B, we measure the interaction dependence of the response  $r(v)$  at two different lattice wavevectors of  $k_0 \approx 0.3 k_F$  and  $k_0 \approx 2 k_F$ . The results are shown in Fig. 5.8 A and B. For a lattice wavevector of  $k_0 \approx 0.3 k_F$ , we clearly observe the presence of a well-defined sound mode with an onset velocity that increases as a function of interaction strength. In the crossover region ( $\ln(k_F a_{2D}) \approx 0.5$ ), the peak smoothly broadens into a continuum as pair breaking becomes the dominant excitation in the system. For  $k_0 \approx 2 k_F$ , the excitations are free particle excitations of dimers on the BEC side and transform into pair-breaking excitations on the BCS side of the resonance. We fit the onset velocities for both data sets and use the smaller of the two values as the critical velocity of the system (Fig. 5.8 C).

The measured critical velocities scale with the speed of sound on the BEC side of the resonance, measured in the previous section. They show a maximum in the crossover and decrease again as pair breaking becomes dominant in the BCS regime. We observe that the measured critical velocities become compatible with  $v_c = 0$  at  $\ln(k_F a_{2D}) \approx 2.3$ , indicating that the phase transition to the normal state

has been crossed. Remarkably, the maximum of  $v_c$  at an interaction strength of  $\ln(k_F a_{2D}) \approx 0$  indicates that fermionic 2D superfluids are most stable in the strongly correlated crossover regime. This is in agreement with measurements of the critical temperature in the 2D BEC-BCS crossover [139] and similar to the behavior of three-dimensional Fermi gases [134, 135].



# 6

## COMPARING 2D AND 3D SUPERFLUIDS

*After establishing superfluidity of 2D Fermi gases in the last chapter, this chapter is dedicated to a long-lasting question: What is the influence of reduced dimensionality on superfluidity? To answer this question, I will use the results of the pairing gap obtained in Chap. 3 and compare them with similar measurements in 2D Fermi gases. The following chapter is based on the publication [138]*

*L. Sobirey, H. Biss, N. Luick, M. Bohlen, H. Moritz, and T. Lompe,  
Physical Review Letters, 129(8), 083601 (2022).*

*A detailed analysis including a comparison with the pairing gaps in solid-state materials can be found in the PhD thesis of the lead author on this project, Lennart Sobirey [16]. I contributed to the execution of the experiments presented in the following and the interpretation of our results.*

Since 1987, many materials belonging to the class of high- $T_C$  superconductors have been discovered, which have higher critical temperatures and stronger interactions than conventional BCS superconductors [140, 141]. This is intriguing because in two dimensions, where thermal and quantum fluctuations play a more important role, less robust long-range order is expected [106]. In superconductors, the dimensionality of these systems cannot be changed without altering other properties as well, so it is difficult to extract what role the reduced dimensionality has on their stability [142].

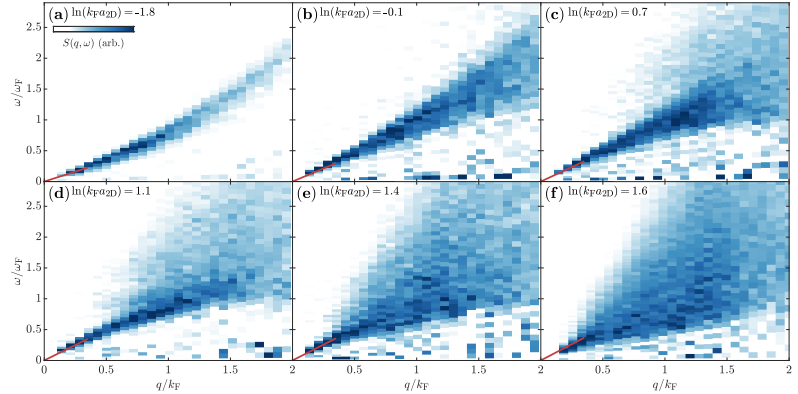
Therefore, we use our ultracold Fermi gases as a model system to perform a quantitative comparison between 2D and 3D superfluids by comparing their pairing gaps. The gap is well suited for this purpose since it directly determines both the critical velocity and the critical temperature of a fermionic superfluid, and thus constitutes an excellent measure of its stability. For that, we will first discuss the measurement of the dynamic structure factor of 2D Fermi gases and the extraction of the pairing gap.

### 6.1 Dynamic structure factor in 2D Fermi gases

In order to determine the pairing gap, we use momentum resolved Bragg spectroscopy to measure the dynamic structure factor  $S(\mathbf{q}, \omega)$  of the superfluid in the two-dimensional BEC-BCS crossover.

The results of these measurements are shown in Fig. 6.1. Similar to the 3D measurements, we observe two different types of excitations: The first are collective excitations of the superfluid, which are visible as a linear sound mode at low momentum transfers ( $q \ll k_F$ ). Its slope is in excellent agreement with measurements of the speed of sound discussed in Chap. 5.1 (red lines in Fig. 6.1). The second type

**Figure 6.1:** Measurements of the dynamic structure factor  $S(q, \omega)$  taken at different values of the 2D interaction parameter  $\ln(k_F a_{2D})$  in the BEC-BCS crossover. For strong attractive interactions ((a), the system consists of tightly bound molecules which are excited as unbroken pairs, and consequently  $S(q, \omega)$  shows the Bogoliubov dispersion of an interacting Bose gas. Moving into the crossover regime ((b),(c),(d)), the pairs become more weakly bound and pair-breaking excitations begin to appear at higher momenta. These excitations become more pronounced as we approach the BCS limit where the system shows the expected broad pair-breaking continuum ((e),(f)). In addition to these pair-breaking excitations, it is also possible to excite sound waves in the superfluid. These appear in our spectra as a linear mode at low momenta, with a slope that corresponds to the speed of sound in the system and is in excellent agreement with the measurement discussed in Chap. 5.1 (red lines). The behavior observed in ((c)-(h)) closely resembles our results obtained in 3D Fermi gases.



of excitations are single-particle excitations. These are clearly visible for BCS superfluids with weak attractive interactions (Fig. 6.1 (e),(f)), where a pronounced continuum of pair-breaking excitations is visible.

As the interparticle attraction increases towards the BEC regime, the size of the pairing gap grows, causing the onset of the pair-breaking continuum to move to higher energies. Similar to the 3D results, the onset of the pair-breaking continuum moves towards higher momenta as the pairs are transformed from weakly bound Cooper pairs to tightly bound molecules. This trend continues into the BEC regime, where the molecules are so tightly bound that pair-breaking excitations become completely suppressed. The excitation spectrum follows here the Bogoliubov dispersion relation of a superfluid Bose gas (see Fig. 6.1 (a)).

Overall, compared to our measurements of 3D Fermi gases, the measured excitation spectra are qualitatively very similar. However, smaller qualitative differences can be observed: Compared to the 3D measurements, the Bogoliubov mode shows a stronger broadening in the BEC regime, where the reason is unknown to us. In addition, the suppression of the pair-breaking continuum at low momentum due to the presence of the collective mode is weaker in 2D.

## 6.2 The pairing gap in 2D Fermi gases

To determine the pairing gap  $\Delta$  from our measurements, we determine the onset energy of the pair-breaking continuum. Although the onset is partially masked by the presence of the Goldstone mode, it is nevertheless possible to extract the gap by using two different methods.

The first method, already used for the 3D system, measures the onset of the pair-breaking continuum at low momentum where collective excitations are well separated from the continuum (Fig. 6.2). We identify the onset frequency  $\omega_{\text{onset}}$  with  $2\Delta_{\text{gap}}$ , where we introduce the excitation gap  $\Delta_{\text{gap}}$  whose relation with the pairing gap  $\Delta$  we explain below.

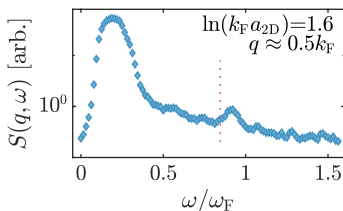


**Figure 6.2:** Measuring both the collective mode and pair breaking excitations at fixed momentum transfer. Here, we use strong driving to reveal the onset of the suppressed pair-breaking excitations at  $2\Delta_{\text{gap}}$  (dotted red line).

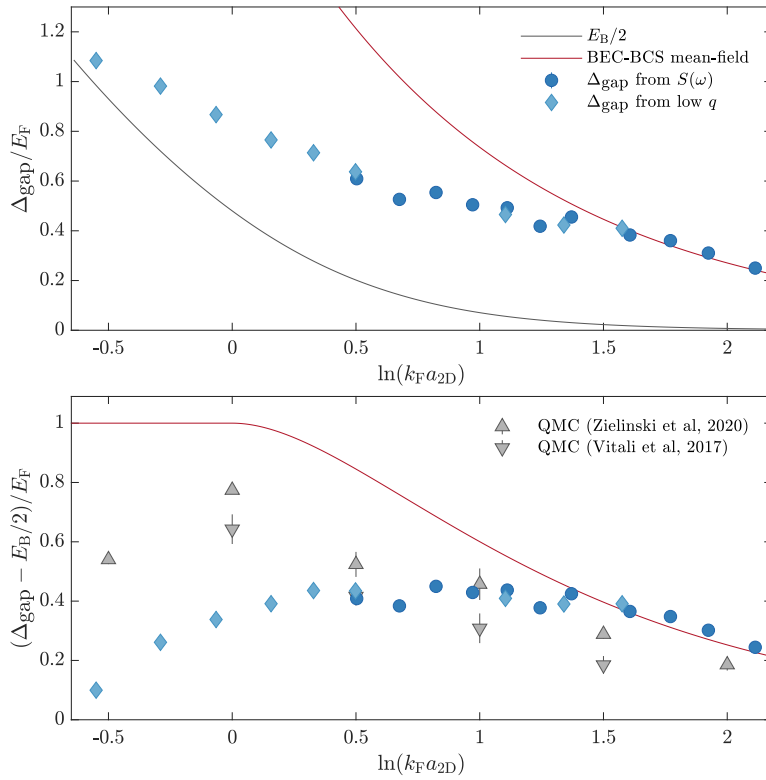


**Figure 6.4:** Upper panel: Measured excitation gap  $\Delta_{\text{gap}}$  as a function of the interaction strength. For systems with a positive chemical potential ( $\ln(k_{\text{F}}a_{2\text{D}}) > 0.3$ ), we can directly identify the excitation gap with the pairing gap  $\Delta$ . For the four leftmost points the excitation gap corresponds to  $\sqrt{\mu^2 + \Delta^2}$ . The different symbols distinguish results obtained using either the peak of  $S(\omega)$  (blue dots) or the strong driving at low  $q$  (light blue diamonds). The contribution  $E_{\text{B}}$  of the two-body bound state to the gap is shown as a solid line. In the BCS regime the data is in agreement with the mean-field BEC-BCS prediction (red line), but deviates in the strongly correlated crossover regime. Lower panel: In order to isolate the many-body contribution, we subtract the binding energy and plot  $\Delta_{\text{gap}} - E_{\text{B}}/2$ . This allows us to compare our measurements with quantum Monte-Carlo calculations (gray triangles, [144, 145]) which show compared to the mean-field prediction better agreement in the crossover, but still deviate from the measurements in the BEC regime.

In regions where both modes are not well separated, we use a second method, in which we first integrate the full dynamic structure factor  $S(q, \omega)$  over the momentum axis to obtain  $S(\omega)$ , which describes the probability of creating an excitation of energy  $\hbar\omega$  for any momentum  $\hbar q$ . The resulting line shape of  $S(\omega)$  is expected to be qualitatively similar to the observed Raman response of s-wave BCS superconductors [143] which shows a sharp peak at  $2\Delta_{\text{gap}}$  followed by a slower decay. This peak is expected to be broadened due to density inhomogeneities. In addition, due to the presence of the collective mode in our neutral superfluid at low energy, an additional background appears at all frequencies. Therefore, we fit a phenomenological line shape of a linear increase followed by a Gaussian decay and identify the intersection point as  $2\Delta_{\text{gap}}$  (Fig. 6.3).

The resulting values of the excitation gap  $\Delta_{\text{gap}}$  are plotted in Fig. 6.4. For positive chemical potentials<sup>52</sup> ( $\ln(k_{\text{F}}a_{2\text{D}}) \geq 0.3$ ) we can directly identify the excitation gap  $\Delta_{\text{gap}}$  with the pairing gap  $\Delta$ . For negative chemical potentials, which affect the four leftmost measurements presented in Fig. 6.4, excitation gap is not given by  $\Delta_{\text{gap}} = \Delta$  but  $\Delta_{\text{gap}} = \sqrt{\mu^2 + \Delta^2}$ . We have chosen here to plot the raw measured excitation gap  $\Delta_{\text{gap}}$  rather than extracting the order parameter  $\Delta$  using a chemical potential from an external theory.

In addition, we plot the confinement-induced binding energy  $E_{\text{B}}$  of the bare two-body bound state (black line) in Fig. 6.4. For smaller attractive interactions in the BCS regime, the two-body binding energy

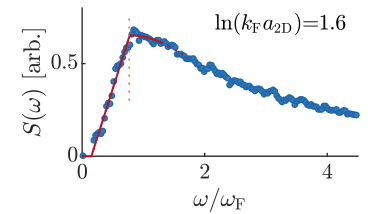
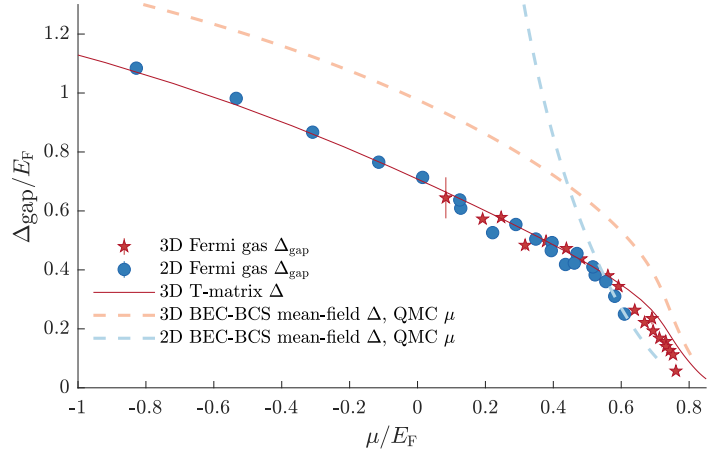


**Figure 6.3:** Dynamic structure factor  $S(\omega)$  obtained by integrating  $S(q, \omega)$  over the momentum axis. A phenomenological lineshape (solid red line) is fitted to extract the peak position which is located at  $2\Delta_{\text{gap}}$  (dotted red line).

<sup>52</sup> We obtain the threshold by taking the reduced chemical potential  $\mu + E_{\text{B}}/2$  from QMC calculations [119] and subtracting the confinement induced binding energy from Eq. 4.8.

**Figure 6.5:** We compare the gaps of fermionic superfluids with different dimensionality by plotting both measured pairing gaps  $\Delta/E_F$  of quasi-2D (blue circles) and 3D (red stars) Fermi gases as a function of the chemical potential  $\mu/E_F$  taken from QMC calculations [44, 119]. The measurements of the gap collapse onto a single curve. This is unexpected because the mean-field predictions have a qualitatively different behavior in 3D (orange dashed line) and 2D (blue dashed line). The second unexpected observation is that the 2D data is also well-described by the T-matrix calculations performed for a 3D Fermi gas (red line [88]).



is negligible, and the gap is entirely due to many-body effects. When the crossover regime is entered, the bare two-body binding energy starts to contribute significantly to the observed excitation gap. To separate these two contributions to the gap, we subtract the known value of the two-body binding energy from our measurements. As can be seen in Fig. 6.4, the remaining many-body contribution  $\Delta - E_B/2$  grows with increasing interactions in the BCS regime, reaches a maximum in the crossover regime, and then decreases again towards the BEC side of the resonance. Here, the contribution of the two-body bound state begins to dominate as the gas becomes a BEC of deeply bound molecules.

When comparing these results with theory, we find that they agree excellently with mean-field theory (Eq. 4.10) in the BCS regime, which is remarkable because the observed gap  $\Delta \approx 0.3E_F$  has considerable size. However, in the strongly correlated crossover region ( $\ln(k_F a_{2D}) \approx 1$ ) the gap starts to deviate from the mean-field result. This is not surprising because for negative chemical potentials (in mean-field for  $\ln(k_F a_{2D}) < 0$ ), the mean-field excitation gap is

$$\Delta_{\text{gap}} = \sqrt{\mu^2 + \Delta^2} = E_F + \frac{E_B}{2}.$$

resulting in a constant many body contribution of  $\Delta_{\text{gap}} - \frac{E_B}{2} = E_F$ . Here, Quantum Monte Carlo (QMC) simulations [144–146] agree better with our data in the crossover, but still predict higher values of  $\Delta_{\text{gap}} - E_B/2$  in the BEC regime.

### 6.3 Comparing pairing gaps in 2D and 3D Fermi gases

Next, we will compare the pairing gaps between 2D and 3D fermionic superfluids. To perform such a comparison, we need to find a suitable parametrization of the interaction strength, since the dimensionless interaction parameters  $\ln(k_F a_{2D})$  and  $1/k_F a_{3D}$  that we used up to now cannot be directly compared.

We parametrize the interaction strength with the normalized chemical potential  $\mu/E_F$  of the fermions. This choice is motivated by the fact that the chemical potential is a basic thermodynamic quantity that is defined independently of dimensionality and has well-known and monotonous relations to the 2D and 3D interaction parameters  $\ln(k_F a_{2D})$  and  $1/k_F a_{3D}$  [28, 44, 118, 119]. Therefore, we can make our comparison by plotting the pairing gap  $\Delta/E_F$  as a function of the chemical potential  $\mu/E_F$  for two- and three-dimensional systems. The results are shown in Fig. 6.5.

Remarkably, we find that within the accuracy of our measurements, the results for  $\Delta/E_F$  obtained for quasi-2D and 3D Fermi gases collapse onto a single curve. This suggests that for strongly interacting Fermi gases, the gap follows a single universal function  $f(\mu/E_F) = \Delta/E_F$  of the interaction strength that is independent of the dimensionality of the system. The function  $f(\mu/E_F)$  appears to be well described by T-matrix calculations for 3D Fermi gases [88], but qualitatively disagrees with theoretical predictions for 2D Fermi gases. This discrepancy between our measurements and theoretical predictions for two-dimensional systems is unlikely to result from finite-temperature effects or excitations along the tightly confined axis: Temperature effects are not expected to significantly affect the gap or the chemical potential, as our system is well below the critical temperature, and excitations in the third direction would be expected to affect only the data in the BCS regime where the chemical potential is still smaller than but becomes comparable to  $\hbar\omega_z$ . Consequently, our measurements imply that, for a given coupling strength, there is no inherent difference in the stability of fermionic superfluidity between two- and three-dimensional quantum gases.

As we perform our experiments in an ideal model system, it is natural to ask how these apply to more complex materials with 2D and 3D geometries. For this, we would like to point the reader to the thesis of Lennart Sobirey [16], where a comparison to solid state materials is performed. These comparisons strongly suggest that, matching the conclusion drawn here, it is not the dimensionality but rather strong interactions resulting in small pair sizes that are key to achieving large excitation gaps.



## Part II

### IMBALANCED FERMI GASES



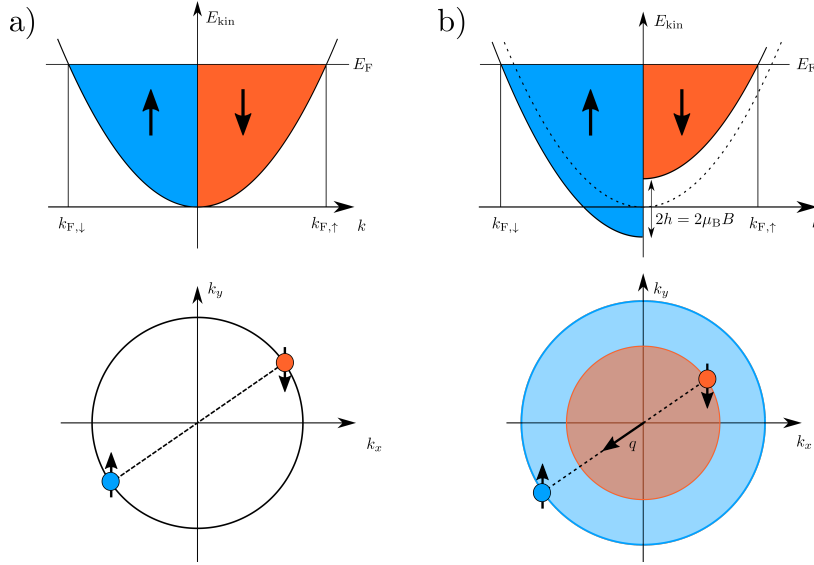


**Figure 7.1:** (a) In a superconductor without an external magnetic field the dispersion curves of both spin states are equal. This results in a balanced mixture of both spin states for a given chemical potential, which makes Cooper pairing at the same momentum possible. (b) In an external magnetic field, both dispersion curves are shifted with respect to each other. This can result in an imbalanced spin mixture where both spin up and down fermions have different Fermi wavevectors. Here, Cooper pairing may occur by allowing Cooper pairs with non-zero momentum  $\hbar\mathbf{q}$  [147, 148]. Adapted from [149].

### 7.1 Superfluidity with spin-imbalance

The Cooper pairing mechanism, which forms the basis for fermionic s-wave superfluidity and superconductivity, critically relies on the availability of another fermion of opposite spin to pair with for each fermion. This raises the question of what happens when the number of fermions in both spin states is imbalanced so that the Fermi surfaces of both spin states do not overlap anymore in momentum space. In a superconductor, the spin composition of electrons can be influenced by applying an external magnetic field which energetically favors one spin state. Chandrasekhar and Clogston (CC) predicted that the BCS state at zero temperature remains unpolarized until a critical magnetic field, called the CC or Pauli limit, is reached [150, 151]. Here, the energy gain of electrons flipping their spin exceeds the gain due to Cooper pairing, and the system performs a first-order transition into a spin-imbanced normal phase.

However, as pointed out by Fulde and Ferrell (FF) [147] as well as by Larkin and Ovchinnikov (LO) [148], superfluidity can even exist above this limit when allowing for Cooper pairs which have a finite center-of-mass momentum  $\hbar\mathbf{q}$  (Fig. 7.1). The resulting FFLO states are striking because they have an order parameter that varies spatially with periodicity  $\delta x = 2\pi/q$ .

In general, phases beyond the CC limit are not easy to explore in superconductors because the magnetic field necessary to induce

<sup>53</sup> For a full review of FFLO signatures in layered superconductors we recommend Ref. [153].

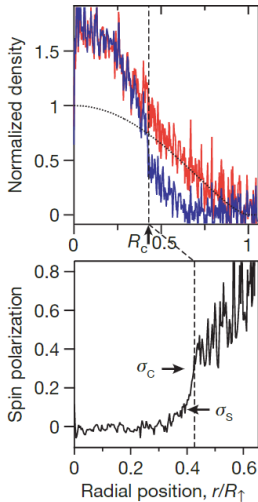


**Figure 7.2:** Phase separation of a spin-imbalanced Fermi gas in a harmonic trap. The local density of majority (red) and minority (blue) atoms shows that the system is balanced in the center, and the excess majority atoms are pushed to the outer part of the trap. Here, a measurement below the tricritical temperature is shown, where the local polarization shown in the lowest panel jumps at the vertical dashed line. This proves that a certain range of local polarizations is not allowed and a first-order transition occurs. Adapted from [158].

**Figure 7.3:** (a) Finite-temperature phase diagram of a unitary Fermi gas. At finite temperature, excess fermions can mix with the superfluid paired phase (blue area). Above a certain polarization, superfluidity breaks down and the system becomes normal (green). Interestingly, below a tricritical point a forbidden region (yellow) opens up where excess fermions are not miscible and phase separation has to occur, characteristic for a first-order transition. (b) The qualitative similar behavior is also found in bosonic superfluid  $^4\text{He}$ . Here, for a low fraction  $x$  of fermionic  $^3\text{He}$  the system stays superfluid while it breaks down above a certain temperature dependent  $^3\text{He}$  concentration. Similarly to the unitary Fermi gas, below a tricritical line, the superfluid to normal transition becomes first order and region where phase separation occurs opens up.

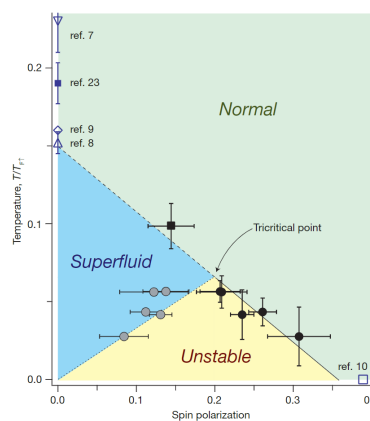
a spin-imbalance also couples to the orbital motion of the charged electron, giving rise to a more stringent limit than the CC limit, the so-called orbital limit [152]. This effect is absent in two-dimensional layered superconductors, where the orbital effect is suppressed if the magnetic field is parallel to the two-dimensional superconducting planes. In these systems, several signatures for FFLO states have been observed<sup>53</sup>, e.g. the upturn of the critical field beyond the Pauli limit [154, 155], the detection of spin-polarized quasiparticles [156], and a spatial sinusoidal modulation of the spin density in nuclear magnetic resonance measurements [157], but a direct evidence is still missing [153].

Another way to avoid orbital effects is to utilize ultracold neutral Fermi gases where the preparation process can be tailored to yield a precisely controlled spin imbalance which is maintained due to small relaxation rates between spin states. An overview over the existing experimental studies of spin of spin-imbalanced Fermi gases in three and two dimensions is given in the following sections.

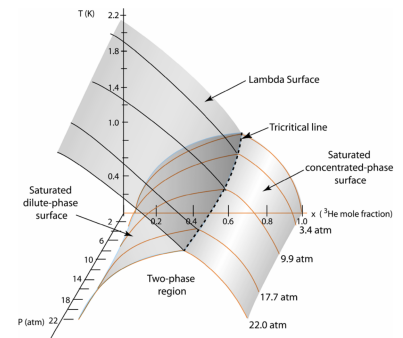
## 7.2 Studies of 3D spin-imbalanced Fermi gases

In the year 2006, the first imbalanced Fermi gases were realized in the groups of Wolfgang Ketterle (MIT) [52, 54, 158–165] and Randy Hulet (Rice) [166, 167]. Their findings were that an imbalanced Fermi gas trapped in a three-dimensional harmonic potential undergoes phase separation into an almost balanced superfluid central phase and a normal imbalanced outer shell (Fig. 7.2, [158, 162, 166, 167]). For temperatures below a tricritical point, the local polarization jumps at the transition from the central superfluid phase to the outer normal phase. Thus, there exists a region of forbidden polarizations which is characteristic for a first-order transition, analogous to the first-order transition in  $^3\text{He}$ - $^4\text{He}$  mixtures (see Fig. 7.3b).

In addition, they could demonstrate that the central phase is superfluid by inducing vortices and that superfluidity vanishes in accordance with the CC limit (Fig. 7.4, [159]).



(a) Phase-diagram of the spin-imbalanced unitary Fermi gas. Adapted from [158].



(b) Phase-diagram of a  $^3\text{He}$ - $^4\text{He}$  mixture. The pressure axis does not exist in a). Adapted from [168, 169].

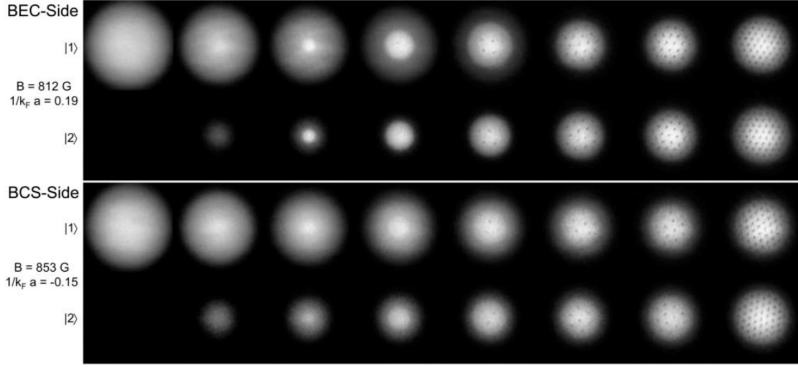


**Figure 7.4:** Observation of superfluidity in a 3D Fermi gas with a spin-imbalance. In both the BEC and the BCS regime, systems with decreasing imbalances are prepared from the left to the right. Below a certain imbalance, a regular vortex lattice becomes visible in the central part of the cloud proofing superfluidity. Adapted from [159].

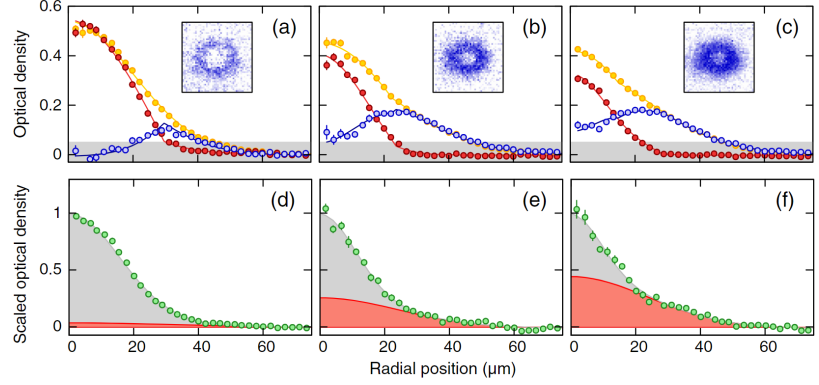
The exciting realization of imbalanced Fermi gases spurred a multitude of further experiments. Some of them focused on the normal polarized state, for instance studies of the normal ground state [52] as well as the Fermi polaron and its transition to a molecule in the BEC regime [165]. In addition, the normal to superfluid transition driven by imbalance rather than temperature was studied [160]. As discussed in Sect. 2.4.1, a small imbalance can also be used to create quasiparticle excitations on top of a balanced gas to study the pairing gap using RF spectroscopy [54]. Another important study done in the group of C. Salomon measured the equation of state of an imbalanced Fermi gas [170]. In this work, the pressure as a function of the interaction strength and the chemical potential of both spin components was extracted. In particular, they could benchmark quantitative results from the balanced core against many-body theories for a balanced gas in the BEC-BCS crossover, including the 3D QMC calculations [44] used in the previous chapter.

The FFLO state could not be observed in these experiments with ultracold 3D gases. This is not surprising as in three dimensions the FFLO phase is only predicted to exist in a small area of the phase diagram and at very low temperatures  $T/T_F < 0.05$  [171]. These issues may be of less importance in lower dimensions, where the FFLO phase is expected to be more stable due to a larger overlap of both Fermi surfaces. According to [172], 2D systems are particularly promising candidates for the observation of FFLO phases whereas in 1D the competition by other phases, namely, charge density waves and spin density waves, is stronger. This is, however, debated as it has for instance been shown that the role of dimensionality becomes less important for strong interactions [173].

### 7.3 Studies of 2D spin-imbalanced Fermi gases

So far, two studies of two-dimensional imbalanced Fermi gases have been reported [174, 175]. In the first experiment [174] from the group of J.E. Thomas (North Carolina), quasi-2D Fermi gases were realized by loading multiple layers of a 1D optical lattice and confining the gas in the radial direction with a harmonic potential. Interestingly,

**Figure 7.5:** Phase separation of an 2D spin-imbalanced Fermi gas at 780 G in a harmonic trap for global polarizations  $P = 0.25, 0.55, 0.75$  (a-c). The yellow, red and blue lines show the radial density of the majority, minority and their difference, respectively. The lower row shows the corresponding radial density after 3 ms ToF and a double Gaussian fit to the data. Adapted from [175].



the experimental results show a qualitatively similar behavior to that of 3D imbalanced Fermi gases. In the BEC regime, they found that the excess atoms are pushed out of the central region resulting in a balanced center. In the BCS regime, the balanced region shrinks to a central point such that the imbalance increases continuously for increasing radii. In this regime, they found reasonable agreement with a 2D polaron model.

The second experiment [175] from the group of Waseem Bakr (Princeton) realized an imbalanced Fermi gas in a single layer of a 1D optical lattice. Consistent with the results in the Thomas group, they observed that in the case of low global imbalances, the central region has an imbalance of zero. Towards larger radii, the imbalance increases continuously (Fig. 7.5). In addition, they observed a bimodal structure after a short time of flight for systems in the BEC regime and interpreted this as first evidence for pair condensation in the central region. Interestingly, this indication for pair condensation also appeared when the central region was slightly imbalanced. However, as mentioned in Ref. [11], it should be noted that although pair condensation is expected, a bimodal structure has also been observed in weakly repulsive 2D Bose gases that were not condensed [176] and 2D Fermi gases that were above the critical temperature [139].

Currently, several open questions remain. The first question concerns the order of the transition from the balanced central to the outer imbalanced region. If the central balanced region is superfluid, this phase should transition at a specific radius into a normal phase as the superfluid phase cannot support a particular imbalance anymore. If this phase transition is of first order, a jump in the local imbalance should occur at this radius. Although it is predicted in two-dimensional mean-field theory at zero temperature, there are no indications of such a jump and, thus, experimental evidences of a first-order transition are missing so far. It is unclear whether the first-order transition is absent due to increased quantum fluctuations in 2D or whether the temperatures  $T/T_F = 0.1$  [175] reached so far were too high, as these are close to the critical temperatures of a balanced two-dimensional Fermi gas in the crossover regime measured in [139].

One difficulty in these measurements is to reliably detect the jump of polarization after radial averaging at a specific radius. We can revisit this question in a different potential, a box potential. Here, the absence of a harmonic confinement does not favor the formation of a central balanced core. Instead, if a first-order transition is present, one expects at a spontaneous formation of superfluid domains with a small imbalance and normal domains, which contain all remaining excess fermions. This separation into domains could be observed directly with in situ imaging. If the phase transition is of second order, no formation of domains occurs. Instead, we would observe for all imbalances a homogeneous density distribution. This homogeneous gas would be depending on the imbalance either superfluid or normal.

The nature of the phase brings us to the second remaining question. Up to now it has been unclear whether the central region observed in imbalanced 2D Fermi gases is superfluid. Bragg spectroscopy introduced in the first part of my thesis should give us a direct way to measure the critical velocity in different imbalanced phases. If we find a first-order transition, a nucleation point, which we can add with a weak harmonic confinement in our trap, will nucleate the superfluid phase in the central part of the trap such that we can probe this region and not the normal phase with a Bragg lattice. If a first-order transition is missing, this is not needed, and we can probe the imbalanced gas, which has a constant density and imbalance throughout the box trap.

In the following chapters, we will show imbalanced quasi-2D Fermi gases which show no signs of a first-order transition but indications that they are superfluid.



## 8.1 Overview of the preparation

In this chapter, the preparation of an imbalanced two-dimensional Fermi gas is described. This preparation is challenging as we have to remove particles from one spin state. This produces holes deep in the Fermi sea, which requires substantial extra cooling afterwards. An additional challenge arises around the question of when and how to make the transition to a 2D system. Reaching an imbalanced Fermi gas in 2D hence requires considerable experimental finesse, yet the effort has allowed us to create imbalanced Fermi gases close to the 2D regime ( $k_B T \ll \hbar\omega_z$ ,  $\mu \approx \hbar\omega_z$ ) which are at least a factor of 2 colder than previously reported.

In short, the preparation scheme is sketched in Fig. 8.1. It consists of the following steps:

- We start in an attractive oblate dipole trap (the *squeeze trap*) with a balanced 2D gas with  $N_1 = N_2$ , where  $N_1$  and  $N_2$  denote the number of fermions in the lowest two spin states.
- Then, the balanced gas is transferred into a single minimum of a repulsive 1D lattice (the *accordion trap*) in order to enter the 2D regime. To create an imbalance, the gas is first adiabatically ramped into the deep BCS regime to reduce interactions.
- Here, a partial transfer of atoms from the 2nd to the 3rd lowest hyperfine state is performed,
- followed by a removal of atoms in the third state with resonant light. The removal heats up the remaining atoms considerably, since holes in the second lowest spin states are introduced at all energies. In addition, the ejection procedure itself imparts some momentum to the remaining atoms.
- Hence, an additional evaporation step is performed in the final box potential.

The removal of some atoms results in a lower number of minority atoms  $N_2$  than majority atoms  $N_1$ , which yields a finite global polarization defined by

$$P = \frac{N_1 - N_2}{N_1 + N_2}, \quad (8.1)$$

such that  $P = 1$  corresponds to a fully polarized gas and  $P = 0$  to a balanced gas. With the preparation scheme sketched above, we achieve temperatures of  $T/T_F = 0.05 \pm 0.01$  for global polarizations of  $P = 0.17 \pm 0.06$  in the BEC regime (Fig. 8.2). These temperatures are significantly lower than the  $T \sim 0.1T_F$  reported previously [175]

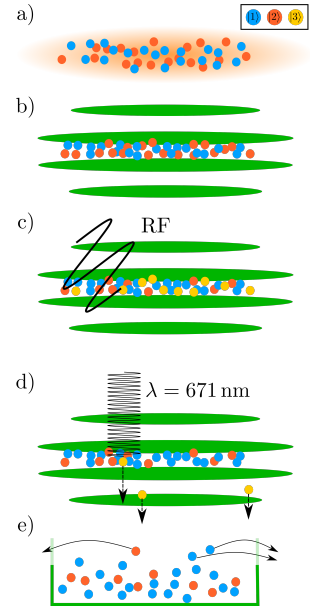


**Figure 8.1:** Preparation scheme for a spin-imbalanced Fermi gas. Three different spin states, the lowest three hyperfine states  $|1\rangle$  (blue),  $|2\rangle$  (red) and  $|3\rangle$  (yellow) are depicted as dots.

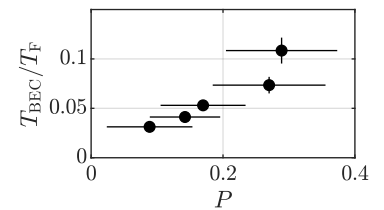


**Figure 8.2:** Temperatures obtained for different imbalances  $P$  after the last evaporation step.

and nearly as cold as the coldest balanced 2D systems reported with  $T \sim 0.03T_F$  [177]. For larger polarizations, the temperature starts to increase because more momentum is added to the remaining atoms during the ejection scheme and the evaporation becomes less efficient as fewer particles remain in the trap.

The following is a detailed discussion of the preparation scheme for the reader interested in the technical details. The important question of whether the imbalanced homogeneous systems we prepare are superfluid will be discussed in the next chapter 9.

## 8.2 Detailed discussion of the preparation

### 8.2.1 Step 0: Creating a balanced 2D Fermi gas

We will begin discussing the preparation scheme by starting with evaporative cooling in the squeeze trap, followed by the transfer into the 2D trap. During these steps, the number of atoms in both the lowest and second lowest hyperfine states remains equal, resulting in a balanced mixture.

After the MOT phase and first evaporative cooling in a resonator enhanced dipole trap, the atoms are transferred to the science cell using a transport trap. In the science cell, the magnetic field is ramped from 0 to 870 G and an evaporation from 5 W to 200 mW is performed within 1 s. Then, the atoms are loaded in 100 ms into the squeeze trap at 1 W. In the following, the magnetic field is ramped in 300 ms to the BEC regime at 750 G. Here, the squeeze trap is then evaporated in 1 s to a power of 25 mW still retaining a relatively high atom number for further evaporation. During the evaporation a well-defined spilling threshold is created by adding a vertical potential gradient via a magnetic field gradient. While this first evaporation to a rather low trap depth already resulting in quantum degenerate gas is in principle not strictly required, it is necessary to reduce the strong initial relative particle number fluctuations of well over 20 % to below 5 %.

Next, the balanced cloud of atoms is transferred to the 2D trap in several steps. In the first step, the gas is loaded into the radially confining repulsive ring trap. To decrease the cloud size such that the cloud fits into the ring, the squeeze trap is slightly compressed by increasing it from 25 mW to 50 mW in 200 ms before turning on the ring potential in 50 ms up to a value of 11 mW. Then, the field is ramped adiabatically to 832 G in 200 ms. Now, the adiabatic transfer into the final vertical confinement, the accordion lattice, happens in four steps:

1. First, the accordion lattice is set to a large lattice constant of 20  $\mu\text{m}$  and the power is increased from 0 to 250 mW in 300 ms. This power is a trade off between two requirements: First, the potential barrier between two lattice minima should be high enough to suppress tunneling to the adjacent layers. We found experimentally that this requires powers above 200 mW. The second requirement is that the

transfer is adiabatic. Here, a shallow lattice with lower potential gradients helps as it reduces the necessary timescales needed for an adiabatic transfer.

2. After the accordion lattice is turned on, the squeeze trap is turned off linearly in 300 ms, releasing the atoms into one layer of the large accordion lattice.
3. Then, by moving a galvo mirror, the accordion lattice constant is reduced continuously from  $20\ \mu\text{m}$  to  $3\ \mu\text{m}$  in 200 ms which compresses the gas adiabatically. We found that releasing the atoms from the squeeze trap before the final compression of the accordion lattice is crucial for an adiabatic transfer. A potential cause for this may be a slight vertical misalignment between the attractive squeeze trap maximum and the targeted minimum of the compressed accordion trap, resulting in a vertical oscillation of the gas, even when the transfer is relatively slow.
4. In a final step, the accordion power is ramped up from 250 mW to 500 mW in 50 ms to reach a vertical trapping frequency of 9 kHz.

Using an accordion lattice has the advantage that the initial loading can start at a large lattice constant of  $20\ \mu\text{m}$ . Therefore, it is always guaranteed that the atoms are loaded into a single layer, even if there is a slight vertical misalignment of the squeeze trap with respect to the vertical lattice minimum. The vertical lattice used in previous experiments had a static lattice constant of  $3\ \mu\text{m}$  and required regular alignment with respect to the squeeze trap to avoid occupation of adjacent layers. The accordion lattice setup is described in Appendix F.

### 8.2.2 Techniques to create an imbalance in a 2D Fermi gas

By loading the gas into a single vertical layer we prepared a quasi-2D Fermi gas with a balanced mixture of the lowest two hyperfine states  $|1\rangle$  and  $|2\rangle$ . To increase readability we will use the numbers 1, 2, and 3 in the following to refer to the states  $|1\rangle$ ,  $|2\rangle$ , and  $|3\rangle$ . In the next step, we will remove some atoms in one hyperfine state to create an imbalanced gas.

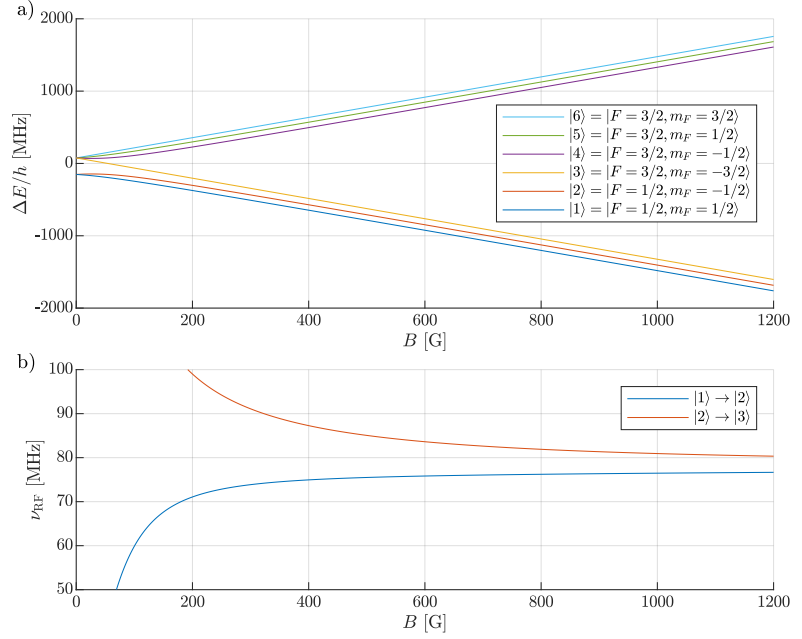
For that, we will discuss the following two techniques<sup>54</sup>:

1. Spin-selective magnetic trapping. Here, a static difference of the magnetic dipole moment of both spin states is combined with a magnetic gradient, which allows to spill only atoms having one spin from the trap. This method requires the two spin states to have substantially different magnetic moment, which is only the case for fields well below 100 G, i.e. well below the fields at which broad Feshbach resonances exist. Particularly at  $B \approx 27\ \text{G}$ , the magnetic moment of the state 2 becomes zero. Here, a magnetic field gradient allows one to just spill atoms in state 1. This method has been used in the Princeton group studying imbalanced 2D Fermi-Hubbard systems<sup>55</sup> [178].

<sup>54</sup> Another possible way to remove one spin state is a spin-selective dipole trap. This can be done with light closely detuned to the  $D_1$  and  $D_2$  transition to induce an electric dipole moment of opposite sign for both spin states. However, the small fine structure splitting of  $^6\text{Li}$  and the corresponding large spontaneous scattering rates of these closely detuned traps make this method impractical.

<sup>55</sup> In that work, the final magnetic field was always below the broad Feshbach resonance such that the Fermi gas is always in the upper branch of the Feshbach resonance and no bosonic dimers are formed.

**Figure 8.3:** (a) According to the Breit-Rabi equation (Appendix E, Eq. E.2), the ground state  $^2S_{1/2}$  of  $^6\text{Li}$  splits into six hyperfine states. They are labeled in ascending energy from  $|1\rangle$  to  $|6\rangle$ . For large fields the coupling to the electron spin  $m_j = \pm 1/2$  dominates resulting in two triplets of high- and low-field seeking states. (b) We restrict our self to high-field seekers. For a radio-frequency transfer, the magnetic field must be varied with a frequency corresponding to the energy difference between states ( $|1\rangle$ - $|2\rangle$ ) or ( $|2\rangle$ - $|3\rangle$ ).



2. Ejection of one spin state with resonant light. In this method, one spin state is removed with light resonant with the  $D_1$  or  $D_2$  transition.

<sup>56</sup> In Ref. [175] the RF transfer and the subsequent removal of atoms in state 3 was done at the zero crossing of the 1-2 scattering length at 537 G. Then the magnetic field was ramped to large fields  $\sim 800$  G for evaporation and the final experiment. When the Feshbach resonance is approached from below all minority atoms will start to pair up with majority atoms to populate the Feshbach molecule branch at lower energy. The corresponding binding energy is transferred to kinetic energy in 3-body collisions. Most of this resulting heat was probably removed by the final evaporation step. When ramping down from a cold system at 832 G, the zero crossing of the 1-2 scattering length at 537 G cannot be accessed because all atoms are lost due to the decay of Feshbach molecules into lower lying vibrational states.

<sup>57</sup> We will remove the in-vacuum resonator from the preparation chain in the future and load atoms directly from the MOT into a deep transport trap created with a 200 W 1064 nm laser. This will eliminate the evaporation in the resonator-enhanced dipole trap which is a dominant source to the particle number instabilities and allow us to implement preparation schemes using spin-selective magnetic trapping.

The second method, ejection of one spin state with resonant light, was first used in the study of the 2D bulk system in the Princeton group [175]. We follow this method with some modifications<sup>56</sup> (as in Ref. [174]). In this method detrimental effects one has to consider are off-resonant scattering from the other spin state and the possibility that an atom absorbs photons yet does not leave the trap but rather heats up the remaining atoms. Therefore, the atoms to be removed are first transferred to spin state 3, such that the ejection light pulse is off-resonant with state 1 and 2. Here, starting with an initial balanced mix of state 1 and 2 evaporated at 832 G, the magnetic field is ramped to  $B \sim 1000$  G to decrease the scattering length between all three spin states. At this field, an RF transfer from 2 to 3 is performed and all atoms in state 3 are ejected using resonant light.

This scheme, as we shall see, has the unfortunate disadvantage that at high magnetic fields no zero crossing of the scattering length exists such that the spin states are always interacting, making removal of one spin state without heating by momentum transfer to the others more difficult. However, the practical advantages are that we can use the stable atom number after the efficient evaporation in the squeeze trap at high magnetic fields<sup>57</sup>. An additional advantage is that no heating can occur due to the formation of Feshbach molecules because we do not ramp a cold gas from low magnetic fields to the broad Feshbach resonance.

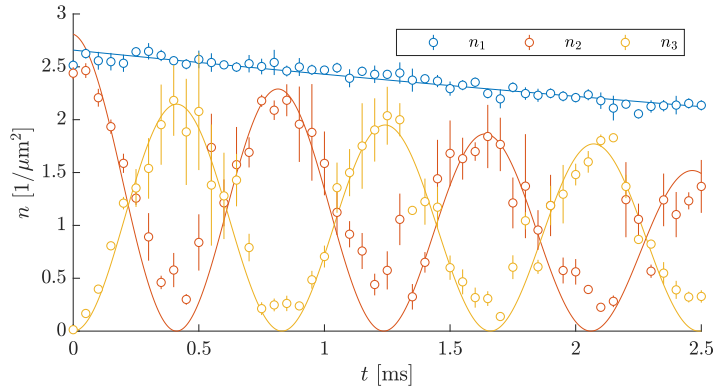


**Figure 8.4:** Rabi oscillations of state 2 and 3 with a Rabi rate of  $\Omega_R = 2\pi \cdot 1.2$  MHz. We observe here a slow decrease of all densities involved. Particularly, we observe that the density in state 1 which does not participate in the Rabi oscillation goes down. The likely reason for that are three-body losses.

### 8.2.3 Step 1: Radio-frequency transfer

In this section, we will discuss the first step of the imbalance procedure in detail, the RF transfer of atoms from state 2 to state 3.

After preparing the 2D gas with a balanced 1-2 mixture we ramp the magnetic field to 1000G in 250 ms to minimize the interaction strength between 3-1 and 3-2 during and after the resonant pulse. Here, all pair-wise 3D scattering lengths are negative (see Fig. 2.3) such that in 3D no bound states and in quasi-2D only shallow confinement induced bound states exist. At the same time, we ramp the ring potential from 11 mW to 17 mW to avoid spilling atoms when the chemical potential and temperature increases during the creation of the spin-imbalance. For the RF transfer, we place a one-loop coil close to the atom position to rapidly vary the magnetic field  $B$ . Positioning it as close as possible to the atom position is crucial, as measurements with a pick-up coil showed a reduction in intensity  $I \propto B^2$  of about 5 dB every 1 cm.

In order to transfer atoms from state 2 to 3 at 1000 G, we induce Rabi oscillations between state 2 and 3 by turning on the RF of<sup>58</sup>  $\nu_{\text{RF}} = 80.9$  MHz (see Fig. 8.3 in Appendix E). Here, atoms in state 1 do not participate in the Rabi oscillation because the 1-2 transition is far detuned ( $\nu_{\text{RF}} = 76.5$  MHz). As long as the RF is turned on, the Rabi oscillation creates a two-component mixture of atoms in state 1 and atoms in a time-varying superposition of state 2 and 3.

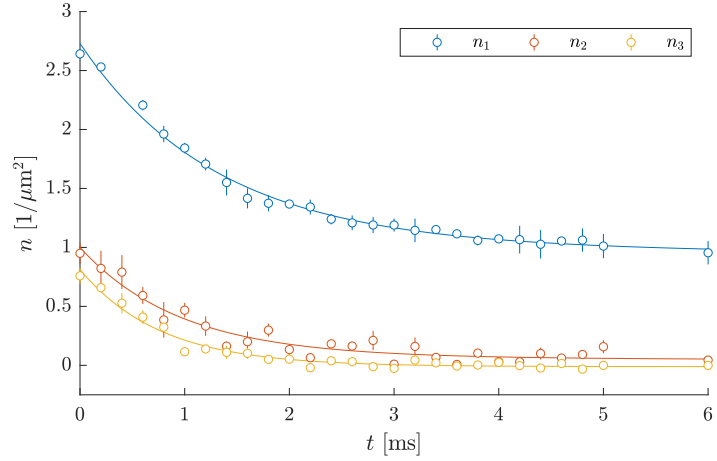
To characterize the temporal behavior, decoherence and possible loss mechanisms, we vary the time the RF stays on and immediately image atoms in state 1, 2, and 3 afterwards (Fig. 8.4). As expected, we observe a Rabi oscillation between state 2 and 3 with a Rabi rate<sup>59</sup> of  $\Omega_R = 2\pi \cdot 1.2$  kHz. In addition, we observe that the number of atoms in state 1 and the total number of atoms in state 2 and 3 decreases with a lifetime of  $\tau = 9$  ms.

As will see next, the likely reason for these losses are inelastic collisions where two atoms form a deep dimer while providing the excess energy to a third atom. In principle, this process is not allowed for a two-component mixture because the three-body collision has to

<sup>58</sup> We compensate for small variations in the magnetic field by optimizing the frequency for maximum transfer at a short pulse length.

<sup>59</sup> As discussed further below, we later increase the Rabi rate to  $\Omega_R = 5.5$  kHz.

**Figure 8.5:** Measurement of the three-body recombination of a three-component mixture shows a lifetime of 1 ms. The solid lines are fits of an exponential decay.



The three-body recombination rate can be enhanced due to Efimov resonances which are discussed in detail in Ref. [179]

involve at least two identical fermions which is not possible for s-wave scattering. Thus, the observed losses hints to a slow decoherence of the coherent 2+3 superposition into states 2 and 3, creating effectively a three-component mixture which allows for inelastic collisions. In order to characterize the time scale of these inelastic collisions, we prepare a three-component mixture by applying an RF pulse of length  $t \approx \Omega_R^{-1}\pi/2$ , which creates a three-component mixture with relative densities  $n_1 : n_2 : n_3 \approx 60\% : 22\% : 18\%$ . Then, after turning off the RF, we wait for a varying time to observe the in situ losses due to three-body recombination by imaging all three states (Fig. 8.5). For all three states, we observe a lifetime of approximately 1 ms.

The heating from three-body losses can be neglected when the amount of atoms which decohere during the RF pulse is small, which is the case if the RF pulse length is significantly smaller than the lifetime of 1 ms. This is not the case for the Rabi oscillations shown in Fig. 8.4, but by optimizing the RF coupling to the coil we could increase the Rabi rate to  $\Omega_R = 2\pi \cdot 5.5 \text{ kHz}$ , which allows for a  $\pi/2$  pulse in  $\sim 100 \mu\text{s}$ .

However, we encountered instabilities in the ratio of transferred atoms when using a Rabi pulse, possibly due to a experimental fluctuations of the pulse length. Instead, we found that a Landau-Zener transition [180] is more stable. A Landau-Zener transition works by detuning the RF frequency continuously over a range  $2\pi\Delta f \gg \Omega_R$  centered on the resonance between both hyperfine states. If the sweep of the RF frequency is performed sufficiently slowly, this allows for an adiabatic transfer of all state 2 atoms to state 3 atoms. Thus, we can achieve the same effect as if we would apply a resonant  $\pi$ -pulse. If instead a fast sweep is performed, a diabatic passage occurs and all atoms stay in their hyperfine state 2. Thus, by varying the sweep rate  $\dot{\omega}$  of the RF frequency the fraction of atoms transferred from 2 to 3 is given by the probability for an adiabatic transfer<sup>60</sup>

<sup>60</sup> Where  $\Omega_R = 2\pi\nu_R$  and  $\dot{\omega} = 2\pi\dot{\nu}$ .

$$P_{LZ} = 1 - \exp\left(-2\pi \frac{\Omega_R^2}{\dot{\omega}}\right). \quad (8.2)$$

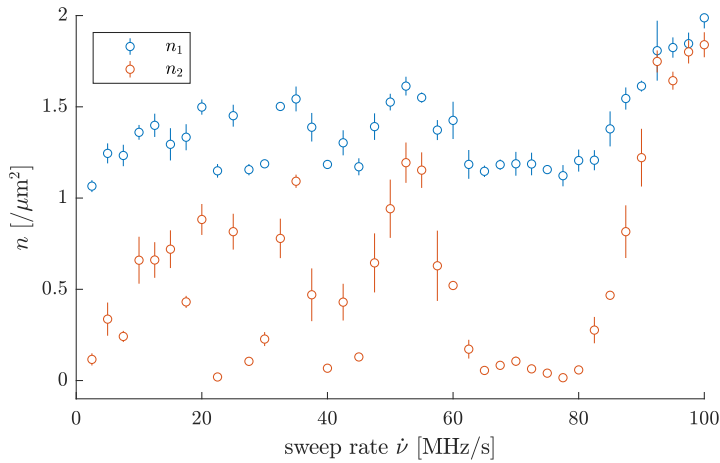


**Figure 8.6:** Resulting population of atoms after a narrow Landau-Zener (LZ) sweep from 2 to 3. After the LZ sweep, atoms in state 3 were ejected as discussed in the next section and are therefore not shown here. The population in state 2 shows here an oscillatory behavior because the condition  $2\pi\Delta f/\Omega_R \gg 1$  is not fulfilled, which results in so-called coherent Landau-Zener oscillations. Sweep rates between 80 MHz/s and 90 MHz/s allow for a quick and stable transfer of atoms from state 2 to 3.

In the experiment, we see that the range of sweep rates between 80 MHz/s and 90 MHz/s allows us to quickly transfer a varying fraction of atoms from state 2 to state 3 (Fig. 8.6). The transfer in this range happens during a sweep time of less than 200  $\mu$ s and is therefore sufficiently short to avoid three-body losses. Thus, we have found a reliable way to transfer a varying number of atoms from state 2 to state 3. In Sect. 8.2.4, we will remove all atoms transferred to state 3 with a resonant light pulse.

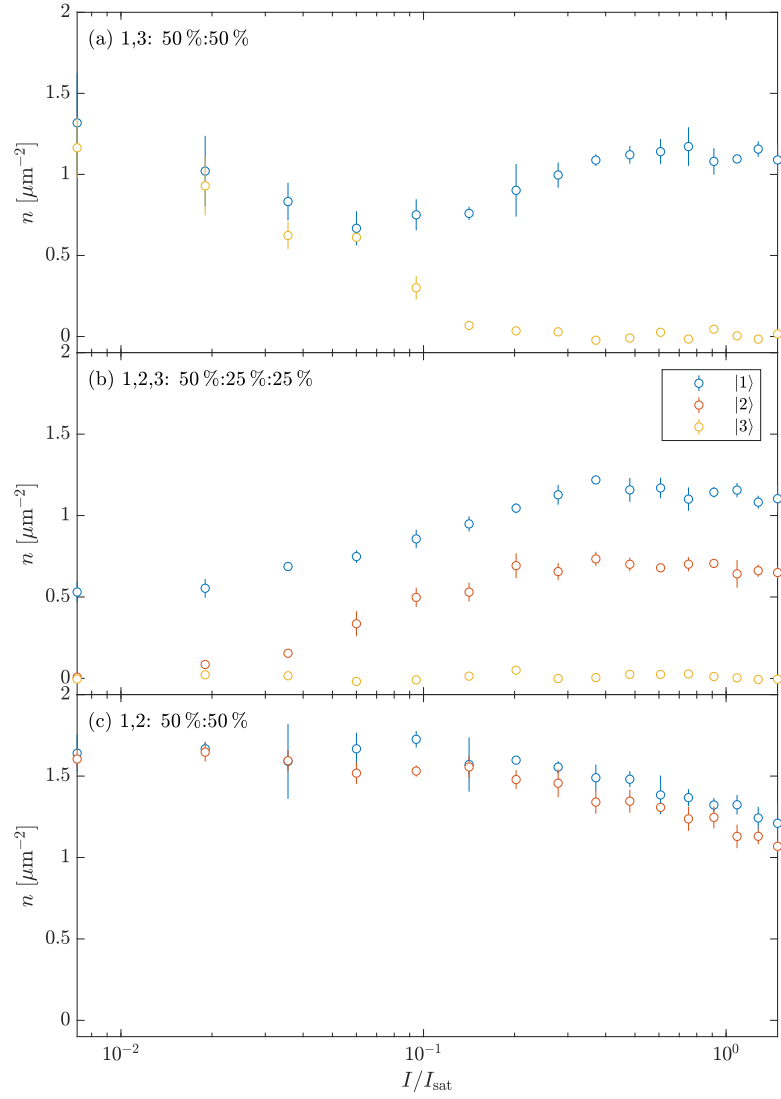
For completeness, the complex dynamics observed in Fig. 8.6 are discussed in more detail below. In short, it originates from the fact that we perform frequency sweeps over a frequency range  $\Delta f$  too narrow for Eq. 8.2 to hold. The motivation behind the narrow frequency range is to limit the sweep time and associated losses. Due to the narrow sweep state 2 does not follow the drive adiabatically to state 3 but coherent oscillations between state 2 and 3 occur.

The sweep time is reduced to address the situation where atoms in state 2 are only partially transferred to state 3, resulting in a three-body mixture already present during the sweep. This three-body mixture is susceptible to three-body losses, making it crucial to keep the sweep time short. Unfortunately, with our experimentally achievable Rabi rate a proper Landau-Zener transition where the relative frequency range obeys  $2\pi\Delta f/\Omega_R \gg 1$  and the transition rate  $\dot{\omega}$  is much smaller than  $\Omega_R^2$  is too slow to avoid three-body losses. Therefore, we restrict the frequency sweep to a narrow frequency range of just  $\Delta f = 16$  kHz.

The remaining atoms in state 2 and 1 after such a transfer are shown in Fig. 8.6. The oscillations<sup>61</sup> observed in Fig. 8.6 occur because the condition  $2\pi\Delta f/\Omega_R \gg 1$  necessary for the Landau-Zener formula to be valid, is not fulfilled for  $2\pi\Delta f/\Omega_R \approx 3$ . Instead, we see here coherent driving during the frequency sweep causing a so-called coherent Landau-Zener oscillations [181].

<sup>61</sup> Later measurements revealed that the dynamics shown here are still oscillatory for sweep rates above 100 MHz/s

**Figure 8.7:** Characterization of an  $2\ \mu\text{s}$  ejection pulse resonant with state 3. For each panel, a different initial mixture was prepared using an RF pulse: (a) balanced 1-3 mixture, (b) 1,2,3 mixture with ratios 50%:25%:25%, (c) balanced 1-2 mixture.



#### 8.2.4 Step 2: Ejection of the third state

In this section, we discuss in detail the removal of all atoms in state 3 with a resonant light pulse. This step is done immediately after the RF transfer from state 2 to state 3 in order to avoid heating and losses due to three-body recombination. We are using the same beam used for absorption imaging but tune the light frequency such that it is resonant with state 3.

To find out how much light intensity we need to remove all atoms in state 3, we prepare a two-component 1-3 mixture (Fig. 8.7 a) using an RF transfer. Then atoms in state 3 are ejected with varying light intensities for a pulse length of  $2\ \mu\text{s}$  followed by a magnetic field ramp time of 200 ms before imaging state 1 or 3. The intensities are normalized by the saturation intensity

$$I_{\text{sat}} = \frac{\pi\hbar c\Gamma}{3\lambda^3}. \quad (8.3)$$

We observe that intensities of  $I \gtrsim 0.2I_{\text{sat}}$  seem to be sufficient to remove all atoms in state 3.

As discussed further below, we find in the measurements performed in Fig. 8.7 b and Fig. 8.7 c that it is optimal to select an intensity of  $I = 0.3 I_{\text{sat}}$ . This intensity is high enough to remove all atoms in state 3 fast enough to minimize collisions with state 1 and 2 atoms and it is small enough such that off-resonant scattering with 1 and 2 does not lead to strong losses.

We start the more in-depth discussion, by characterizing what happens after a partial transfer by preparing a 1-2-3 mixture<sup>62</sup> using an appropriately chosen RF transfer (Fig. 8.7 b). As in the first measurement, we apply the ejection pulse with state 3 with varying intensities. We see that regardless of the intensity, all atoms in state 3 are gone. This is expected for intensities  $I \gtrsim 0.2I_{\text{sat}}$  where all atoms in state 3 are directly removed by the ejection pulse. To understand what happens for low intensities  $I \lesssim 0.2I_{\text{sat}}$ , we have to consider the observed losses in state 1 and 2. Apparently, atoms in state 3 are lost due to three-body recombination with atoms in state 1 and 2 during the 200 ms ramp time before imaging.

There are two additional effects alongside three-body recombination, namely, off-resonant scattering at large intensities and interaction effects at low intensities, which we will discuss in the following. We can investigate off-resonant scattering exclusively by preparing a 1-2 mixture and keeping the ejection pulse still resonant with the now unoccupied state 3 (Fig. 8.7 c). We observe that the density in both state 1 and state 2 starts to decrease at  $I \gtrsim 0.1 I_{\text{sat}}$  (Fig. 8.7 c). The relative loss of atoms in state 2 and state 1 is 25 % at  $I = I_{\text{sat}}$ . Theoretically, the expected off-resonant scattering rate follows<sup>63</sup>

$$\Gamma_{\text{SC}} = \frac{\Gamma}{2} \frac{I/I_{\text{sat}}}{1 + I/I_{\text{sat}} + \left(\frac{2\Delta}{\Gamma}\right)^2} \quad (8.4)$$

for a detuning  $\Delta$ , natural linewidth  $\Gamma$ , and intensity  $I$  normalized by the saturation intensity (Eq. 8.3). By inserting  $\Gamma/\Delta = 6 \text{ MHz}/80 \text{ MHz}$  we obtain a scattering rate of  $\Gamma = 0.026 \mu\text{s}^{-1}$  at  $I = I_{\text{sat}}$  for state 2. Thus, the resulting losses due to spontaneous scattering should only amount to 5 % (1 %) for state 2 (1) within the  $2 \mu\text{s}$  pulse time. The exact reasons for the significantly larger losses observed both in state 2 and especially, in state 1, are unknown. One possible explanation, a broader laser linewidth, was excluded by beating the laser with a second laser and observing a linewidth below 1 MHz. We suspect that a broad spectral underground may be the cause for the unexpected losses.

To shed light on the second effect, i.e. heating and subsequent loss of state 1 and 2 atoms caused by collisions with the accelerating state 3 atoms, we revisit the measurement with a balanced 1-3 mixture shown in Fig. 8.7 a. Here, we would naively expect that state 1 is only effected by off-resonant scattering which we observed in the 1-2 mixture (Fig. 8.7 c). However, quite surprisingly, the number of atoms in state 1 follows the number of atoms in state 3 for low intensities.

<sup>62</sup> The initial density ratios in this measurement are 50 % : 25 % : 25 %.

<sup>63</sup> For  $\Delta \gg \Gamma$  the equation can be simplified to  $\Gamma_{\text{SC}} = \frac{3\pi c^2}{2h\omega_0^3} (\gamma/\Delta)^2 I(r)$  [182]

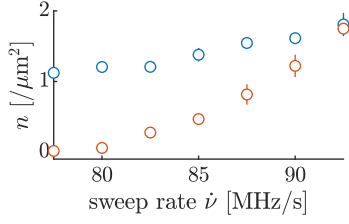


**Figure 8.8:** Zoomed-in plot of Fig. 8.6. The coherent Landau-Zener sweep is combined with the ejection pulse to prepare systems ranging from full polarized (left) to a balanced system (right).

Only above a threshold intensity of  $I \sim 0.1 I_{\text{sat}}$ , the state 1 density decouples from atoms in state 3.

We explain the decrease of atoms in state 1, which is strongest around  $I \sim 0.06 I_{\text{sat}}$ , by the fact that the scattering length  $a_{13}$  is still large at 1000 G resulting in a strong interaction between the ejected state 3 and state 1. Here, one possible explanation is that atoms in state 3, after absorbing a photon, may transfer some momentum to atoms in state 1, causing them to leave the trap instead. The same behavior should be true for the interaction between 2 and 3 because the scattering length between these has a similar amplitude.

With all these effects in mind, we have to choose an intensity for the ejection pulse which minimizes the discussed losses. The heuristic approach we use is quite simple. We choose the intensity which results in the largest number of remaining atoms in state 1 and 2, which is  $I = 0.3 I_{\text{sat}}$  (Fig. 8.7 b). This will yield the highest density and therefore most efficient evaporation in the next step. In conclusion, we can combine now the coherent Landau-Zener sweep with the ejection of atoms in state 3 to prepare systems stretching from a balanced gas to a fully state-1-polarized gas (Fig. 8.8).

### 8.2.5 Step 3: Final evaporation

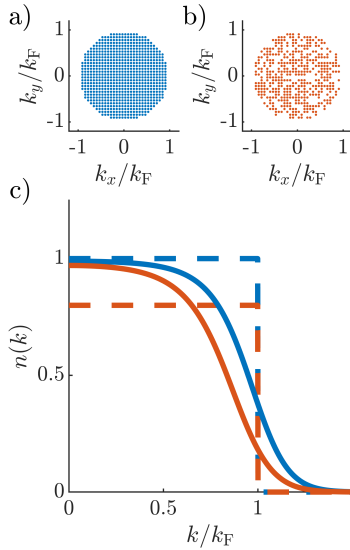


**Figure 8.9:** a) Sketch of 2D Fermi distribution in state 1. b) Sketch of the 2D Fermi distribution in state 2 after a momentum independent removal of some fermions using radio frequency. c) This leads to a uniform decrease in the occupation number  $n(k)$  (dashed lines) which causes after thermalization a broadening of both Fermi distributions (solid lines).

After creating the particle imbalance using the RF sweep and ejection pulse in the last two sections, we face one problem: Initially, we started with a cold balanced system where in the  $T = 0$  non-interacting limit all states up to the Fermi momentum are filled. With the RF transfer, however, we removed some atoms in state 2 independent of their momentum. Therefore, the momentum distribution in state 2 now contains many holes, even deep within the Fermi sea (Fig. 8.9). If we just let the system thermalize, the momentum distribution will again approach a Fermi-Dirac distribution but with a significantly increased temperature. On top of this effect, we expect additional heating due to the two effects discussed above, i.e. the off-resonant scattering from the ejection pulse and the momentum transfer from ejected state 3 atoms.

Therefore, we perform a final evaporation by reducing the height of the radial ring potential. To increase the evaporation efficiency, we increase the atom density by shrinking the diameter of the ring confinement. For that, we utilize the fact that the ring diameter tapers towards the top (see 3D box in Fig. 3.1) and adjust the trap position vertically by moving the upper microscope objective responsible for projection the ring potential onto the atoms.

For the final evaporation we study a system prepared with an initial spin-imbalance of  $P \approx 0.2$  (Fig. 8.10).

We ramp the magnetic field in 200 ms from 1000 G created by the Feshbach coils to 832 G created by the Helmholtz coils in order to increase interactions and remove the residual underlying harmonic potential caused by the Feshbach coils. Thus, only the antitrapping of  $\omega_r \sim 2\pi i \cdot 24$  Hz from the accordion lattice remains and evaporated

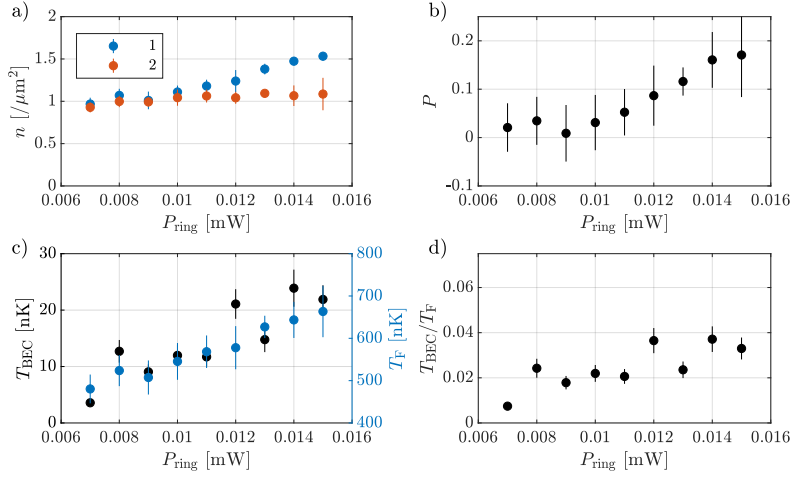


**Figure 8.10:** Characterization of the final ring evaporation starting with a polarization of  $P = 0.17 \pm 0.09$ . (a) The evaporation leads immediately to a loss of atoms in state 1. (b) This balances the gas and results in  $P = (N_1 - N_2)/(N_1 + N_2) = 0$ . (c) At the same time, the evaporation reduces the absolute temperature  $T_{\text{BEC}}$  measured in the BEC regime. While the loss of particles lowers the Fermi temperature of the corresponding balanced system  $T_{\text{F}}$ , (d) shows that the normalized temperature is still reduced by the evaporation.

atoms do not accumulate outside the ring potential but leave the system.

Then, we reduce the ring potential within 1 s from 17 mW to a varying power to perform forced evaporation (Fig. 8.10). We see that the evaporation removes more atoms in state 1 because the chemical potential of state 1 is higher than of state 2 (Fig. 8.10 a). This results in a tendency to balance the gas (Fig. 8.10 b). To measure the temperature, we perform matter-wave imaging by ramping the system into the BEC regime and performing a ToF measurement. This technique, explained in more detail in the next chapter, is based on performing a Boltzmann fit to high momentum tail of the dimers to obtain a temperature in the BEC regime  $T_{\text{BEC}}$  (Fig. 8.10 c).

If we divide this temperature in the BEC regime by the Fermi temperature corresponding to the Fermi energy of the balanced system with the same number of fermions we obtain a normalized temperature<sup>64</sup> of  $T_{\text{BEC}}/T_{\text{F}} = 0.04 \pm 0.01$  at polarizations of  $P = 0.17 \pm 0.06$  (Fig. 8.10 d). We observe that the polarization decreases for lower evaporation powers as excess majority atoms are spilled preferably. Thus, the system is balanced for evaporation powers below 10 mW. While the normalized temperature,  $T_{\text{BEC}}/T_{\text{F}}$ , is reduced by about 50 % from 15 mW to 10 mW, we choose a rather high evaporation depth of 15 mW in order to minimize the loss in polarization. After preparing these spin-imbalanced systems we proceed now to next the section, where we analyze the density profile, the momentum distribution and the excitation spectrum of these gases in more detail.

<sup>64</sup> In later experiments which are discussed in the next chapter, the temperature increases slightly to  $T_{\text{BEC}}/T_{\text{F}} = 0.05 \pm 0.01$ .



In this section, we discuss the experimental results obtained using the imbalanced Fermi gases as prepared in the last chapter. We first study the density profiles and the momentum distribution of the imbalanced gas trapped in a box potential. Then, we discuss the excitation spectrum obtained using Bragg spectroscopy. In chapter 10, we discuss how these results could match the theoretical predictions.

### 9.1 Density profiles and momentum distribution

The preparation method discussed in the last chapter allows us to prepare a cold ( $T_{\text{BEC}}/T_{\text{F}} < 0.1$ ) imbalanced system for a global polarization of up to  $P \approx 0.25$  (Fig. 9.1).

We examine exemplary density profiles in Fig. 9.2 a for a gas with a global polarization<sup>65</sup> of  $P = 0.17 \pm 0.06$  and  $T_{\text{BEC}}/T_{\text{F}} = 0.05 \pm 0.01$  at a Feshbach field of  $B = 832$  G, which would correspond to the unitary point in 3D. For each spin state we average over  $\sim 20$  realizations and determine the total polarization using the average density in both spin states. Most of the given error in the polarization comes from a 5% single-shot density fluctuation and could be eliminated in the future by imaging both spin states in one realization simultaneously. The 3D unitary point corresponds to an effective 2D interaction strength (Eq. 4.7) of  $\ln(k_{\text{F}}a_{2\text{D}}) = 0.6$  at our densities. Surprisingly, the density distribution of both state 1 and state 2 is homogeneous and we do not see any formation of domains. Consequently, the local polarization  $p = (n_1 - n_2)/(n_1 + n_2)$  is nonzero and almost constant throughout the system (Fig. 9.2 b).

<sup>65</sup>The corresponding particle ratio is  $N_1 : N_2 = 41.5\% : 58.5\%$ .

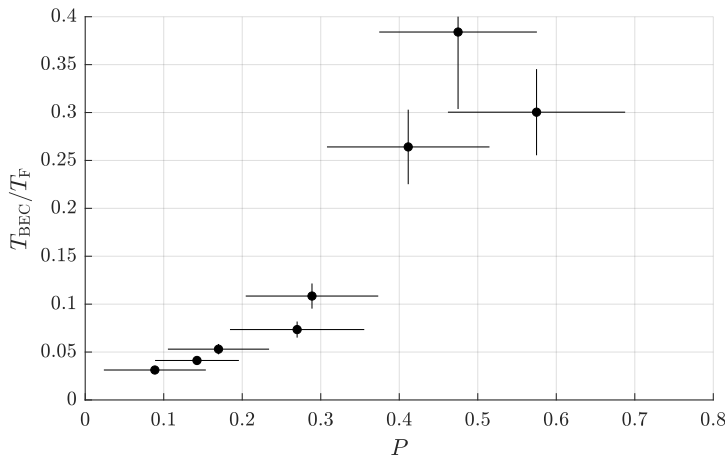
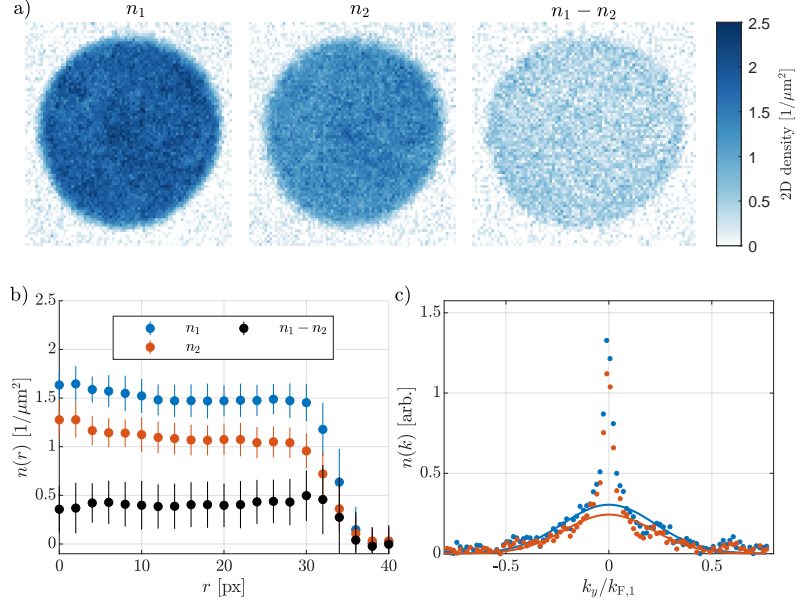


**Figure 9.1:** Overview of imbalanced Fermi gases after final evaporation. The x-axis shows the final polarization while the y-axis shows the temperature measured in the BEC regime. It is normalized by the Fermi temperature  $T_{\text{F}}$  corresponding to the non-interacting balanced system with the same number of atoms.

**Figure 9.2:** (a) Density distribution of spin-imbalanced Fermi gas with a polarization of  $P = 0.17 \pm 0.06$  imaged at 832 G of the majority (left), minority (center) and the difference (right). The observed density distribution is flat and does not show any sign of phase separation. (b) The radial average shows a slight increase in the center of the trap. (c) A ToF measurement of the same system at 750 G does not show a bimodal distribution. A Gaussian fit to the high momentum distribution of the minority results in a temperature of  $T_{\text{BEC}} = 36 \pm 3$  nK.



The 2D densities averaged over the ring are  $n_1 = 1.55 \mu\text{m}^{-2}$ ,  $n_2 = 1.1 \mu\text{m}^{-2}$  which corresponds to a 2D Fermi energy

$$E_{\text{F}} = \frac{\hbar^2 2\pi}{2m} n_{\text{total}} = \frac{\hbar^2 4\pi}{2m} \frac{n_1 + n_2}{2} = \hbar \cdot 14 \text{ kHz} \quad (9.1)$$

in the limit of a noninteracting Fermi gas. If we compare this with the vertical trapping frequency of  $\nu_z = 9 \text{ kHz}$  we notice that the noninteracting Fermi gas populates both the ground state and the first excited state<sup>66</sup>. Thus, we are not strictly in the 2D limit  $E_{\text{F}} < \hbar\omega_z$ , but in the 2D to 3D crossover, where the occupation of the ground state and the first excited state has an effect on the density of states.

To obtain insight into the temperature of the gas, we ramp the same system adiabatically to the BEC regime at  $B = 750 \text{ G}$  ( $\ln(k_{\text{F}a_{2\text{D}}}) = -1.7$ ) and perform matter wave imaging to project the momentum distribution onto the density distribution [81]. To do this, we let the gas evolve for a time of flight (ToF) of  $t = T/4$  in the remaining magnetic harmonic potential with a radial trapping frequency of  $\omega_r = 2\pi \cdot 27.3 \text{ Hz}$  before performing absorption imaging of either state 1 or 2. In the BEC regime, all minority atoms in state 2 form bosonic dimers with a corresponding atom in state 1. The excess majority atoms in state 1 remain unbound fermions. Thus, the momentum distribution of state 2 atoms directly reflects the momentum distribution of all dimers.

The ToF measurement reveals a bimodal structure for both state 1 and state 2 (Fig. 9.2 c). We perform a Boltzmann fit to the high-momentum wing of state 2, which should exclusively consist of dimers with mass  $m_{\text{d}} = 2m$ , and extract a temperature of  $T_{\text{BEC}} = 36 \pm 3 \text{ nK}$ . If we divide this temperature by the Fermi temperature corresponding to the Fermi energy of the balanced system with the same number of fermions (Eq. 9.1),  $T_{\text{F}} = E_{\text{F}}/k_{\text{B}} = 670 \text{ nK}$ , we obtain a nor-

<sup>66</sup> This reduces the Fermi energy of the non-interacting gas by 18% compared to the 2D Fermi energy (Eq. 9.1) we use in our analysis.

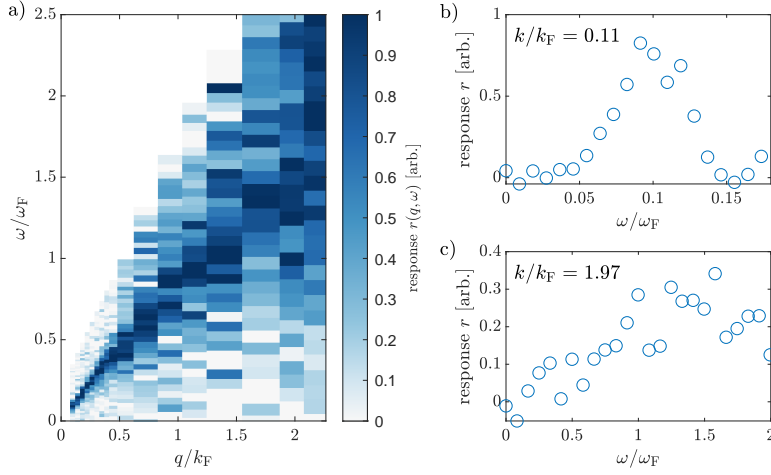


**Figure 9.3:** (a) Bragg spectroscopy of an imbalanced Fermi gas with  $E_{F,1} = h \cdot 12.2$  kHz,  $E_{F,2} = h \cdot 9.7$  kHz and  $P = 0.11 \pm 0.06$ . At low momentum, a linear sound mode is visible, which merges at larger momenta into a continuum of excitations. (b) A slice at low momentum shows a clear gap in the excitation spectrum at low energies. (c) At large momenta, the situation is not conclusive because the signal-to-noise ratio of the data is not that good. The trace shown here in particular, does not show the absence of excitations at low momentum, while at other momenta (see a)) there appears to be a pairing gap.

malized temperature of  $T_{\text{BEC}}/T_F = 0.05 \pm 0.01$ . This temperature is significantly lower than the temperature  $T/T_F = 0.10 \pm 0.03$  measured for 2D imbalanced gases in the BEC regime (730 – 780 G) prepared in Ref. [175].

Balanced quasi-2D Fermi gases showed an increase<sup>67</sup> of the temperature by a factor 2 when the interaction strength was changed adiabatically from  $\ln(k_F a_{2D}) \approx -3.5$  to  $\ln(k_F a_{2D}) \approx 0.5$  (Fig S3 in Ref. [139]). The corresponding temperature of our gas at 832 G ( $\ln(k_F a_{2D}) = 0.6$ ) should therefore be  $T/T_F \approx 0.1 \pm 0.02$ , which is below the critical temperature of  $T_c \approx 0.14 T_F$  at this interaction strength for a balanced gas<sup>68</sup>.

Therefore, the question arises of whether the gas is superfluid. To obtain these insights, we employ Bragg spectroscopy to find out if the excitation spectrum shows a pairing gap.

## 9.2 Excitation spectrum

In Fig. 9.3 a we show the excitation spectrum for an imbalanced system with  $P = 0.11 \pm 0.06$ . Similarly to the spectra for balanced systems discussed in this thesis, the excitation spectrum features a linear sound mode at low momenta and a broad continuum of excitations at high momenta. At low momenta, a gap in the excitation spectrum is clearly visible which corresponds to a nonzero critical velocity (Fig. 9.3 b). At high momentum, this is not so clear because the signal-to-noise ratio deteriorates. There are momentum traces, which show a gap in the excitation spectrum, but there are also traces, for example, the one shown in Fig. 9.3 c in which excitations appear at all energies. Thus, it is not clear whether the gas has an excitation gap at large momenta. While the narrow sound mode and the excitation gap at low momentum seem to indicate that the system is in a superfluid state, the low-lying excitations observed at large momenta results in a Landau critical velocity of zero.

<sup>67</sup> Interestingly, Ref. [118] reports a decrease of the absolute temperature from the BEC to the BCS regime (Table II in Ref. [118]). However, this decrease can be attributed to a decrease in the total number of atoms and thus  $T_F$  (Table IV in Ref. [118]), resulting in an effective increase of  $T/T_F$  in this experiment as well.

<sup>68</sup> We take here the interpolated value of the critical temperatures measured at interaction strengths  $\ln(k_F a_{2D}) = 0.2$  and  $\ln(k_F a_{2D}) = 0.79$  in Ref. [139].

<sup>69</sup> Even at finite temperature  $T \ll \Delta/k_B$  the number of thermal excitations is very small due to an exponential suppression of  $\sim e^{-k_B T/\Delta}$ .

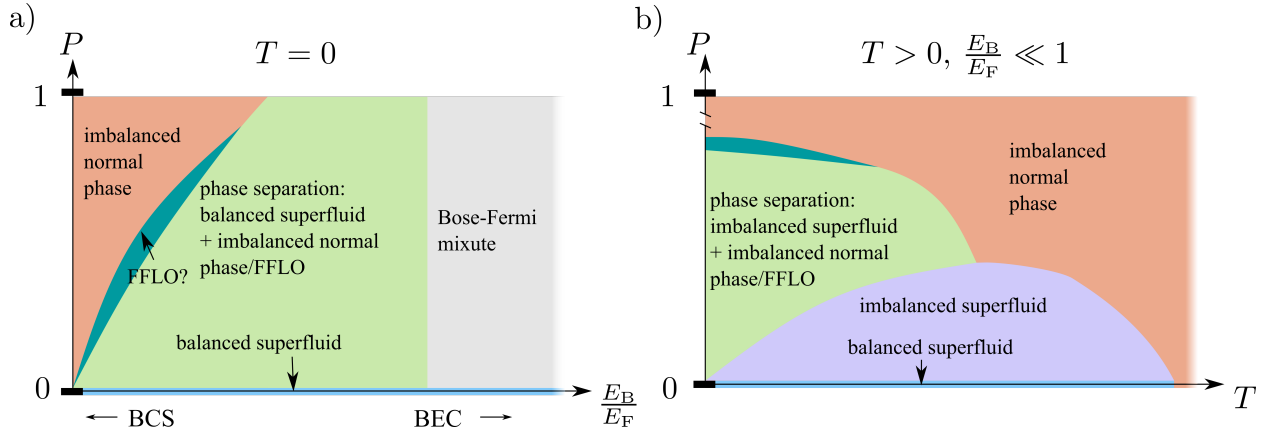
<sup>70</sup> Or alternatively, if the whole system is set into rotation, where the relative velocity to the trap walls is smaller than a critical velocity, the normal fraction dampen, a part of the total density, will dampen out while the superfluid fraction, the remaining density, will rotate frictionless.

Some of these gapless excitations at large momenta may arise due to presence of unbound fermions. For that we have to consider that for a balanced gas at  $T = 0$  no gapless excitations<sup>69</sup> are present at finite momentum and the Landau criterion is fulfilled when all possible excitations of the system are considered.

However, in the finite-temperature imbalanced Sarma phase, which we will discuss in the next chapter in Sect. 10.4, excess fermions exist in the gas in the form of quasiparticle excitations. These quasiparticle excitations themselves are not gapped, resulting in a Landau critical velocity of zero if excitations of these quasiparticles are also taken into account.

Nevertheless, the total system might be superfluid because the paired fraction will resist any phase change<sup>70</sup>. In this case, measurements of the excitation spectrum with a higher signal-to-noise ratio might be useful to differentiate excitations from the paired and unpaired part of the system. Alternatively, measurements of the phase stiffness could be performed by observing a vortex lattice when rotating the gas.

In summary, a part of the observed excitations could be explained by gapless excitations of unpaired fermions which coexist with paired fermions.



In the previous chapter, we observed a homogeneous imbalanced Fermi gas close to the quasi-2D regime, which exhibits signs of superfluidity. This triggers the question how a superfluid phase can support a particle imbalance. To answer that we discuss in detail the phase diagram of 2D imbalanced Fermi gases in this chapter.

To give an overview of the discussion we summarize the  $T = 0$  phase diagram in Fig. 10.1 a. In the BCS regime, the superfluid phase with a constant order parameter can only exist in a balanced state. As soon as some imbalance is introduced, the balanced superfluid state breaks down, and a first-order transition to an imbalanced normal gas occurs. In a box potential where the spin imbalance  $P = (N_1 - N_2)/(N_1 + N_2)$  is fixed, the first-order transition manifests itself in a phase-separated state, where balanced superfluid regions are surrounded by an imbalanced normal gas. Above a critical polarization, these superfluid regions vanish and the full gas becomes normal. Around this critical polarization, an intermediate phase, a superfluid with a spatial oscillating order parameter (FFLO) might be present.

In the BEC regime, the situation differs because imbalanced Fermi gases map here to a Bose-Fermi mixture as all minority atoms bind with an equal amount of majority atoms to form dimers. These dimers condense, and deep in the BEC regime, the bosonic condensate can tolerate an arbitrary amount of the remaining majority fermions, resulting in a magnetized superfluid.

As we will find out, we can rule out the two superfluid phases which support a homogeneous imbalance at  $T = 0$ , the FFLO phase in the BCS regime and the magnetized superfluid in the BEC regime, for the interaction strengths and imbalances in our experiments.

**Figure 10.1:** Overview of the phase diagram for 2D imbalanced Fermi gases with spin imbalance  $P$ . (a) First we consider the zero-temperature scenario. The interaction strength is parameterized by the binding energy  $E_B/E_F$ , such that the BCS regime is on the left and the BEC regime on the right. At  $P = 0$ , a balanced superfluid is present at all interaction strengths. If an imbalance is introduced, a phase-separated state with balanced superfluid domains immersed in an imbalanced normal phase occurs (light green). Above a critical polarization, these domains cease to exist and the complete gas is normal (red). In between, a superfluid with a spatially oscillating order parameter, an FFLO phase, might be present (dark green). Deep in the BEC regime, no phase separation occurs because excess fermions are tolerated by the condensate of dimers (gray). (b) In the BCS regime, the finite-temperature phase diagram reveals another phase: An imbalanced superfluid with constant order parameter (purple). Here, the BCS state tolerates excess fermions in the form of quasiparticle excitations.

Therefore, we discuss in Sect. 10.4 the finite-temperature phase diagram sketched in Fig. 10.1 b. Finite temperature allows for a new phase, an imbalanced superfluid state with a constant order parameter. The mechanism is here that a superfluid can support some imbalance in the form of thermal quasiparticle excitations. This is a likely candidate for the observed phase but there are no calculations available for our exact experimental parameters to perform a quantitative comparison.

Thus, if the above phase diagrams represent the nature of our quasi-2D system we can have two possible scenarios: We prepared either a superfluid with an imbalance where no phase separation occurs or the system is in the imbalanced normal phase.

In the following, we will discuss the mean-field theory of 2D imbalanced Fermi gases in detail. Then, we discuss as one beyond mean-field effect the magnetized superfluid in the BEC regime, address the FFLO phase, and discuss the effect of finite temperature.

### 10.1 Mean-field phases

A spin imbalance can generally be realized in two ways. The first is to impose a spin imbalance, as we do in this thesis. The second is to alter the chemical potential of both spin states with respect to each other using an external magnetic field. The system will automatically imbalance itself if spin flips are energetically allowed.

Following Ref. [183] we will start with the second scenario which is described by the grand canonical ensemble, where the mean chemical potential  $\mu = (\mu_\uparrow + \mu_\downarrow)/2$  and the chemical potential difference  $h = (\mu_\uparrow - \mu_\downarrow)/2$ , called *Zeeman field*, are both fixed. We will progress in a two-step process to the first scenario, described by the canonical ensemble with fixed number of atoms in both spin states.

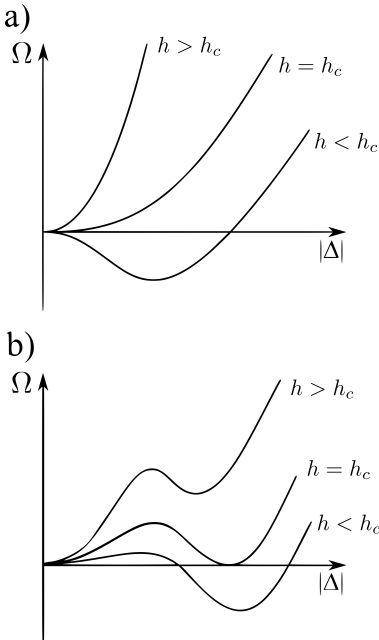


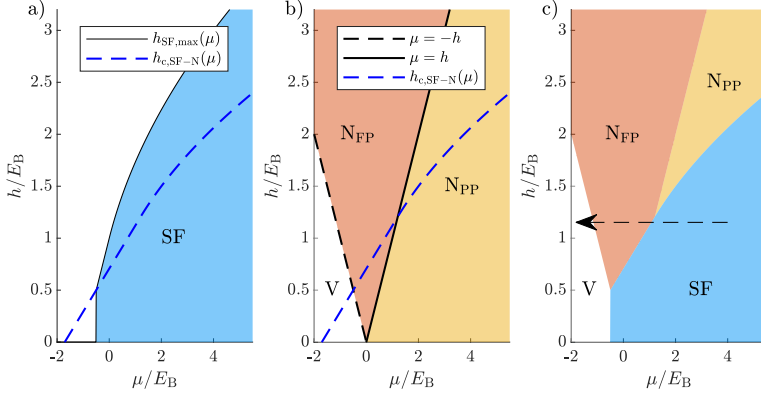
**Figure 10.2:** a) For a second-order phase transition, the grand potential  $\Omega(|\Delta|)$  as a function of the order parameter  $\Delta$  as a function of the transition Zeeman field  $h_c$ . b) A first-order transition occurs if the potential has two local minima at the transition Zeeman field.

#### GRAND CANONICAL ENSEMBLE (FIXED $\mu$ AND $h$ )

We start in the grand canonical ensemble with fixed  $\mu$  and  $h$ . Here, BCS mean-field theory at  $T = 0$  allows one to write down an analytical expression for the grand potential  $\Omega(\mu, h, \Delta, E_B)$  which can be found in Eq. 6 in Ref. [184]. The goal is to find the stable phases in the grand canonical ensemble for a given chemical potential  $\mu$  and Zeeman field  $h$ . The stable phases correspond to minima of the grand potential  $\Omega$ .

The grand potential  $\Omega$  has two minima, one at an order parameter  $\Delta(\mu) = \sqrt{2E_B E_F(\mu)} = \sqrt{E_B(E_B + 2\mu)}$  corresponding to the unpolarized superfluid phase (SF) and one at  $\Delta = 0$  corresponding to the polarized normal phase (N). Both are separated by a local maximum in the grand potential (Fig. 10.2 b). Therefore, the normal to superfluid transition is of first order because the system transitions from one local minimum to another local minimum, which results in a sudden change of the order parameter from 0 to a finite value.

Starting with the superfluid phase, the local minimum corresponding to this phase can only exist as long as the Zeeman field  $h$  is smaller



than the excitation gap for quasiparticle excitations [183],

$$h < h_{\text{SF,max}}(\mu) = \sqrt{\Delta(\mu)^2 + \mu^2 \Theta(-\mu)} \quad (10.1)$$

where the heaviside function  $\Theta(x)$  accounts for the larger excitation gap for negative chemical potentials. The area  $h < h_{\text{SF,max}}$  is depicted in Fig. 10.3 a. The total density  $n_{\text{total}} = n_{\uparrow} + n_{\downarrow}$  and the magnetization  $m = n_{\uparrow} - n_{\downarrow}$  of the superfluid phase, can be derived by considering the grand potential [183],

$$\Omega_{\text{SF}}(\mu) = -\frac{m}{\hbar^2 2\pi} \left( \mu + \frac{E_B}{2} \right)^2, \quad (10.2)$$

which depends only on the chemical potential. We take the derivative of the grand potential with respect to the chemical potential and field  $h$ , respectively, which yields

$$n_{\text{SF,total}} = \frac{m}{\pi \hbar^2} E_F(\mu) = \frac{m}{\pi \hbar^2} \left( \mu + \frac{E_B}{2} \right),$$

$$m_{\text{SF}} = 0.$$

We see here that the superfluid phase is balanced because the grand potential does not depend on  $h$ .

There also exists a nonzero solution of the gap equation if  $h$  is larger than the gap in the excitation spectrum ( $h > h_{\text{SF,max}}$ ) which corresponds to so-called Sarma superfluid or breached pair phase [185–187]. In this phase, majority atoms are placed at the Fermi surface by creating quasiparticle excitations with energy below  $h$  (Fig. 10.4). This allows for a superfluid with a finite magnetization. However, at  $T = 0$ , this phase corresponds to the local maximum of the grand potential in-between the minima of the balanced superfluid and normal phase, and is therefore not stable.

The normal phase does not have any critical Zeeman field, because the grand potential has a stationary point at  $\Delta = 0$  for any  $h$  and  $\mu$ . The value of the grand potential at this stationary point is [183]

$$\Omega_{\text{N}}(\mu, h) = -\frac{m}{\hbar^2 4\pi} [(\mu - h)^2 \Theta(\mu - h) + (\mu + h)^2 \Theta(\mu + h)]. \quad (10.3)$$

**Figure 10.3:** Phase diagram in the grand canonical ensemble. (a) The superfluid phase with a nonzero order parameter  $\Delta$  can exist as long as the Zeeman field  $h$  is smaller than the excitation gap (blue area, Eq. 10.1). (b) The normal phase is divided into three regions: A partially polarized phase (PP) where both spin states are present, a fully polarized Fermi gas (FP), and vacuum without any particles. The grand canonical potential of the normal phase is less than that of the superfluid phase for  $h > h_{\text{c,SF-N}}$  (Eq. 10.5, blue dashed). (c) We obtain the complete phase diagram by choosing the phase that minimizes the grand canonical potential, the superfluid phase from (a) for  $h < h_{\text{c,SF-N}}$  and the normal phases from (b) for  $h > h_{\text{c,SF-N}}$ . The dashed arrow indicates exemplary different phases which can be encountered in a harmonic trap when going from the center to the outside: A central balanced superfluid phase that is surrounded by a normal fully polarized shell.

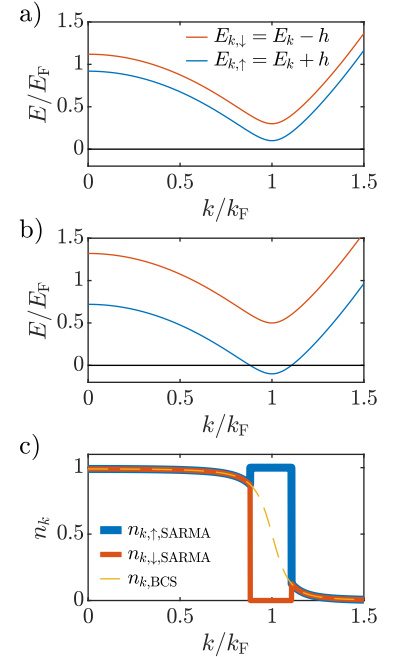


**Figure 10.4:** In the presence of a Zeeman field  $h$ , the BCS single-particle excitations split up into two excitations, depending if a spin-up (blue line) or spin-down particle (red line) is added to the system [185]. (a) For  $h < \Delta$  the system stays in the BCS state. (b) For  $h > \Delta$ , the excitations for the spin-up particles have a negative energy and become occupied. This breaks the BCS state but allows for the unstable Sarma superfluid. In this phase extra spin-up fermion are placed around the Fermi surface. (c) Thus, its momentum distribution (blue and red) is fully polarized around the Fermi surface, deviating from the BCS momentum distribution (orange dashed).

The role of the different terms becomes clear if we calculate the total density and magnetization taking again the derivative with respect to  $\mu$  and  $h$ , respectively,

$$n_{N,\text{total}} = \frac{m}{\pi\hbar^2}\mu\Theta(\mu - h) + \frac{m}{2\pi\hbar^2}(\mu + h)\Theta(h - \mu),$$

$$m_N = \frac{m}{\pi\hbar^2}h\Theta(\mu - h) + \frac{m}{2\pi\hbar^2}(\mu + h)\Theta(h - \mu).$$

The heaviside functions divide the phase diagram into three normal phases (Fig. 10.3 b): For  $\mu < -h$  the density is  $n_{N,\text{total}} = 0$  and the ground state is the vacuum. For  $-h < \mu < h$ , only the last term is nonzero. In this phase only spin-up fermions are present; the system is fully polarized. The remaining region ( $\mu > h$ ) in the parameter space is a partially polarized normal state<sup>71</sup>, with a polarization of

$$P_{\text{PP}}(h) = m_N/n_{N,\text{total}} = h/\mu = h/E_F. \quad (10.4)$$

To construct the full phase diagram, we determine if for a given set of  $(\mu, h)$  either the normal phase or the superfluid phase is the ground state, i.e. has the lowest grand potential. For that we find the line in the  $(\mu, h)$ -parameter space where  $\Omega_{\text{SF}}(\mu, h) = \Omega_{\text{N}}(\mu, h)$ , which separates both phases. Solving this equation<sup>72</sup> gives us a critical field [183]

$$h_c(\mu) = \sqrt{E_B \left( \mu + \frac{E_B}{4} \right)} \Theta(\mu - h_0) + \left[ (\sqrt{2} - 1)\mu + \frac{E_B}{\sqrt{2}} \right] \Theta(h_0 - \mu), \quad (10.5)$$

where  $h_0 = (\sqrt{2} + 1)E_B/2$  separates between the partially ( $\mu > h_0$ ) and fully polarized normal phase ( $\mu < h_0$ ). This line is plotted both in Fig. 10.3 a and Fig. 10.3 b.

We assemble the final phase diagram by taking into account the superfluid phase for  $h < h_c(\mu)$  and the normal phases for  $h > h_c(\mu)$  (Fig. 10.3 c). The phase diagram has four phases: The vacuum, the fully polarized phase, the partially polarized phase, and the balanced superfluid phase.

This phase diagram allows us, as is done in Sec. VI in [183] in detail, to predict the radii at which phase transitions occur for an imbalanced gas in a harmonic trap. Here, the number of particles  $N_1$  and  $N_2$  instead of  $\mu$  and  $h$  are fixed but the locally varying chemical potential allows us to consider the trap as a collection of grand canonical ensembles that can exchange particles with each other. Therefore, the total number of trapped particles  $N_1$  and  $N_1$  can be related to a spatially varying chemical potential  $\mu(r) = \mu_0 - m\omega^2 r^2/2$  and a constant Zeeman field  $h$  throughout the trap. The observed phases in the harmonic trap then simply lie on a line with  $h = \text{const}$  and  $\mu = \mu(r)$ , as indicated by an arrow in Fig. 10.3 c. The center of the trap corresponds to the rightmost point of the arrow. Here, the gas is balanced and in the superfluid phase. An increasing radius in the harmonic trap corresponds to a decreasing local chemical potential. Thus, we enter above a certain radius a region where the gas becomes normal and fully polarized. Further out, the beginning of the vacuum phase marks the outer rim of the trapped gas. In general, the excess

<sup>71</sup> We group the balanced normal state ( $h = 0$ ) into the a partially polarized normal phase. For this case we get as expected  $n_{N,\text{total}} = \mu m/(\pi\hbar^2)$  and  $m_N = 0$

<sup>72</sup> We note here for later consideration that this condition is equivalent to having the same pressure in both phases because of  $\mathcal{P}(\mu, h, \Delta) = -\Omega(\mu, h, \Delta)$ .

majority atoms are always located in the outer normal shell(s) because the superfluid phase does not tolerate any imbalance. Thus, the magnetization jumps from 0 to a finite value at the radius where the superfluid to normal transition occurs. This is characteristic of a first-order phase transition and, as discussed in Sect. 7.2, has been experimentally observed in 3D imbalanced Fermi gases [162].

#### SEMIGRAND CANONICAL ENSEMBLE WITH FIXED $n_{\text{total}}$ AND $h$

To obtain the phase diagram where both the density and the particle imbalance are fixed, we now consider as a first step a system where the total atoms density  $n_{\text{total}}$  is constant instead of its conjugate variable, the chemical potential  $\mu$ . The second variable, the Zeeman field  $h$  remains for now as an external parameter. To construct the phase diagram, we minimize a new thermodynamic potential, the free energy, of both the superfluid and normal phase. Then, we discuss how a third phase, a phase-separated state, arises. Finally, we construct the phase diagram of all three phases.

The system considered here with constant atom density and fixed Zeeman field  $h$  is very particular, as we remove the external reservoir that has a defined chemical potential  $\mu$  the gas could use to exchange particles. Thus, with respect to the conjugate pair  $(\mu, n_{\text{total}})$  we go from a grand canonical ensemble to a canonical ensemble.

On the other hand, we still allow the system to flip spins and settle on a magnetization  $m = n_1 - n_2$  as it prefers because of the fixed Zeeman field  $h$ . The fixed Zeeman field  $h$  can be understood as a reservoir, which the system can use to exchange a spin-down particle with a spin-up particle at a cost  $h$ . Thus, with regard to the conjugate pair  $(h, m)$  the system is still in a grand canonical ensemble. Therefore, this type of system is also called *semigrand* canonical ensemble [188].

To obtain the phase diagram for this ensemble the free energy defined by

$$\mathcal{F}(n_{\text{total}}, h) = \mu n_{\text{total}} - \mathcal{P}(\mu, h) \quad (10.6)$$

must be minimized. For that, we first have to express the chemical potential for the superfluid and the normal phase in terms of the density  $n_{\text{total}}$ . For convenience, we use in the following the Fermi energy instead, which depends on the total density by  $E_F = \hbar^2 2\pi n_{\text{total}} / (2m)$ . One obtains a chemical potential of

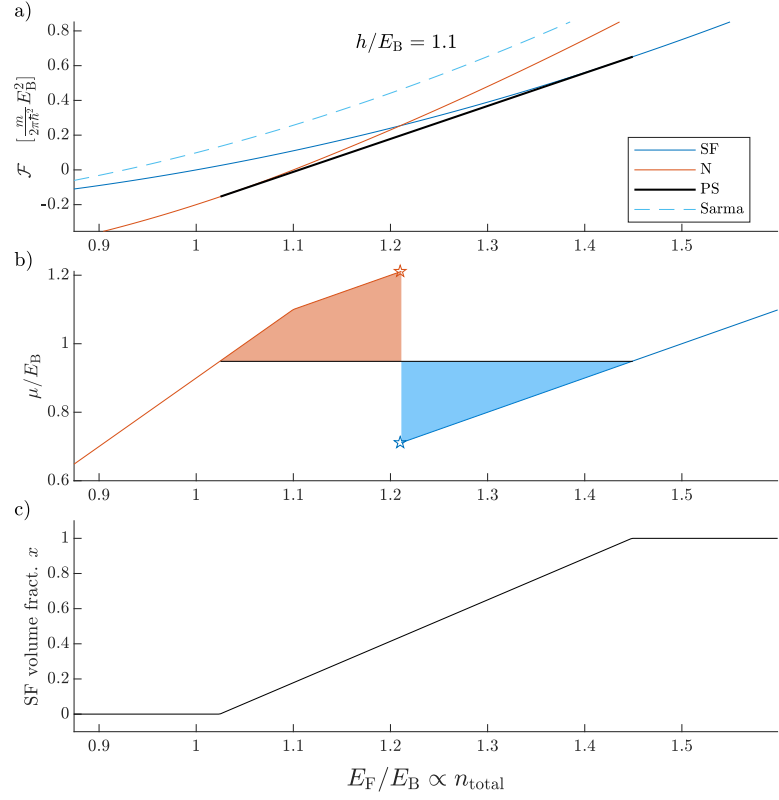
$$\mu_{\text{SF}}(E_F) = E_F - \frac{E_B}{2}$$

for the superfluid phase, and

$$\mu_{\text{N}}(E_F) = E_F \Theta(E_F - h) + (2E_F - h) \Theta(h - E_F)$$

for the normal phase [183]. If we insert these relations into the definition of the free energy (Eq. 10.6) and use the grand potential of the superfluid (Eq. 10.2) and normal phase (Eq. 10.3), respectively,

**Figure 10.5:** (a) In the semigrand canonical ensemble the free energy of the gas is minimized. Here, we show the free energy for a fixed Zeeman field  $h = 1.1 E_B$  and varying total densities. If only the superfluid and normal phases were possible, the transition from the superfluid to the normal phase would occur in this example at  $E_{F,c} = 1.21 E_B$ . However, around this critical Fermi energy there exists a third phase which has a lower free energy: A phase-separated state in which a part of the total volume is superfluid and another part is normal. (b) In a phase transition from a homogeneous normal phase to a homogeneous superfluid phase, the chemical potential would jump from the red star to the blue star, which indicates that these phases are unstable towards a phase-separated state. The chemical potential of this state can be constructed with a Maxwell construction, where we construct its chemical potential graphically by finding a horizontal line such that the red and blue areas are equal. (c) The volume fraction of the superfluid phase continuously increases in the phase-separated state. It approaches 1 when the phase-separated state smoothly transitions into the superfluid phase.



we get [183]

$$\mathcal{F}_{\text{SF}}(E_F) = \frac{\hbar^2}{2\pi m} (E_F^2 - E_B^2),$$

$$\mathcal{F}_{\text{N}}(E_F, h) = \frac{\hbar^2}{2\pi m} [(E_F^2 - h^2)\Theta(E_F - h) + 2(E_F^2 - h)\Theta(h - E_F)].$$

If these two phases, the homogeneous superfluid and the homogeneous normal phase, were the only possible phases, a first-order transition would occur if both free energies are equal at a critical Fermi energy of

$$E_{F,c}(h) = \frac{h^2}{E_B} \Theta(h - E_B) + (2h - E_B)\Theta(E_B - h),$$

<sup>73</sup> We solve  $E_{F,c}(h_c) = E_F$  for  $h_c$ .

or equivalently<sup>73</sup>, at a critical Zeeman field

$$h_c(E_F) = \sqrt{E_B E_F} \Theta(E_F - E_B) + \frac{1}{2}(E_F + E_B)\Theta(E_B - E_F).$$

The latter expression is the CC limit or Pauli limit. For the range  $E_B < E_F$ , it agrees with the 3D result in the BCS limit,  $h_c = \sqrt{E_B E_F} = \Delta/\sqrt{2}$ . The free energy of both phases are plotted in Fig. 10.5 a exemplary for a constant  $h/E_B = 1.1$  demonstrating that a phase transition should occur at a critical Fermi energy  $E_{F,c} = 1.21 E_B$ .

However, there is a third phase, the phase-separated state, in addition to the two previously mentioned phases. For that we examine the chemical potential of the normal and superfluid phase at the transition point  $E_F = E_{F,c}$  (Fig. 10.5 b). We notice that there is a jump from

$\mu_N(E_{F,c})$  to a smaller  $\mu_{SF}(E_{F,c})$ . At this point, the derivative  $\partial\mu/\partial n$  is negative, which means that it is favorable for both phases to increase their density to decrease the total energy. Therefore, the system is unstable towards phase separation. This results in a phase-separated state where a part of the total volume is in the superfluid phase and another part in the normal phase.

The condition for phase separation is that the pressure of the superfluid and the normal phase are the same,

$$\mathcal{P}_{SF}(\mu_{PS}) = \mathcal{P}_N(\mu_{PS}, h).$$

This condition can be solved analytically to find a constant<sup>74</sup> chemical potential [183],

$$\mu_{PS}(h) = \left( \frac{h^2}{E_B} - \frac{E_B}{4} \right) \Theta(h - h_0) + \frac{\sqrt{2}h - E_B}{2 - \sqrt{2}} \Theta(h_0 - h).$$

Alternatively, the chemical potential of the phase-separated state can be found using a Maxwell construction (Fig. 10.5 b). In this technique, the value of the chemical potential in the phase-separated state is found by constructing a horizontal line in the plot of  $\mu$  vs.  $n_{\text{total}}$  such that the red and blue area in Fig. 10.5 b become equal.

The phase separation creates a smooth transition from a fully normal to a fully superfluid gas as shown in Fig. 10.5 c. For an increasing total density, a larger and larger part of the system becomes superfluid until the superfluid phase is reached. We confirm that the phase-separated state is indeed the ground state by plotting its free energy in Fig. 10.5 a, which is given by

$$\mathcal{F}_{PS}(E_F, h) = \mu_{PS}(h)n_{\text{total}}(E_F) - \mathcal{P}(h)$$

where  $\mathcal{P}(h) = \mathcal{P}_{SF}(\mu_{PS}(h))$ .

With all three possible phases discussed, we can now construct the phase diagram for fixed  $E_F$  and  $h$ . In the experiment, commonly not the density (and thus Fermi energy) but the binding energy  $E_B$  is varied to change the interaction strength. Therefore, we use  $h/E_F$  and  $\eta = E_B/E_F$  as the axes for the phase diagram.

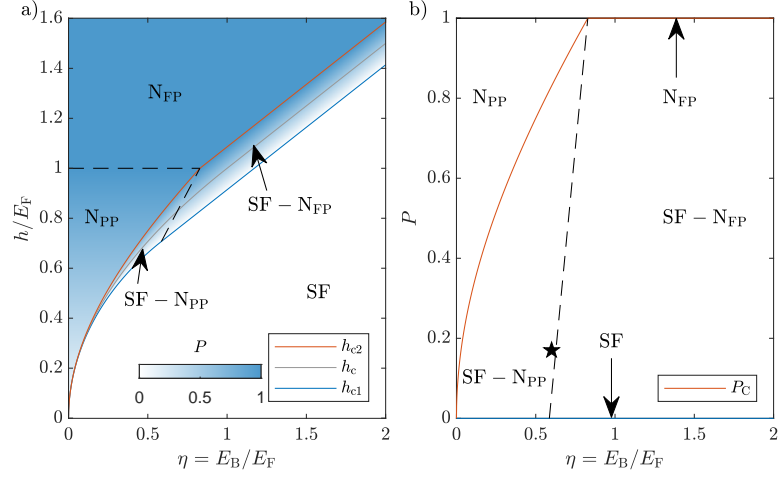
For the phase diagram, we need to find two critical Zeeman fields  $h_{c1}$  and  $h_{c2}$  that separate the different phases. The first one separates the superfluid phase and the phase-separated state. A transition from one phase to the other occurs when both chemical potentials are equal  $\mu_{PS}(h, E_B) = \mu_{SF}(E_F, E_B)$ . This condition can be solved for  $h$  to obtain the critical field  $h_{c1}(\eta)$ . The second critical field  $h_{c2}(\eta)$  marks the transition the phase-separated state to the normal phase and can be obtained by solving  $\mu_{PS}(h, E_B) = \mu_N(h, E_F)$  for  $h$ . The explicit definition for both critical fields can be found in Eq. 22 in Ref. [183].

Using both critical fields we construct the resulting phase diagram in Fig. 10.6 a. The balanced superfluid phase exists at low Zeeman fields  $h$ . Its critical field  $h_{c1}$  decreases for decreasing binding energies because the excitation gap protecting the superfluid state becomes smaller. Above this critical field, two phase-separated states exist.

<sup>74</sup>It is constant with respect to  $E_F$ , it however depends on the second independent parameter  $h$ .

We also show in Fig. 10.5 a the free energy of the Sarma phase. Its free energy is greater than that of all other phases demonstrating that it is a metastable state in the semigrand canonical as well.

**Figure 10.6:** (a) Phase diagram for the semi-grand canonical ensemble with fixed  $h$  and  $n_{\text{total}}$ . We encode these two degrees of freedom in the parameters  $h/E_F$  and  $\eta = E_B/E_F$ . In this ensemble, in between the critical fields  $h_{c1}$  and  $h_{c2}$ , two new phase-separated states appear. These have spatially separated normal and superfluid phases. The color scale shows the global polarization of the respective phases. The critical field  $h_c$  would mark the transition from the superfluid to the normal phase if phase separation would not occur. (b) Phase diagram for the canonical ensemble with fixed global polarization  $P = (N_1 - N_2)/(N_1 + N_2)$  and total density  $n_{\text{total}}$ . It can be obtained by scaling the y-axis of the semigrand canonical phase diagram according to its global polarization. The superfluid and fully polarized phases are reduced to a line at  $P = 0$  and  $P = 1$ , respectively. For  $P > P_c$  all superfluid domains disappear. The black star indicates our experimental parameters.



For low binding energies, superfluid domains coexist with partially polarized normal domains (SF– $N_{PP}$ ) while at larger binding energies, superfluid domains coexist with fully polarized normal domains (SF– $N_{FP}$ ). Above the critical field  $h_{c2}$  the system transitions into the partially polarized ( $N_{PP}$ ) and fully polarized phase ( $N_{FP}$ ).

Fig. 10.6 a shows in addition the global polarization in a color scale. In the superfluid phase, which extends up to  $h = h_{c1}$ , the global polarization is zero. In the phase-separated state ( $h_{c1} < h < h_{c2}$ ), the global polarization increases continuously and follows [183]

$$P_{PS}(h) = 2 \frac{h^2 - h_{c1}^2}{E_F E_B^2} \Theta(h - h_0) + \frac{(\sqrt{2} + 1)^2 (h - h_{c1}(\eta))}{E_F} \Theta(h_0 - h). \quad (10.7)$$

The polarization of the partially polarized phase follows Eq. 10.4.

#### CANONICAL ENSEMBLE WITH FIXED $n_{\text{total}}$ AND IMBALANCE $P$

As the last step, we now exchange the second parameter, the Zeeman field  $h$  with its conjugate variable, the particle imbalance  $P = (N_1 - N_2)/(N_2 + N_1)$ . This ensemble describes the imbalanced gas with a fixed number of particles in both spin states  $N_1$  and  $N_2$  prepared in our experiment. In the following, we derive the phase diagram, which is a fast process as it only requires rescaling the y-axis of the previous phase diagram. Finally, we discuss that a phase-separated state with a partially-polarized normal and superfluid phase is predicted for the imbalanced gas prepared and analyzed in the last chapter.

The free energy of the canonical ensemble is

$$\mathcal{F}(n_{\text{total}}, P, \Delta) = \mu n_{\text{total}} - hP - \mathcal{P},$$

which we would have to minimize repeating the procedure we followed for the previous statistical ensembles. However, this is not necessary, since there exists a well-defined and unambiguous relationship between the imbalance  $P$  and Zeeman field  $h/E_F$  for a given interaction strength  $\eta = E_B/E_F$  (Eq. 10.7 and color scale in Fig. 10.6 a).

Thus, the number of phases does not change when going from the semigrand canonical to the canonical ensemble and we can simply obtain the phase diagram by mapping the Zeeman field  $h$  to the particle imbalance  $P$  in a  $\eta$ -dependent way. The resulting phase diagram is shown in Fig. 10.6 b.

We find that the superfluid and fully polarized phases are reduced to lines at  $P = 0$  and  $P = 1$  in this ensemble. In between, the phase-separated states  $SF - N_{PP}$  and  $SF - N_{FP}$  dominate the phase diagram. The critical field  $h_{c2}$ , where the phase-separated state transitions into the normal partially-polarized phase in the semigrand canonical ensemble, is mapped to a critical imbalance defined by [183]

$$P_C = P_{PS}(h = h_{c2}) = \sqrt{\eta \left(1 + \frac{\eta}{4}\right)} \Theta(\eta_2 - \eta) + \Theta(\eta - \eta_2),$$

which is depicted as a red line in Fig. 10.6 b.

This phase diagram allows us to make a comparison with the experimental data of our quasi-2D system. We consider the system with densities  $n_1 = 1.55 \mu\text{m}^{-2}$ ,  $n_2 = 1.1 \mu\text{m}^{-2}$ , and global polarization  $P = 0.17 \pm 0.06$ , which we have examined in Sect. 9.1. Its effective 2D interaction strength is  $\eta = \ln(k_F a_{2D}) = 0.6$  which corresponds using Eq. 4.2 to a binding energy of

$$\frac{E_B}{E_F} = \frac{2}{a_{2D}^2 k_F^2} = 2e^{-2\eta} = 0.6$$

The corresponding point in the phase diagram lies within the  $SF - N_{PP}$  separated state (black star in Fig. 10.6 b).

In our experiment, we do not observe phase separation, but a homogeneous polarization throughout the cloud, which shows indications of superfluidity. Apparently, the  $T = 0$  mean-field description of the 2D BEC-BCS crossover cannot explain an imbalanced superfluid phase but predicts phase separation instead. Therefore, we discuss in the following the limitations of this approach, namely beyond mean-field effects, more exotic phases, and the neglect of finite temperatures.

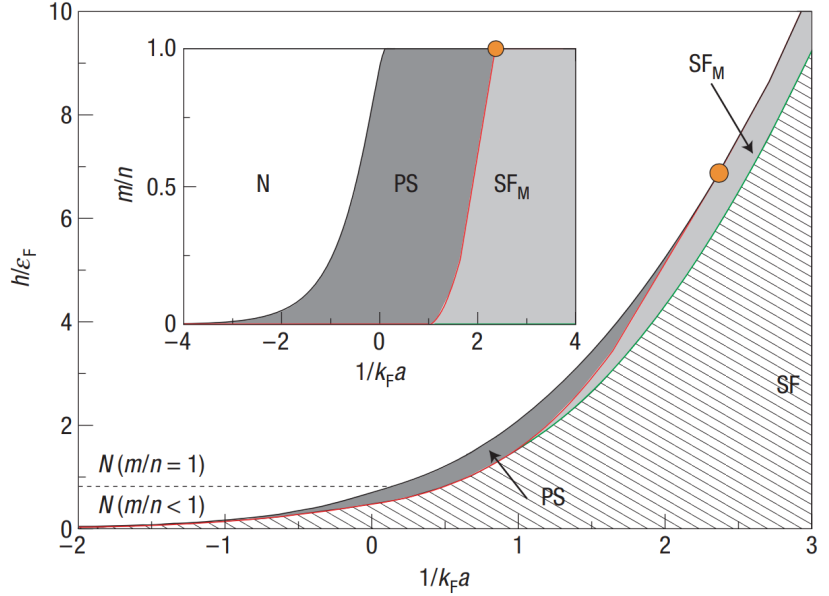
## 10.2 Beyond mean-field in the BEC regime

If we compare the 2D mean-field imbalanced phase diagram to a 3D mean-field phase diagram (inset of Fig. 10.7), we notice a qualitative difference. In 3D mean-field theory, a phase where excess fermions can mix with the condensate of bosonic dimers is predicted in the BEC regime, which is called *magnetized superfluid* ( $SF_M$ ). This phase is a Fermi-Bose mixture<sup>75</sup>, where the excess majority fermions coexist with the bosonic superfluid. It would be a candidate for the phases we observe because it is locally imbalanced but superfluid. In the following, we discuss why it is missing in the mean field phase diagram and derive its location in the phase diagram by considering dimer-atom and dimer-dimer interactions. We will find that this phase is located deep within the BEC regime at large binding energies and cannot explain an imbalanced superfluid in the crossover regime.

<sup>75</sup> The fact, that this is a Bose-Fermi mixture has been used in [164] to experimentally verify the dimer-dimer and dimer-atom scattering length,  $a_{dd} = 0.6a$  and  $a_{ad} = 1.18a$  in a 3D gas.

Despite the absence of a Fermi surface of the minority species, this system can be understood as the BEC limit of the Sarma phase [183, 187].

**Figure 10.7:** Mean-field phase diagram of a 3D spin-imbalanced Fermi gas at  $T = 0$  in the semigrand canonical ensemble. In the BEC regime, a phase where excess fermions can enter the bosonic superfluid phase is possible, a *magnetized superfluid* ( $SF_M$ ). This phase is absent in the 2D mean-field phase diagram. The inset shows the phase diagram in the canonical ensemble with fixed polarization  $P = m/n$ . Adapted from [171].



<sup>76</sup> Similarly, the speed of sound does not approach zero as the dimer-dimer repulsion becomes weaker but is constant  $v_s = v_F/\sqrt{2}$ , which contradicts the experimental evidence presented in Sec. 5.1.

The absence of the magnetized superfluid phase in 2D mean-field theory is related to the greater importance of beyond mean-field terms in the 2D BEC limit. Even for balanced gases, we notice that for instance the reduced chemical potential<sup>76</sup> does not approach zero in the BEC regime but stays constant,  $\tilde{\mu} = \mu + E_B/2 = E_F - E_B/2 + E_B/2 = E_F$ . On the contrary, in 3D, mean-field theory predicts that the reduced chemical potential approaches zero in the BEC limit which shows that it is adequate to describe the BEC-BCS crossover qualitatively (see Fig. 2.4 on p. 17).

Mean-field theory fails in the 2D BEC limit because any dimer-dimer or atom-dimer interactions are absent [146]. The underlying reason for this is that fluctuations play a greater role in lower dimensions [189, 190]. In lower dimensions, particles have fewer neighbors they interact with and therefore the interaction does not average out as much. Hence, considering just the average interaction is less reliable and, therefore, results in a complete neglect of any dimer-dimer and atom-dimer interactions in 2D. For balanced 2D gases, these issues have been resolved by extending the theory beyond the mean field level by considering pair fluctuations in the number equation [190, 191].

<sup>77</sup> As an approximation we use here an expression for the total energy which does not take higher orders in both coupling constant  $g_{BF}$  and  $g_{BB}$  into account. This approximation slightly underestimates the total energy in the crossover regime. Thus, the resulting critical binding energy is only approximately correct.

For imbalanced 2D gases, we extend the phase diagram by manually taking the dimer-dimer and dimer-atom interaction into account following Ref. [184]. For that we consider the energy of a Fermi-Bose mixture, where the bosonic density equals the minority density,  $n_B = n_\downarrow$ , and the fermionic density the excess density  $n_{F,\text{exc.}} = n_\uparrow - n_\downarrow$ . The total energy<sup>77</sup> of the Fermi-Bose mixture is given by

$$E = \frac{\alpha}{2} n_{F,\text{exc.}}^2 + \frac{g_{BB} n_B^2}{2} + g_{BF} n_B n_{F,\text{exc.}}, \quad (10.8)$$

with  $\alpha = 2\pi\hbar^2/m$  and the dimer-dimer interaction strength [112]

$$g_{\text{BB}} = \frac{\hbar^2}{m_{\text{d}}} \frac{-4\pi}{\log(k_{\text{F}}^2 a_{\text{dd}}^2) - \log(4\pi)} \quad (10.9)$$

with  $m_{\text{d}} = 2m$  and dimer-atom interaction strength [146]

$$g_{\text{BF}} = \frac{\hbar^2}{m_{\mu}} \frac{-2\pi}{\log(k_{\text{F}}^2 a_{\text{ad}}^2) - \log(4\pi)} \quad (10.10)$$

with the reduced mass  $m_{\mu} = \frac{2}{3}m$ . We use the relations  $a_{\text{dd}} = 0.55 a_{2\text{D}}$  [146, 192] and  $a_{\text{ad}} = 1.26 a_{2\text{D}}$  [193] for the dimer-dimer and dimer-atom scattering length, respectively. Here,  $a_{2\text{D}}$  is the atom-atom scattering length introduced in chapter 4.

The phase, in which bosons and fermions coexist, the *miscible phase*, is more stable than the phase-separated state if the energy is a minimum with respect to both densities  $n_{\text{F,exc}}$  and  $n_{\text{B}}$ . The necessary condition for that is that the matrix  $H_{i,j} = \partial^2 E / \partial n_i \partial n_j$  with  $i, j \in \{\text{B}, \text{F}\}$  has a positive determinant [184]. This condition is

$$\alpha g_{\text{BB}} - g_{\text{BF}}^2 > 0 \rightarrow \alpha g_{\text{BB}} > g_{\text{BF}}^2. \quad (10.11)$$

Taking these insights from Ref. [184] we can now extend the phase diagram. The identity  $k_{\text{F}}^2 a_{2\text{D}}^2 = 2E_{\text{F}}/E_{\text{B}}$  allows us to express both  $g_{\text{BB}}$  and  $g_{\text{BF}}$  in terms of  $E_{\text{B}}/E_{\text{F}}$ . If we plot both the LHS and RHS of the inequality (Eq. 10.11) we find that the miscible phase becomes unstable towards phase separation for  $E_{\text{B}}/E_{\text{F}} < 7.28$  (Fig. 10.8).

The condition for a miscible Bose-Fermi mixture in 2D (Eq. 10.11) does not depend on the density of the excess fermions  $n_{\text{F,exc}}$  and thus not on the polarization  $P$ . The consequence is that as soon as the condition  $E_{\text{B}}/E_{\text{F}} > 7.28$  is reached an arbitrary number of excess fermions are miscible in the superfluid dimer phase. This results in a straight vertical line in the  $P$  vs.  $E_{\text{B}}/E_{\text{F}}$  phase diagram (Fig. 10.9).

This behavior differs from the situation in 3D, where in a certain interaction range the magnetized superfluid has a critical polarization which is smaller than one (see red line in the inset of Fig. 10.7).

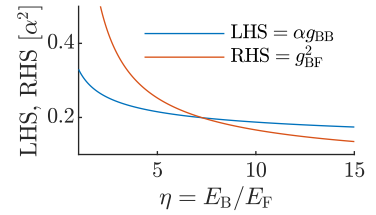
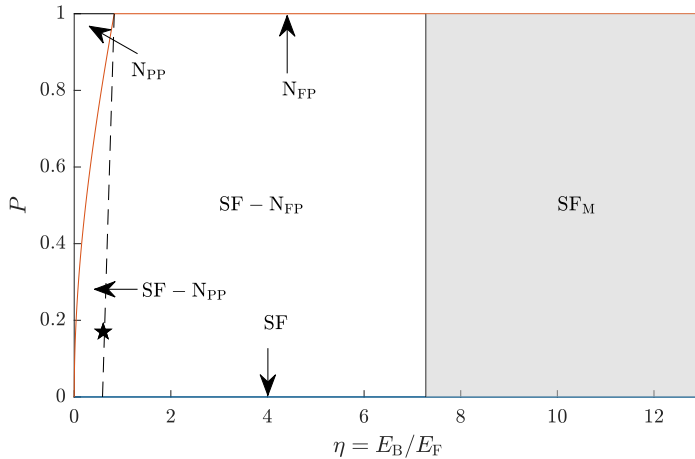
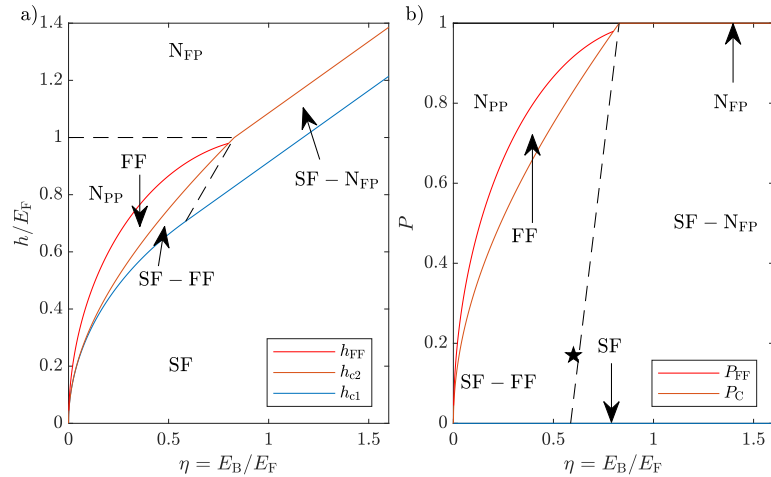


**Figure 10.8:** The miscibility condition  $g_{\text{BB}}\alpha > g_{\text{BF}}^2$  for a Bose-Fermi mixture consisting out of dimers and excess fermions is only fulfilled for  $E_{\text{B}}/E_{\text{F}} > 7.28$ .

**Figure 10.9:** Canonical phase diagram taking account the magnetized superfluid phase at large binding energies  $E_{\text{B}}/E_{\text{F}} > 7.28$ .

**Figure 10.10:** Mean-field phase diagram for an imbalanced 2D Fermi gas including the FF phase.



The reason for that is that if we did the analogue derivation of the miscibility condition for a 3D Bose-Fermi mixture a dependence on  $n_{F,exc.}$  would remain due to the  $n^{2/3}$  scaling of the Fermi energy in 3D.

In conclusion, we see here that the absence of the magnetized superfluid in the mean-field calculations is not an intrinsic property of 2D but shows us how crucial beyond-mean-field terms are in two dimensions [184]. We notice that the critical binding energy required for the miscible phase is much larger than the effective binding energy in our experiment. We can thus exclude a Bose-Fermi mixture as a possible explanation for the observed phase.

### 10.3 Exotic phases

In our search for possible phases we have taken up to now the superfluid, normal, and Sarma phases into consideration but ignored other more exotic phases. Some of them belong to the family of FFLO phases [172, 194, 195] that have in common that the order parameter has a spatial periodicity. In the following, we review the mean-field phase diagram where the phase proposed by Fulde and Ferrel (FF)[147] has been taken into account. Its order parameter has the form

$$\Delta(\mathbf{x}) = \Delta_0 \exp(i\mathbf{q} \cdot \mathbf{x}),$$

where the wavevector  $\mathbf{q} = \mathbf{k}_{F,\uparrow} - \mathbf{k}_{F,\downarrow}$  can be interpreted as the center-of-mass momentum of the Cooper pairs. We find that this phase replaces the partially polarized phase in some parts of the phase diagram, resulting in a pure FF phase at large imbalances and a phase-separated state SF – FF, where both the superfluid and FF phase coexist.

The mean-field calculations for a 2D imbalanced Fermi gas were done in Ref. [196]. In the semigrand canonical ensemble, where both  $E_F$  and  $h$  are fixed, the FF to PP transition happens at a critical Zeeman

field of

$$h_{\text{FF}} = \sqrt{2E_{\text{F}} - E_{\text{B}}}. \quad (10.12)$$

This translates to a critical polarization  $P_{\text{FF}} = h_{\text{FF}}/E_{\text{F}}$  in the canonical ensemble, where the Fermi energy  $E_{\text{F}}$  and polarization  $P$  are fixed.

The resulting phase diagrams for the semigrand and canonical ensemble are shown in Fig. 10.10. The FF state exists for small binding energies in a horn shaped area where previously the partially polarized phase was located<sup>78</sup>. The transition to the partially polarized phase is of second order [197, 198] such that no phase-separated  $N_{\text{pp}} - \text{FFLO}$  state occurs. The transition between the SF and FF phase is, however, of first order [197, 198] resulting in a SF – FF phase-separated state.

Larkin and Ovchinnikov (LO) proposed a second ansatz in which the order parameter consists of two opposite plane waves and follows  $\Delta(\mathbf{x}) = \Delta_0 \cos(\mathbf{q} \cdot \mathbf{x})$ . This ansatz and higher plane-wave FFLO states result in states with a slightly lower total energy than the FF state but are more complicated to calculate [194]. They occupy a similar region as the FF state in the phase diagram<sup>79</sup>. Interestingly, in this phase, the order parameter crosses zero with periodicity  $\delta x = 2\pi/q$ . At these zero crossings, the effective repulsion of the paired atoms is not as strong, such that the excess majority atoms accumulate at these nodal lines. This would correspond, to a periodicity of  $\delta x = 9 \mu\text{m}$  for a polarization of  $P = 0.17$  which is above the resolution of our imaging setup. However, we do not see any sign of such a density accumulation in the absorption images of state 1.

In general, the FFLO state is challenged by effects beyond the mean field which arise at finite temperature. A study of the effect of finite temperature in 2D on FFLO states showed that phase fluctuations have a strong effect on the stability of the FFLO state, resulting in very low critical temperatures [198]. Along similar lines, another recent study suggests that pairing fluctuations lead to an instability of any FFLO states in three and two dimensions [199].

The FFLO theory can be extended to non-exclusive or communal pairing between majority and minority atoms, resulting in a state that has condensate fraction peaks at multiple momenta [200]. In addition, various other interesting phases have been predicted for 2D imbalanced Fermi gases, which we do not discuss here. These include the existence of the Sarma phase if phase fluctuations are taken into account in the BCS regime at  $T = 0$  [201] and triplet p-wave pairing which is driven by the Kohn-Luttinger mechanism where minority fermions experience an effective attractive interaction due to the polarization of background majority atoms [113].

#### 10.4 Finite temperature phases

In this section, we discuss the effect of finite temperature on the phase diagram. We point out that in 3D, finite temperature allows for a BCS state with a finite imbalance which crosses over into a stable finite-temperature realization of the Sarma phase. Then, we review finite-

<sup>78</sup> There is a small intrusion into the superfluid phase we do not consider here.

<sup>79</sup> See Fig. 7 in Ref. [194]

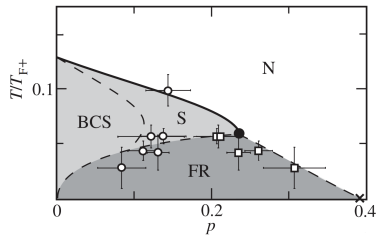


**Figure 10.11:** The phase diagram of the 3D unitary Fermi gas. At zero temperature, a first-order transition results in a forbidden region (FR) where phase separation occurs. Here, the BCS state does not tolerate any imbalance. For finite temperatures, however, the BCS state crosses over into a gapless Sarma phase (S), which happens at the line  $h = \Delta$  (dashed line within bright gray area). Adapted from Chap. 13 in [9].

<sup>80</sup> For temperatures above the tricritical point, the transition occurs also at a finite imbalance but becomes second order.

temperature calculations done in the 2D BCS limit, which show a similar behavior making it plausible that we prepared an imbalanced finite-temperature superfluid.

To start, we revisit the experimental evidence in 3D. Here, studies of spin-imbalanced unitary Fermi gases (Fig. 10.11, see also Fig. 7.3a) showed that the central superfluid core in a harmonic trap can tolerate a finite polarization before a first-order<sup>80</sup> transition to the outer normal shell occurs. The reason for the tolerance of an imbalance is that at finite temperature the balanced superfluid coexists with thermal excitations. These thermal quasiparticle excitations can be spin-imbalanced and thus carry some excess majority atoms [162, 171].

For large imbalances  $P$  the corresponding value of the Zeeman field  $h$  of the system can become larger than the excitation gap  $\Delta$  such that the condition  $h < \Delta$  for the BCS state is not fulfilled. At  $T = 0$  a possible but unstable phase for  $\Delta > h$  is the Sarma phase, which is visualized in Fig. 10.4 on p. 99. The Sarma phase contains a population of quasiparticle excitations in the ground state at the Fermi surface. At finite temperature, the Sarma phase can become stable such that a transition into this phase can happen at  $h = \Delta$ . This is indicated by the dashed line in the bright gray area in Fig. 10.11. The quasiparticle excitations present in the Sarma phase can be further excited at arbitrarily low energies, resulting in a gapless superfluid [185].

The transition between the imbalanced BCS phase and the Sarma phase is a crossover because the Fermi surfaces in both phases are smoothed out due to temperature [185]. Since it is a crossover where both phases are superfluid but support an imbalance we can refer to both as an imbalanced finite-temperature superfluid with a constant order parameter.

For 2D spin-imbalanced Fermi gases, finite temperature calculations were done in Ref. [202] using a Gaussian pair fluctuation approach<sup>81</sup>. These calculations are shown in Fig. 10.12. We see in the inset that the superfluid phase can tolerate a spin-imbalance to a certain degree at finite temperatures (blue region). The available calculations extend up to a maximum binding energy  $E_B/E_F = 0.1$ . At this binding energy the polarization of the superfluid phase reaches a maximum of  $P \approx 0.07$  at  $T \approx 0.07 T_F$ . We expect that the highest possible polarization increases towards larger binding energies because this phase must smoothly connect to the  $T = 0$  magnetized superfluid phase ( $SF_m$ ) discussed in Sect. 10.2, which supports polarizations  $P$  in the range  $[0, 1)$ .

Our experimental data are taken at an interaction strength of  $E_B/E_F = 0.6$ , which is larger than the maximum binding energy of  $E_B/E_F = 0.1$  in these calculations. The overall trend towards larger binding energies makes it plausible that the  $P = 0.17$  gas could be an imbalanced finite-temperature superfluid where the finite temperature of  $T = 0.05 T_F$  might be responsible for the absence of phase separation. However, as we do not know the exact critical polariza-

<sup>81</sup> This is a path-integral calculation which takes phase fluctuations into account. For more details on this approach we can recommend Chap. 16 in Ref. [203].

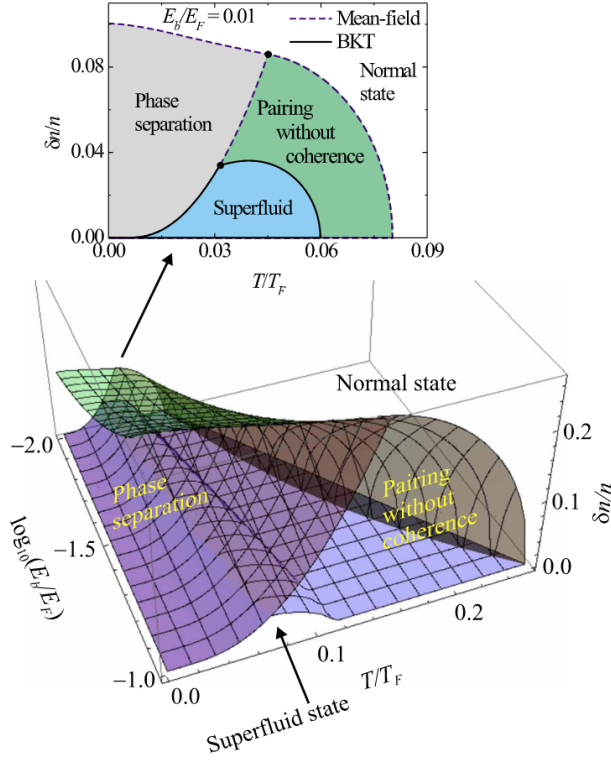


**Figure 10.12:** Finite-temperature Phase diagram of an imbalanced 2D phase diagram. If we fix for instance the interaction strength to  $E_B/E_F = 0.01$  (upper panel), we find at  $T = 0$  that a finite imbalance  $P = \delta n/n$  results in a phase-separated state (as in 3D, see Fig. 10.6 b). In the balanced limit ( $P = \delta n/n = 0$ ), the gas transitions at  $T_{\text{BKT}} \approx 0.06 T_F$  into a normal state where pairs are present but not coherent. If we allow both finite temperatures and finite imbalance, we see that the superfluid state can persist up to an imbalance of  $P = 0.04$  at  $T \approx 0.04 T_F$ . The three-dimensional plot (lower panel) shows that both the maximum temperature and maximum polarization of the superfluid state increases for with  $E_B/E_F$ . Adapted from [202].

tion at our interaction strength, we cannot exclude that our system is predicted to be in the imbalanced normal phase.

#### OPEN QUESTIONS

The discussion in this chapter gives rise to many open questions which can be addressed in the future. On the experimental side, a fully conclusive check of whether the gas is superfluid is missing. In addition, the phase diagrams indicate that larger polarizations might be required to observe a first-order transition. Furthermore, it would be advantageous to increase the vertical confinement to bring the gas fully into the 2D regime.

On the theory side, calculations covering beyond mean-field effects at finite temperature in 2D and possibly in the 2D to 3D crossover at strong interactions would be very helpful. Here, it is an open question whether the confinement-induced bound state that exists for all interaction strengths in 2D is properly included. This confinement-induced bound state also exists in 1D, where this has been taken into account for imbalanced Fermi gases [204]. They found that atoms tend to form zero-momentum confinement-induced bound states which compete with the FFLO phase. This suggests that this bound state should also be taken into account in 2D and its effect on the phase diagram should be studied. However, we are not aware of any 2D calculations that have addressed this aspect.



## CONCLUSION

In this thesis, I have presented studies of the excitation spectra of ultracold 2D and 3D fermionic superfluids trapped in box potentials.

The first main result of this thesis are measurements of the excitation spectrum of a 3D Fermi gas in the BEC-BCS crossover. We measured the low-energy excitation spectrum with full energy and momentum resolution using Bragg spectroscopy. We obtain comprehensive spectra that reveal single-particle and collective modes which offer us unprecedented insights into the many-body physics of the Fermi gas for varying interaction strengths and show how the character of the superfluid changes from bosonic to fermionic throughout the BEC-BCS crossover. One prominent feature are the collective sound modes. They continuously evolve from the bosonic limit, where they correspond to the well-known Bogoliubov excitations, to the fermionic limit, featuring an increasing slope and hence increasing speed of sound and a change of curvature.

In between both limits, we examine the unitary Fermi gas, which has been intensively studied because of its universal nature. Here, our spectra show how the collective mode merges into the second prominent feature of the excitation spectrum, the pair-breaking continuum. This pair-breaking continuum is gapped, showing directly how the ground state is protected against low-energy single-particle excitations. We confirm previous measurements of the pairing gap around the unitary point and extend them into the BCS regime. In this fashion, we provide quantitative measurements of an important quantity of the many-body system across the BEC-BCS crossover, which we use to benchmark theoretical calculations. We find excellent agreement with self-consistent T-matrix calculations in the BEC and crossover regime, but calculations taking particle-hole correlations into account agree better with our results in the BCS regime. Thus, our measurements show that the theoretical understanding is not fully conclusive yet and highlight potentials for further theoretical investigations.

A major focus of this thesis is on superfluidity in gases confined to two dimensions, where the motion in the third spatial dimension is frozen out. In two dimensions, quantum fluctuations play a more significant role compared to three dimensions, leading to a breakdown of long-range order. Quasi-long range order and hence superfluidity is only restored through the Berezinskii-Kosterlitz-Thouless (BKT) mechanism. I present studies performed in close collaboration with the lead PhD student on that project, Lennart Sobirey, in which we use Bragg spectroscopy to examine the critical velocity and the full excitation spectrum. Using the results from the first part, these measurements allow for a direct comparison of the pairing gap between two-dimensional and three-dimensional superfluids. Surpris-

ingly, we find that it is not dimensionality but rather strong interactions that seem to play a crucial role in achieving a large pairing gap.

The second major outcome of my thesis involves the preparation of a cold imbalanced Fermi gas in a box trap close to the 2D regime. Ultra-cold spin-imbalanced Fermi gases are of fundamental interest as they enable to study superfluidity in novel regimes which are hardly accessible in condensed matter systems. Control of the spin-imbalance represents an additional parameter to study the transition from the normal to the superfluid state as well as the stability and nature of the emerging superfluid. In two-dimensional systems there are fundamental open questions concerning the order of the phase transition from normal to the superfluid state and more importantly, the nature of the superfluid ground state. One key question is whether phases with spatially varying order parameters such as the elusive FFLO state can exist. Creating a spin-imbalance presents a significant challenge, as our imbalancing procedure leads to heating, and subsequent evaporation tends to balance the gas again. Despite these difficulties, we achieved the preparation of a cold spin-imbalanced gas close to the 2D regime.

Interestingly, the gas does not show any signs of phase separation, ruling out a first-order transition at the achieved temperatures and spin imbalances in stark contrast to the expected zero-temperature phase diagrams theoretically predicted. The measurement of the excitation spectrum indicates a nonzero critical velocity at small momenta but is not fully conclusive at large momenta. To classify the observed imbalance phase, we discuss the phase diagram of 2D imbalanced Fermi gases in the BEC-BCS crossover in detail. This analysis reveals that the prepared gas could be either in a finite-temperature superfluid phase with a constant order parameter, which allows for excess fermions in the form of thermal excitations, or that it could be in a normal imbalanced phase. In addition to its significance for the experimental findings presented, the comprehensive discussion of the phase diagrams serves as an overview for future research on 2D imbalanced Fermi gases.

## Outlook

The experimental apparatus used in this thesis is very flexible, allowing one to study many exciting topics in the future. Various optical potentials can be used to confine gases vertically (endcaps, static lattice, accordion lattice) and radially (DMDs, axicons) and to probe the gas dynamically (phase imprints, Bragg spectroscopy). In addition, a recent upgrade of the apparatus in the course of this thesis allows us to quickly install new optomechanical elements in the vicinity of the glass cell. In the following, I will give an outlook on selected fascinating topics that can be explored in the future.

*Spin-spin structure factor.* In this thesis we used Bragg spectroscopy to measure the response to a density perturbation. One can also study

the response to a spin-selective perturbation to measure the spin dynamic structure factor, which has been done at large momentum and energy [77]. However, a low-momentum and low-energy measurement of the spin dynamic structure factor is still missing. The key advantage of studying the response to a spin-dependent potential is that this perturbation would not couple to the collective mode, so that only the coupling to pair-breaking excitations should remain [46, 205]. This would simplify the extraction of the pairing gap at low momentum as its signal is not obscured by the collective sound mode present in our measurements of the density dynamic structure factor. This particularly affects systems where the detection of heating is more difficult due to a smaller condensate fraction, for example in balanced gases close to  $T_c$  or in spin-imbalanced gases. However, the small detuning required to imprint a spin-selective potential results in a large scattering rate making this method difficult to implement [70]. Here, an alternative method presented in Ref. [206] could be realized that creates a spin-dependent potential with light frequencies between the  $D_1$ - and  $D_2$ -lines, resulting in larger detunings and, therefore, smaller scattering rates.

*2D-3D crossover.* With the new accordion lattice installed during this thesis both the intensity and crossing angle of the lattice beams can be controlled. Therefore, the confinement strength and tunneling probability between adjacent layers can be tuned independently. This opens the way to study the crossover from two to three dimensions [207, 208] allowing us to measure the pairing gap, the behavior of collective modes, and to perform comparisons with theoretical predictions of the 2D-3D crossover [209].

*RF dressing* While developing the scheme to prepare imbalanced Fermi gases, we noticed that it might be possible to create long-lived two-component superfluids where one component is an RF-dressed state consisting of a coherent superposition of two hyperfine states. This could open the way to control the interaction strength using RF dressing [210] similar to experiments performed with bosons [211, 212]. If this technique can be established as an alternative way to tune the interaction strength, it would allow for a wide range of new experiments. As an example, a magnetic gradient could be used to locally change the effective detuning, resulting in a local change of the effective interaction strength. This would allow the realization of a spatial BEC-BCS crossover, which has been theorized for superconducting p-n junctions [213] and recently been observed in FeSe monolayers [214]. The interesting difference to previous experiments is that in this proposed in-situ realization of the BEC-BCS crossover the whole system is thermalized and at the same absolute temperature  $T$ . Thus, thermodynamic quantities, such as the chemical potential, could be extracted for varying interaction strengths but at a constant temperature.

*Imbalanced Fermi gases* Building and further improving on our preparation of imbalanced Fermi gases close to the 2D regime at unprecedentedly low temperatures, it is very tempting to investigate ex-

otic FFLO phases with spatial varying order parameter. These phases break the translational symmetry such that a second collective mode arises, which is gapless at  $q = 2q_{\text{FFLO}} = 2(k_{F,\uparrow} - k_{F,\downarrow})$  [215]. This mode is predicted to be coupled to both a density- and spin-dependent Bragg perturbation and thus should be visible in measurements of both the spin and density structure factor [215]. As the existence of FFLO phases is predicted only at very low temperatures, one could use these signatures of mode softening to study precursors of the FFLO state, where the energy of excitations is not gapless, but already reduced compared to the balanced case [195]. Another exciting avenue is to try to stabilize the FFLO state or the precursor state by increasing the nesting effect with an external static lattice [195].

For these experiments, different preparation schemes can be explored, e.g. schemes where one spin state is spilled with a magnetic gradient at low fields or with a narrow p-wave resonance of one particular spin state. This will allow us to increase the polarization for low temperatures, and this will open the way to observe phase separation and to map out the entire phase diagram.

Overall, we see that there are a variety of exciting topics that can be explored in the future using both balanced and imbalanced Fermi gases.

# A

## CALIBRATION OF AUXILIARY IMAGING SYSTEM

In order to reconstruct the 3D density of the gas loaded into the box potential from a 2D column density we need to determine the box height. For that, we perform absorption imaging from the side. In the following, we will calibrate the magnification of this imaging system using the Kapitza-Dirac effect. It consists of two measurements. In the first measurement, the static vertical 1D lattice used in Chap. 3 to create a 2D gas is projected through the imaging system to measure its periodicity  $d_{\text{px}}$  on the camera in units of pixel. The relationship to the periodicity at the atom position is given by

$$d = \frac{s_{\text{px}}}{M} d_{\text{px}}, \quad (\text{A.1})$$

where  $M$  denotes the magnification of the imaging system and  $s_{\text{px}} = 7.5 \mu\text{m}/\text{px}$  the camera pixel size.

In a second measurement, atoms trapped in one layer of the 1D lattice are subjected to a short pulse of the same lattice. If the pulse is sufficiently strong, we enter the Kapitza-Dirac regime, resulting in the imprinting of momenta  $p_z = \pm n 2\hbar k_{\text{latt.}} = \pm n 2\hbar 2\pi/(2d)$  on the atoms, where  $n$  denotes integers. These different classes can be distinguished after time of flight, as depicted in Fig. A.1. The velocity from the class of atoms with momentum  $2\hbar k_{\text{latt.}}$  in units of pixels can be measured and follows

$$v_{\text{px}} = \frac{M}{s_{\text{px}}} v = \frac{M}{s_{\text{px}}} \frac{2\hbar k_{\text{latt.}}}{m_d} = \frac{M}{s_{\text{px}}} \frac{\hbar 2\pi}{dm_d}. \quad (\text{A.2})$$

We obtain the final magnification by substituting Eq. A.1 into Eq. A.2 and solving for the magnification,

$$M = s_{\text{px}} \left( \frac{v_{\text{px}} d_{\text{px}} m_d}{2\pi \hbar} \right)^{1/2} = 6.85 \pm 0.03,$$

which corresponds to an effective pixel size

$$s_{\text{px}}/M = (1.0950 \pm 0.0005) \frac{\mu\text{m}}{\text{px}}.$$

This value is in agreement with the effective pixel size of

$$(1.14 \pm 0.17) \frac{\mu\text{m}}{\text{px}}$$

obtained from a cross-calibration with the main imaging system using the diameter of the box along the  $y$ -axis as a reference accessible from both imaging directions (see Fig. 3.1).

A third method involves the slight vertical anticonfinement of the magnetic field generated by the Feshbach coils: The saddle position of the magnetic field can be changed by creating an additional vertical

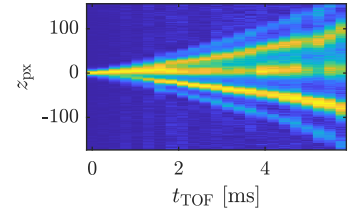


**Figure A.1:** A Kapitza-Dirac measurement is used to calibrate the magnification of the auxiliary imaging system. The density distributions, integrated along the  $x$ -axis, are shown for various time of flights after momentum has been imprinted along the  $z$ -axis.

magnetic gradient with the set of coils that is normally used to compensate for the effect of gravity. Here, the saddle movement at the atom position for a given current through these coils is accurately known from the current required for this compensation. Meanwhile, its change on the camera can be determined from time of flight measurements as the atoms roll off the anticonfinement potential along the  $z$ -axis. The obtained pixel size is  $(1.07 \pm 0.13) \mu\text{m}/\text{px}$  which is in agreement with the results of the previous two methods.

Using the effective pixel size of the Kapitza-Dirac calibration, we can determine the vertical extension of the gas in the box potential. First, we take the absorption image of the 3D gas from the side (lower panel in Fig. 3.1) and integrate along the  $x$ -axis to obtain the distribution  $n(z)$ . We then take the full width at half maximum of the integrated density to obtain a height of  $b_{\text{px}} = 39 \text{ px}$  that corresponds according to the calibration to  $b = 43 \mu\text{m}$ .

# B

## DENSITY CALIBRATION

We calibrate the density measurement in the 3D Box presented in Chap. 3 using a system with a known equation of state (EOS), a unitary Fermi gas. We prepare a unitary Fermi gas with a similar number of atoms but in a hybrid trap, where the endcaps are left in place but the radial ring confinement is turned off. Instead, the atoms are held along the radial direction by a weak magnetic trap that provides a harmonic confinement  $V(r) = m\omega_r^2 r^2/2$  with  $\omega_r = 2\pi \cdot 29.8$  Hz. The resulting density distribution is shown in Fig. B.1.

In this configuration, the local density  $n(r)$  of the gas follows the harmonic confinement and decreases towards higher radii  $r$  since the local chemical potential decreases according to the local density approximation as  $\mu(r) = \mu(r=0) - V(r)$ . In the central region of the cloud, the local Fermi temperature  $T_F(r)$  is high enough that  $T/T_F(r) \ll 1$ , and the local chemical potential is in good approximation given by

$$\mu(r) = \xi E_F(r),$$

with the local Fermi energy

$$E_F(r) = \hbar^2 \frac{(6\pi^2 n(r))^{2/3}}{2m}$$

and the Bertsch parameter  $\xi = 0.370(9)$  [15, 28].

For our calibration, we perform a linear fit of the local Fermi energy  $\tilde{E}_F \propto \tilde{n}^{2/3}$  for small radii and determine the central chemical potential  $\mu_0$  from its crossing with the x-axis (Fig. B.1). We compare the chemical potential with the central Fermi energy  $E_F$ , which is the crossing of the fit with the y-axis. We obtain  $\mu_0 = \hbar \times 1.23$  kHz and  $\tilde{E}_F = \hbar \times 2.68$  kHz. Their ratio deviates from the Bertsch parameter. Therefore, we introduce a correction factor for the density  $n_{3D} = \alpha \tilde{n}_{3D}$

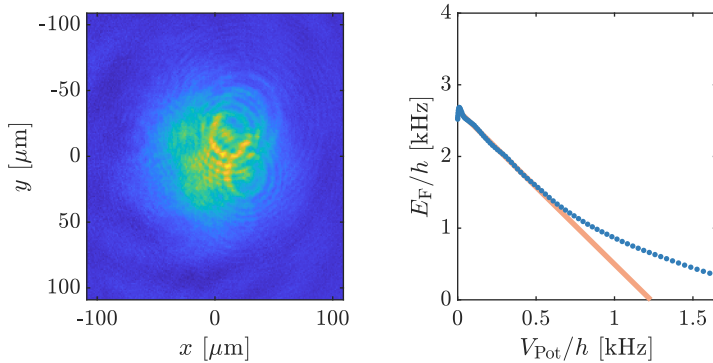


**Figure B.1:** Density calibration using a unitary Fermi gas in a hybrid trap where the vertical confinement by the endcaps is kept on but the radial confinement is turned off. The left panel shows the density distribution. In the right panel, we show the radial average of the local Fermi energy  $E_F(\tilde{n}(r)) \propto \tilde{n}(r)^{2/3}$  in dependence on the local potential height  $V(r)$  (blue dots). A linear fit in the central region (solid orange) allows us to extract the chemical potential and to determine a correction factor  $\alpha$  for the density (see text).

such that  $E_F = \alpha^{2/3} \tilde{E}_F$ . We find

$$\alpha = \left( \frac{\mu_0}{\xi \tilde{E}_F} \right)^{3/2} = 1.38(7)(5),$$

<sup>82</sup> These uncertainties in the density propagate to relative systematic uncertainties of 4% and 3% in the Fermi energy.

where the first parenthesis gives our error in the determination of the linear fit and the second parenthesis denotes the error due to the uncertainty of the Bertsch parameter<sup>82</sup>.

# C

## SPEED OF SOUND FROM QMC CALCULATIONS

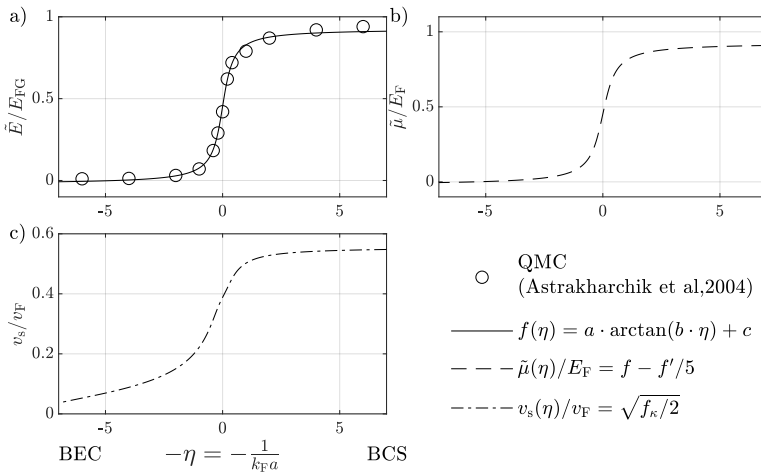
In the following, we extract the speed of sound from quantum Monte Carlo (QMC) calculations [44] which is shown in in Fig. 3.9c as a dashed line. The QMC calculations provide us for a given interaction strength  $\eta = (k_F a_{3D})^{-1}$  with the total energy  $E(\eta)$  of the  $T = 0$  ground state. In Ref. [44] the total energy also includes the binding energy of the dimers and approaches  $E(\eta) \sim -NE_B/2$  in the BEC limit. We are here, however, interested in the collective behavior of the dimers and therefore subtract the two-body binding energy to obtain

$$\tilde{E}(\eta) = E(\eta) + NE_B/2 = f(\eta)E_{FG} \quad (C.1)$$

where  $E_{FG} = \frac{3}{5}NE_F$  is the total energy of the non-interacting Fermi gas. This quantity is plotted in Fig. 2 of Ref. [44] and reproduced in Fig. C.1 a. The function  $f(\eta)$  is a continuous function which goes from 0 in BEC limit to 1 in the non-interacting BCS limit and is obtained by fitting an empirical parametrization  $f(\eta) = a \cdot \arctan(b \cdot \eta) + c$  to the numerical values of the QMC calculation<sup>83</sup>. Compared to the parametrization in Ref. [216] we use here one continuous function throughout the crossover in order to have a properly defined derivative  $\partial f/\partial \eta$  at the unitary point.

To derive the speed of sound, we first calculate the reduced chemical potential  $\tilde{\mu} = \mu + E_B/2$  by taking the derivative with respect to the particle number,

$$\tilde{\mu} = \frac{\partial \tilde{E}}{\partial N} = \frac{\partial (fE_{FG})}{\partial N} = \frac{\partial f}{\partial \eta} \frac{\partial \eta}{\partial N} E_{FG} + f \frac{\partial E_{FG}}{\partial N} = E_F \left( -f' \frac{\eta}{5} + f \right), \quad (C.2)$$



<sup>83</sup> We obtain for our parametrization  $a = 0.302$ ,  $b = 2.9$  and  $c = 0.45$ .

**Figure C.1:** Derivation of the speed of sound from the QMC equation of state. (a) Empirical fit (solid line) to the reduced total energy  $\tilde{E}$  from QMC calculations (dots [44]). (b) By taking the derivative a reduced chemical potential  $\tilde{\mu}$  (dashed line) can be calculated. (c) A second derivative yields the speed of sound (dashed dotted line).

where we introduced the abbreviation  $f' = \partial f / \partial \eta$  and used the relations

$$\frac{\partial \eta}{\partial N} = -\frac{\eta}{3N} \frac{\partial E_{FG}}{\partial N} = E_F.$$

As we see in Fig. C.1 b, the reduced chemical potential  $\tilde{\mu}$  smoothly connects the BEC limit where  $\tilde{\mu} \sim gn/2$  to the BCS limit where  $\tilde{\mu} \sim E_F$ .

In a second step, we derive the chemical potential with respect to the density to obtain the inverse compressibility

$$\frac{\partial \tilde{\mu}}{\partial n} = \frac{E_F}{n} \left( \frac{2}{3}f - \frac{2}{5}f'\eta + \frac{1}{15}f''\eta^2 \right) \equiv \frac{E_F}{n} f_\kappa, \quad (\text{C.3})$$

where we introduced the inverse compressibility scaling function  $f_\kappa$ .

The speed of sound is then given by

$$c = \sqrt{\frac{n}{m} \frac{\partial \mu}{\partial n}} = \sqrt{\frac{n}{m} \frac{E_F f_\kappa}{n}} = v_F \sqrt{\frac{f_\kappa}{2}}, \quad (\text{C.4})$$

which is plotted in Fig. C.1 c.

# D

## SYSTEMATIC UNCERTAINTIES ON THE PAIRING GAP

Here, we summarize the different sources of systematic uncertainties and their influence on the measured pairing gaps in Chap. 3.

The gap determination should not depend on the momentum for  $q < 2k_\mu = 2\sqrt{2m\mu/\hbar^2}$  and experimentally we observe an upper limit of 5% for the  $q$ -dependence of  $\Delta/E_F$ , where data was available.

The choice of a fit function for the onset of the pair-breaking continuum introduces a systematic uncertainty. If we apply the bilinear fit to the measurements in the BCS regime where the fit of QRPA calculations is also applicable, we find that the values of the gap determined from the transition point are shifted systematically down by  $0.03 E_F$ . However, as the absolute value of the gap increases towards the crossover regime, the relative difference between both methods decreases. This difference between both fits can be understood as an estimate of the systematic error introduced by the choice of a fit function, namely, a systematic uncertainty of  $0.03 E_F$  for  $\Delta$ .

The uncertainties of the density calibration discussed above, namely the confidence interval for the fit to  $dE_F(r)/dV(r)$  and the error of the literature value for the Bertsch parameter [15], result in uncertainties for  $\Delta/E_F$  of 4% and 3%, respectively. An additional systematic error arises due to the non-zero curvature of the magnetic offset field which affects the homogeneity of the sample. It can be estimated by comparing the potential inhomogeneity to the chemical potential of the gas. The resulting error for  $\Delta/E_F$  is  $0.02 E_F/\mu$  which translates to a relative uncertainty of the gap of  $\sim 15\%$  throughout the crossover.

Furthermore, we can use the theoretical prediction for the entropy-dependence of the gap from Ref. [88] to estimate the influence of entropy uncertainties discussed in the next section. Both the entropy measurement uncertainty of  $0.09 Nk_B$  and the entropy variation of  $0.07 Nk_B$  across the BEC-BCS crossover correspond to a systematic uncertainty of approximately  $0.02 E_F$  on  $\Delta$ .



# E

## MAGNETIC FIELD DEPENDENCE OF THE GROUND STATE

To obtain the RF frequencies required for a transfer from one hyperfine state we discuss here briefly how the ground state  $^2S_{1/2}$  splits up into six hyperfine states in an external magnetic field  $B$ . The energy shift of a hyperfine state  $|F, m_F\rangle$  with total angular momentum  $F = \{3/2, 1/2\}$  and the corresponding magnetic quantum number  $|m_F| \leq F$  is given by the Breit-Rabi equation [217, 218],

$$\Delta E = -\frac{h\nu_{\text{HF}}}{2(2I+1)} + \mu_B g_I m_F B + h\nu_{\text{HF}}(F-I) \sqrt{1 + \frac{2m_F x}{I + \frac{1}{2}} + x^2} \quad (\text{E.1})$$

$$\text{with } x = \frac{(g_J - g_I)\mu_B B}{h\nu_{\text{HF}}} \quad (\text{E.2})$$

the hyperfine splitting  $\nu_{\text{HF}} = 228.205\,26$  MHz, nuclear spin  $I = 1$ , Bohr magneton  $\mu_B$ , and Landé  $g$ -factors  $g_J = 2.00232$  and  $g_I = -0.000448$ . For the stretched state where  $|m_F| = I + 1/2 = 3/2$ , the last term is replaced by

$$h\nu_{\text{HF}}(F-I) (1 + \text{sgn}(m_F)x),$$

where  $\text{sgn}$  is the sign operator. Fig. 8.3 a shows how the ground state splits up into three high-field and three low-field seeking states, which are numbered in ascending order. The energy difference between state 1 and 2, and state 2 and 3, is shown in Fig. 8.3 b for varying magnetic fields.



# F

## THE ACCORDION LATTICE

During this thesis, we installed a so-called *accordion* lattice in the experiment. This new 1D optical lattice has compared to the lattice previously used to create 2D Fermi gases an adjustable lattice spacing. Such a lattice allows us to vary the vertical confinement continuously while keeping the atoms in the trap. It has been implemented for 1D and 2D lattices before [219–223].

Similar to the Bragg setup presented in Chap. 3.2, the underlying idea is to change the periodicity of a 1D lattice by adjusting the crossing angle of two interfering beams. A detailed discussion of the setup including beam shaping, treatment of the polarization, alignment and full characterization can be found in the thesis of Jonas Faltinath [84]. In short, we create an interference pattern by creating two blue-detuned 532 nm laser beams of variable spatial displacement with respect to each other and sending them through a common lens.

To achieve that, we use a mirror mounted on a galvo motor<sup>84</sup> and convert the angle offset into a spatial offset with an  $f = 50$  mm placed 50 mm behind the galvo mirror (Fig. F.1). The galvo mirror and the collimating lens are installed in a common mount to simplify alignment and to create a compact setup. Then, the displaced beam is split up into two parallel beams by using a custom polarizing beam splitter<sup>85</sup> rotated by  $45^\circ$ . The resulting co-propagating beams are passed through a focusing lens in front of the glass cell, which crosses both beams in the focal plane and creates a 1D lattice at the atom position.

By changing the control voltage of the galvo motor, the deflection of the beam and thus the displacement after the cube can be varied. This varies the final crossing angle at the atom position, thereby changing

<sup>84</sup> We use the Thorlabs GVS301 which allows rotation angles of  $\pm 12.5^\circ$  with an accuracy of  $15 \mu\text{rad}$ .

<sup>85</sup> We use an 1 inch polarizing cube from Altechna with a coating that minimizes the reflection for a  $45^\circ$  entrance angle.

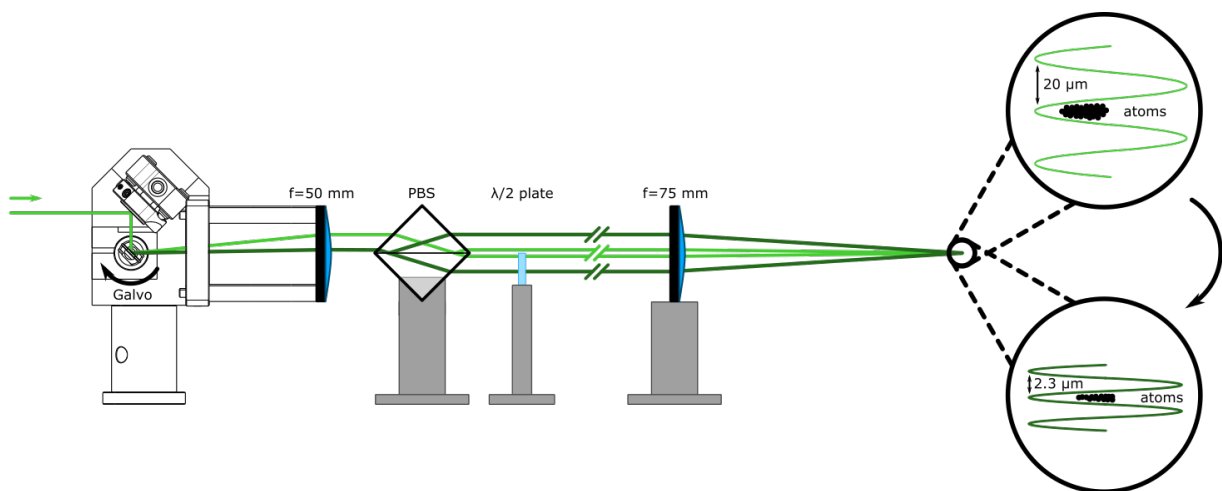


**Figure F.1:** In the accordion setup a galvo mirror deflects the incoming beam which is collimated by a 50 mm lens. Then, the beam is split into two using a custom polarizing beam splitter rotated by  $45^\circ$ . Both co-propagating beams are finally focussed onto the atoms, resulting in a 1D lattice. This setup allows to change the lattice constant continuously from  $20 \mu\text{m}$  to  $2.3 \mu\text{m}$  by changing the deflection angle of the galvo mirror. Adapted from [84].

**Figure F.2:** Interference pattern for different lattice constants when scanning from small lattice constants (bottom, small galvo deflection angle) to large lattice constants (top, large galvo deflection angle) in a test setup. For each lattice constant, a sum over the trivial axis of the interference pattern is taken, and shown as a row. The stability of the central maximum of the interference pattern demonstrates that the relative phase between both beams stays almost constant when changing the lattice constant. In the experiment, we choose a minimum next to the central maximum to confine the atom cloud vertically. Adapted from [84].

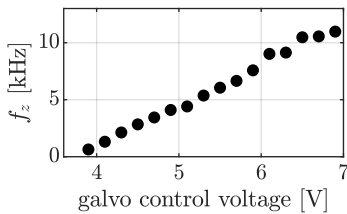
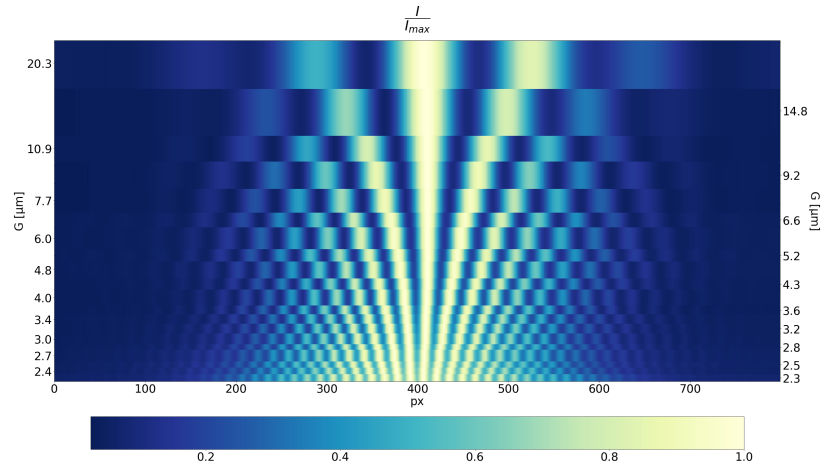


**Figure F.3:** Trapping frequencies of the accordion lattice for increasing galvo control voltages. These correspond to decreasing galvo deflection angles and increasing crossing angles at the atom position. These measurements are taken for a total beam power of 500 mW and a gas at 832 G.

the lattice spacing. Here we note, that a smaller galvo deflection angle corresponds to a larger crossing angle at the atom position because the cube transforms a small displacement into a large displacement and vice versa (see Fig.F.1).

Before installing the accordion lattice in the experiment, we characterized the interference pattern in a test setup which showed that lattice constants in the range of  $2.3 \mu\text{m}$  to  $20 \mu\text{m}$  can be achieved (Fig.F.2). After installation in the experiment, we use parametric heating to verify that the trapping frequency can be varied using the galvo control voltage while keeping the beam power constant (Fig.F.3).

With this setup the loading from the squeeze trap can take place at a large lattice constant such that spilling into adjacent layers does not occur, thereby simplifying the atom transfer. In addition, the accordion lattice allows for a simple check if a single layer is loaded by increasing the lattice constant and performing absorption imaging from the side. This complements the kick-and-probe technique developed previously to resolve if one or two sites are loaded in a constant 1D lattice [81].

In addition to simplify loading a balanced 2D system, the accordion trap can confine clouds with large vertical extent, e.g. imbalanced gases in the squeeze trap, into a single layer. Furthermore, it enables us to study the effect of different confinements while keeping the beam power high, thus suppressing the tunneling rate between adjacent layers.

## BIBLIOGRAPHY

- <sup>1</sup>P. W. Anderson: *More is different*, "Science" vol. 177, no. 4047, 393–396 (1972) (cited on page 9).
- <sup>2</sup>J. Bardeen, L. N. Cooper, and J. R. Schrieffer: *Theory of superconductivity*, "Phys. Rev." vol. 108, no. 5, 1175–1204 (1957) (cited on pages 9, 13, 16).
- <sup>3</sup>L. Landau: *Theory of the superfluidity of helium II*, "Phys. Rev." vol. 60, no. 4, 356–358 (1941) (cited on pages 9, 61).
- <sup>4</sup>R. P. Feynman: *Simulating physics with computers*, "Int. J. Theor. Phys." vol. 21, no. 6, 467–488 (1982) (cited on page 10).
- <sup>5</sup>I. Bloch, J. Dalibard, and W. Zwerger: *Many-body physics with ultracold gases*, "Rev. Mod. Phys." vol. 80, no. 3, 885–964 (2008) (cited on pages 10, 14, 18, 55).
- <sup>6</sup>W. Ketterle and M. W. Zwierlein: *Making, probing and understanding ultracold fermi gases*, (2008) (cited on pages 10, 15–17, 19, 20, 24, 33, 34).
- <sup>7</sup>S. Giorgini, L. P. Pitaevskii, and S. Stringari: *Theory of ultracold atomic fermi gases*, "Rev. Mod. Phys." vol. 80, no. 4, 1215–1274 (2008) (cited on page 10).
- <sup>8</sup>C. Chin, R. Grimm, P. Julienne, and E. Tiesinga: *Feshbach resonances in ultracold gases*, "Rev. Mod. Phys." vol. 82, no. 2, 1225–1286 (2010) (cited on pages 10, 14).
- <sup>9</sup>W. Zwerger: *The BCS-BEC crossover and the unitary fermi gas*, Vol. 836, Springer Berlin Heidelberg 2012 (cited on pages 10, 19, 43, 110).
- <sup>10</sup>M. M. Parish: *The BCS–BEC crossover*, in *Cold atoms*, IMPERIAL COLLEGE PRESS Nov. 2014, pp. 179–197 (cited on pages 10, 19).
- <sup>11</sup>M. Yu Kagan and A. V. Turlapov: *BCS – BEC crossover, collective excitations, and hydrodynamics of superfluid quantum liquids and gases*, en, "Phys.-Usp." vol. 62, no. 3, 215 (2019) (cited on pages 10, 78).
- <sup>12</sup>H. K. Onnes: *The superconductivity of mercury*, "Comm. Phys. Lab. Univ. Leiden" vol. 122, 122–124 (1911) (cited on page 13).
- <sup>13</sup>A. J. Leggett: *Diatomic molecules and cooper pairs*, "Modern Trends in the Theory of Condensed Matter", 13–27 (1980) (cited on pages 13, 19).
- <sup>14</sup>P. Nozières and S. Schmitt-Rink: *Bose condensation in an attractive fermion gas: from weak to strong coupling superconductivity*, "J. Low Temp. Phys." vol. 59, no. 3, 195–211 (1985) (cited on page 13).
- <sup>15</sup>G. Zürn, T. Lompe, A. N. Wenz, S. Jochim, P. S. Julienne, and J. M. Hutson: *Precise characterization of 6Li feshbach resonances using trap-sideband-resolved RF spectroscopy of weakly bound molecules*, en, "Phys. Rev. Lett." vol. 110, no. 13, 135301 (2013) (cited on pages 14, 15, 25, 119, 123).
- <sup>16</sup>L. Sobirey: *Superfluidity in two-dimensional fermi gases*, en, PhD thesis, Sept. 2021 (cited on pages 16, 30, 46, 59, 63, 67, 71).
- <sup>17</sup>M. Marini, F. Pistolesi, and G. C. Strinati: *Evolution from BCS superconductivity to bose condensation: analytic results for the crossover in three dimensions*, 1998 (cited on page 16).
- <sup>18</sup>C. N. Yang: *Concept of Off-Diagonal Long-Range order and the quantum phases of liquid he and of superconductors*, "Rev. Mod. Phys." vol. 34, no. 4, 694–704 (1962) (cited on page 17).

- <sup>19</sup>A. J. Leggett: *The order parameter as a macroscopic quantum wavefunction*, in *Connectivity and superconductivity*, edited by J. Berger and J. Rubinstein, Berlin, Heidelberg: Springer Berlin Heidelberg 2000, pp. 230–238 (cited on pages 18, 51).
- <sup>20</sup>P. A. Murthy: *Emergent phenomena in two-dimensional fermi systems*, PhD thesis, University of Heidelberg 2018 (cited on page 18).
- <sup>21</sup>C. J. Pethick and H. Smith: *Bose-Einstein condensation in dilute gases*, en, Cambridge University Press Sept. 2008 (cited on page 18).
- <sup>22</sup>L. Salasnich, N. Manini, and A. Parola: *Condensate fraction of a fermi gas in the BCS-BEC crossover*, “Phys. Rev. A” vol. 72, no. 2, 023621 (2005) (cited on page 18).
- <sup>23</sup>G. Ortiz and J. Dukelsky: *BCS-to-BEC crossover from the exact BCS solution*, “Phys. Rev. A” vol. 72, no. 4, 043611 (2005) (cited on page 18).
- <sup>24</sup>M. Mc Neil Forbes: *The unitary fermi gas: an overview*, 2012 (cited on page 19).
- <sup>25</sup>M. Horikoshi and M. Kuwata-Gonokami: *Cold atom quantum simulator for dilute neutron matter*, “Int. J. Mod. Phys. E” vol. 28, no. 01n02, 1930001 (2019) (cited on page 19).
- <sup>26</sup>R. G. Newton: *Scattering theory of waves and particles*, Springer Berlin Heidelberg 1982 (cited on page 19).
- <sup>27</sup>M. Horikoshi, S. Nakajima, M. Ueda, and T. Mukaiyama: *Measurement of universal thermodynamic functions for a unitary fermi gas*, en, “Science” vol. 327, no. 5964, 442–445 (2010) (cited on page 19).
- <sup>28</sup>M. J. H. Ku, A. T. Sommer, L. W. Cheuk, and M. W. Zwierlein: *Revealing the superfluid lambda transition in the universal thermodynamics of a unitary fermi gas*, en, “Science” vol. 335, no. 6068, 563–567 (2012) (cited on pages 19, 39, 45, 71, 119).
- <sup>29</sup>M. G. Lingham, K. Fenech, S. Hoinka, and C. J. Vale: *Local observation of pair condensation in a fermi gas at unitarity*, en, “Phys. Rev. Lett.” vol. 112, no. 10, 100404 (2014) (cited on page 19).
- <sup>30</sup>Z. Yan, P. B. Patel, B. Mukherjee, R. J. Fletcher, J. Struck, and M. W. Zwierlein: *Boiling a unitary fermi liquid*, en, “Phys. Rev. Lett.” vol. 122, no. 9, 093401 (2019) (cited on pages 19, 39).
- <sup>31</sup>C. Carcy, S. Hoinka, M. G. Lingham, P. Dyke, C. C. N. Kuhn, H. Hu, and C. J. Vale: *Contact and sum rules in a Near-Uniform fermi gas at unitarity*, en, “Phys. Rev. Lett.” vol. 122, no. 20, 203401 (2019) (cited on page 19).
- <sup>32</sup>C. C. N. Kuhn, S. Hoinka, I. Herrera, P. Dyke, J. J. Kinnunen, G. M. Bruun, and C. J. Vale: *High-Frequency sound in a unitary fermi gas*, en, “Phys. Rev. Lett.” vol. 124, no. 15, 150401 (2020) (cited on pages 19, 43, 44).
- <sup>33</sup>X. Li, X. Luo, S. Wang, K. Xie, X.-P. Liu, H. Hu, Y.-A. Chen, X.-C. Yao, and J.-W. Pan: *Second sound attenuation near quantum criticality*, en, “Science” vol. 375, no. 6580, 528–533 (2022) (cited on page 19).
- <sup>34</sup>Z. Yan, P. B. Patel, B. Mukherjee, C. J. Vale, R. J. Fletcher, and M. Zwierlein: *Thermography of the superfluid transition in a strongly interacting fermi gas*, (2022) (cited on page 19).
- <sup>35</sup>N. N. Bogoljubov: *On a new method in the theory of superconductivity*, “Il Nuovo Cimento (1955-1965)” vol. 7, no. 6, 794–805 (1958) (cited on page 20).
- <sup>36</sup>J. G. Valatin: *Comments on the theory of superconductivity*, “Il Nuovo Cimento (1955-1965)” vol. 7, no. 6, 843–857 (1958) (cited on page 20).
- <sup>37</sup>J. R. Schrieffer: *Theory of superconductivity*, Westview Press 1971 (cited on page 21).
- <sup>38</sup>P. W. Anderson: *Higgs, anderson and all that*, en, “Nat. Phys.” vol. 11, no. 2, 93–93 (2015) (cited on page 21).

- <sup>39</sup>P. W. Anderson: *Random-Phase approximation in the theory of superconductivity*, 1958 (cited on pages 21, 22, 44).
- <sup>40</sup>R. Combescot, M. Y. Kagan, and S. Stringari: *Collective mode of homogeneous superfluid fermi gases in the BEC-BCS crossover*, “Phys. Rev. A” vol. 74, no. 4, 042717 (2006) (cited on pages 22, 34, 43, 44, 47).
- <sup>41</sup>A. Bardasis and J. R. Schrieffer: *Excitons and plasmons in superconductors*, “Phys. Rev.” vol. 121, no. 4, 1050–1062 (1961) (cited on page 22).
- <sup>42</sup>P. Zou, E. D. Kuhnle, C. J. Vale, and H. Hu: *Quantitative comparison between theoretical predictions and experimental results for bragg spectroscopy of a strongly interacting fermi superfluid*, “Phys. Rev. A” vol. 82, no. 6, 061605 (2010) (cited on page 22).
- <sup>43</sup>N. Bogolubov: *ON THE THEORY OF SUPERFLUIDITY \**, “Journal of Physics” (1946) (cited on page 22).
- <sup>44</sup>G. E. Astrakharchik, J. Boronat, J. Casulleras, and S. Giorgini: *Equation of state of a fermi gas in the BEC-BCS crossover: a quantum monte carlo study*, en, “Phys. Rev. Lett.” vol. 93, no. 20, 200404 (2004) (cited on pages 22, 45, 70, 71, 77, 121).
- <sup>45</sup>J. Goldstone: *Field theories with superconductor solutions*, “Il Nuovo Cimento (1955-1965)” vol. 19, no. 1, 154–164 (1961) (cited on page 22).
- <sup>46</sup>H. Zhao, X. Gao, W. Liang, P. Zou, and F. Yuan: *Dynamical structure factors of a two-dimensional fermi superfluid within random phase approximation*, en, “New J. Phys.” vol. 22, no. 9, 093012 (2020) (cited on pages 22, 115).
- <sup>47</sup>D. Pekker and C. M. Varma: *Amplitude/Higgs modes in condensed matter physics*, “Annu. Rev. Condens. Matter Phys.” vol. 6, no. 1, 269–297 (2015) (cited on page 22).
- <sup>48</sup>D. S. Petrov, C. Salomon, and G. V. Shlyapnikov: *Weakly bound dimers of fermionic atoms*, en, “Phys. Rev. Lett.” vol. 93, no. 9, 090404 (2004) (cited on page 22).
- <sup>49</sup>C. J. Vale and M. Zwierlein: *Spectroscopic probes of quantum gases*, en, “Nat. Phys.” vol. 17, no. 12, 1305–1315 (2021) (cited on page 24).
- <sup>50</sup>C. Chin, M. Bartenstein, A. Altmeyer, S. Riedl, S. Jochim, J. H. Denschlag, and R. Grimm: *Observation of the pairing gap in a strongly interacting fermi gas*, en, “Science” vol. 305, no. 5687, 1128–1130 (2004) (cited on page 25).
- <sup>51</sup>J. Kinnunen, M. Rodríguez, and P. Törmä: *Pairing gap and in-gap excitations in trapped fermionic superfluids*, en, “Science” vol. 305, no. 5687, 1131–1133 (2004) (cited on page 25).
- <sup>52</sup>C. H. Schunck, Y. Shin, A. Schirotzek, M. W. Zwierlein, and W. Ketterle: *Pairing without superfluidity: the ground state of an imbalanced fermi mixture*, en, “Science” vol. 316, no. 5826, 867–870 (2007) (cited on pages 25, 76, 77).
- <sup>53</sup>C. H. Schunck, Y.-I. Shin, A. Schirotzek, and W. Ketterle: *Determination of the fermion pair size in a resonantly interacting superfluid*, en, “Nature” vol. 454, no. 7205, 739–743 (2008) (cited on page 25).
- <sup>54</sup>A. Schirotzek, Y.-I. Shin, C. H. Schunck, and W. Ketterle: *Determination of the superfluid gap in atomic fermi gases by quasiparticle spectroscopy*, en, “Phys. Rev. Lett.” vol. 101, no. 14, 140403 (2008) (cited on pages 25, 47, 76, 77).
- <sup>55</sup>A. Damascelli, Z. Hussain, and Z.-X. Shen: *Angle-resolved photoemission studies of the cuprate superconductors*, “Rev. Mod. Phys.” vol. 75, no. 2, 473–541 (2003) (cited on page 26).
- <sup>56</sup>J. A. Sobota, Y. He, and Z.-X. Shen: *Angle-resolved photoemission studies of quantum materials*, “Rev. Mod. Phys.” vol. 93, no. 2, 025006 (2021) (cited on page 26).

- <sup>57</sup>J. P. Gaebler, J. T. Stewart, T. E. Drake, D. S. Jin, A. Perali, P. Pieri, and G. C. Strinati: *Observation of pseudogap behaviour in a strongly interacting fermi gas*, “Nat. Phys.” vol. 6, no. 8, 569–573 (2010) (cited on page 26).
- <sup>58</sup>J. T. Stewart, J. P. Gaebler, and D. S. Jin: *Using photoemission spectroscopy to probe a strongly interacting fermi gas*, en, “Nature” vol. 454, no. 7205, 744–747 (2008) (cited on page 26).
- <sup>59</sup>S. Tan: *Energetics of a strongly correlated fermi gas*, “Ann. Phys.” vol. 323, no. 12, 2952–2970 (2008) (cited on pages 26, 34).
- <sup>60</sup>W. Schneider and M. Randeria: *Universal short-distance structure of the single-particle spectral function of dilute fermi gases*, “Phys. Rev. A” vol. 81, no. 2, 021601 (2010) (cited on page 26).
- <sup>61</sup>K. Sturm: *Dynamic structure factor: an introduction*, 1993 (cited on page 27).
- <sup>62</sup>W. L. Bragg: *The diffraction of short electromagnetic waves by a crystal*, in Proceedings of the cambridge philosophical society (1913) (cited on page 27).
- <sup>63</sup>P. L. Kapitza and P. A. M. Dirac: *The reflection of electrons from standing light waves*, “Math. Proc. Cambridge Philos. Soc.” vol. 29, no. 2, 297–300 (1933) (cited on page 28).
- <sup>64</sup>P. L. Gould, G. A. Ruff, and D. E. Pritchard: *Diffraction of atoms by light: the near-resonant Kapitza-Dirac effect*, “Phys. Rev. Lett.” vol. 56, no. 8, 827–830 (1986) (cited on page 28).
- <sup>65</sup>D. L. Freimund, K. Aflatooni, and H. Batelaan: *Observation of the Kapitza-Dirac effect*, en, “Nature” vol. 413, no. 6852, 142–143 (2001) (cited on page 28).
- <sup>66</sup>J. Stenger, S. Inouye, A. P. Chikkatur, D. M. Stamper-Kurn, D. E. Pritchard, and W. Ketterle: *Bragg spectroscopy of a Bose-Einstein condensate*, “Phys. Rev. Lett.” vol. 82, no. 23, 4569–4573 (1999) (cited on page 28).
- <sup>67</sup>D. M. Stamper-Kurn, A. P. Chikkatur, A. Görlitz, S. Inouye, S. Gupta, D. E. Pritchard, and W. Ketterle: *Excitation of phonons in a Bose-Einstein condensate by light scattering*, (1999) (cited on pages 28, 30).
- <sup>68</sup>J. Steinhauer, R. Ozeri, N. Katz, and N. Davidson: *Excitation spectrum of a Bose-Einstein condensate*, en, “Phys. Rev. Lett.” vol. 88, no. 12, 120407 (2002) (cited on pages 29, 30).
- <sup>69</sup>R. Ozeri, N. Katz, J. Steinhauer, and N. Davidson: *Colloquium: bulk bogoliubov excitations in a Bose-Einstein condensate*, 2005 (cited on page 29).
- <sup>70</sup>S. Hoinka: *Precision bragg spectroscopy of the density and spin response of a strongly interacting fermi gas*, PhD thesis, Swinburne University of Technology 2014 (cited on pages 29, 115).
- <sup>71</sup>E. Kuhnle: *Studies of universality in strongly interacting 6 li fermi gases with bragg spectroscopy*, PhD thesis, Swinburne University of Technology 2011 (cited on page 30).
- <sup>72</sup>P. Zou, F. Dalfovo, R. Sharma, X.-J. Liu, and H. Hu: *Dynamic structure factor of a strongly correlated fermi superfluid within a density functional theory approach*, en, “New J. Phys.” vol. 18, no. 11, 113044 (2016) (cited on pages 34, 44).
- <sup>73</sup>G. M. Bruun and G. Baym: *Bragg spectroscopy of cold atomic fermi gases*, “Phys. Rev. A” vol. 74, no. 3, 033623 (2006) (cited on page 34).
- <sup>74</sup>G. Veeravalli, E. Kuhnle, P. Dyke, and C. J. Vale: *Bragg spectroscopy of a strongly interacting fermi gas*, en, “Phys. Rev. Lett.” vol. 101, no. 25, 250403 (2008) (cited on page 34).
- <sup>75</sup>E. D. Kuhnle, S. Hoinka, H. Hu, P. Dyke, P. Hannaford, and C. J. Vale: *Studies of the universal contact in a strongly interacting fermi gas using bragg spectroscopy*, en, “New J. Phys.” vol. 13, no. 5, 055010 (2011) (cited on page 34).

- <sup>76</sup>S. Hoinka, M. Lingham, K. Fenech, H. Hu, C. J. Vale, J. E. Drut, and S. Gandolfi: *Precise determination of the structure factor and contact in a unitary fermi gas*, en, “Phys. Rev. Lett.” vol. 110, no. 5, 055305 (2013) (cited on page 34).
- <sup>77</sup>S. Hoinka, M. Lingham, M. Delehay, and C. J. Vale: *Dynamic spin response of a strongly interacting fermi gas*, en, “Phys. Rev. Lett.” vol. 109, no. 5, 050403 (2012) (cited on pages 34, 115).
- <sup>78</sup>S. Hoinka, P. Dyke, M. G. Lingham, J. J. Kinnunen, G. M. Bruun, and C. J. Vale: *Goldstone mode and pair-breaking excitations in atomic fermi superfluids*, “Nat. Phys.” vol. 13, no. 10, 943–946 (2017) (cited on pages 34, 35, 43–47).
- <sup>79</sup>H. Biss, L. Sobirey, N. Luick, M. Bohlen, J. J. Kinnunen, G. M. Bruun, T. Lompe, and H. Moritz: *Excitation spectrum and superfluid gap of an ultracold fermi gas*, “Phys. Rev. Lett.” vol. 128, no. 10, 100401 (2022) (cited on page 37).
- <sup>80</sup>N. Navon, R. P. Smith, and Z. Hadzibabic: *Quantum gases in optical boxes*, en, “Nat. Phys.” vol. 17, no. 12, 1334–1341 (2021) (cited on page 37).
- <sup>81</sup>K. Hueck: *A homogeneous, two-dimensional fermi gas*, PhD thesis, Universität Hamburg 2017 (cited on pages 37, 41, 94, 128).
- <sup>82</sup>A. L. Gaunt, T. F. Schmidutz, I. Gotlibovych, R. P. Smith, and Z. Hadzibabic: *Bose-Einstein condensation of atoms in a uniform potential*, en, “Phys. Rev. Lett.” vol. 110, no. 20, 200406 (2013) (cited on page 38).
- <sup>83</sup>B. Mukherjee, Z. Yan, P. B. Patel, Z. Hadzibabic, T. Yefsah, J. Struck, and M. W. Zwierlein: *Homogeneous atomic fermi gases*, en, “Phys. Rev. Lett.” vol. 118, no. 12, 123401 (2017) (cited on page 38).
- <sup>84</sup>J. Faltinath: *Strongly correlated fermi gases in two and three dimensions*, MA thesis, University of Hamburg Mar. 2022 (cited on pages 38, 127, 128).
- <sup>85</sup>K. Hueck, N. Luick, L. Sobirey, J. Siegl, T. Lompe, and H. Moritz: *Two-Dimensional homogeneous fermi gases*, en, “Phys. Rev. Lett.” vol. 120, no. 6, 060402 (2018) (cited on page 38).
- <sup>86</sup>K. Hueck, N. Luick, L. Sobirey, J. Siegl, T. Lompe, H. Moritz, L. W. Clark, and C. Chin: *Calibrating high intensity absorption imaging of ultracold atoms*, en, “Opt. Express” vol. 25, no. 8, 8670–8679 (2017) (cited on page 38).
- <sup>87</sup>A. Brunello, F. Dalfovo, L. Pitaevskii, S. Stringari, and F. Zambelli: *Momentum transferred to a trapped Bose-Einstein condensate by stimulated light scattering*, “Phys. Rev. A” vol. 64, no. 6, 063614 (2001) (cited on page 41).
- <sup>88</sup>R. Haussmann, W. Rantner, S. Cerrito, and W. Zwerger: *Thermodynamics of the BCS-BEC crossover*, “Phys. Rev. A” vol. 75, no. 2, 023610 (2007) (cited on pages 43, 47, 48, 50, 70, 71, 123).
- <sup>89</sup>T.-L. Ho: *Universal thermodynamics of degenerate quantum gases in the unitarity limit*, en, “Phys. Rev. Lett.” vol. 92, no. 9, 090402 (2004) (cited on page 43).
- <sup>90</sup>P. B. Patel, Z. Yan, B. Mukherjee, R. J. Fletcher, J. Struck, and M. W. Zwierlein: *Universal sound diffusion in a strongly interacting fermi gas*, en, “Science” vol. 370, no. 6521, 1222–1226 (2020) (cited on page 43).
- <sup>91</sup>P. Pieri, L. Pisani, and G. C. Strinati: *BCS-BEC crossover at finite temperature in the broken-symmetry phase*, “Phys. Rev. B Condens. Matter” vol. 70, no. 9, 094508 (2004) (cited on page 44).
- <sup>92</sup>R. Haussmann, M. Punk, and W. Zwerger: *Spectral functions and rf response of ultracold fermionic atoms*, “Phys. Rev. A” vol. 80, no. 6, 063612 (2009) (cited on pages 45, 46).

- <sup>93</sup>H. Kurkjian, Y. Castin, and A. Sinatra: *Concavity of the collective excitation branch of a fermi gas in the BEC-BCS crossover*, “Phys. Rev. A” vol. 93, no. 1, 013623 (2016) (cited on page 45).
- <sup>94</sup>P. Zou, H. Hu, and X.-J. Liu: *Low-momentum dynamic structure factor of a strongly interacting fermi gas at finite temperature: the goldstone phonon and its landau damping*, “Phys. Rev. A” vol. 98, no. 1, 011602 (2018) (cited on pages 45, 46).
- <sup>95</sup>L. D. Landau and I. M. Khalatnikov: *Theory of viscosity of helium II. 1. collisions of elementary excitations in helium II*, “Zhurnal Eksperimentalnoi i Teoreticheskoi Fiziki” vol. 19, 637 (1949) (cited on page 45).
- <sup>96</sup>S. T. Beliaev: *Application of the methods of quantum field theory to a system of bosons*, “SOVIET PHYSICS JETP-USSR” vol. 7, no. 2, 289–299 (1958) (cited on page 45).
- <sup>97</sup>A. J. Leggett: *WHERE is the energy saved in cuprate superconductivity?*, “J. Phys. Chem. Solids” vol. 59, no. 10, 1729–1732 (1998) (cited on page 46).
- <sup>98</sup>H. P. Büchler, P. Zoller, and W. Zwerger: *Spectroscopy of superfluid pairing in atomic fermi gases*, en, “Phys. Rev. Lett.” vol. 93, no. 8, 080401 (2004) (cited on page 46).
- <sup>99</sup>L. Pisani, P. Pieri, and G. C. Strinati: *Gap equation with pairing correlations beyond the mean-field approximation and its equivalence to a Hugenholtz-Pines condition for fermion pairs*, “Phys. Rev. B Condens. Matter” vol. 98, no. 10, 104507 (2018) (cited on pages 47, 48).
- <sup>100</sup>H. Heiselberg, C. J. Pethick, H. Smith, and L. Viverit: *Influence of induced interactions on the superfluid transition in dilute fermi gases*, en, “Phys. Rev. Lett.” vol. 85, no. 12, 2418–2421 (2000) (cited on page 48).
- <sup>101</sup>L. P. Gor’kov and T. K. Melik-Barkhudarov: *Contribution to the theory of superfluidity in an imperfect fermi gas*, “Sov. Phys. JETP” vol. 13, no. 5, 1018 (1961) (cited on page 48).
- <sup>102</sup>A. Gezerlis and J. Carlson: *Strongly paired fermions: cold atoms and neutron matter*, “Phys. Rev. C Nucl. Phys.” vol. 77, no. 3, 032801 (2008) (cited on page 49).
- <sup>103</sup>J. Carlson and S. Reddy: *Superfluid pairing gap in strong coupling*, en, “Phys. Rev. Lett.” vol. 100, no. 15, 150403 (2008) (cited on page 49).
- <sup>104</sup>A. Bulgac, J. E. Drut, and P. Magierski: *Quantum monte carlo simulations of the BCS-BEC crossover at finite temperature*, “Phys. Rev. A” vol. 78, no. 2, 023625 (2008) (cited on page 49).
- <sup>105</sup>T. Abe and R. Seki: *From low-density neutron matter to the unitary limit*, “Phys. Rev. C Nucl. Phys.” vol. 79, no. 5, 054003 (2009) (cited on page 49).
- <sup>106</sup>N. D. Mermin and H. Wagner: *Absence of ferromagnetism or antiferromagnetism in one- or Two-Dimensional isotropic heisenberg models*, “Phys. Rev. Lett.” vol. 17, no. 22, 1133–1136 (1966) (cited on pages 51, 67).
- <sup>107</sup>J. M. Kosterlitz and D. J. Thouless: *Ordering, metastability and phase transitions in two-dimensional systems*, en, “J. Phys. C: Solid State Phys.” vol. 6, no. 7, 1181 (1973) (cited on page 51).
- <sup>108</sup>V. L. Berezinskii: *DESTRUCTION OF LONG-RANGE ORDER IN ONE-DIMENSIONAL AND TWO-DIMENSIONAL SYSTEMS POSSESSING a CONTINUOUS SYMMETRY GROUP. II. QUANTUM SYSTEMS*, “SOVIET PHYSICS JETP” vol. 34, no. 3 (1972) (cited on page 51).
- <sup>109</sup>Z. Hadzibabic and J. Dalibard: *Two-dimensional bose fluids: an atomic physics perspective*, “La Rivista del Nuovo Cimento” vol. 34, no. 6, 389–434 (2011) (cited on pages 51, 52).
- <sup>110</sup>P. C. Hohenberg: *Existence of Long-Range order in one and two dimensions*, “Phys. Rev.” vol. 158, no. 2, 383–386 (1967) (cited on page 51).

- <sup>111</sup>P. A. Murthy, I. Boettcher, L. Bayha, M. Holzmann, D. Kedar, M. Neidig, M. G. Ries, A. N. Wenz, G. Zürn, and S. Jochim: *Observation of the Berezinskii-Kosterlitz-Thouless phase transition in an ultracold fermi gas*, en, “Phys. Rev. Lett.” vol. 115, no. 1, 010401 (2015) (cited on page 52).
- <sup>112</sup>J. Levinsen and M. M. Parish: *STRONGLY INTERACTING TWO-DIMENSIONAL FERMI GASES*, in *Annual review of cold atoms and molecules*, Vol. 3, Annual Review of Cold Atoms and Molecules, WORLD SCIENTIFIC Feb. 2015, pp. 1–75 (cited on pages 52, 107).
- <sup>113</sup>A. V. Turlapov and M. Yu Kagan: *Fermi-to-Bose crossover in a trapped quasi-2d gas of fermionic atoms*, en, “J. Phys. Condens. Matter” vol. 29, no. 38, 383004 (2017) (cited on pages 52, 53, 109).
- <sup>114</sup>M. W. Zwierlein: *High-temperature superfluidity in an ultracold fermi gas*, PhD thesis, Massachusetts Institute of Technology Feb. 2007 (cited on page 52).
- <sup>115</sup>N. C. Luick: *An ideal josephson junction in an ultracold two-dimensional fermi gas*, en, PhD thesis, 2020 (cited on page 53).
- <sup>116</sup>P. Dyke, K. Fenech, T. Pepler, M. G. Lingham, S. Hoinka, W. Zhang, S.-G. Peng, B. Mulkerin, H. Hu, X.-J. Liu, and C. J. Vale: *Criteria for two-dimensional kinematics in an interacting fermi gas*, “Phys. Rev. A” vol. 93, no. 1, 011603 (2016) (cited on page 53).
- <sup>117</sup>D. S. Petrov and G. V. Shlyapnikov: *Interatomic collisions in a tightly confined bose gas*, “Phys. Rev. A” vol. 64, no. 1, 012706 (2001) (cited on page 53).
- <sup>118</sup>I. Boettcher, L. Bayha, D. Kedar, P. A. Murthy, M. Neidig, M. G. Ries, A. N. Wenz, G. Zürn, S. Jochim, and T. Enss: *Equation of state of ultracold fermions in the 2D BEC-BCS crossover region*, en, “Phys. Rev. Lett.” vol. 116, no. 4, 045303 (2016) (cited on pages 54, 71, 95).
- <sup>119</sup>H. Shi, S. Chiesa, and S. Zhang: *Ground-state properties of strongly interacting fermi gases in two dimensions*, “Phys. Rev. A” vol. 92, no. 3, 033603 (2015) (cited on pages 54, 69–71).
- <sup>120</sup>V. Makhalov, K. Martiyanov, and A. Turlapov: *Ground-state pressure of quasi-2d fermi and bose gases*, en, “Phys. Rev. Lett.” vol. 112, no. 4, 045301 (2014) (cited on page 55).
- <sup>121</sup>M. Randeria, J. M. Duan, and L. Y. Shieh: *Bound states, cooper pairing, and bose condensation in two dimensions*, en, “Phys. Rev. Lett.” vol. 62, no. 9, 981–984 (1989) (cited on page 56).
- <sup>122</sup>M. Randeria, J. M. Duan, and L. Y. Shieh: *Superconductivity in a two-dimensional fermi gas: evolution from cooper pairing to bose condensation*, en, “Phys. Rev. B Condens. Matter” vol. 41, no. 1, 327–343 (1990) (cited on page 56).
- <sup>123</sup>M. Bohlen, L. Sobirey, N. Luick, H. Biss, T. Enss, T. Lompe, and H. Moritz: *Sound propagation and Quantum-Limited damping in a Two-Dimensional fermi gas*, en, “Phys. Rev. Lett.” vol. 124, no. 24, 240403 (2020) (cited on pages 59, 60).
- <sup>124</sup>L. Sobirey, N. Luick, M. Bohlen, H. Biss, H. Moritz, and T. Lompe: *Observation of superfluidity in a strongly correlated two-dimensional fermi gas*, en, “Science” vol. 372, no. 6544, 844–846 (2021) (cited on page 59).
- <sup>125</sup>M. Bohlen: *Sound propagation and quantum-limited damping in an ultracold two-dimensional fermi gas*, PhD thesis, PSL Research University; École Normale Supérieure 2020 (cited on pages 59, 60).
- <sup>126</sup>A. J. Leggett: *Superfluidity*, “Rev. Mod. Phys.” vol. 71, no. 2, S318–S323 (1999) (cited on page 61).
- <sup>127</sup>C. Ryu, M. F. Andersen, P. Cladé, V. Natarajan, K. Helmerson, and W. D. Phillips: *Observation of persistent flow of a Bose-Einstein condensate in a toroidal trap*, en, “Phys. Rev. Lett.” vol. 99, no. 26, 260401 (2007) (cited on page 61).
- <sup>128</sup>S. Moulder, S. Beattie, R. P. Smith, N. Tammuz, and Z. Hadzibabic: *Quantized supercurrent decay in an annular Bose-Einstein condensate*, “Phys. Rev. A” vol. 86, no. 1, 013629 (2012) (cited on page 61).

- <sup>129</sup>S. Beattie, S. Moulder, R. J. Fletcher, and Z. Hadzibabic: *Persistent currents in spinor condensates*, en, "Phys. Rev. Lett." vol. 110, no. 2, 025301 (2013) (cited on page 61).
- <sup>130</sup>Y. Cai, D. G. Allman, P. Sabharwal, and K. C. Wright: *Persistent currents in rings of ultracold fermionic atoms*, en, "Phys. Rev. Lett." vol. 128, no. 15, 150401 (2022) (cited on page 61).
- <sup>131</sup>G. Del Pace, K. Xhani, A. Muzi Falconi, M. Fedrizzi, N. Grani, D. Hernandez Rajkov, M. Inguscio, F. Scazza, W. J. Kwon, and G. Roati: *Imprinting persistent currents in tunable fermionic rings*, "Phys. Rev. X" vol. 12, no. 4, 041037 (2022) (cited on page 61).
- <sup>132</sup>C. Raman, M. Köhl, R. Onofrio, D. S. Durfee, C. E. Kuklewicz, Z. Hadzibabic, and W. Ketterle: *Evidence for a critical velocity in a Bose-Einstein condensed gas*, "Phys. Rev. Lett." vol. 83, no. 13, 2502–2505 (1999) (cited on page 62).
- <sup>133</sup>R. Desbuquois, L. Chomaz, T. Yefsah, J. Léonard, J. Beugnon, C. Weitenberg, and J. Dalibard: *Superfluid behaviour of a two-dimensional bose gas*, (2012) (cited on page 62).
- <sup>134</sup>W. Weimer, K. Morgener, V. P. Singh, J. Siegl, K. Hueck, N. Luick, L. Mathey, and H. Moritz: *Critical velocity in the BEC-BCS crossover*, en, "Phys. Rev. Lett." vol. 114, no. 9, 095301 (2015) (cited on pages 62, 65).
- <sup>135</sup>D. E. Miller, J. K. Chin, C. A. Stan, Y. Liu, W. Setiawan, C. Sanner, and W. Ketterle: *Critical velocity for superfluid flow across the BEC-BCS crossover*, en, "Phys. Rev. Lett." vol. 99, no. 7, 070402 (2007) (cited on pages 62, 65).
- <sup>136</sup>L.-C. Ha, L. W. Clark, C. V. Parker, B. M. Anderson, and C. Chin: *Roton-maxon excitation spectrum of bose condensates in a shaken optical lattice*, en, "Phys. Rev. Lett." vol. 114, no. 5, 055301 (2015) (cited on page 62).
- <sup>137</sup>G. E. Astrakharchik and L. P. Pitaevskii: *Motion of a heavy impurity through a Bose-Einstein condensate*, "Phys. Rev. A" vol. 70, no. 1, 013608 (2004) (cited on page 62).
- <sup>138</sup>L. Sobirey, H. Biss, N. Luick, M. Bohlen, H. Moritz, and T. Lompe: *Observing the influence of reduced dimensionality on fermionic superfluids*, en, "Phys. Rev. Lett." vol. 129, no. 8, 083601 (2022) (cited on pages 63, 67).
- <sup>139</sup>M. G. Ries, A. N. Wenz, G. Zürn, L. Bayha, I. Boettcher, D. Kedar, P. A. Murthy, M. Neidig, T. Lompe, and S. Jochim: *Observation of pair condensation in the Quasi-2D BEC-BCS crossover*, en, "Phys. Rev. Lett." vol. 114, no. 23, 230401 (2015) (cited on pages 65, 78, 95).
- <sup>140</sup>J. G. Bednorz and K. A. Müller: *Possible hightc superconductivity in the Ba-La-Cu-O system*, "Z. Phys. B: Condens. Matter" vol. 64, no. 2, 189–193 (1986) (cited on page 67).
- <sup>141</sup>Y. J. Uemura, L. P. Le, G. M. Luke, B. J. Sternlieb, W. D. Wu, J. H. Brewer, T. M. Riseman, C. L. Seaman, M. B. Maple, M. Ishikawa, D. G. Hinks, J. D. Jorgensen, G. Saito, and H. Yamochi: *Basic similarities among cuprate, bismuthate, organic, chevrel-phase, and heavy-fermion superconductors shown by penetration-depth measurements*, en, "Phys. Rev. Lett." vol. 66, no. 20, 2665–2668 (1991) (cited on page 67).
- <sup>142</sup>Y. Yu, L. Ma, P. Cai, R. Zhong, C. Ye, J. Shen, G. D. Gu, X. H. Chen, and Y. Zhang: *High-temperature superconductivity in monolayer Bi<sub>2</sub>Sr<sub>2</sub>CaCu<sub>2</sub>O<sub>8+δ</sub>*, en, "Nature" vol. 575, no. 7781, 156–163 (2019) (cited on page 67).
- <sup>143</sup>T. P. Devereaux and R. Hackl: *Inelastic light scattering from correlated electrons*, "Rev. Mod. Phys." vol. 79, no. 1, 175–233 (2007) (cited on page 69).
- <sup>144</sup>E. Vitali, H. Shi, M. Qin, and S. Zhang: *Visualizing the BEC-BCS crossover in a two-dimensional fermi gas: pairing gaps and dynamical response functions from ab initio computations*, "Phys. Rev. A" vol. 96, no. 6, 061601 (2017) (cited on pages 69, 70).

- <sup>145</sup>T. Zielinski, B. Ross, and A. Gezerlis: *Pairing in two-dimensional fermi gases with a coordinate-space potential*, “Phys. Rev. A” vol. 101, no. 3, 033601 (2020) (cited on pages 69, 70).
- <sup>146</sup>G. Bertaina and S. Giorgini: *BCS-BEC crossover in a two-dimensional fermi gas*, en, “Phys. Rev. Lett.” vol. 106, no. 11, 110403 (2011) (cited on pages 70, 106, 107).
- <sup>147</sup>P. Fulde and R. A. Ferrell: *Superconductivity in a strong Spin-Exchange field*, “Phys. Rev.” vol. 135, no. 3A, A550–A563 (1964) (cited on pages 75, 108).
- <sup>148</sup>A. I. Larkin and Y. N. Ovchinnikov: *NONUNIFORM STATE OF SUPERCONDUCTORS*, ru, “Zh. Eksperim. i Teor. Fiz.” vol. : 47 (1964) (cited on page 75).
- <sup>149</sup>G. Zwicknagl and J. Wosnitzer: *Kompromissbereite supraleitung*, “Phys. J.” vol. 31 (2015) (cited on page 75).
- <sup>150</sup>B. S. Chandrasekhar: *A NOTE ON THE MAXIMUM CRITICAL FIELD OF HIGH-FIELD SUPERCONDUCTORS*, “Appl. Phys. Lett.” vol. 1, no. 1, 7–8 (1962) (cited on page 75).
- <sup>151</sup>A. M. Clogston: *Upper limit for the critical field in hard superconductors*, “Phys. Rev. Lett.” vol. 9, no. 6, 266–267 (1962) (cited on page 75).
- <sup>152</sup>L. P. Gor’kov: *The critical supercooling field in superconductivity theory*, “Soviet Physics JETP” vol. 10, 593–599 (1960) (cited on page 76).
- <sup>153</sup>M. D. Croitoru and A. I. Buzdin: *In search of unambiguous evidence of the Fulde–Ferrell–Larkin–Ovchinnikov state in Quasi-Low dimensional superconductors*, en, “Z. Phys. B: Condens. Matter” vol. 2, no. 3, 30 (2017) (cited on page 76).
- <sup>154</sup>R. Lortz, Y. Wang, A. Demuer, P. H. M. Böttger, B. Bergk, G. Zwicknagl, Y. Nakazawa, and J. Wosnitzer: *Calorimetric evidence for a Fulde-Ferrell-Larkin-Ovchinnikov superconducting state in the layered organic superconductor kappa-(BEDT-TTF)<sub>2</sub>Cu(NCS)<sub>2</sub>*, en, “Phys. Rev. Lett.” vol. 99, no. 18, 187002 (2007) (cited on page 76).
- <sup>155</sup>R. Beyer, B. Bergk, S. Yasin, J. A. Schlueter, and J. Wosnitzer: *Angle-dependent evolution of the Fulde-Ferrell-Larkin-Ovchinnikov state in an organic superconductor*, en, “Phys. Rev. Lett.” vol. 109, no. 2, 027003 (2012) (cited on page 76).
- <sup>156</sup>H. Mayaffre, S. Krämer, M. Horvatić, C. Berthier, K. Miyagawa, K. Kanoda, and V. F. Mitrović: *Evidence of andreev bound states as a hallmark of the FFLO phase in kappa-(BEDT-TTF)<sub>2</sub>Cu(NCS)<sub>2</sub>*, en, “Nat. Phys.” vol. 10, no. 12, 928–932 (2014) (cited on page 76).
- <sup>157</sup>K. Kinjo, M. Manago, S. Kitagawa, Z. Q. Mao, S. Yonezawa, Y. Maeno, and K. Ishida: *Superconducting spin smecticity evidencing the Fulde-Ferrell-Larkin-Ovchinnikov state in Sr<sub>2</sub>RuO<sub>4</sub>*, en, “Science” vol. 376, no. 6591, 397–400 (2022) (cited on page 76).
- <sup>158</sup>Y. Shin, M. W. Zwierlein, C. H. Schunck, A. Schirotzek, and W. Ketterle: *Observation of phase separation in a strongly interacting imbalanced fermi gas*, en, “Phys. Rev. Lett.” vol. 97, no. 3, 030401 (2006) (cited on page 76).
- <sup>159</sup>M. W. Zwierlein, A. Schirotzek, C. H. Schunck, and W. Ketterle: *Fermionic superfluidity with imbalanced spin populations*, en, “Science” vol. 311, no. 5760, 492–496 (2006) (cited on pages 76, 77).
- <sup>160</sup>M. W. Zwierlein, C. H. Schunck, A. Schirotzek, and W. Ketterle: *Direct observation of the superfluid phase transition in ultracold fermi gases*, en, “Nature” vol. 442, no. 7098, 54–58 (2006) (cited on pages 76, 77).
- <sup>161</sup>Y. Shin, C. H. Schunck, A. Schirotzek, and W. Ketterle: *Tomographic rf spectroscopy of a trapped fermi gas at unitarity*, en, “Phys. Rev. Lett.” vol. 99, no. 9, 090403 (2007) (cited on page 76).

- <sup>162</sup>Y.-I. Shin, C. H. Schunck, A. Schirotzek, and W. Ketterle: *Phase diagram of a two-component fermi gas with resonant interactions*, en, "Nature" vol. 451, no. 7179, 689–693 (2008) (cited on pages 76, 101, 110).
- <sup>163</sup>Y.-I. Shin: *Determination of the equation of state of a polarized fermi gas at unitarity*, "Phys. Rev. A" vol. 77, no. 4, 041603 (2008) (cited on page 76).
- <sup>164</sup>Y.-I. Shin, A. Schirotzek, C. H. Schunck, and W. Ketterle: *Realization of a strongly interacting Bose-Fermi mixture from a two-component fermi gas*, en, "Phys. Rev. Lett." vol. 101, no. 7, 070404 (2008) (cited on pages 76, 105).
- <sup>165</sup>A. Schirotzek, C.-H. Wu, A. Sommer, and M. W. Zwierlein: *Observation of fermi polarons in a tunable fermi liquid of ultracold atoms*, en, "Phys. Rev. Lett." vol. 102, no. 23, 230402 (2009) (cited on pages 76, 77).
- <sup>166</sup>G. B. Partridge, W. Li, R. I. Kamar, Y.-A. Liao, and R. G. Hulet: *Pairing and phase separation in a polarized fermi gas*, en, "Science" vol. 311, no. 5760, 503–505 (2006) (cited on page 76).
- <sup>167</sup>G. B. Partridge, W. Li, Y. A. Liao, R. G. Hulet, M. Haque, and H. T. C. Stoof: *Deformation of a trapped fermi gas with unequal spin populations*, en, "Phys. Rev. Lett." vol. 97, no. 19, 190407 (2006) (cited on page 76).
- <sup>168</sup>G. Chaudhry and J. G. Brisson: *Thermodynamic properties of liquid  $^3\text{He}$ - $^4\text{He}$  mixtures between 0.15 K and 1.8 K*, "J. Low Temp. Phys." vol. 155, no. 5, 235–289 (2009) (cited on page 76).
- <sup>169</sup>J. del Cueto, R. L. Johnson, T. Rohde, F. H. Wirth, and E. H. Graf: *EXPERIMENTS IN  $^3\text{He}$ - $^4\text{He}$  LIQUID MIXTURES NEAR THE TRICRITICAL POINT*, en, "Le Journal de Physique Colloques" vol. 41, no. C7, C7–133–C7–136 (1980) (cited on page 76).
- <sup>170</sup>N. Navon, S. Nascimbène, F. Chevy, and C. Salomon: *The equation of state of a low-temperature fermi gas with tunable interactions*, en, "Science" vol. 328, no. 5979, 729–732 (2010) (cited on page 77).
- <sup>171</sup>M. M. Parish, F. M. Marchetti, A. Lamacraft, and B. D. Simons: *Finite-temperature phase diagram of a polarized fermi condensate*, en, "Nat. Phys." vol. 3, no. 2, 124–128 (2007) (cited on pages 77, 106, 110).
- <sup>172</sup>H. Shimahara: *Theory of the Fulde–Ferrell–Larkin–Ovchinnikov state and application to Quasi-Low-dimensional organic superconductors*, in *The physics of organic superconductors and conductors*, edited by A. Lebed, Berlin, Heidelberg: Springer Berlin Heidelberg 2008, pp. 687–704 (cited on pages 77, 108).
- <sup>173</sup>A. Ptok: *The influence of the dimensionality of the system on the realization of unconventional Fulde-Ferrell-Larkin-Ovchinnikov pairing in ultra-cold fermi gases*, en, "J. Phys. Condens. Matter" vol. 29, no. 47, 475901 (2017) (cited on page 77).
- <sup>174</sup>W. Ong, C. Cheng, I. Arakelyan, and J. E. Thomas: *Spin-imbalanced quasi-two-dimensional fermi gases*, en, "Phys. Rev. Lett." vol. 114, no. 11, 110403 (2015) (cited on pages 77, 84).
- <sup>175</sup>D. Mitra, P. T. Brown, P. Schauß, S. S. Kondov, and W. S. Bakr: *Phase separation and pair condensation in a Spin-Imbalanced 2D fermi gas*, en, "Phys. Rev. Lett." vol. 117, no. 9, 093601 (2016) (cited on pages 77, 78, 81, 84, 95).
- <sup>176</sup>P. Cladé, C. Ryu, A. Ramanathan, K. Helmerson, and W. D. Phillips: *Observation of a 2D bose gas: from thermal to quasicondensate to superfluid*, en, "Phys. Rev. Lett." vol. 102, no. 17, 170401 (2009) (cited on page 78).
- <sup>177</sup>N. Luick, L. Sobirey, M. Bohlen, V. P. Singh, L. Mathey, T. Lompe, and H. Moritz: *An ideal josephson junction in an ultracold two-dimensional fermi gas*, en, "Science" vol. 369, no. 6499, 89–91 (2020) (cited on page 82).

- <sup>178</sup>P. T. Brown, D. Mitra, E. Guardado-Sanchez, P. Schauß, S. S. Kondov, E. Khatami, T. Paiva, N. Trivedi, D. A. Huse, and W. S. Bakr: *Spin-imbalance in a 2D Fermi-Hubbard system*, en, “Science” vol. 357, no. 6358, 1385–1388 (2017) (cited on page 83).
- <sup>179</sup>T. Lompe: *Efimov physics in a three-component fermi gas*, PhD thesis, Ruperto-Carola University of Heidelberg, Germany June 2011 (cited on page 86).
- <sup>180</sup>C. Zener and R. H. Fowler: *Non-adiabatic crossing of energy levels*, “Proceedings of the Royal Society of London. Series A, Containing Papers of a Mathematical and Physical Character” vol. 137, no. 833, 696–702 (1932) (cited on page 86).
- <sup>181</sup>G. Sun, X. Wen, M. Gong, D.-W. Zhang, Y. Yu, S.-L. Zhu, J. Chen, P. Wu, and S. Han: *Observation of coherent oscillation in single-passage Landau-Zener transitions*, en, “Sci. Rep.” vol. 5, 8463 (2015) (cited on page 87).
- <sup>182</sup>R. Grimm, M. Weidemüller, and Y. B. Ovchinnikov: *Optical dipole traps for neutral atoms*, (1999) (cited on page 89).
- <sup>183</sup>L. He and P. Zhuang: *Phase diagram of a cold polarized fermi gas in two dimensions*, “Phys. Rev. A” vol. 78, no. 3, 033613 (2008) (cited on pages 98–105).
- <sup>184</sup>J. Tempere, M. Wouters, and J. T. Devreese: *Imbalanced fermi superfluid in a one-dimensional optical potential*, “Phys. Rev. B Condens. Matter” vol. 75, no. 18, 184526 (2007) (cited on pages 98, 106–108).
- <sup>185</sup>K. B. Gubbels and H. T. C. Stoof: *Imbalanced fermi gases at unitarity*, (2012) (cited on pages 99, 110).
- <sup>186</sup>G. Sarma: *On the influence of a uniform exchange field acting on the spins of the conduction electrons in a superconductor*, “J. Phys. Chem. Solids” vol. 24, no. 8, 1029–1032 (1963) (cited on page 99).
- <sup>187</sup>I. Boettcher, T. K. Herbst, J. M. Pawłowski, N. Strodthoff, L. von Smekal, and C. Wetterich: *Sarma phase in relativistic and non-relativistic systems*, “Phys. Lett. B” vol. 742, 86–93 (2015) (cited on pages 99, 105).
- <sup>188</sup>A. Mori, B. B. Laird, Y. Kangawa, T. Ito, and A. Koukitu: *Semigrand canonical monte carlo simulation with Gibbs-Duhem integration technique for alloy phase diagrams*, en, “Mater. Phy. Mech.” vol. 6, no. 1, 49–57 (2003) (cited on page 101).
- <sup>189</sup>G. Bighin and L. Salasnich: *Finite-temperature quantum fluctuations in two-dimensional fermi superfluids*, “Phys. Rev. B Condens. Matter” vol. 93, no. 1, 014519 (2016) (cited on page 106).
- <sup>190</sup>G. Bighin and L. Salasnich: *Renormalization of the superfluid density in the two-dimensional BCS-BEC crossover*, “Int. J. Mod. Phys. B” vol. 32, no. 17, 1840022 (2018) (cited on page 106).
- <sup>191</sup>L. Salasnich: *Goldstone and higgs hydrodynamics in the BCS-BEC crossover*, en, “Z. Phys. B: Condens. Matter” vol. 2, no. 2, 22 (2017) (cited on page 106).
- <sup>192</sup>D. S. Petrov, M. A. Baranov, and G. V. Shlyapnikov: *Superfluid transition in quasi-two-dimensional fermi gases*, “Phys. Rev. A” vol. 67, no. 3, 031601 (2003) (cited on page 107).
- <sup>193</sup>V. Ngampruetikorn, M. M. Parish, and J. Levinsen: *Three-body problem in a two-dimensional fermi gas*, en, “EPL” vol. 102, no. 1, 13001 (2013) (cited on page 107).
- <sup>194</sup>U. Toniolo, B. Mulkerin, X.-J. Liu, and H. Hu: *Larkin-Ovchinnikov superfluidity in a two-dimensional imbalanced atomic fermi gas*, “Phys. Rev. A” vol. 95, no. 1, 013603 (2017) (cited on pages 108, 109).
- <sup>195</sup>J. J. Kinnunen, J. E. Baarsma, J.-P. Martikainen, and P. Törmä: *The Fulde-Ferrell-Larkin-Ovchinnikov state for ultracold fermions in lattice and harmonic potentials: a review*, en, “Rep. Prog. Phys.” vol. 81, no. 4, 046401 (2018) (cited on pages 108, 116).

- <sup>196</sup>D. E. Sheehy: *Fulde-Ferrell-Larkin-Ovchinnikov state of two-dimensional imbalanced fermi gases*, “Phys. Rev. A” vol. 92, no. 5, 053631 (2015) (cited on page 108).
- <sup>197</sup>G. J. Conduit, P. H. Conlon, and B. D. Simons: *Superfluidity at the BEC-BCS crossover in two-dimensional fermi gases with population and mass imbalance*, “Phys. Rev. A” vol. 77, no. 5, 053617 (2008) (cited on page 109).
- <sup>198</sup>S. Yin, J.-P. Martikainen, and P. Törmä: *Fulde-Ferrell states and Berezinskii-Kosterlitz-Thouless phase transition in two-dimensional imbalanced fermi gases*, “Phys. Rev. B Condens. Matter” vol. 89, no. 1, 014507 (2014) (cited on page 109).
- <sup>199</sup>J. Wang, Y. Che, L. Zhang, and Q. Chen: *Instability of Fulde-Ferrell-Larkin-Ovchinnikov states in atomic fermi gases in three and two dimensions*, “Phys. Rev. B Condens. Matter” vol. 97, no. 13, 134513 (2018) (cited on page 109).
- <sup>200</sup>D. C. W. Foo and G. J. Conduit: *Diffusion monte carlo study of a spin-imbalanced two-dimensional fermi gas with attractive interactions*, “Phys. Rev. A” vol. 100, no. 6, 063602 (2019) (cited on page 109).
- <sup>201</sup>P. Strack and P. Jakubczyk: *Fluctuations of imbalanced fermionic superfluids in two dimensions induce continuous quantum phase transitions and Non-Fermi-Liquid behavior*, “Phys. Rev. X” vol. 4, no. 2, 021012 (2014) (cited on page 109).
- <sup>202</sup>J. Tempere, S. N. Klimin, and J. T. Devreese: *Effect of population imbalance on the Berezinskii-Kosterlitz-Thouless phase transition in a superfluid fermi gas*, “Phys. Rev. A” vol. 79, no. 5, 053637 (2009) (cited on pages 110, 111).
- <sup>203</sup>A. Gabovich: *Superconductors: materials, properties and applications*, en, BoD – Books on Demand Oct. 2012 (cited on page 110).
- <sup>204</sup>F. Heidrich-Meisner, A. E. Feiguin, U. Schollwöck, and W. Zwerger: *BCS-BEC crossover and the disappearance of Fulde-Ferrell-Larkin-Ovchinnikov correlations in a spin-imbalanced one-dimensional fermi gas*, “Phys. Rev. A” vol. 81, no. 2, 10.1103/physreva.81.023629 (2010) (cited on page 111).
- <sup>205</sup>S. Stringari: *Density and spin response function of a normal fermi gas at unitarity*, en, “Phys. Rev. Lett.” vol. 102, no. 11, 110406 (2009) (cited on page 115).
- <sup>206</sup>A. T. M. Falconi: *Realization of spin-dependent optical potentials for quantum transport in ultracold fermi gases*, PhD thesis, University of Milan 2021 (cited on page 115).
- <sup>207</sup>P. Dyke, E. D. Kuhnle, S. Whitlock, H. Hu, M. Mark, S. Hoinka, M. Lingham, P. Hannaford, and C. J. Vale: *Crossover from 2D to 3D in a weakly interacting fermi gas*, en, “Phys. Rev. Lett.” vol. 106, no. 10, 105304 (2011) (cited on page 115).
- <sup>208</sup>T. Peppler, P. Dyke, M. Zamorano, I. Herrera, S. Hoinka, and C. J. Vale: *Quantum anomaly and 2D-3D crossover in strongly interacting fermi gases*, en, “Phys. Rev. Lett.” vol. 121, no. 12, 120402 (2018) (cited on page 115).
- <sup>209</sup>A. M. Fischer and M. M. Parish: *BCS-BEC crossover in a quasi-two-dimensional fermi gas*, “Phys. Rev. A” vol. 88, no. 2, 023612 (2013) (cited on page 115).
- <sup>210</sup>Y. Ding, J. P. D’Incao, and C. H. Greene: *Effective control of cold collisions with radio-frequency fields*, “Phys. Rev. A” vol. 95, no. 2, 022709 (2017) (cited on page 115).
- <sup>211</sup>J. Sanz, A. Frölian, C. S. Chisholm, C. R. Cabrera, and L. Tarruell: *Interaction control and bright solitons in coherently coupled Bose-Einstein condensates*, en, “Phys. Rev. Lett.” vol. 128, no. 1, 013201 (2022) (cited on page 115).
- <sup>212</sup>E. Nicklas, H. Strobel, T. Zibold, C. Gross, B. A. Malomed, P. G. Kevrekidis, and M. K. Oberthaler: *Rabi flopping induces spatial demixing dynamics*, en, “Phys. Rev. Lett.” vol. 107, no. 19, 193001 (2011) (cited on page 115).

- <sup>213</sup>A. Niroula, G. Rai, S. Haas, and S. Kettemann: *Spatial BCS-BEC crossover in superconducting p{-}n junctions*, “Phys. Rev. B Condens. Matter” vol. 101, no. 9, 094514 (2020) (cited on page 115).
- <sup>214</sup>H. Lin, W. Huang, G. Rai, Y. Yin, L. He, Q.-K. Xue, S. Haas, S. Kettemann, X. Chen, and S.-H. Ji: *Real-space BCS-BEC crossover in FeSe monolayers*, “Phys. Rev. B Condens. Matter” vol. 107, no. 10, 104517 (2023) (cited on page 115).
- <sup>215</sup>J. M. Edge and N. R. Cooper: *Signature of the Fulde-Ferrell-Larkin-Ovchinnikov phase in the collective modes of a trapped ultracold fermi gas*, en, “Phys. Rev. Lett.” vol. 103, no. 6, 065301 (2009) (cited on page 116).
- <sup>216</sup>N. Manini and L. Salasnich: *Bulk and collective properties of a dilute fermi gas in the BCS-BEC crossover*, “Phys. Rev. A” vol. 71, no. 3, 033625 (2005) (cited on page 121).
- <sup>217</sup>G. Breit and I. I. Rabi: *Measurement of nuclear spin*, “Phys. Rev.” vol. 38, no. 11, 2082–2083 (1931) (cited on page 125).
- <sup>218</sup>S. Jochim: *Bose-Einstein condensation of molecules*, PhD thesis, Leopold-Franzens-Universitat Innsbruck 2004 (cited on page 125).
- <sup>219</sup>J. H. Huckans: *Optical lattices and quantum degenerate <sup>87</sup>Rb in reduced dimensions*, PhD thesis, 2006 (cited on page 127).
- <sup>220</sup>T. C. Li, H. Kelkar, D. Medellin, and M. G. Raizen: *Real-time control of the periodicity of a standing wave: an optical accordion*, en, “Opt. Express” vol. 16, no. 8, 5465–5470 (2008) (cited on page 127).
- <sup>221</sup>S. Al-Assam, R. A. Williams, and C. J. Foot: *Ultracold atoms in an optical lattice with dynamically variable periodicity*, “Phys. Rev. A” vol. 82, no. 2, 021604 (2010) (cited on page 127).
- <sup>222</sup>F. G. Huber: *Site-Resolved imaging with the fermi gas microscope*, PhD thesis, Harvard University 2014 (cited on page 127).
- <sup>223</sup>J. L. Ville, T. Bienaimé, R. Saint-Jalm, L. Corman, M. Aidelsburger, L. Chomaz, K. Kleinlein, D. Perconte, S. Nascimbène, J. Dalibard, and J. Beugnon: *Loading and compression of a single two-dimensional bose gas in an optical accordion*, “Phys. Rev. A” vol. 95, no. 1, 013632 (2017) (cited on page 127).



## DANKSAGUNG

An dieser Stelle möchte ich mich gerne bei allen lieben Menschen bedanken, die mich in den vergangenen Jahren begleitet haben und ohne deren Unterstützung diese Arbeit nicht möglich gewesen wäre.

Besonders bedanke ich mich bei Henning für die exzellente Betreuung meiner Doktorarbeit. Dein Enthusiasmus für Physik hat mich von Anfang an angesteckt und hat mich immer wieder sehr motiviert. Ich schätze deine sehr engagierte Betreuung und dein hilfreiches Feedback. Diese zusammen mit deiner Geduld haben es mir ermöglicht, mich weiterzuentwickeln und in meine Aufgaben reinzuwachsen.

Ganz herzlich möchte ich mich bei all den lieben Menschen bedanken, mit denen ich in den letzten Jahren im Labor zusammenarbeiten durfte. Dazu gehören Thomas, Lennart, Niclas und Markus, die mich mit dem Experiment vertraut gemacht haben und am Anfang meiner Doktorarbeit dafür gesorgt haben, dass ich mich sofort wohl gefühlt habe. Die Zeit mit euch war sehr spannend, denn es ging direkt mit aufregenden Experimenten los.

Des Weiteren möchte ich mich bei Cesar, René und Jonas für die großartige Zusammenarbeit und den unzähligen spannenden Diskussionen in der zweiten Hälfte meiner Doktorarbeit bedanken. Zusammen haben wir aufwendig das Experiment umgebaut und viele Herausforderungen gemeistert. Dabei mangelte es nie an guten Sprüchen im Labor. Ich freue mich sehr, bald wieder mit euch im Labor zusammen zu arbeiten.

Bei Alexandra, Martin und Leon möchte ich mich dafür bedanken, dass ihr von Beginn an immer für Fragen und späte Diskussionen da wart und so alternative Perspektiven geboten habt. Auch allen anderen täglichen Begleiter:innen aus der Gruppe möchte ich sagen: Ihr seid wunderbare Kolleg:innen und ich freue mich, mit euch Zeit zu verbringen!

Ich möchte mich gerne bei Ludwig für die gute Betreuung und die vielen sehr aufschlussreichen Diskussionen, die maßgeblich mein theoretisches Verständnis vorangebracht haben, bedanken.

Zu guter Letzt gilt mein Dank meiner Familie, meinen Freund:innen und besonders Helke. Ich bin so dankbar solch einen lieben Menschen in meinem Leben zu haben. Deine Zuversicht und dein Rat haben erheblich zu dem Gelingen dieser Arbeit beigetragen.



## EIDESSTATTLICHE VERSICHERUNG

Hiermit versichere ich an Eides statt, die vorliegende Dissertationsschrift selbst verfasst und keine anderen als die angegebenen Hilfsmittel und Quellen benutzt zu haben.

Hamburg, den 03.08.2023

---

Unterschrift der Doktorandin / des Doktoranden